

LIQUID CRYSTAL-GOLD NANOPARTICLE COMPOSITES

By

Hao Qi

A thesis submitted to the Faculty of Graduate Studies in partial fulfillment of the
requirements for the degree of

Doctor of Philosophy

Department of Chemistry

University of Manitoba

Winnipeg, MB, Canada

R3T 2N2

© Copyright by Hao Qi, 2009

Abstract

Studies of liquid crystal (LC) /Au nanoparticle (NP) composites have been pursued in columnar and in nematic phases of thermotropic LCs.

Using LCs forming a columnar phase, we found that different functionalities on the corona of the Au NPs (hydrophobic vs. hydrophilic) display unique effects on the stability and ordering of the columnar LC phase.

Doping nematic LCs with non-chiral or chiral Au NPs causes the formation of textures commonly observed for chiral nematic LCs, i.e., the formation of somewhat uniform stripe textures or patterns separated by areas of homeotropic alignment of LC molecules. Two scenarios are proposed. In the first scenario, the Au NPs form topological chain-like defects and the remaining Au NPs reside at the interface inducing vertical alignment of the LC molecules. In the second scenario, chiral Au NPs transfer chirality to the nematic LC host. Further, induced circular dichroism studies proved the second scenario. Using the same chiral Au NP systems, the origin of chirality of Au NPs has also been studied, and a powerful methodology has been proposed to unravel the puzzle of chirality of chiral ligand-protected Au NPs.

Further investigations of these texture phenomena led to the discovery of using metal NPs to control the orientation and alignment of LCs. In due course, a dual alignment and electro-optical switching behaviour was found using alkylthiol-capped Au NPs doped into a nematic LC with positive dielectric anisotropy in planar nematic LC cells. This study was also expanded to Ag and CdTe NPs, which showed the same phenomenon, and all investigated NPs significantly reduced the voltage needed to re-orient the LCs in an electric field (threshold voltage).

Starting from basic and moving on to more application-oriented research, we finally also initiated structure-property relationship studies of LC/NP composites.

Acknowledgements

This work may not be possible without the help of many individuals.

I would like to first thank my supervisor and mentor Dr. T. Hegmann for his wisdom, guidance, patience and assistance. I am his first student, one of the five people who first came to the lab in 2004, and the last one among the five people leaving the lab – many new faces have come and gone during these years. Numerous memories in these five years - I remember all the details of the extensive discussion of research in his office, I remember the color along the red river outside the window, I remember in the first winter, I came to the lab at 10 o'clock at night to check the reaction, and the bus was late, when I went back home, it was already midnight...

I would like to thank my committee members: Dr. M. Freund, Dr. D. Oliver and Dr. J. O'Neil for their comments and guidance during this project. Questions at my annual reports gave me lots of help for my research: one example is that Dr. Freund asked me what would happen if I fill the pure LC in the cell before filling the LC/NP mixture, which gave me an direct help to sample preparation; another one is that I remember at my first annual report, Dr. Oliver suggested me that it is maybe better that the research topic may not be too broad, I didn't realize the importance of the meaning until several years later; Dr. J. O'Neil gave me lots of help with my chirality related research.

I would like to thank the following labmates: Andrea Lepp, Ngoc On, Piao Piao Wei, Rodney Smith, Michael Tekeste, Vinith Yathindranath, Brandy Kinkead and James Tansley.

Last but most important, I want to thank my dear wife Lei Zhang, for everything. I also thank my parents and my baby daughter. Life is meaningless without love.

Table of Contents

Abstract.....	i
Acknowledgements.....	iii
Contributions of Authors.....	xi
List of Abbreviations	xii
List of Figures	xiv
List of Tables	xxiv
Chapter 1: Liquid Crystals and Gold Nanoparticles - Introduction and Background	1
1.1 Introduction.....	1
1.2 Liquid Crystals	2
1.2.1 Liquid Crystal Materials and Liquid Crystal Phase	2
1.2.2 Characterization of LCs.....	8
1.2.2.1 Polarizing Optical Microscopy and LC Textures.....	9
1.2.2.2 Differential scanning calorimetry.....	13
1.2.2.3 X-ray Diffraction	14
1.2.3 Liquid Crystal Displays (LCDs)	18
1.3 Gold Nanoparticles	26
1.3.1 Synthesis of Au NPs	26
1.3.2 Characterization of Au NPs	28
1.3.3 Assembly of Au NPs	34
References.....	40
Chapter 2: Liquid crystal / nanoparticle composites – A Review.....	52

2.1 Tuning NP Properties Using LCs	52
2.1.1 NP Assembly.....	52
2.1.1.1 NPs Forming LC Phases.....	53
2.1.1.2 NPs Decorated with LC Molecules.....	54
2.1.1.3 NPs Suspended in LC Hosts	56
2.1.2 Other Properties of NPs.....	58
2.2 Modulating LC properties using NPs.....	59
2.2.1 Defect formation via doping particles	59
2.2.2 Electro-optical properties of LCs and emerging display related applications using NP doping	62
2.3 Concluding Remarks and Outline of the Thesis	64
Reference	66
Chapter 3: Materials and Methods	75
3.1 Materials.....	75
3.1.1 LCs	75
3.1.2 Au NPs.....	76
3.2 Methods	80
3.2.1 Characterization of the Au NPs.....	80
3.2.2 Characterization of LCs and LC/Au NP composites.....	80
References	82
Chapter 4: Effects of hydrophilic and hydrophobic gold nanoclusters on the stability and ordering of bolaamphiphilic liquid crystals.....	84
Abstract	85

4.1 Introduction	85
4.2 Experimental	88
4.2.1 General methods	88
4.2.2 Synthesis	90
4.3 Results and discussion	91
4.3.1 Thermal properties	91
4.3.2 Structural characterization	91
4.4 Conclusions	98
Acknowledgements	100
References.....	100
Appendix A: Supplementary Information for Chapter 4.....	105
Chapter 5: Formation of periodic stripe patterns in nematic liquid crystals doped with functionalized gold nanoparticles.....	113
Abstract	114
5.1 Introduction	115
5.2 Experimental	119
5.2.1 General methods	119
5.2.2 Synthesis of Au nanoclusters (Au1–Au4)	122
5.2.3 LC–nanoparticle mixtures	124
5.3 Results and discussion	125
5.3.1 Optical activity and circular dichroism	125
5.3.2 Mixtures with nematic LCs	128
5.4 Conclusions	135

Acknowledgements	137
References and notes.....	137
Appendix B: Supplementary Information for Chapter 5	142
Chapter 6: Chirality transfer in nematic liquid crystals doped with (<i>S</i>)-naproxen-functionalized gold nanoclusters: an induced circular dichroism study	151
Abstract	152
6.1 Introduction	153
6.2 Experimental	156
6.3 Results and discussion	157
6.4 Conclusions	169
Acknowledgements	170
References.....	170
Chapter 7: Postsynthesis Racemization and Place Exchange Reactions: Another Step to Unravel the Origin of Chirality for Chiral Ligand-Capped Gold Nanoparticles	176
Abstract.....	177
7.1 Introduction.....	177
7.2 Experimental	181
7.3 Results and Discussion.....	183
7.3.1 In-Situ-Synthesized Chiral Mixed-Monolayer Au NPs	183
7.3.2 Postsynthesis Racemization.....	186
7.3.3 Place Exchange Reaction	189

7.4 Conclusion.....	194
Acknowledgements.....	195
References	195
Appendix C: Supplementary Information for Chapter 7	199
Chapter 8: Unprecedented Dual Alignment Mode and Freedericksz Transition in Planar Nematic Liquid Crystal Cells Doped with Gold Nanoclusters	214
Abstract.....	215
8.1. Introduction.....	215
8.2 Experimental	220
8.3 Results and Discussion	223
8.3.1 Qualitative Alignment and Electro-optics	223
8.3.2 Quantitative Electro-optics	229
8.3.3 Model	236
8.4 Conclusion.....	241
References	241
Appendix D: Supplementary Information for Chapter 8	246
Chapter 9: Effects of functionalized metal and semiconductor nanoparticles in nematic liquid crystal phases	254
Abstract.....	255
9. 1. Introduction.....	255
9.2 Experimental	260
9.2.1 Materials	260

9.2.2 Sample preparation	261
9.2.3 Methods	262
9.3 Results and Discussion	263
9.3.1 Felix-2900-03 doped with Au NPs (Au ₃)	264
9.3.2 Felix-2900-03 doped with Ag NPs (Ag ₁)	265
9.3.3 Felix-2900-03 doped with CdTe (QD2)	267
9.3.4 8CB doped with CdTe (QD1 and QD2)	271
9.4 Conclusion	272
Acknowledgements	273
References	274
Chapter 10: Miscibility and alignment effects of mixed monolayer cyanobiphenyl	
liquid crystal-capped gold nanoparticles in nematic cyanobiphenyl liquid	
crystal hosts.....	278
Abstract	279
10.1 Introduction	279
10.2 Experimental	281
10.2.1 General.....	281
10.2.2 Synthesis	283
10.2.3 Compatibility Studies	283
10.3 Results and Discussion	287
10.3.1 Optical inspection and effects between untreated glass slides	287
10.3.2 Effects in planar ITO cells with polyimide alignment layers	292
10.4 Conclusion	302

Acknowledgements	303
References	304
Appendix E: Supplementary Information for Chapter 10.....	308
Chapter 11: Conclusions, Future Work and Outlook	313
11.1 Conclusions	313
11.2 Future Work and Outlook	317
References	319
Copyright	321

Contributions of Authors

- Chapter 4: Effects of hydrophilic and hydrophobic gold nanoclusters on the stability and ordering of bolaamphiphilic liquid crystals
H. Qi, A. Lepp, P. A. Heiney, T. Hegmann, *J. Mater. Chem.* **2007**, *17*, 2139-2144.
- Chapter 5: Formation of periodic stripe patterns in nematic liquid crystals doped with functionalized gold nanoparticles
H. Qi, T. Hegmann, *J. Mater. Chem.* **2006**, *16*, 4197-4205.
- Chapter 6: Chirality transfer in nematic liquid crystals doped with (*S*)-naproxen-functionalized gold nanoclusters: an induced circular dichroism study
H. Qi, J. O'Neil, T. Hegmann, *J. Mater. Chem.* **2008**, *18*, 374-380.
- Chapter 7: Postsynthesis Racemization and Place Exchange Reactions: Another Step to Unravel the Origin of Chirality for Chiral Ligand-Capped Gold Nanoparticles
H. Qi, T. Hegmann, *J. Am. Chem. Soc.* **2008**, *130*, 14201-14206.
- Chapter 8: Unprecedented Dual Alignment Mode and Freedericksz Transition in Planar Nematic Liquid Crystal Cells Doped with Gold Nanoclusters
H. Qi, B. Kinhead, T. Hegmann, *Adv. Funct. Mater.* **2008**, *18*, 212-221.
- Chapter 9: Effects of functionalized metal and semiconductor nanoparticles in nematic liquid crystal phases
H. Qi, B. Kinhead, T. Hegmann, *Proc. SPIE* **2008**, *6911*, 691106
- Chapter 10: Miscibility and alignment effects of mixed monolayer cyanobiphenyl liquid crystal-capped gold nanoparticles in nematic cyanobiphenyl liquid crystal hosts
H. Qi, B. Kinhead, V. M. Marx, H. R. Zhang, T. Hegmann, *ChemPhysChem*. *In press*.

The work presented was mainly performed by the author, as supervised by Dr. T. Hegmann. A. Lepp performed several steps for the synthesis of the bolaamphiphilic LCs in Chapter 4. P. A. Heiney performed the x-ray measurements for Chapter 4. J. O'Neil gave help and suggestions for CD measurement in Chapter 5. B. Kinhead synthesized the CdTe QDs presented in Chapters 8 and 9 as well as did the electro-optic measurements for Chapter 10. V. M. Marx synthesized the thiol used in Chapter 10. H. R. Zhang did the TEM measurements shown in Chapter 10.

List of Abbreviations

Au NPs	Gold Nanoparticles
CD	Circular Dichroism
cmc	Critical micelle concentration
Col _h	Hexagonal columnar phase
Col _{ob}	Oblique columnar phase
Col _r	Rectangular columnar phase
Col _{tet}	Tetragonal columnar phase
Cr	Crystalline phase
Cub	Cubic phase
Cub _I	Micellar cubic phase
Cub _V	Bicontinuous cubic phase
DLS	Dynamic light scattering
DSC	Differential Scanning Calorimetry
EDS	Energy dispersive x-ray spectroscopy
EELS	Electron energy-loss spectroscopy
FWHM	Full width at half-maximum
HOPG	Highly ordered pyrolytic graphite
Iso	Isotropic phase
IPS	In-plane switching mode
LC	Liquid Crystals
LCD	Liquid crystal display
MVA	Multi-domain vertical alignment mode

N	Nematic phase
N*	Chiral nematic phase
N _D	Discotic nematic phase
N _u	Uniaxial nematic phase
N _{Col}	Columnar nematic phase
NMR	Nuclear magnetic resonance
PDLC	Polymer dispersed LC mode
POM	Polarized Optical Microscopy
PPE	Poly(paraphenylene)
PVA	Patterned vertical alignment mode
PVP	Poly(vinyl-pyrrolidone)
SmA	Smectic A phase
SmC	Smectic C phase
SmC*	Chiral Smectic C phase
SPR	Surface Plasmon Resonance
STN	Super twisted nematic mode
TEM	Transmission Electron Microscopy
TGB	Twist grain boundary phase
TN	Twisted nematic mode
TOAB	Tetraoctylammonium bromide
UV-vis	Ultraviolet – visible absorption spectroscopy
XRD	x-ray diffraction

List of Figures

Fig. 1.1. Typical examples (and molecular shapes) of the main types of molecules forming LC phases.....	3
Fig. 1.2. Presentation of the main types of nematic and positional ordered thermotropic LC phases formed by rod-like, disk-like.....	5
Fig. 1.3. Presentation of the main types of lyotropic LC phases.....	8
Fig. 1.4. Schematic setup of a polarized optical microscope.....	9
Fig. 1.5. Several examples of typical LC textures.....	11
Fig. 1.6. Illustration of DSC sample block.....	13
Fig. 1.7. DSC plots of 8CB with phase transition temperatures and chemical structure.....	14
Fig. 1.8. X-ray diffraction from two planes in a crystal material.....	15
Fig. 1.9. Schematic of X-ray diffraction experimental set up.	16
Fig. 1.10. Local structure and x-ray powder pattern from unaligned LC samples.....	18
Fig. 1.11. Schematic illustration of LC response in electric field.....	20
Fig. 1.12. Schematic illustration of Freedericksz transition.....	20
Fig. 1.13. The three basic types of deformation in LCs.....	20
Fig. 1.14. Nematic LC textures in (a) untreated surface; (b) planar condition; (c) homeotropic condition.	21
Fig. 1.15. Examples of LCD modes: (a) TN mode, (b) IPS mode, and (c) MVA mode.	24
Fig. 1.16. Formation of Au NPs by the Brust-Schiffrin method.....	26
Fig. 1.17. Examples of Au NP functionalization.....	27
Fig. 1.18. Schematic of a TEM set-up.....	28
Fig. 1.19. TEM image of dodecane thiol protected Au NPs	29
Fig. 1.20. XRD spectra of triethylene glycol-terminated pentyl thiol-protected Au	

NPs.....	30
Fig. 1.21. Schematic illustration of the origin of SPR of spherical Au NPs.....	31
Fig. 1.22. UV-vis spectra of Au NPs.....	31
Fig. 1.23. NMR spectra of (a) free (<i>S</i>)-naproxen-functionalized dodecane thiol (b) (<i>S</i>)-naproxen-functionalized dodecane thiol protected Au NPs.	32
Fig. 1.24. TEM image of an AB ₂ type superlattice of Au and Ag NPs stabilised by decanethiol.....	34
Fig. 1.25. TEM image of linear assembly of Au NPs aggregates.....	35
Fig. 1.26. TEM image of a string of PPE, decorated with two chains of [Au ₅₅] clusters.....	36
Fig. 1.27. TEM images of Au NP double helices.....	38
Fig. 2.1. (a) TEM image of CdSe nanorods with width of approximately 4.2 nm and length of 40 nm. (b) Image of liquid crystalline phase in concentrated solution of CdSe nanocrystals using a polarized light optical microscope.....	52
Fig. 2.2. (a) Schematic representation of the Au NP synthesis using LC thiols in a place exchange reaction, and (b) polarized light optical photomicrograph image of the Au NPs showing the typical nematic <i>Schlieren</i> texture.....	54
Fig. 2.3. (a) Scheme of organizing carbon nanotubes with an LC solvent (b) An AFM image of aligned multi-walled carbon nanotubes.....	56
Fig. 2.4. Typical defects created by spherical particles in nematic LCs.....	60
Fig. 4.1. (a) Structure and LC phase morphology of the SmA and Col _r (c2mm) phases formed by 1 and 2 . (b) Gold nanoclusters Au1 and Au2 used in dispersions with the bolaamphiphilic liquid crystals 1 and 2 . (c, d) TEM images of the gold clusters: (c) Au1 , and (d) Au2	83
Fig. 4.2. Polarized optical photomicrographs of the NP–LC mixtures on cooling from the isotropic liquid phase.....	87
Fig. 4.3. Stability of the columnar phase of 2 vs. concentration of suspended nanoclusters obtained by DSC.....	88
Fig. 4.4. TEM images of the gold clusters dispersed in the liquid crystal phases of 1 and 2 :	90

Fig. 4.5.	SAXS of (a) pure 2 (<i>c2mm</i>) at 95 °C on heating, (b) 5 wt% Au1 in 2 at 90 °C on cooling, (c) 5 wt% Au2 in 2 at 105 °C on cooling, (d) 10 wt% Au2 in 2 at 103 °C on cooling, and (e) least-square fits to diffractogram (d), (200) peak positions: $q_2 = 0.3700 \text{ \AA}^{-1}$, $q_3 = 0.3753 \text{ \AA}^{-1}$ indicating the coexistence of two Col _r phases with slightly different lattice parameters.....	91
Fig. 4.6.	POM micrographs of the 10 wt% Au2 in 2 mixture.....	93
Fig. S4.1.	UV-vis spectrum of Au NPs (Au1, Au2).....	101
Fig. S4.2.	TEM and size distribution of Au NPs.....	101
Fig. S4.3.	Wide-angle Powder XRD of Au1 and Au2.....	102
Fig. S4.4.	TEM image of mixture of gold nanoclusters in LCs.....	103
Fig. S4.5.	DSC for Au2 in 2	105
Fig. S4.6.	Main text Fig. 4.6 with enlarged segments.....	107
Fig. 5.1.	POM micrographs (crossed polarizers) of the N phase of LC and LC/NP mixture taken on cooling from just below the Iso–N phase transition (T_{NI}).....	112
Fig. 5.2.	(a) Structures and phase transition temperatures (°C) of LC1–LC3 . (b) General (truncated) cuboctahedral shape of the gold colloids, and structures of thiolate capping agents.....	113
Fig. 5.3.	TEM micrographs of the gold nanoclusters:.....	117
Fig. 5.4.	CD spectra of (a) Au1 , and (b) Au2 . CD and UV-vis spectra of: (c) Au3 , (d) Au4 , and (e) 3b	121
Fig. 5.5.	POM micrographs of the N-phase taken on cooling from just below the Iso–N phase transition (T_{NI}). (a) Coexisting stripe domains and fingerprint texture of 1 wt% Au2 in LC1 (68 °C). 5 wt% Au3 in LC1 at 44 °C (b) crossed polarizers, and (c) parallel polarizers.....	125
Fig. 5.6.	POM micrographs (crossed polarizers) of the N phase of 5 wt% Au1 in LC1 taken on cooling from just below the Iso–N phase transition (cooling rate < 1 °C min ⁻¹).....	126
Fig. 5.7.	(a) Formation of a hyperbolic hedgehog produced by a particle with homeotropic anchoring conditions; (b) schematic representation of a chain-like particle aggregate formed by interaction of topological	

dipoles.....	129
Fig. 5.8. Simplified model for the organization of the gold nanoparticles in the N-LCs	130
Fig. S5.1. UV-vis spectra of Au1-Au4	139
Fig. S5.2. CD spectra of Au1-Au4 and thiol 3b in chloroform.	141
Fig. S5.3. CD spectra of Au1 in chloroform at three different oncentrations.....	141
Fig. S5.4. TEM micrographs and size distribution of Au1-Au4	144
Fig. S5.5. XRD spectrum of Au1-Au4	144
Fig. S5.6. POM micrographs of stripe pattern texture of the N phase of: (a) 5wt% Au1 in LC1 (64 °C), and (b) 5wt% Au4 in LC1 (56 °C) taken on cooling from the isotropic liquid phase.	145
Fig. 6.1. (a) Photo of prepared sample; (b) structure and phase transition temperature (°C) of 5CB and (<i>S</i>)-naproxen.; (c) gold nanoclusters and structure of thiolate protecting agents	152
Fig. 6.2. POM micrographs of the N or N* phases at room temperature after cooling from the isotropic liquid phase at a cooling rate of 1°C/min: (a) marble texture of the N phase of pure 5CB; (b) oily-streak texture of the N* phase of 5CB doped with 0.1 wt% (<i>S</i>)-Naproxen, and (c) doped with 0.01wt% (<i>S</i>)-Naproxen.....	153
Fig. 6.3. (a) UV-vis absorption spectrum of a 12 μm thin film of pure 5CB. (b) CD spectra of a 12 μm thin film of pure 5CB at different rotating angles. (c) UV-vis absorption spectra of thin films of 5CB and 5CB doped with 0.1wt% (<i>S</i>)-Naproxen prepared by drop-casting on Quartz. (d) CD spectra of 12 μm thin film of 5CB doped with 0.1wt% and 0.01wt% (<i>S</i>)-Naproxen. Rotation of the LC film around its normal did not change the shape (sign, intensity) of the spectrum.....	154
Fig. 6.4. POM micrographs of (a) 5CB doped with 5 wt% Au2 at the transition from the isotropic liquid to the N*-LC phase (34.6 °C), (b) 5CB doped with 5 wt% Au2 at room temperature, (c) 5CB doped with 1 wt% Au2 at room temperature, (d) 5CB doped with 5 wt% Au3 at 33.9 °C on cooling, (e) 5CB doped with 5 wt% Au3 at room temperature, and (f) 5CB doped with 0.5 wt% Au3 at room temperature.....	158
Fig. 6.5. CD spectra at different sample angular rotation angles of (a) 5CB doped with 5 wt% Au2 , (b) 5CB doped 1 wt% Au2 , (c) 5CB doped with 5 wt% Au3 , and	

(d) 5CB doped with 0.5 wt% Au3	160
Fig. 6.6. POM micrograph of 5CB doped with 1 wt% Au1 : (a) at 33.4 °C, (b) at room temperature (slow cooling), and (c) at room temperature showing no-stripes after rapid cooling.....	162
Fig. 6.7. CD spectra of 5CB doped with 1 wt% Au1 showing birefringent stripes at different sample rotation angles.....	163
Fig. 7.1. CD spectra of (a) (<i>S</i>)- 1 , (b) (\pm)- 1 (after racemization), (c) Au1 , (d) Au4 , (e) Au2 , (f) Au5 , and (g) Au3	180
Fig. 7.2. HR-TEM images of (a) Au1 , (b) Au4 , (c) Au2 , and (d) Au5	183
Fig. 7.3. TEM images of (a) Au7 and (b) Au9 and HR-TEM images of (c) Au8 , (d) Au10 , and (e) Au11	186
Fig. 7.4. CD spectra of (a) Au9 , (b) Au10 , and (c) Au11	187
Fig. S7.1. CD spectra of: (a) Au1 , (b) Au4 . Absorption spectra from CD measurements of: (c) Au1 ; (d) Au4	195
Fig. S7.2. CD spectra of: (a) Au2 , (b) Au5 ; Absorption spectra from CD measurements of: (c) Au2 , (d) Au5	196
Fig. S7.3. (a) CD spectrum of Au3 . (b) Absorption spectrum from CD measurement of Au3	196
Fig. S7.4. (a) CD spectrum of Au9 . (b) Absorption spectrum from CD measurement of Au9	197
Fig. S7.5. CD spectra of: (a) Au10 , (b) Au11 . Absorption spectra from CD measurements of: (c) Au10 , (d) Au11	197
Fig. S7.6. CD spectra of: (a) (<i>S</i>)- 1 , (b) (<i>S</i>)- 1 after racemization. Absorption spectra from CD measurements (HT) of: (c) (<i>S</i>)- 1 ; (d) (<i>S</i>)- 1 after racemization.	198
Fig. S7.7. ¹ H NMR spectra of: (a) Au1 ; (b) Au1 after I ₂ induced NP decomposition.; (c) Au4 ; (d) Au4 after I ₂ induced NP decomposition.	199
Fig. S7.8. ¹ H NMR spectra of: (a) Au2 , (b) Au2 after I ₂ induced NP decomposition, (c) Au5 ; (d) Au5 after I ₂ induced NP decomposition.....	200
Fig. S7.9. ¹ H NMR spectrum of (a) Au9 ; (b) Au9 after I ₂ induced NP	

decomposition.....	201
Fig. S7.10. ¹ H NMR spectra of: (a) Au10 ; (b) Au10 after I ₂ induced NP decomposition, (c) Au11 ; (d) Au11 after I ₂ induced NP decomposition.....	201
Fig. S7.11. ¹ H NMR spectrum of (<i>S</i>)- 1	202
Fig. S7.12. HR-TEM images and size distribution histograms: (a) Au1 ; (b) Au4	203
Fig. S7.13. HR-TEM images and size distribution histograms of: (a) Au2 ; (b) Au5	204
Fig. S7.14. TEM images and size distribution histograms of: (a) Au7 , (b) Au9	205
Fig. S7.15. HR-TEM images and size distribution histograms of: (a) Au8 ; (b) Au10 ; (c) Au11	206
Fig. S7.16. Enlarged HR-TEM images of Au2 and Au5 (after hydrolysis of Au2)	207
Fig. 8.1. Schematic representation of the response of an N-LC to an applied electric field.....	213
Fig. 8.2. a) Structure and phase transition temperatures of Felix-2900-03 b) Schematic representation of the alkyl thiolate-capped gold clusters. HR-TEM images of: c) hexane thiolate-capped Au1 and d) dodecane thiolated-capped Au2	217
Fig. 8.3. Polarized optical photomicrographs of Felix-2900-03 N-LC (mixtures containing 5 wt% dodecane thiolate-capped gold nanoclusters (Au2) after filling the cell at field-OFF.....	218
Fig. 8.4. Decreasing the number of chainlike particle aggregates (birefringent stripes). a–c) Polarized optical photomicrographs of Felix-2900-03 containing 5 wt% Au2 after heating the cell to the isotropic liquid phase followed by cooling to the N-phase at field-ON (cell gap: 5.0 μm); a) at $E = 1.4 \text{ V } \mu\text{m}^{-1}$, b) at $E = 2.2 \text{ V } \mu\text{m}^{-1}$, and c) at $E = 3.2 \text{ V } \mu\text{m}^{-1}$. d) Polarized optical photomicrograph of Felix-2900-03 containing 5 wt% Au2 (cell gap: 6.8 μm). e) Felix-2900-03 containing 10 wt% Au2 after filling the cell at field-OFF (the entire cell shows uniform homeotropic alignment).....	221
Fig. 8.5. Structures of 5CB and 8CB together with phase transition temperatures as well as literature values of the dielectric anisotropy and threshold voltage (5CB only).....	223
Fig. 8.6. a) POM image of 8CB doped with 5 wt% Au1 (partial homeotropic	

alignment), b) POM image of 5CB doped with 10 wt% Au1 (homeotropic alignment with linear particle aggregates (birefringent stripes). Both images were obtained by slow cooling from the isotropic liquid phase at field-OFF.....	224
Fig. 8.7. Plots of threshold voltage V_{th} vs. $T_{Iso}-T$ of Felix-2900-03 with Au NP dopant.....	227
Fig. 8.8. Plots of the relative dielectric permittivity (dielectric constant) parallel $\epsilon_{ }$ and across the long molecular axis ϵ_{\perp} vs. $T_{Iso}-T$ of Felix-2900-03 with Au NP dopant.....	230
Fig. 8.9. Plots of $\epsilon_{ }$ and ϵ_{\perp} vs. $T_{Iso}-T$ of Felix-2900-03 doped with either 5 or 10 wt% of Au1 or Au2 using cells treated with the cooling at field-OFF regime (homeotropic alignment): a) Au1 ; b) Au2	231
Fig. 8.10. Demonstration of the initial orientation and electric-field-driven reorientation of the N-LC molecules under cell preparation conditions described in the 1st experiment, that is, filling and cooling the cell at field-OFF (upper section), and after heating above the clearing point and subsequent cooling to the N-phase at field-ON (lower section). Representative thin-film textures (as observed between crossed polarizers) accompany each model.....	233
Fig. 8.11. Polarized optical photomicroscopy images of the homeotropic alignment and birefringent stripes of Felix-2900-03 doped with 5 wt% of: a) hexane thiolate-capped Ag nanoclusters (size: 4.2 ± 0.7 nm), b) hexane thiolate-capped CdTe quantum dots (size: 3.9 ± 0.3 nm).....	233
Fig. S8.1. Applying an electric field across the cell at ($E > E_{th}$) a director re-orientation is observed ($E = 1.6-3.0$ V/micron). A further increase of the applied field ($E \gg E_{th}$; $E = 8.0$ V/micron) the bulk of the N-LC molecules aligns along the applied electric field producing homeotropic alignment (black and white arrows indicate polarizer/analyzer position, the red arrow indicates rubbing direction of the polyimide alignment layers).....	241
Fig. S8.2. (left) HR-TEM image of hexane thiolate-capped Ag clusters (4.2 ± 0.7 nm); (right) HR-TEM image of hexane thiolate-capped CdTe quantum dots (3.9 ± 0.3 nm).....	243
Fig. 9.1. (a) Polarized optical photomicrograph of the LC (Felix-2900-03) in the N-phase doped with 5wt% dodecane thiolate capped gold nanoparticles at 55 °C in a planar ITO-test cell on cooling from the isotropic liquid phase at field-ON – both the field addressed and non-field addressed area is shown to demonstrate the impact of the electric-field/thermal history showing the	

coexistence of birefringent stripes (linear particle aggregates) and homeotropic domains in the non-field-addressed area and a few stripe domains in an otherwise planar aligned field-addressed area, (b) origin of the planar alignment after cooling the cell at field-ON (c) origin of the birefringent stripes (formation linear particle aggregates), and (d) origin of homeotropic alignment due to particles at the N-LC/alignment layer interface (no field or cooling at field-OFF).....254

Fig. 9.2. Structure, phase transition temperatures, dielectric anisotropy $\Delta\epsilon$, and threshold voltage $V_{th}(rms)$ (at $T/T_{Iso}/N = 0.95$) of the two N-LCs and schematic of the synthesized and investigated nanoparticles.....255

Fig. 9.3. High-resolution transmission electron microscope (HR-TEM) images of: (a) **Au3**, (b) **Ag1**, and (c) **QD2**258

Fig. 9.4. $V_{th}(rms)$ vs. $T_{Iso}-T$: (a) \diamond pure Felix-2900-03, \triangle Felix-2900-03 doped with 5wt% **Au2**, \circ Felix-2900-03 doped with 10wt% **Au3**, (b) \times Felix-2900-03 doped with 10wt% **Au2**, \circ Felix-2900-03 doped with 10wt% **Au3**.....259

Fig. 9.5. $\epsilon_{||}$ (ϵ_{\perp}) vs. $T_{Iso}-T$: (a) \diamond pure Felix-2900-03, \times Felix-2900-03 doped with 5wt% **Au2**, (b) \diamond pure Felix-2900-03, \circ Felix-2900-03 doped with 10wt% **Au3**.....260

Fig. 9.6. (a) $V_{th}(rms)$ vs. $T_{Iso}-T$ of cells treated with cooling at field-OFF: \diamond pure Felix-2900-03, \square Felix-2900-03 doped with 5wt% **Au1**, \bullet Felix-2900-03 doped with 5wt% **Ag1**, \blacktriangle Felix-2900-03 doped with 10wt% **Ag1**, (b): \bullet Felix-2900-03 doped with 5wt% **Ag1** treated with cooling at field-ON, \circ Felix-2900-03 doped with 5wt% **Ag1** treated with cooling at field-ON.....261

Fig. 9.7. $\epsilon_{||}$ (ϵ_{\perp}) vs. $T_{Iso}-T$: (a) \diamond pure Felix-2900-03, \bullet Felix-2900-03 doped with 5wt% **Ag1**, \blacktriangle Felix-2900-03 doped with 10wt% **Ag1**, (b) \bullet Felix-2900-03 doped with 5wt% **Ag1** of cells treated with cooling at field-OFF, \circ Felix-2900-03 doped with 5wt% **Ag1** of cells treated with cooling at field-ON.....261

Fig. 9.8. $V_{th}(rms)$ vs. $T_{Iso}-T$ of cells treated with cooling at field-OFF: (a) \diamond pure Felix-2900-03, \triangle Felix-2900-03 doped with 5wt% **Au2**, \blacksquare Felix-2900-03 doped with 5wt% **QD2**, and \square Felix-2900-03 doped with 10wt% **QD2**, (b) \triangle Felix-2900-03 doped with 5wt% **Au2**, \blacksquare Felix-2900-03 doped with 5wt% **QD2**, and \circ doped with 5wt% **Au3**.....263

Fig. 9.9. $\epsilon_{||}$ (ϵ_{\perp}) vs. $T_{Iso}-T$: (a) \diamond pure Felix-2900-03, \blacksquare Felix-2900-03 doped with 5wt% **QD2**, (b) \diamond pure Felix-2900-03, \square Felix-2900-03 doped with 10wt% **QD2**.....263

- Fig. 9.10. Polarized optical photomicrographs of Felix-2900-03 doped with 10wt% **QD2** (arrows indicate polarizer/analyzer orientation) in cells with planar polyimide alignment layers (source: Displaytech Inc.; cell gap: 5 micron) treated with cooling to the N-phase at field-OFF at 67 °C. As described earlier [6], an increase of the nanoparticle concentration results in the disappearance of the birefringent stripe defects producing virtually homogeneous vertical (homeotropic) alignment of Felix-2900-03 in planar cells.....265
- Fig. 9.11. Absorption and emission spectrum of the dodecane thiolate capped quantum dots **QD2** in toluene.....266
- Fig. 10.1. Structures and LC phase transition temperatures of the LC hosts **5CB** and **8CB** and of the nematic **HS10OCB** (top). Schematics of the homogeneous and mixed monolayer gold NPs **Au1–Au4** (bottom).276
- Fig. 10.2. TEM images of the gold NPs: (a) **Au1**, (b) **Au2**, (c) **Au3**, and (d) **Au4**.280
- Fig. 10.3. ¹H NMR spectra of **HS10OCB** (a) and of the corresponding mixed monolayer-protected gold NPs **Au3** (b) and **Au4** (c).....281
- Fig. 10.4. V-vials[®] containing **5CB** doped with **Au1** or **Au3**: (a) right after sample preparation as described in the experimental section and (b) after standing at room temperature overnight (in the nematic phase of **5CB**).....282
- Fig. 10.5. Polarized optical photomicrographs (crossed polarizers left column, slightly uncrossed polarizers right column) of 5 wt% NPs in **5CB** (at $T = T_{\text{Iso/N}} - 5$ °C): (a) **Au1**, (b) **Au3**, (c) **Au2**, and (d) **Au4**.....284
- Fig. 10.6. Polarized optical photomicrographs (crossed polarizers left column, slightly uncrossed polarizers right column) of 5 wt% NPs in **8CB** (at $T = T_{\text{Iso/N}} - 5$ °C): (a) **Au1**, (b) **Au3**, (c) **Au2**, and (d) **Au4**.....286
- Fig. 10.7. Optical photomicrographs (N phase with crossed polarizers left column, N phase with parallel polarizer orientation right column) of 5 wt% NPs in **5CB** (at $T = T_{\text{Iso/N}} - 5$ °C): (a) **Au1**, (b) **Au3**, (c) **Au4**.....288
- Fig. 10.8. Optical photomicrographs (N phase with crossed polarizers left column, N phase with parallel polarizer orientation right column) of 5 wt% NPs in **8CB** (at $T = T_{\text{Iso/N}} - 5$ °C): (a) **Au1** (air bubble in the centre of the image), (b) **Au3**, (c) **Au4**.....289
- Fig. 10.9. Simplified model for the organization of the LC-capped Au NPs (black) and surrounding **5CB** host molecules (blue) at the interface between: (a) glass and

bulk nematic phase, and (b) rubbed polyimide alignment layers (low pre-tilt) and the bulk nematic phase. Note, the two simplified cartoons only show 2-dimensional representations of 3-dimensional, quasi-spherical (cuboctahedral) gold NPs and surrounding LC host molecules.....292

- Fig. S10.1. Selected $C-V$ plots (red) and slope of K_{33} (for some plots) at $T_{\text{Iso/N}} - T = 6 \text{ }^\circ\text{C}$ of: (a) pure **5CB**, (b) **5CB** doped with 5 wt% **Au1**, (c) **5CB** doped with 5 wt% **Au3**, (d) **8CB** doped with **Au3**, and (e) **8CB** doped with 5wt% **Au4**.
.....304
- Fig. S10.2. Selected $C-V$ plots (red) and slope of K_{33} (for some plots) at $T_{\text{Iso/N}} - T = 3 \text{ }^\circ\text{C}$ of: (a) **5CB** doped with 5 wt% **Au1**, (b) **5CB** doped with 5 wt% **Au3**, (c) **8CB** doped with **Au3**.
.....305
- Fig. S10.3. Threshold voltage and dielectric anisotropy vs. reduced temperature for **Au1–Au4** in both **5CB** and **8CB**. Lines between data points are used to show trends (rise or fall of V_{th} or $\Delta\epsilon$) with decreasing temperature (normally no line would be drawn between only two data points).
.....306

List of Tables

Table 3.1 LC structure, phase transitions, phase transition temperatures and source.	74
Table 3.2 Structure of the Au NPs.....	76
Table 4.1 Size, size distribution, formula, and molecular weight (average) of the gold nanoclusters Au1 and Au2.....	86
Table 4.2 Small-angle powder diffraction data (q -values, Miller indices, and lattice parameters for 2 and of Au1 and Au2 in 2)	92
Table 5.1 Average particle size (nm) of the gold nanoparticles Au1–Au4.....	118
Table 7.1. Sizes (nm) and Size Distributions ^a of the Investigated Au NPs	178
Table S8.1 Elastic constants K_{11} , K_{22} , and K_{33} (incl. standard deviations) of Felix-2900-03 doped with Au1 and Au2.....	244
Table S8.2 Specific resistivity R (incl. standard deviations) of Felix-2900-03 doped with Au1 and Au2.....	246
Table S8.3 Comparison of Felix-2900-03 doped with 10 wt% Au1 measured with two different initial setups.....	247
Table 9.1. Electro-optic data of 8CB and 8CB doped with Au1, QD1, and QD2 at $T_{\text{Iso}}-T = 6 \text{ }^{\circ}\text{C}$	267
Table 10.1. Size, size distribution, and NP composition of Au1–Au4.....	280
Table 10.2. Electro-optic data for pure 5CB, pure 8CB and 5 wt% mixtures of Au1, Au3 and Au4 in 5CB as well as 8CB.....	296
Table S10.1. Elemental analysis for Au1 and Au2	307

Chapter 1: Liquid Crystals and Gold Nanoparticles - Introduction and Background

1.1 Introduction

Liquid crystals (LCs) are anisotropic fluids with some degree of ordering at the molecular, i.e., nanoscale level, located in a principal phase diagram between the solid (crystalline) state and the anisotropic liquid state. LCs respond to external fields and interact with surfaces, thus influencing their structure and properties [1]. Liquid crystals are well established in materials science with a significant basic research base as well as technical importance. The concepts of orientational order and collective molecular motion are recognized in bioscience, where LCs serve as model systems for cell membranes and muscles. In addition, LCs have found widespread use in information displays, as sensors, drug delivery vehicles, in photonic band gap structures, as well as in optical elements such as controllable lenses and in lasing. [2, 3] LC science and technology is crossing the boundaries of many fundamental scientific disciplines.

Gold (Au) nanoparticles (NPs) have been the most extensively studied nano-materials since the break-through paper by Brust et al. in 1994 [4]. This paper described a relatively easy synthesis method for Au NPs that allows for control of size, shape and functionalization, and hence size-related electronic, magnetic and optical properties [5]. Applications related to Au NPs can be found in biology/medical fields, in catalysis, and other types of applications such as capillary electrophoresis devices among others [5].

The study of LC-Au NP systems will allow for investigating the combination of the unique properties of LCs and Au NPs with mutual benefits. On the one hand, Au NP

properties can be tuned by surrounding them with LCs introducing changes in localized surface plasmon resonances [6], and more importantly, LCs are unique candidates to manipulate Au NP assembly [7, 8], which is important for exploring the spatial arrangement of Au NPs as well as their related fundamental electronic and optical properties for constructing novel nanoscale devices [9-11]. On the other hand, the properties of LCs can also be affected by the Au NPs such as, for example, the electro-optical properties [12] and alignment of LC molecules used in display applications [13]. Obviously, these twofold advantages are not limited to Au NPs; other NPs can be used as well.

Introduction and background information of the two materials, LCs and Au NPs, will be presented in this chapter. A literature review of LC / NP composites as well as the outline of this thesis is described in Chapter 2. The following chapters of this thesis present the results, the conclusions, and provide an outlook to future work.

1.2 Liquid Crystals

1.2.1 Liquid Crystal Materials and Liquid Crystal Phases

LC phases are observed at the transition from the highly ordered crystalline state with long-range orientational and positional ordering to the disordered liquid state (or *vice versa*) via the formation of one or more intermediate phases. In these phases, the order of the crystalline state is partially lost, and the constituent molecules, aggregates, or particles possess some degree of mobility (i.e., translational, rotational, and/or conformational freedom) [14]. LC materials can be divided into two groups: thermotropic LCs and lyotropic LCs. Thermotropic LC phases are observed by the change of

temperature, while lyotropic LC phases are formed in the presence of a certain amount of a suitable solvent [15, 16].

In principle, there are three somewhat distinct yet overlapping categories for materials capable of forming LC phases: (i) non-amphiphilic anisometric molecules most commonly displaying exclusively thermotropic LC phases; (ii) amphiphilic molecules usually showing lyotropic LC phases; (iii) amphotropic LCs capable of forming both lyotropic as well as thermotropic LC phases (Fig. 1.1) [15].

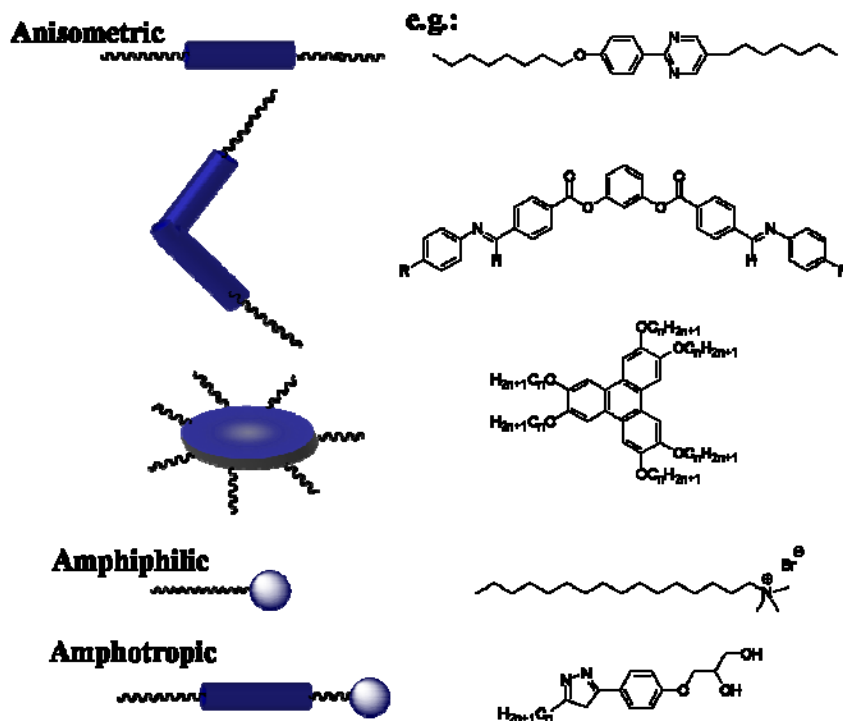


Fig. 1.1. Typical examples (and molecular shapes) of the main types of molecules forming LC phases (adapted from ref. 8).

Thermotropic LCs can be further distinguished by their molecular shape. Examples of linear rod-like (calamitic), disk-like and bent (or banana-like) molecules are shown in Fig. 1.1. The rod-like LCs are the most common and well known LCs. These LCs are widely used in LC displays and other electro-optic devices. The concept of LC phase formation

by rod-like molecules was well established in the early stage of LC research [17]. It was not until 1977, when Chandrasekhar *et al.* reported the first examples of disk-like molecules forming LC phases [18]. Disk-like LCs have found applications such as in molecular electronics and high-efficiency organic photovoltaics [19, 20]. In 1996, Niori *et al.* demonstrated a novel type of LC with a bent rigid core [21]. Bent-core LCs became one of the most exciting research areas within the LC community within less than a decade due to the unusual ferroelectric and antiferroelectric responses, the induction of supramolecular chirality (although the bent-core LC molecules were achiral) and other unique properties [22-24]. There are also other shapes of LCs, such as bricks (sanidic), T-shaped, and cone LCs, among others (dendrimers, rod-coil polymers, etc.) [16].

Regardless of the molecular shape and structure of the constituent entities, LC phases can be classified using elements of symmetry and the degree of long-range ordering (Fig. 1.2 and Fig. 1.3). Whereas LC phase formation in lyotropic LCs is driven by the segregation of hydrophobic and hydrophilic regions of an amphiphilic molecule from a solvent, LC phase formation in thermotropic LCs is driven by the segregation of chemically incompatible subunits from one another, such as the segregation of rigid aromatic cores from flexible alkyl tails within a molecule.

The nematic phase is the least ordered LC phase, and is characterized by constituent molecules that solely possess orientational ordering and no positional ordering. The nematic phase with unidirectional alignment of the molecules can be seen in Fig. 1.2. For nematic LC molecules, the rigid core leads to a parallel organization of these units and the flexible chains provide some degree of mobility to prevent crystallization [22]. Both rod-like and disk-like (as well as bent-core) LC molecules can form nematic phases.

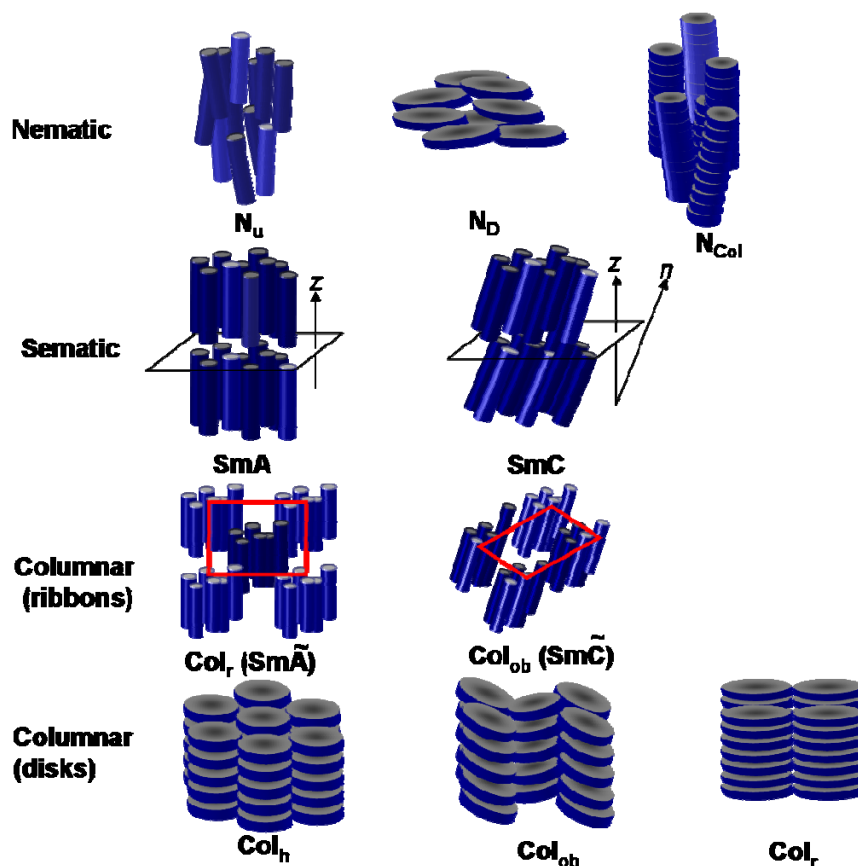


Fig. 1.2. Presentation of the main types of nematic and positional ordered thermotropic LC phases formed by rod-like and disk-like molecules. Abbreviations: N_u = uniaxial nematic phase, N_D = discotic nematic phase, N_{Col} = columnar nematic phase, SmA = smectic-A phase, SmC = smectic-C phase, Col_r = rectangular columnar phase, Col_{ob} = oblique columnar phase, Col_h = hexagonal columnar phase (adapted from ref. 8).

The direction of orientation of nematic LC molecules is called the director \mathbf{n} . The director \mathbf{n} is oriented either parallel to the long molecular axis for rod-like molecules (N_u , uniaxial nematic phase), or parallel to the column axis for columnar aggregates formed by amphiphilic (i.e., rod-like micelles) or disk-like molecules (N_{Col} , columnar nematic phase), or parallel to the short molecular axis for disk-like aggregates of amphiphiles (i.e., plate-like micelles), molecules, or particles (N_D , discotic nematic phase) [25].

Lowering the temperature of an LC material forming a nematic phase, in many instances produces another LC phase (or phases) with additional positional ordering. The

segregation of incompatible parts of the molecules which are otherwise chemically bonded together is a main factor for the long-range positional order in different LC phases. The most prominent LC phases with positional ordering are smectic (Sm), columnar (Col), and cubic (Cub) phases. Elongated rod-like molecules commonly form smectic phases with layer ordering. In the absence of additional positional ordering within the layers, the two most important smectic phases are the smectic-A phase (SmA), in which the long molecular axes of the molecules are perpendicular to the layer planes, and the smectic-C phase (SmC), in which the molecules are tilted by an angle with respect to the layer normal [22]. Rod-like molecules (predominantly polycatenar molecules) have also been reported to form columnar phases (Col_r, Col_{ob}), in which the smectic layers collapse into ribbons that organize in a rectangular or an oblique 2-D lattice.

Disk-like molecules prefer forming columnar phases, in which the disk-like molecules pack to form columns that can further organize into arrays with a different symmetry such as hexagonal (Col_h), rectangular (Col_r), oblique (Col_{ob}), or tetragonal (Col_{tet}) [17, 26].

Besides using different shapes and segregation of incompatible parts to obtain LC materials forming different LC phases, chirality is among one of the major routes to increase the variability of LC phase formation. In the LC regime, chirality can be introduced by several ways: intrinsically chiral molecules form chiral LC phases; doping a small amount of a chiral molecule into non-chiral LC hosts (induced chirality), and one special case for achiral bent-shape molecules that spontaneously form opposite chiral domains [22, 27]. Chirality in LCs causes the formation of helical superstructures in the

nematic phase (chiral nematic phase N^*), in the smectic C phase (SmC^*), in higher-ordered, tilted smectic phases, and can induce additional phases which do not exist for non-chiral LCs, such as blue phases, smectic blue phases, and twist grain boundary (TGB) phases [22].

The typical types of lyotropic LC phases formed by amphiphilic molecules are shown in Fig. 1.3. The amphiphilic character of these molecules encourages phase separation, i.e., the formation of hydrophobic and hydrophilic domains. Depending on the concentration, as well as the shapes of molecules, temperature, and pressure, different LC phases can be formed. LC phases found in lyotropic systems are the lamellar phase, bicontinuous cubic phases, hexagonal columnar phases, and micellar (discontinuous) cubic phases, based on the packing symmetry of the ordered domains. The typical solvent is water. Depending on the ratio of amphiphilic molecule to water, lyotropic LCs can be divided into normal phases (type 1, water excessive) and inverted phases (type 2, water deficient) with the non-curved lamellar phase in the middle of the phase diagram [28]. Starting from pure water, addition of more and more amphiphiles lead at a certain concentration, named the critical micelle concentration (cmc), to the formation of micelles. With increasing amphiphile to water ratio, the phases formed are micellar cubic (Cub_I), hexagonal columnar (Col_h) and bicontinuous cubic (Cub_V). At a certain ratio, curved interfaces are no longer formed and lamellar phases result. A continued increase in the amphiphile-to-water ratio will result in the formation of inverted phases, i.e., the formation of inverse bicontinuous cubic, columnar and micellar cubic phases [29].

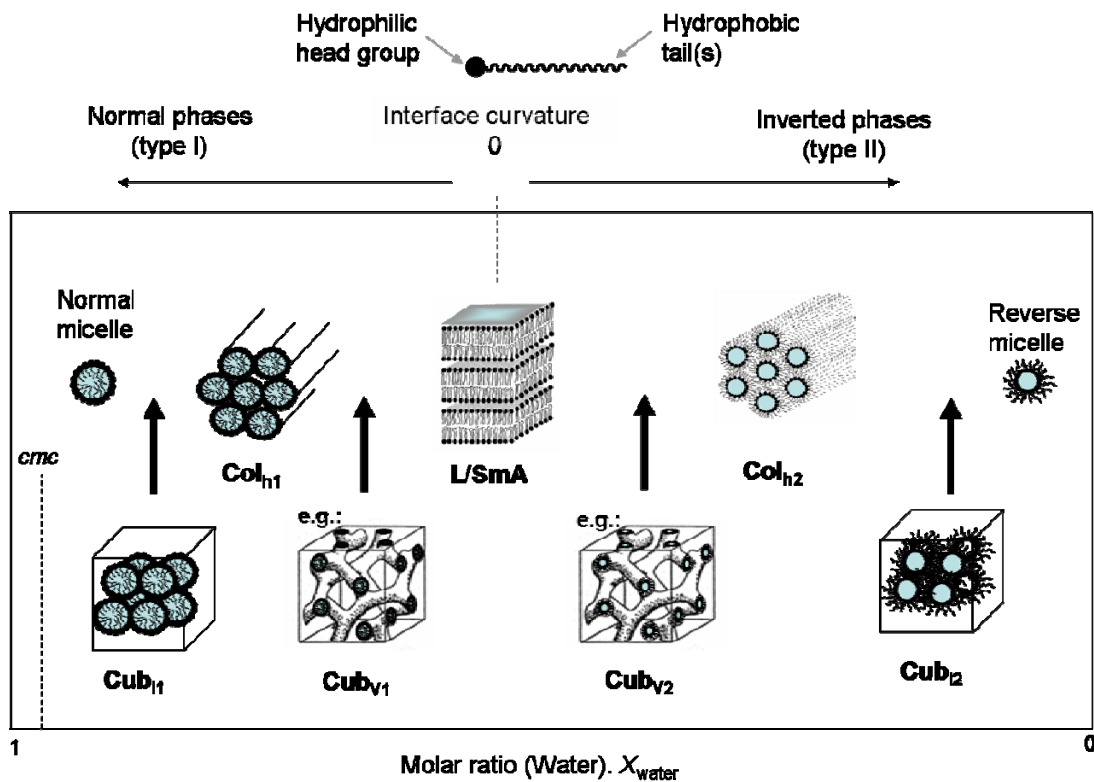


Fig. 1.3. Presentation of the main types of lyotropic LC phases. depending on the interface curvature (molecular shape or concentration in water as the most commonly used solvent). * For abbreviations see caption Fig. 1.2 (adaped from ref. 8).

1.2.2 Characterization of LCs

A polarizing optical microscope, a differential scanning calorimetry (DSC) and an x-ray diffractometer are the three key instruments to characterize LCs. Polarizing optical microscopy along with a heating/cooling stage can provide information about phase transition temperature and phase type by observing typical liquid crystal textures. DSC can give more precise transition temperatures, transition enthalpy values, and the order of the transitions. X-ray diffraction investigates the detailed features of the LC phase structure [30]. In this section, the basic principles of the three instruments will be briefly described, along with typical liquid crystal examples. An introduction to liquid crystal texture formation will also be included in the polarizing optical microscopy section.

1.2.2.1 Polarizing Optical Microscopy and LC Textures

A typical setup of a polarizing optical microscope is shown in Fig 1.4. From the bottom, it consists of a light source, and then the light is linearly polarized by a polarizer. The liquid crystal sample is normally sandwiched between two glass slides and loaded in a heating stage, and then put on the rotating stage (thus, the sample can be precisely rotated in a plane perpendicular to the direction of light propagation). The polarized light then passes into the liquid crystal sample, and due to the birefringence properties of liquid crystal material, the light can partly pass through the analyzer, which is oriented at 90 degrees to the polarizer (cross-polarized), and the typical liquid crystal texture can be observed by eye or recorded by a digital camera. Obviously, without a birefringent sample present, such as the tested liquid crystal material in the isotropic liquid phase, no change to the direction of the polarized light occurs, thus no light can pass through the analyzer. As a result, the field of view will be black.

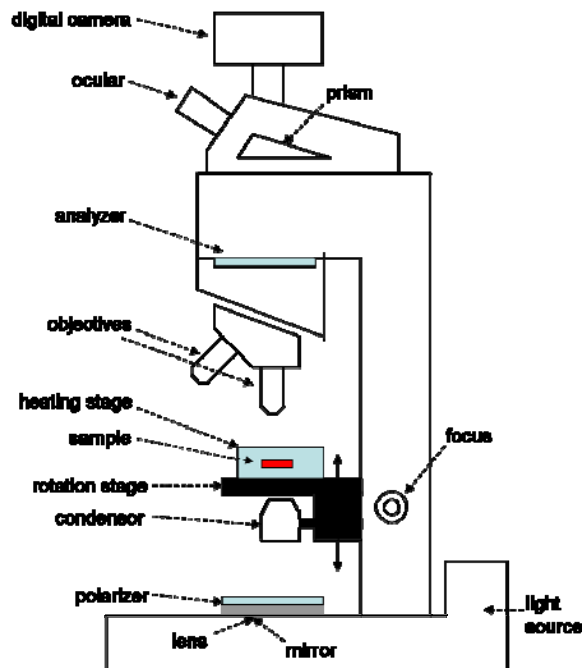


Fig. 1.4. Schematic setup of a polarized optical microscope (adapted from ref. 30).

The birefringence of LCs is due to their anisotropic nature (shape). For anisotropic materials such as LCs or noncubic solids, birefringence occurs because the incident light is split into two components; this is because the velocity as well as the refractive indices of light varies in different direction within these materials. As mentioned earlier, LC molecules tend to point along a common axis. The common axis is called the director \mathbf{n} . Light polarized parallel to \mathbf{n} has a different index of refraction compared with the light polarized perpendicular to \mathbf{n} . Thus, when the polarized light enters the liquid crystal sample, the light is broken into two different components due to the two different refractive indexes. As a result, when the light exits the LC materials, the two rays recombine and the polarization state has been changed and some light can now pass through the analyzer. The color (in most cases, the light source is not monochromatic) and intensity of light passing through the analyzer depends on the local orientation of the LC molecules, as well as the thickness of the sample [30].

Liquid crystal textures observed by polarizing optical microscopy are used to identify different LC phase, as each LC phase can form its own characteristic textures. Several typical LC textures are shown in Fig. 1.5.

The so-called *Schlieren* texture (Fig. 1.5 (a)) is often observed for nematic LC phases sandwiched between untreated glass plates, which promote the LC director parallel to the substrate and the orientation is not homogeneous. *Schlieren* textures exhibit characteristic sets of dark brushes. For example, many four brushes along with a few two brushes can be observed in Fig. 1.5 (a). These dark brushes correspond to the extinction orientation of the nematic LC molecules. Accordingly, the director \mathbf{n} is parallel to either the polarizer or the analyzer axes in these areas. The points, where the two or four brushes meet,

correspond to director singularities and are called disclination points in the structure. These singularities are topological defects. [31]

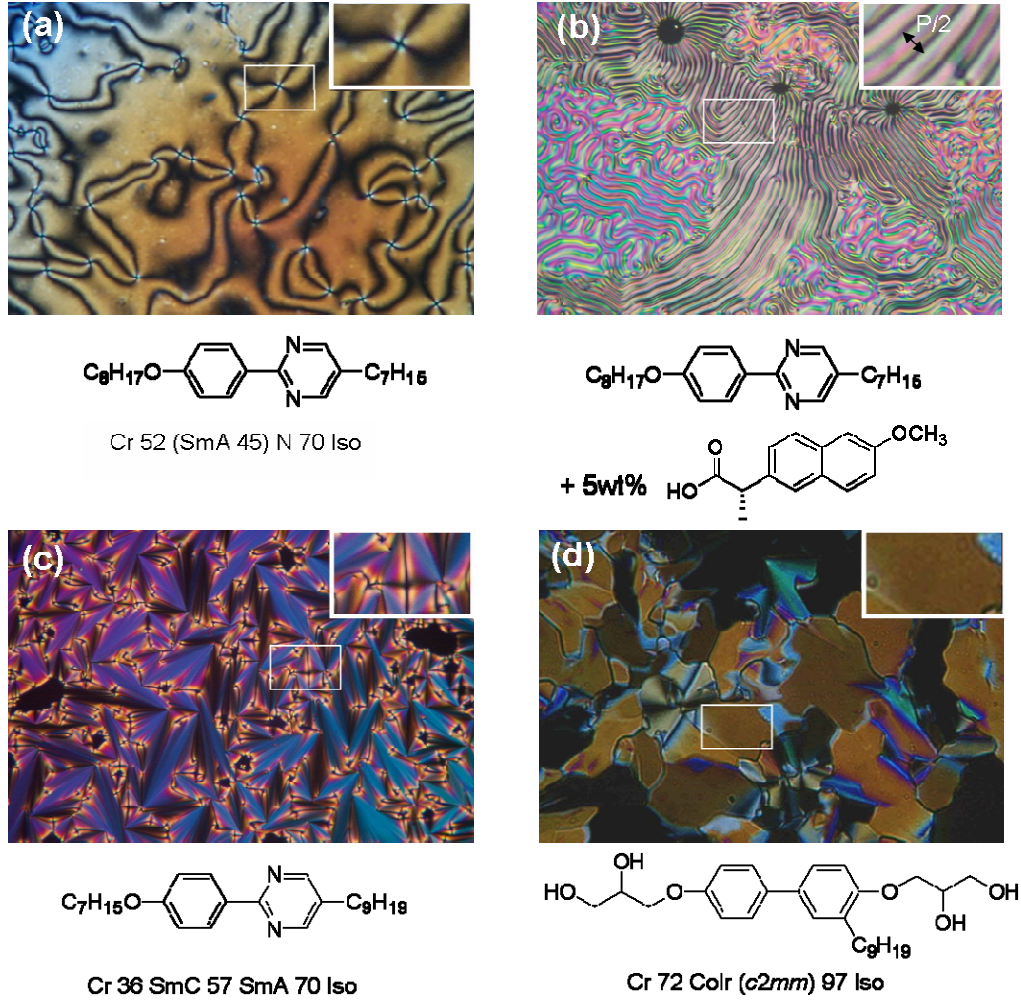


Fig. 1.5. Several examples of typical LC textures: (a) *Schlieren* texture of nematic phase; (b) fingerprint texture of chiral nematic phase; (c) focal conic texture of SmA phase; (d) mosaic texture of Col_r phase

The chiral nematic phase possesses a spontaneous macroscopic helical superstructure. The distance it takes for the director to rotate one full turn (360°) in the helix is called the helical pitch P . The magnitude of the helical pitch can vary from as small as 100 nm to many micrometers. A direct visualization of the helical structure can be resolved for long

helical pitch ($>1 \mu\text{m}$) under homeotropic boundary conditions (LC director vertical to the substrate). One typical structure is shown in Fig. 1.5 (b), called the fingerprint structure. The varying director field leads to an equal distant pattern of dark lines. The dark lines appear when the local director rotates along the direction of light propagation. Due to the head-tail symmetry of the molecules, the periodicity of the equal distant dark lines is half the value of the helical pitch, $P/2$. The non-equal distance in Fig. 1.5 (b) in some areas is mainly due to temperature variation from site to site [31].

Smectic phases are characterized by the formation of a layered structure. The focal conic domain, most typical for SmA phases, can be observed if the orientation of the director is parallel to the surface, i.e., the smectic layers are perpendicular to the surface. One such texture, called focal conic fan texture, is shown in Fig. 1.5 (c), in which case the layers orient in a circular focal conic domain with the layer normal direction pointing to the center of the focal cone. Two such focal cones form a particular structure, the so-called Dupin cyclides, and one such texture is shown in the enlarged area of the figure [32, 33].

The *mosaic* texture is very common for some columnar phases (tetragonal or rectangular columnar). Fig. 1.5(d) shows one such texture. Mosaic textures exhibit larger areas of uniform optical appearance, which varies from domain to domain separated by grain boundaries. Within the areas of uniform optical appearance, the columnar structures are arranged in one specific direction. Rotating the sample in the plane normal to the light propagation can bring the different domains to the extinction position and the appearance of black color is observed. [34, 35]

1.2.2.2 Differential scanning calorimetry

Differential Scanning Calorimetry (DSC) is a powerful tool complementing polarized optical microscopy to study LC phase transitions. Its utilization is in determining the heat supplied or extracted during the phase transition of LCs [36].

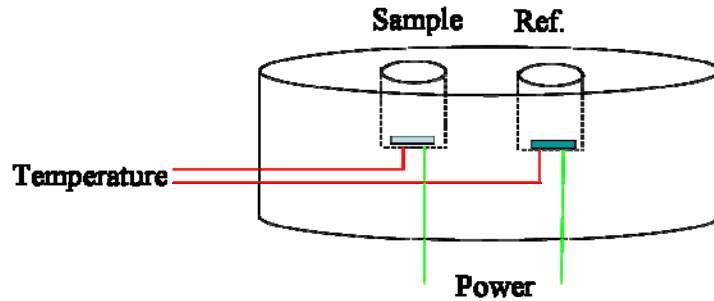


Fig. 1.6. Illustration of DSC sample block (adapted from ref. 37).

A schematic of the temperature-controlled block of a DSC is shown in Fig. 1.6. The sample and reference chambers are located side by side and are heated equally (power compensation DSC). The thermal properties of the sample are compared with a standard reference material which has no phase transition in the same temperature range such as an empty alumina holder (or pan). The temperature of each holder is monitored and heat (power) is supplied to each holder to keep the temperature of the two holders equal. A plot of the difference in the energy supplied against the temperature gives important information about the phase transition, such as the latent heat or a change in heat capacity [36, 37].

A complete DSC trace obtained from a typical LC material (8CB: Cr 22 SmA 32.5 N 40 Iso) is shown as an example to illustrate the use of DSC for characterizing liquid crystals (Fig. 1.7). The top curve in Fig. 1.7 corresponds to the heating process, and the

lower curve is the corresponding cooling process. From the heating process, we can see that a crystalline solid phase-to-SmA phase transition occurs at 22 °C, followed by a transition from the SmA to the nematic phase at 33 °C, and a nematic phase-to-isotropic liquid phase transition at 40 °C. The cooling process shows a significantly lower SmA→Cr phase transition compared to the heating process, which is mainly due to super-cooling of the materials, along with contributions of instrumental hysteresis.

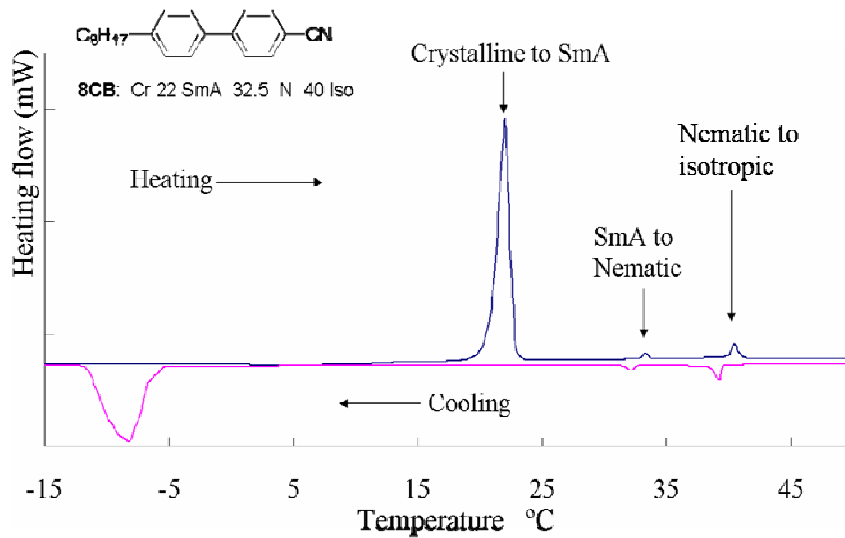


Fig. 1.7 DSC plots of 8CB with phase transition temperatures and chemical structure.

1.2.2.3 X-ray Diffraction

X-ray diffraction plays a key role in the identification of LC phases. The scattering of x-rays by crystalline materials can be divided into elastic and inelastic. Elastic scattering refers to the process where the incident x-ray only changes direction without losing energy; whereas in inelastic scattering both the direction and the energy are changed. Diffraction is elastic scattering. For x-ray diffraction, the scattering arises from the electrons of the atoms. The various scattered wavelets from atoms at different locations

combine together with constructive or destructive interference depending on the phases of the wavelets. The phases reflect the relative positions of the atoms. Thus, the intensity of the diffracted wave in a given direction depends on the spatial distribution of the atoms in the tested materials. Correlations in positions between atoms or groups of atoms leads to a redistribution of the scattering, intense in some directions, weak in others. The degree of redistribution is related to the extent of positional order in the sample. This is the basic principle behind x-ray diffraction for probing the sample's structure [38, 39].

Bragg's law describes the condition for constructive interference of wavelets. As shown in Fig. 1.8, this law states that x-rays reflected from adjacent lattice planes by a distance D can interfere constructively when the path difference between them is an integer multiple of the wavelength λ :

$$2D\sin\theta = n\lambda$$

Where D is the distance between planes, θ is the angle of incidence, n is an integer and λ is the wavelength of the x-rays. [39]

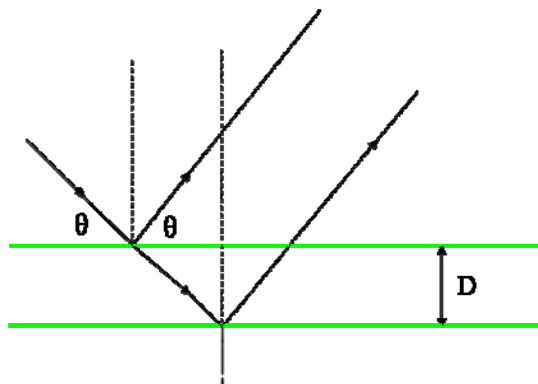


Fig. 1.8 X-ray diffraction from two planes in a crystal material (adapted from ref. 39)

One of the goals of x-ray experiments is to determine the *Bragg* angle that can be related to the lattice constants. X-ray diffraction can also provide information on the

relative orientation and spatial orientation distribution of different sets of planes. A typical setup for small angle x-ray diffraction experiments used in this thesis is shown in Fig. 1.9. It consists of an x-ray source, a monochromator, a vacuum sample chamber with the capability to align LC molecules (for aligned monodomain x-ray diffraction, e.g. using magnetic fields) or using unaligned powder samples (in capillaries) as well as controlling the sample temperature mounted on the goniometer, and a 2-D area detector.

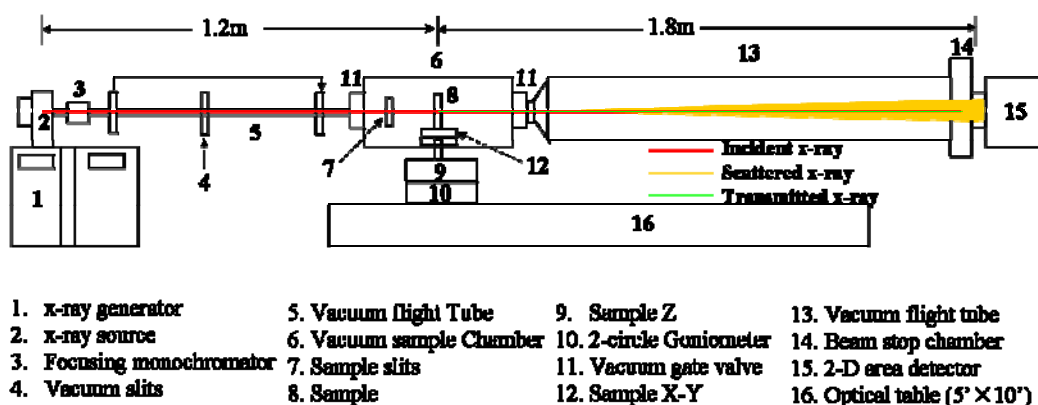


Fig. 1.9 Schematic of X-ray diffraction experimental set up (adapted from ref. 40).

Fig 1.10 shows some typical examples of x-ray patterns (schematic) of unaligned samples of the nematic phase, the SmA phase, and the SmC phase [41] as well as an x-ray pattern at low angles (low- Q ; Q = wave vector) for one particular LC material described in the thesis showing a rectangular columnar (Col_r) phase [42, 43]. The value of Q is related to the separation between molecules or molecular subunits. The sharpness of the peak is related to the extent of periodic separations over large distances, thus the wide-angle peaks relate to the translational order over relatively short distances. For the nematic phase (Fig. 1.10 (a)), which only shows orientational ordering, two diffuse

maxima can be seen in both low-angle and wide-angle regions that are related to the molecular length and molecular width, respectively. For the SmA (Fig. 1.10(b)) and the SmC (Fig. 1.10(c)) phase, one, two or more sharp peaks can be observed at low Q , and these are related to the layer spacing. For the SmA phase, the layer spacing (or distance) d normally is slightly less than the molecular length l_0 due to a combination of imperfect molecular orientational order and conformational disorder within the molecules. If a SmC phase is observed below the SmA phase in a given LC material, in most cases the layer distance d will be reduced, thus the sharp peaks at low Q will move to wider angles (i.e., higher Q). As for the nematic phase, the diffuse wide-angle peak is also observed for the SmA and the SmC phases indicating the distance between the liquid-like alkyl chains, because only orientational ordering can exist within the layers [41]. One particular bolaamphiphilic LC showing a Col_r phase was used in this thesis (for details see Chapter 4), and therefore the related x-ray pattern will here only be briefly discussed (Fig. 1.10 (d)). This mesophase shows a diffuse wide-angle scattering similar to the N, SmA as well as SmC phases discussed previously, which is again attributed to the average distance between liquid-like hydrocarbon chains. At low angles, a set of non-equidistant reflexes can be seen, which can be indexed on the basis of a centered rectangular 2D lattice with space group $c2mm$. [42, 43]

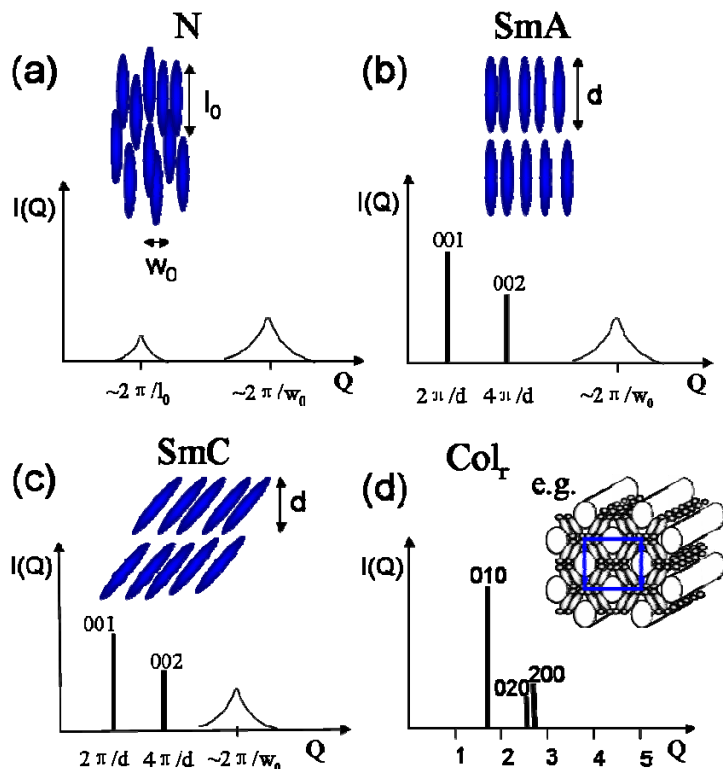


Fig. 1.10 Local structure and x-ray powder pattern from unaligned LC samples of (a) a nematic phase, (b) a SmA phase, (c) a SmC phase, and (d) one example of a Col_r phase at low angle (adapted from ref. 41, 43).

1.2.3 Liquid Crystal Displays

One part of this thesis is concerned with improving the electro-optical properties of nematic LCs as well as controlling the alignment of nematic LC molecules by Au nanoparticles, thus, some background information on liquid crystal display (LCDs) using nematic molecules will be provided in this section. Nematic LC molecules can possess permanent or induced dipole moments along or across the long molecular axis (positive or negative dielectric anisotropy). When an electric field is applied, the overall dipole moment of the molecules tends to orient along the direction of the field. Thus, the director of the molecule can also be changed (see Fig. 1.11). [44] Let us consider the case

of a liquid crystal with a positive dielectric anisotropy uniformly aligned in one direction after an electric field is applied to the cell. For fields with strengths below a certain threshold value, the orientation of the LC molecules remains unchanged. Then, at a certain value of the electric field, the orientation of the LC molecules starts to change and a deformation occurs. This transition is called Fredericksz transition (Fig. 1.12). The value at this certain point is called the *threshold voltage* V_{th} . V_{th} can be measured by monitoring the change of the transmittance, usually at 10% decrease, or can be determined by measuring the capacitance change with increased applied voltage (at 10% increase). [44] For example, in this thesis V_{th} is measured as a 5% change of capacitance, following the method described by Wu *et al.* [45]. The *threshold voltage* V_{th} depends on the dielectric anisotropy $\Delta\epsilon$ and the elastic properties of the nematic LC. The dielectric anisotropy $\Delta\epsilon = \epsilon_{||} - \epsilon_{\perp}$, where $\epsilon_{||}$ and ϵ_{\perp} is the dielectric permittivity along and across the long molecular axis. In this thesis, $\epsilon_{||}$ is measured by $\epsilon_{||} = C_{||} / C_{empty}$, where $C_{||}$ is the capacitance at $V_{th}/V = 0$, and C_{empty} is the measured empty cell capacitance; ϵ_{\perp} is determined as $\epsilon_{\perp} = C_{\perp} / C_{empty}$, where, C_{\perp} is the measured capacitance at $V \ll V_{th}$; obviously, $\Delta\epsilon$ is measured by $\Delta\epsilon = \epsilon_{||} - \epsilon_{\perp}$. The LC molecules at the surface tend to remain in the configuration when an electric field is applied, whereas the LC molecules away from the surface are re-orientated by the electric field. Thus, the result of applying a field is a deformation of the nematic director. In principle, if the LC molecules were free from other influences, the director is free to point in any direction. Once restrained between two glass slides, deformations occur and defect textures are observed, as described in the previous section. Deformations can also occur upon applying an electric field. Once the electric field is turned off, the orientation of LCs will change back to the

original state, which demonstrates the elastic properties of LC materials. Further, there are three types of deformations: splay, twist and bend, as shown in Fig. 1. 13. As a result, there are three related elastic constants: K_{11} , K_{22} , and K_{33} (splay, twist, and bend). The three elastic constants are measured as following: $K_{11} = \left(\frac{V_{th}}{\pi}\right)^2 \Delta\epsilon\epsilon_0$, where, V_{th} is the threshold voltage, ϵ_0 is the dielectric constant, $8.85 \cdot 10^{-12}$ F/m, and $\Delta\epsilon$ is the dielectric anisotropy; K_{22} is estimated as $0.6 K_{11}$; and K_{33} is obtained from the curve fitting algorithm of capacitance-voltage curve. Another characteristic of an LC display device is the *switching time*, which is in part related to the viscosity of the LC in the nematic phase. One more characteristic is the *contrast ratio* of the brightness between the on and off states [44, 46].

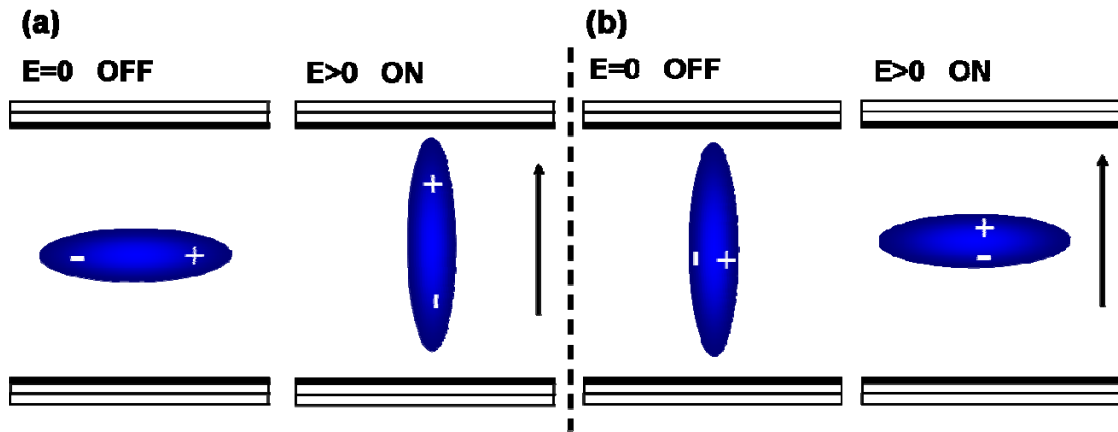


Fig. 1.11. Schematic illustration of LC response to an electric field: (a) LC with positive dielectric anisotropy ($\Delta\epsilon > 0$), and (b) LC with negative dielectric anisotropy ($\Delta\epsilon < 0$).

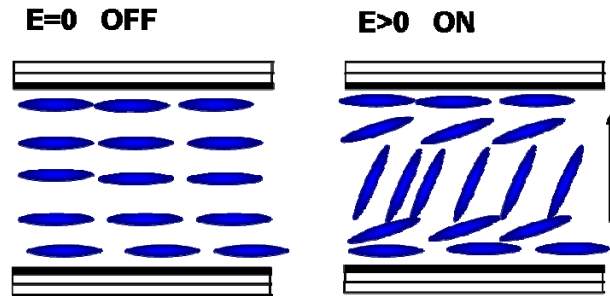


Fig. 1.12. Schematic illustration of Freedericksz transition (adapted from ref. 44).

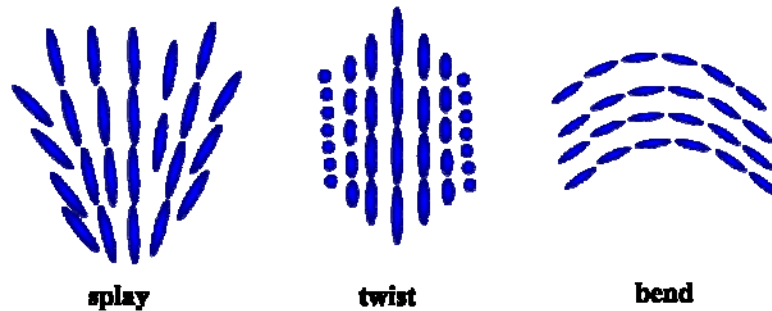


Fig. 1.13. The three basic types of deformations in LCs (adapted from ref. 44).

A pre-requirement for the use of nematic LCs in LCD applications is the alignment of the LC molecules. Without treatment of the surface, the LC molecules tend to orient in different directions forming characteristic defects and defect textures as discussed in section 1.2.2.1. To orient the LC molecules macroscopically, surface treatments are necessary. The entire LC sample can be aligned in a uniform planar orientation if the glass surfaces are uniformly coated with a polymer that is rubbed along one direction before the LC mixture is applied.

Polyimide has been broadly applied for such purpose in display industries. Usually polyimides are spin-coated to the surface, followed by rubbing with a velvet cloth. The rubbing results in microscopic grooves on the polyimide surface and aligns the individual polymer chains. When a LC sample is introduced to such a surface, the LC molecules

adopt a macroscopic alignment – although the alignment mechanism is still not clear, weak dispersion interactions are considered as the most likely possibility [47]. Homeotropic (or vertical) alignment of LCs can be obtained by treatment of the surface with a surfactant such as lecithin [47, 48]. For comparison, the natural *Schlieren* texture of a nematic LC confined between untreated glass surfaces, a planar texture, and a homeotropic texture are shown in Fig. 1.14.

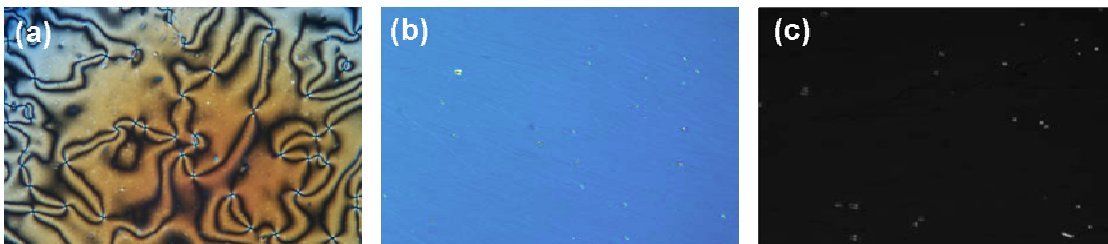


Fig. 1.14 Nematic LC textures in (a) untreated surface; (b) planar condition; (c) homeotropic condition.

There are different modes of LCDs, such as twisted nematic mode (TN) [49], super twisted nematic mode (STN) [50], in-plane switching (IPS) mode [51], polymer dispersed LC (PDLC) mode [52], multi-domain vertical alignment (MVA) mode [53], and patterned vertical alignment (PVA) mode [54]. Examples of LCDs employing TN, IPS or MVA modes are schematically shown in Fig. 1.15. The TN mode LCD was developed in the early 1970s, and was one of the predominant types of LCD used in the past. As shown in Fig. 1.15 (a), the surface induces uniform planar alignment of the LCs. The rubbing directions of the top and bottom alignment layers are 90° to each other, which promotes the director of the nematic LCs sandwiched between the aligning surfaces to also rotate 90° . The polarized light will follow the twist direction of the nematic LC structure and, as a result, the light is also rotated 90° when it strikes the

second polarizer. In this twisted mode the light can pass through the second polarizer. If a reflective LCD is made, a reflector behind the second polarizer will reflect the light back through the cell; and the light emerges from the cell (bright state or ON state). After applying an electric field with the field strength exceeding the threshold voltage of the Fredericksz transition, the LC director configuration changes to a deformed state. As the LC molecules in the bulk rotate 90° in the cell (in principle unwinding the helical state induced by the orthogonal alignment layers), little or no light can pass through the second polarizer (dark or OFF state). Without a reflector, the LCD is called a transmissive LCD. An improved version of the TN LCD mode was introduced in 1985, the so-called *super-twisted nematic* (STN) display mode, where the twist is 270° , instead of 90° [44, 49, 50].

The IPS mode is another broadly applied display mode. As shown in Fig. 1.15 (b), instead of placing the two electrodes on the top and bottom layers of the cell, in the IPS mode the electrodes are placed on the same layer. In the OFF state, the LCs are oriented parallel to one of the polarizers, thus no light can pass through the cell. In the ON state, the electric field rotates the LCs to an angle (not 0° or 90° to the polarizers) while keeping the LCs parallel to the surface. Now, due to the birefringence, the LCs change the linearly polarized light to elliptically polarized light, thus part of the light can pass through the second polarizer. [44, 51]

Compared with TN and IPS mode, which use LCs materials with positive dielectric anisotropy, the vertical alignment (VA) mode LCD uses LCs with negative dielectric anisotropy. Different manufacturers are using slightly different versions of the VA mode such as multi-domain vertical alignment (MVA) and patterned vertical alignment (PVA).

A schematic of a MVA mode display is shown in Fig. 1.15 (c). The VA mode display is a relatively recent development, introduced less than a decade ago, which set a new trend in LCDs with advantages such as ultra-wide viewing angle, high contrast and fast response time [53, 55, 56].

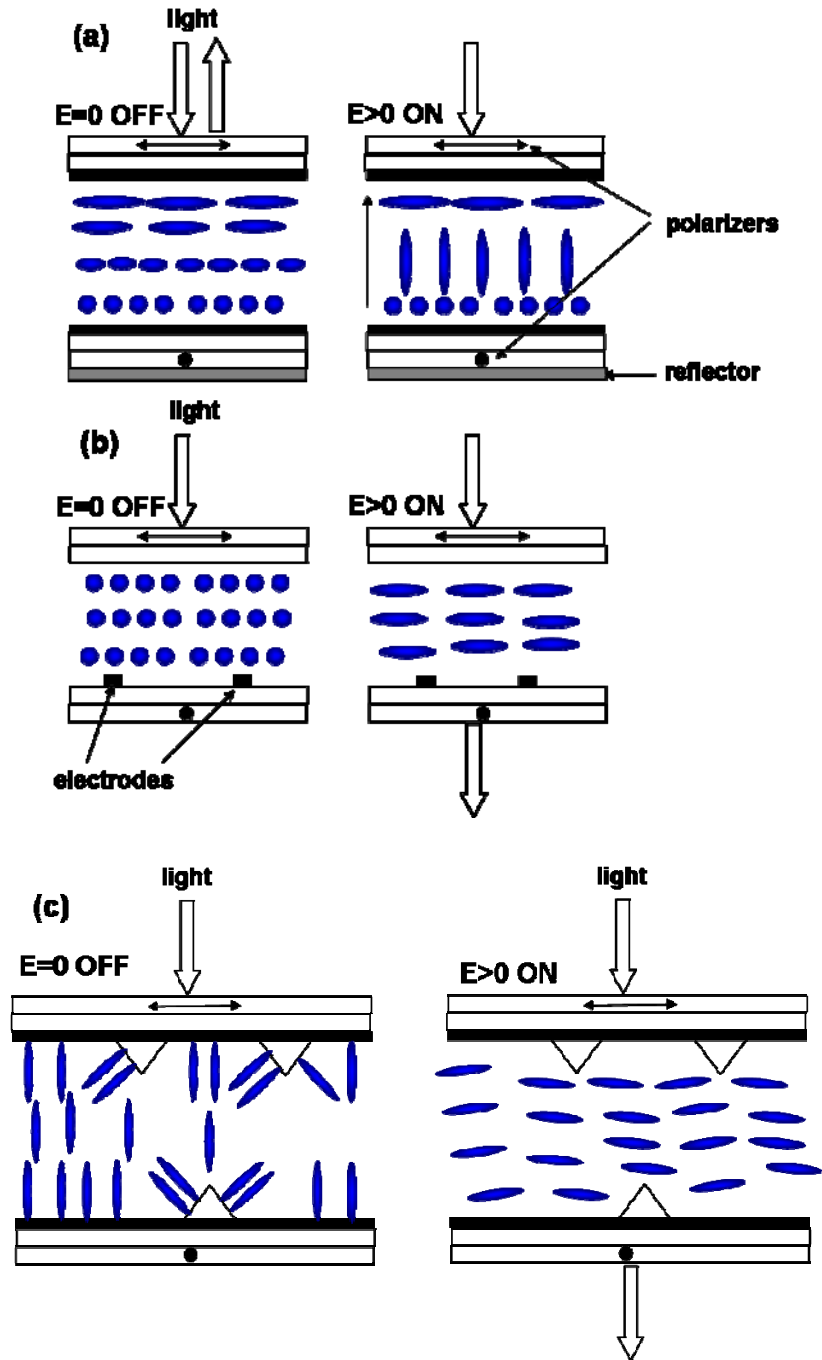


Fig. 1.15. Examples of LCD modes: (a) TN mode, (b) IPS mode, and (c) MVA mode (adapted from ref. 44, 53).

1.3 Gold Nanoparticles

1.3.1 Synthesis of Au NPs

Au NP research is one of the hottest topics in nanoscience and nanotechnology with thousands of papers being published each year [57]. Aqueous solutions of Au colloids containing nanosized Au nanoparticles date back to Roman times [58]. Michael Faraday was first recognized scientifically for studying the formation of Au sols [59]. Using citrate reduction of HAuCl_4 in water to synthesize Au nanoparticles (NPs) was one of the most popular methods for a long time, which was introduced by Turkevitch in 1951 [60]. This method leads to Au NPs with a ca. 20 nm diameter, and the resulting Au NPs are only stable in water. Schmid's method, published in 1981, was the first method providing the formation of Au nanoparticles with a narrow size distribution (1.4 ± 0.4 nm) [61]. The Brust-Schiffrin method, first reported in 1994 [4], has been regarded as a milestone in the research of Au NPs. This method is easy to perform; the prepared Au NPs are commonly thermally and air-stable, and can easily be re-dispersed in organic solvents. This reaction also allows for easy control of size and functionalization of Au NPs [62]. The versatility of this Au nanoparticle synthesis initiated a whole range of research activities centering on the synthesis of Au NPs with different shapes, sizes and functional groups [62-65], the assembly of Au NPs [66-71], and the use of Au NPs in different types of applications such as catalysis, biosensor design, and drug-delivery to name a few [72-78].

The Brust-Schiffrin method starts with a phase transfer of a Au(III) salt (AuCl_4) from the aqueous phase to the organic toluene phase using tetraoctylammonium bromide (TOAB) as the phase-transfer reagent. There, the Au(III) is reduced to Au^0 by NaBH_4 through a possible Au(I)-thiolate precursor [79, 80, 81], and Au NPs form in the presence

of an alkylthiol (Fig. 1.16). After removal of the solvent, the crude NP product is washed with organic solvents to remove extra thiol and TOAB, which can be tedious. The as-synthesized Au NPs are commonly obtained in the form of a black powder and can easily be re-dissolved (or dispersed) in appropriate organic solvents [4]. The size of the Au NPs can be controlled by the thiol / gold ratio and by the speed of addition of the reducing reagent [5]. Brust *et al.* also extended this method to a one-phase method without the use of a phase-transfer reagent in a report published one year later [82].

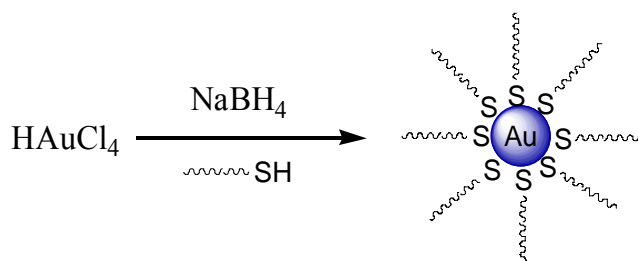


Fig. 1.16. Formation of Au NPs by the Brust-Schiffrin method (adapted from ref. 5).

Functionalization of Au NPs can be realized via three ways: first, using functional thiols to directly synthesize Au NPs [62], second, using a place-exchange method to partly replace some thiols linked to the Au NP surface with other thiols [83], and third, using organic chemistry reactions to modify the thiols already bound to the surface of the Au NPs [75]. Examples of the three methods are shown in Fig. 1.17.

Besides thiols, phosphanes can also be used as stabilisers for synthesizing Au NPs. Both types of Au NPs can be isolated as solid materials and re-dissolved in appropriate solvents [84]. Au NPs synthesized using weakly binding stabilisers such as citrate or amines are often used as seeds to prepare other shapes of Au NPs such as rods [85-87], cubes [88], plates [89], or star-shaped NPs [90].

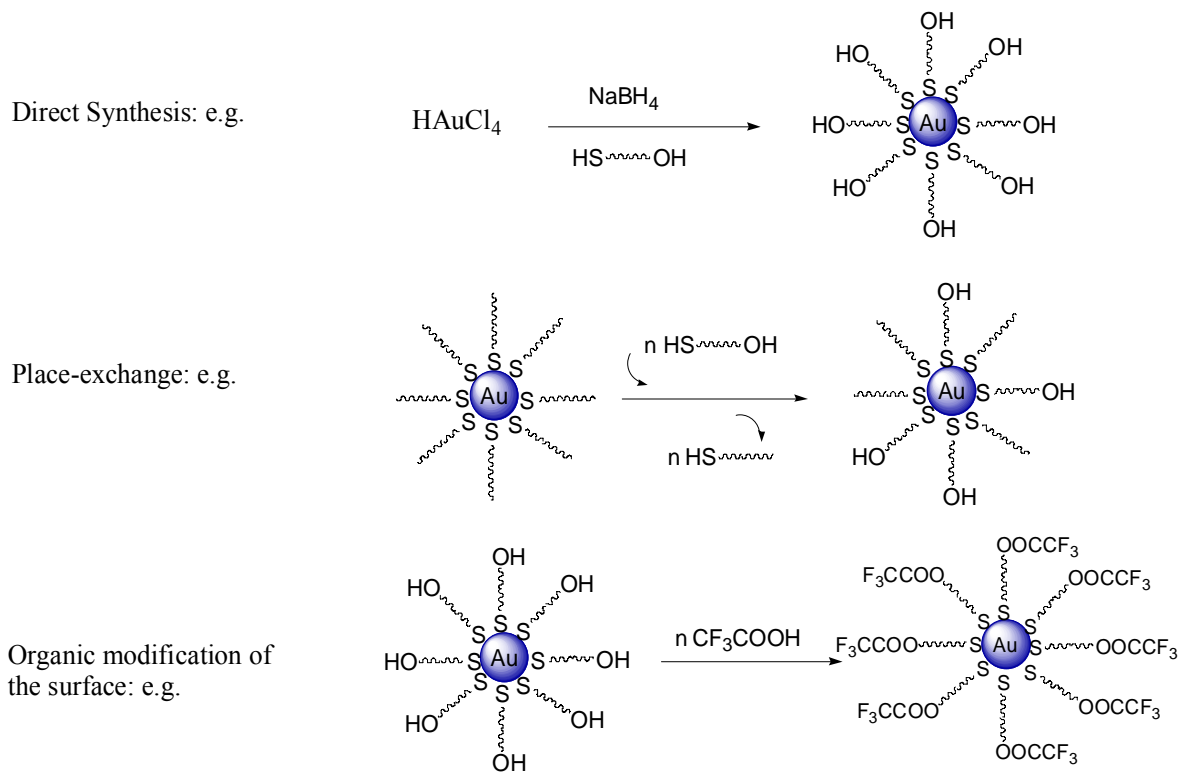


Fig. 1.17. Examples of Au NP functionalization.

1.3.2 Characterization of Au NPs

The size of Au NPs can be determined by three methods, transmission electron microscopy (TEM), which allows for a direct observation of a limited number of NPs, powder x-ray diffraction, which allows calculations of the average size of the Au NPs in the bulk, and UV-vis absorption spectroscopy [91, 92]. Although dynamic light scattering (DLS) is a well known method for size and size distribution analysis of certain NPs, the use of visible light, the strong optical absorbance of Au NPs along with the weak scattering due to the small size results in a very low signal-to-noise ratio, especially for clusters with sizes smaller than 4 nm. Hence, DLS is practically speaking not an ideal method for size analysis of small size as well as polydisperse Au NPs [91]. The purity of

Au NPs can be checked by NMR [5].

TEM has been broadly used in nanomaterials research, because it provides a direct image of size, size distribution and assembly of nanoparticles, as well as quantitative information about the structure and the chemical composition (when coupled with Energy dispersive x-ray spectroscopy (EDS) and electron energy-loss spectroscopy (EELS)). The schematic setup of a TEM instrument is shown in Fig. 1.18. A TEM consists of an illumination system using a thermionic emission source or a field emission source, a specimen stage, an objective lens, a magnification system (with magnification up to 1.5 million times), and a data recording system. EDS and EELS are used for chemical analysis [92].

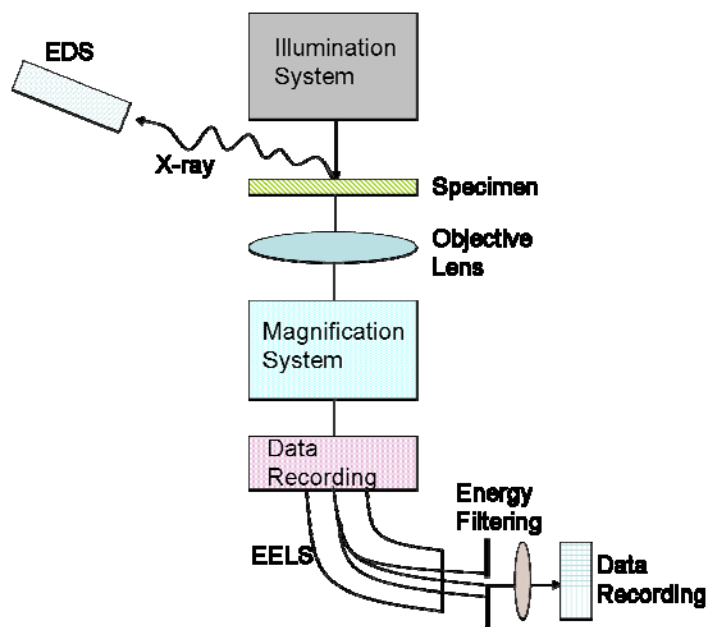


Fig. 1.18. Schematic of a TEM setup (adapted from ref. 91).

An example of a TEM image of dodecane thiol-protected Au NPs with an average size of about 5.5 nm is shown in Fig. 1.19. There are several drawbacks of the TEM technique:

first, the area of view is only a small part of the entire sample, second, it is a two-dimensional image of three-dimensional particles, and third, the resolution of the instrument also provides some error. In some cases, the error can be larger than the size distribution, especially for smaller NPs (<2 nm) [91, 93]. Therefore, XRD and UV-vis spectroscopy are used to allow for a more comprehensive analysis of the entire sample (bulk) [91].

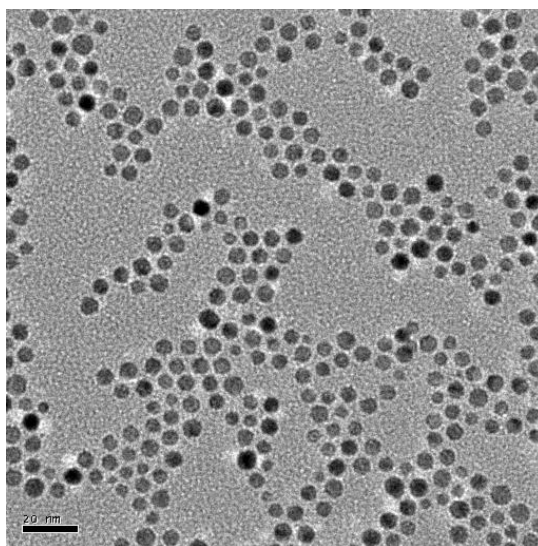


Fig. 1.19. TEM image of dodecane thiol protected Au NPs (Scale bar: 20 nm)

The principle of XRD was already introduced in Section 1.2.2.3. XRD is another traditionally used technique to infer NP size with the use of the Scherrer equation ($D = 0.88\lambda/\beta\cos\theta$), where D is the particle diameter, λ is the x-ray wavelength in nm, β is the full width at half-maximum (FWHM), θ is the Bragg angle, and 0.88 is the Scherrer constant [94]. Fig. 1.20 shows one example of hydrophilic Au NPs (triethylene glycol-terminated pentyl thiolate-protected) used in this thesis with an average size of 7.6 nm based on XRD.

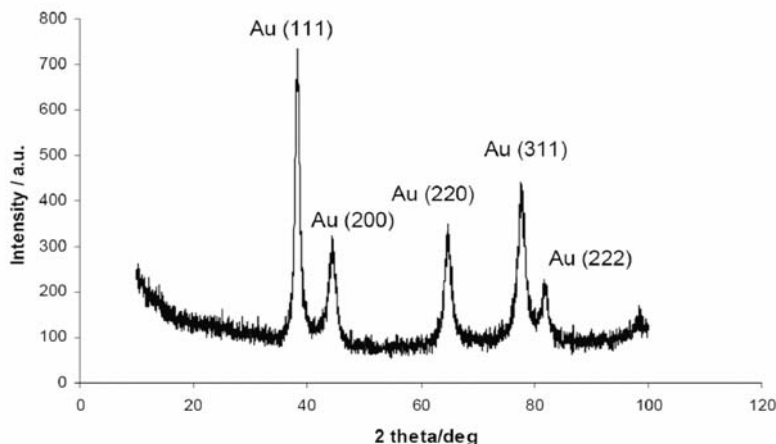


Fig. 1.20. XRD pattern of triethylene glycol-terminated pentyl thiol-protected Au NPs.

UV-vis spectroscopy is another powerful tool to analyze Au NPs. Au NPs display a broad absorption band in the visible region around 520 nm, which is related to the surface plasmon resonance (SPR). SPR is due to the collective oscillations of the free electrons at the nanoparticle's surface (for Au NPs it is the 6s electrons of the conduction band) that is correlated with the electromagnetic field of the light, as shown in Fig. 1.21. It is known that the free electrons in the metal are free to travel within the materials. Taking bulk Au and Ag as an example, the average travel distance is 50 nm, thus, if the particle size is smaller than 50 nm, all the conduction band electrons involving interactions are expected to occur at the surface. When the wavelength of light is much larger than the particle's size, based on the Mie theory, under the irradiation of light, the conduction electrons of the Au NPs start to collectively oscillate at a resonant frequency that is related to the lattice of positive ions. At this frequency, the incident light is absorbed by the NPs, which is known as the SPR peak. The SPR maximum and bandwidth are sensitive to the particle size, shape, temperature, and more importantly, to the surrounding medium's dielectric constant [95, 96]. However, for Au NPs with a size smaller than 2 nm the SPR peak is not

easily detected [96], whereas, for larger size Au NPs, the broad SPR peak around 520 nm is easily observed. Assuming the same stabilizing ligands and the same solvent, the relative different sizes of Au NPs can be discerned by the maximum of the SPR peak. For larger Au NPs, the peak will slightly shift to longer wavelengths. Thus, the color of Au NPs solutions and, therefore UV-vis spectroscopy, can give a rapid feedback on the NP size [91]. The strong dependence of the SPR on the local environment has made Au NPs attractive candidates for sensors and biological applications [72, 74]. Two UV-vis spectra of Au NPs used in this thesis are shown in Fig. 1.22.

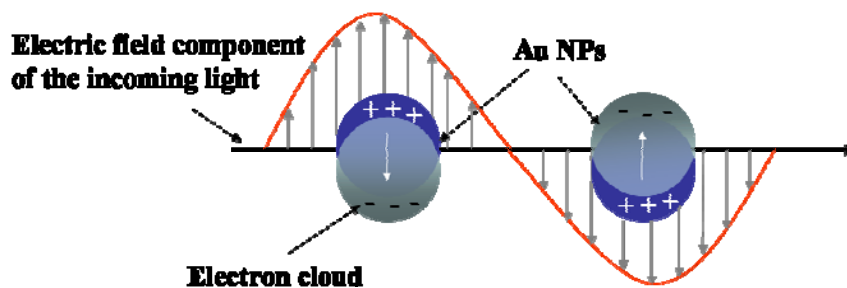


Fig.1.21. Schematic illustration of the origin of the SPR of quasi-spherical Au NPs (adapted from ref. 97).

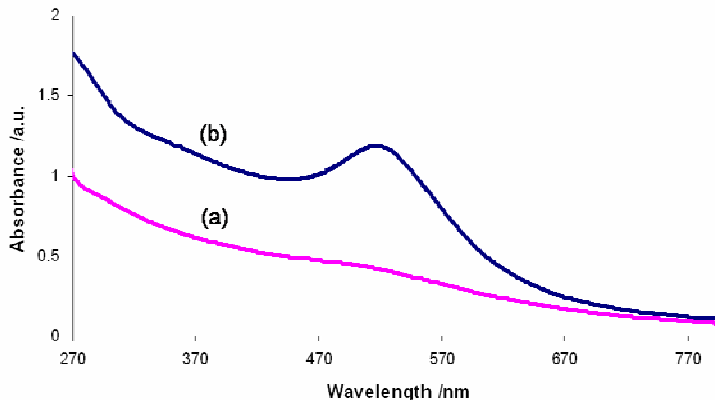


Fig. 1.22. UV-vis spectra of Au NPs: (a) hexane thiol-protected Au NPs with an average size of 2.1 nm, (b) dodecane thiol-protected Au NPs with an average size of 5.5 nm.

The purity of Au NPs (i.e., removal of free, non-bound thiol(s) and phase transfer agent TOAB) can be checked by NMR (^1H and ^{13}C). However, the ^1H spectra commonly suffer from broad signals. This phenomenon is mainly related to spin-spin relaxational broadening effects, to location variations of the Au-S bonds around the NP, and to a gradient of packing density [98-100]. An example of a ^1H NMR spectrum of a type of chiral Au NPs and the corresponding free thiol are shown in Fig. 1.23. ^1H NMR spectroscopy has also been used to determine the ratio of two (or more) types of thiols in mixed-monolayer protected Au NPs using the integration of relevant peaks. A more accurate method is using I_2 to decompose the NPs to quantitatively liberate the thiol ligands as disulfides before using ^1H NMR to determine the ratio. [98] While there is often no significant difference between the ratios determined by the two methods, a comparison between the two methods is useful and often necessary. [98, 101]

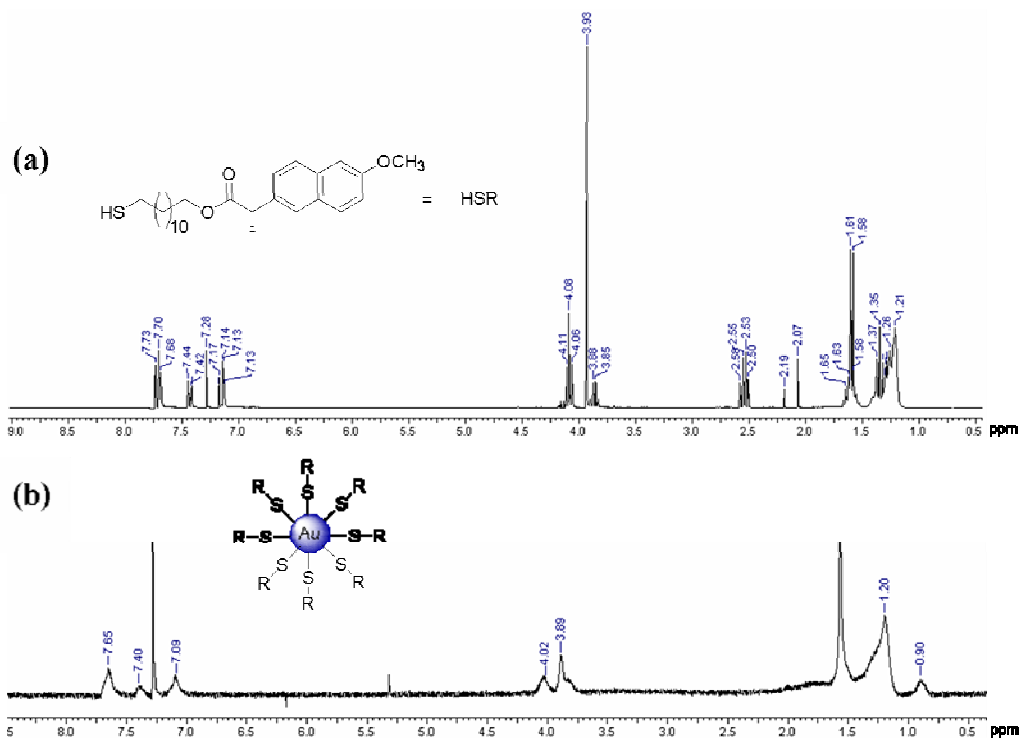


Fig. 1.23. ^1H NMR spectra of (a) free (*S*)-naproxen-functionalized dodecane thiol (b) (*S*)-naproxen-functionalized dodecane thiol protected Au NPs.

Elemental analysis has also been broadly used to determine the composition of NPs [4, 102-104]. After determining the size of the Au NPs using TEM or XRD, the sum formula of the Au NP composition can be calculated following the protocol by Heath *et al.* assuming a quasi-spherical particle [105]: the number of gold atoms per cluster $N_{\text{Au}} = 4\pi r^3/3v_g$, where r is the radius (Å) of NPs, and v_g is the volume of a gold atom ($v_g = 17 \text{ \AA}^3$); the average number of thiolates per particle is calculated by $n_{\text{thiol}} = 4\pi r^2/21.4 \text{ \AA}^2$. Then, the percentage of C, H, S as well as other elements in the thiolates can be calculated and can be confirmed by elemental analysis. If using mixture of different thiols to synthesize Au NPs, the relative ratio of different thiols can also be confirmed by elemental analysis after forming the formula based on the size and the ^1H NMR spectrum. [104]

Aside from the techniques mentioned above, there is a long list of instruments used for Au NP characterization such as scanning tunneling (STM) and atomic force microscopy (AFM) for size determination [62], x-ray photoelectron spectroscopy (XPS) for determining the oxidation state of the Au atoms [4], and FT-IR spectroscopy for studying thiolate ligand conformations [99].

1.3.3 Assembly of Au NPs

The assembly of Au NPs has been extensively studied over the past years, particularly with the aim of forming ordered and predictable arrays that can utilize the unique properties of Au NPs as well as the collective properties of Au NP arrays for the construction of nano-devices [64-71]. Typically, two approaches are used: a *top-down* approach using lithographic techniques or a *bottom-up* approach using self-assembly.

Compared to the *top-down* approach, *bottom-up* fabrication offers a number of advantages such as experimental simplicity, low cost, and the possibility of 3-dimensional assembly [106].

Au NPs intrinsically possess self-assembly properties. In the early stage it was found that Au NPs can spontaneously form highly ordered superlattices simply by slow evaporation of an organic solvent on a suitable substrate such as highly ordered pyrolytic graphite (HOPG) [107-111], as shown in Fig. 1.24. Later on, superlattices of other particles stabilized in various ways were also observed, indicating that this might be a universal phenomenon [112, 113].

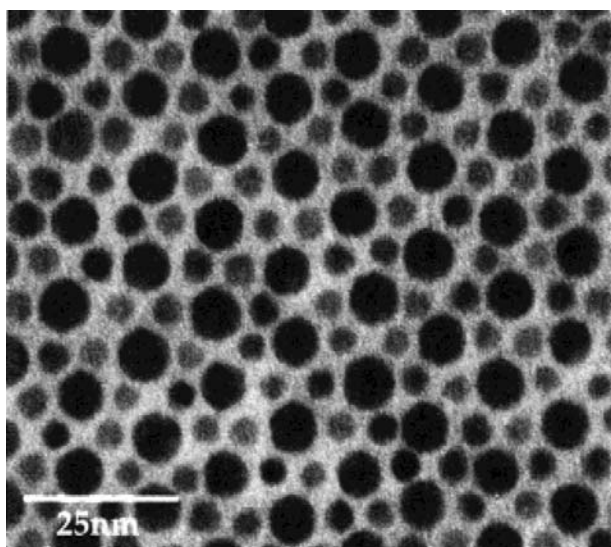


Fig. 1.24. TEM image of an AB₂ type superlattice of Au and Ag NPs stabilised by decanethiol. The larger particles are Au. Reprinted with permission from ref. [111]

This phenomenon was later on extended to approaches that would chemically modify the outer layer of the Au NPs. Such examples include 2-dimensional micelle and vesicle-like organization of Au NPs using mixed ligand shells of phosphinine and thiol [114], as well as ring and chain formations of nanorods [115-120].

Chemical linkage of Au NPs is another way to assemble Au NPs. Using dithiols to link

Au NPs has been studied for years, especially by the Schmid group, which demonstrated the formation of a 3-dimensional crystalline structure as well as the formation of an ordered 2-dimensional thin film [121]. Using a cleavable dithiol linker, reversible aggregation and de-aggregation of Au NPs can be induced [122]. An interesting chain-like assembly of spherical aggregates of Au NPs was observed by the Brust group using 1,9-nonanedithiol as bridging ligands [123] (Fig. 1.25). More recently, Stellacci *et al.* used Au NPs with a stabilizing shell of 1-nonanethiol and 4-methybenzenethiol, and then exchanged the ligands at the “pole” sites of the Au NPs with a thiol molecule bearing a carboxylic acid group. Polymerization of the Au NPs via a diamine linker induced the formation of beautiful Au NP chains [124, 125].

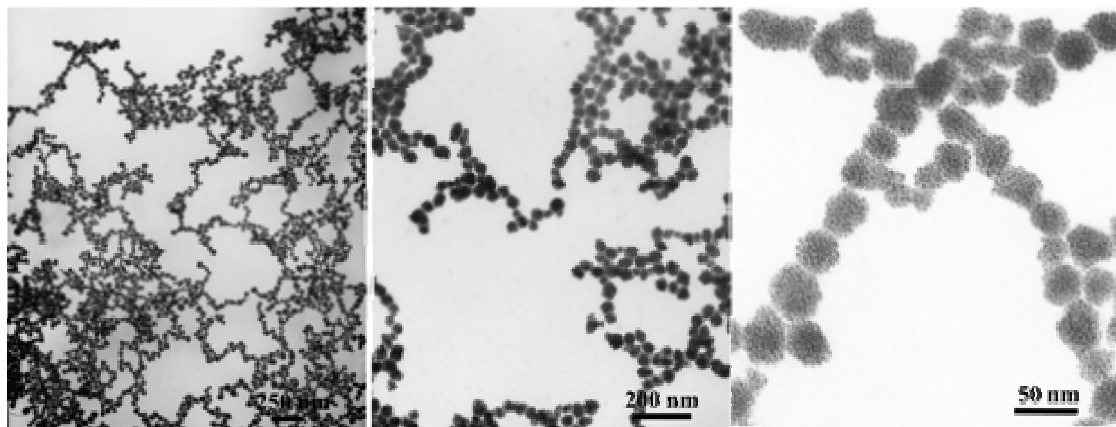


Fig. 1.25. TEM image of linear assembly of Au NPs aggregates. Each assembly aggregate is formed by linking 5-8 nm Au NPs using 1,9-nonanedithiol. Reprinted with permission from ref. [123]

Another viable class of materials capable of templating the assembly of Au NPs are polymers. Particularly attractive here are 1-dimensional assembly and in some studies also 2 and 3-dimensional assembly, if sufficient attraction (or molecular recognition) between the ligands of the Au NP and the polymer is realized [121, 126]. Schmid *et al.* used isooctyl-substituted poly(paraphenylenethynyl) (PPE-i-octyl) to chemisorb

$\text{Au}_{55}(\text{PPh}_3)_{12}\text{C}_{16}$ into a 1-dimensional arrangement along the polymer string [127] (Fig. 1.26). Poly(vinyl-pyrrolidone) (PVP) was also used by the same group to chemisorb Au_{55} NPs via the phenyl groups and generate a stable network of PVP decorated with Au NPs [128]. The Rotello group used carboxylic acid terminated Au NPs and an amine-functionlized random copolymer to obtain a controllable NP array using binary Au NP-polymer and ternary Au NP-polymer-Au NP assembly processes [129]. H-bonding interactions and π - π stacking were also employed in polymer-directed assembly of Au NPs [130-132]. Kramer and coworkers used thiol-terminated polymers on gold nanoparticles to create lines of particles that localized at the interface between the polystyrene and poly(2-vinylpyridine) microdomains [133]. Modification of Au NPs with photoactive groups was explored by Ozawa *et al.*, who attached Au NPs to porphyrin polymers resulting in the formation of 1-dimensional Au nanowires [134].

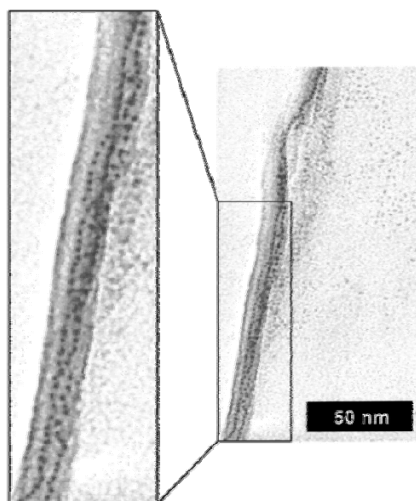


Fig. 1.26. TEM image of a string of PPE, decorated with two chains of $[\text{Au}_{55}]$ clusters. Reprinted with permission from ref. [127]

It is also possible to template predictable structures of Au NPs with a non-modified ligand shell [135]. The Yoshino group used Langmuir-Blodgett films to align Au NPs into 1-dimensional arrays [136]. Bjornholm and coworkers employed an amphiphilic poly (paraphenylene) as templating agent for the formation of a 2-dimensional Au NP network on a water surface [137].

Biomolecule-directed assembly of Au NPs is another important approach. Examples include DNA [74], proteins [138] and viruses [139]. One advantage of DNA for self-assembly is the high base-pairing specificity and the predictable DNA construction [74]. The first reports of templating Au NP array formation using DNA was published in 1996 independently by the Mirkin and the Alivisatos groups [140, 141]. Mirkin's group used short, single stranded oligonucleotides bound with thiol linkers to Au NPs. Using a linking DNA which is complementary to the strands linked to the NPs a three-dimensional Au NP network was formed [140], which is remotely related to the dithiol linker approach discussed earlier. The Alivisatos group used a method similar to using a polymer to form a 1-dimensional assembly of Au NPs. The Au NPs were first linked with an oligonucleotide and then bound to its complementary sequence on a longer single-stranded DNA, thus distributing the Au NPs evenly in a 1-dimensional fashion [141]. Using DNA to assemble Au as well as other NPs has been extensively studied over the past ten years and has been reviewed by the Mirkin and Simon groups [74, 142]. More recent breakthroughs in this area include that a crystalline structure can be obtained with carefully designed DNA sequences connecting the Au NPs [143, 144], and that highly ordered Au NP double helices can be formed using a new peptide-based method [145], as shown in Fig. 1.27.

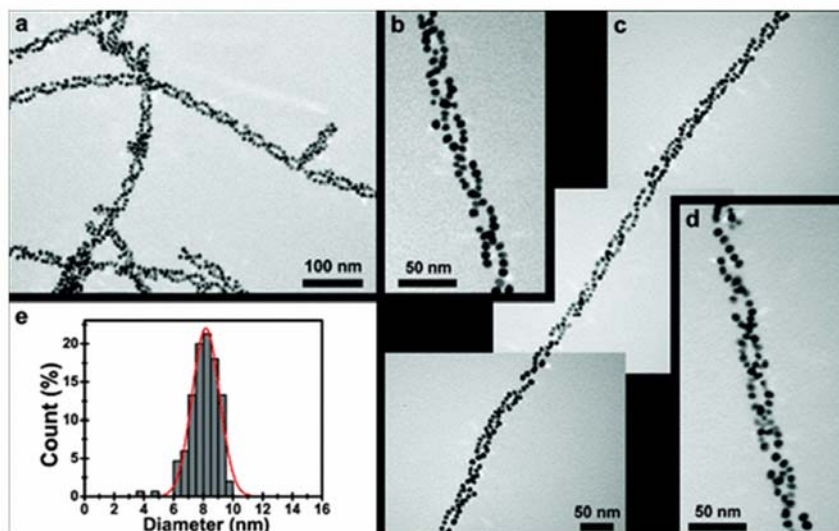


Fig. 1.27. TEM images of Au NP double helices; size distribution of Au NPs is also presented. Reprinted with permission from ref. [145].

The McMillan group used crystalline protein templates that form hollow, double-ring structures to guide the formation of 2-dimensional arrays of Au NPs up to 20 μm in diameter [138]. Blum and coworkers used different mutants of Cowpea Mosaic Virus as scaffolds to bind 2 and 5 nm Au NPs at specific locations on the virus resulting in 3-dimensional patterns of Au NPs with fixed interparticle distances [139].

In summary, along with the breakthrough of a versatile and easy synthesis of Au NPs, the assembly of Au NPs has been broadly studied over the past years, and various array structures can be achieved in a predictable fashion. Despite these advances, assembling NPs into well-defined superstructures amenable to practical use still remains a challenge, and continuing research is needed to develop more facile and efficient methods [65, 145].

This is the point where liquid crystals enter the picture. The intrinsic self-assembly properties of LCs and the diverse phase morphologies of LC phases with ordering in one, two, or even three dimensions, makes LCs unique candidates for templating and ordering

Au NP in different arrays. In addition, such NP arrays in LC matrices can be potentially tuned by temperature and electric or magnetic field, which makes this method distinctive from all other methods mentioned above.

This is the initial objective of this thesis, i.e., controlling the assembly of Au NPs using LC hosts. With the progress of the research work, we found that LC/NP composites can have much broader and profound effect, not only on the assembly of NPs. The properties of the LC hosts themselves are strongly influenced by a very small amount of Au NP dopant. To set the stage for the thesis, a comprehensive literature review of nanoparticle-liquid crystal systems is presented in chapter 2.

References

- [1] G. W. Gray, in *Handbook of Liquid Crystals*, Vol. 1, D. Demus, J. Goodby, G. W. Gray, H. W. Spiess, V. Vill, eds., (Wiley-VCH, Weinheim, **1998**), pp. 1-16.
- [2] B. Bahadur eds., *Liquid Crystals-Application and Uses* (World Scientific, Singapore, **1990**).
- [3] D. Demus, J. Goodby, G. W. Gray, H.W. Spiess, V. Vill eds., *Handbook of Liquid Crystals* (Wiley-VCH, Weinheim, **1998**) pp. 731-896.
- [4] M. Brust, M. Walker, D. Bethell, D. J. Schiffrin, R. Whyman, *Chem. Commun.* **1994**, 801-802.

Note: As this thesis is “paper-based” thesis, the results of research are presented in a way as they were published at peer-reviewed journals. Due to the copyright issue, self-contained references have been included in individual research chapters, thus, other part of thesis (introduction, conclusion) also use this constant style.

- [5] M. Daniel, D. Astruc, *Chem. Rev.* **2004**, *104*, 293-346.
- [6] G. M. Koenig Jr., B. T. Gettelfinger, J. J. de Pablo, N. L. Abbott, *Nano Lett.* **2008**, *8*, 2362-2368.
- [7] J. W. Goodby, I. M. Saez, S. J. Cowling, V. Gortz, M. Draper, A. W. Hall, S. Sia, G. Cosquer, S-E. Lee, E. P. Raynes, *Angew. Chem., Int. Ed.* **2008**, *47*, 2754- 2787.
- [8] T. Hegmann, H. Qi, V. M. Marx, *J. Inorg. Organomet. Polym. Mater.* **2007**, *17*, 483-508.
- [9] L. Qin, M. J. Banholzer, J. E. Millstone, C. A. Mirkin, *Nano Lett.* **2007**, *7*, 3849-3853.
- [10] W. Huang, W. Qian, P. K. Jain, M. A. El-Sayed, *Nano Lett.* **2007**, *7*, 3227-3234.
- [11] J. P. You, J. H. Choi, S. Kim, X. Li, R. S. Williams, R. Ragan, *Nano Lett.* **2006**, *6*, 1858-1862.
- [12] S. K. Prasad, K. L. Sandhya, G. G. Nair, U. S. Hiremath, C. V. Yelamaggad, S. Sampath, *Liq. Cryst.* **2006**, *33*, 1121-1125.
- [13] H. Qi, B. Kinkead, T. Hegmann, *Adv. Funct. Mater.* **2008**, *18*, 212-221.
- [14] P. Collings, M. Hird, *Introduction to Liquid Crystals* (Taylor & Francis, **1997**).
- [15] C. Tschierske, *Prog. Polym. Sci.* **1996**, *21*, 775-852.
- [16] C. Tschierske, *J. Mater. Chem.* **1998**, *8*, 1485-1508.
- [17] S. Laschat, A. Baro, N. Steinke, F. Giesselmann, C. Hgele, G. Scalia, R. Judele, E. Kapatsina, S. Sauer, A. Schreivogel, M. Tosoni. *Angew. Chem., Int. Ed.* **2007**, *46*, 4832-4887.
- [18] S. Chandrasekhar, B. K. Sadashiva, K. A. Suresh, *Pramana* **1977**, *9*, 471-480.
- [19] S. Xiao, M. Myers, Q. Miao, S. Sanaur, K. Pang, M. L. Steigerwald, C. Nuckolls,

Angew. Chem., Int. Ed. **2005**, *44*, 7390-7394.

- [20] L. Schmidt-Mende, A. FechtenkRtter, K. Mqlen, E. Moons, R. H. Friend, J. D. Mackenzie, *Science* **2001**, *293*, 1119-1122.
- [21] T. Niori, T. Sekine, J. Watanabe, T. Furukawa, H. Takezoe, *J. Mater. Chem.* **1996**, *6*, 1231-1233.
- [22] R. Reddy, C. Tschierske, *J. Mater. Chem.* **2006**, *16*, 907-961
- [23] M. B. Ros, J. L. Serrano, M. Fuente, C. L. Folcia, *J. Mater. Chem.* **2005**, *15*, 5093-5098.
- [24] J. Etxebarria, M. B. Ros, *J. Mater. Chem.* **2008**, *18*, 2919-2926.
- [25] D. Demus, J. Goodby, G. W. Gray, H. W. Spiess, V. Vill, eds., *Handbook of Liquid Crystals*, Vol. 2a, chpt. III,(Wiley-VCH, Weinheim, **1998**), pp. 47-302 and S. Chandrasekhar, Vol. 2b, pp. 749-780.
- [26] S. Kumar, *Chem. Soc. Rev.* **2006**, *35*, 83-109.
- [27] I. Dierking, *Textures of Liquid Crystals*, (Wiley-VCH, Weinheim, **2003**), pp. 16-18.
- [28] D. Gin, J. E. Bara, R. D. Noble, B. J. Elliott, *Macromol. Rapid Commun.* **2008**, *29*, 367-389.
- [29] J. M. Seddon, R. H. Templer, *Phil. Trans. R. Sot. Land. A.* **1993**, *344*, 377-401.
- [30] I. Dierking, *Textures of Liquid Crystals*, (Wiley-VCH, Weinheim, **2003**), pp. 32-42.
- [31] I. Dierking, *Textures of Liquid Crystals*, (Wiley-VCH, Weinheim, **2003**), pp. 52-74.
- [32] I. Dierking, *Textures of Liquid Crystals*, (Wiley-VCH, Weinheim, **2003**), pp.

91-96.

- [33] A. Donald, A. Windle and S. Hanna, *Liquid Crystalline Polymers*, (Cambridge University Press, **2006**), p. 292-351.
- [34] I. Dierking, *Textures of Liquid Crystals*, (Wiley-VCH, Weinheim, **2003**), pp. 135-149.
- [35] Y. Bouligand, in *Handbook of Liquid Crystals*, Vol. 1, D. Demus, J. Goodby, G. W. Gray, H. W. Spiess, V. Vill, eds.,(Wiley-VCH, Weinheim, **1998**), pp. 406-453.
- [36] J. Thoen in *Handbook of Liquid Crystals*, Vol. 1, D. Demus, J. Goodby, G. W. Gray, H. W. Spiess, V. Vill, eds.,(Wiley-VCH, Weinheim, **1998**), pp. 310-334.
- [37] Q. Jang, K. Lu, in *Handbook of Nanophase and Nanostructured Materials*. Vol 2. Z. L. Wang, Y. Liu, Z. Zhang eds (Kluwer Academic, Plenum, **2003**), pp. 358-384.
- [38] X. L. Wang, J. L. Robertson, in *Handbook of Nanophase and Nanostructured Materials*. Vol 2. Z. L. Wang, Y. Liu, Z. Zhang, eds. (Kluwer Academic, Plenum, **2003**), pp. 1-28.
- [39] S. Kumar, in *Liquid Crystals: Experimental Study of Physical Properties and Phase Transitions*. S. Kumar ed. (Cambridge, **2001**), pp. 65-95.
- [40] <http://www.mrl.ucsb.edu/mrl/centralfacilities/xray/instruments/saxs.html>
- [41] J. M. Seddon, in *Handbook of Liquid Crystals*, Vol. 1, D. Demus, J. Goodby, G. W. Gray, H. W. Spiess, V. Vill, eds.,(Wiley-VCH, Weinheim, **1998**), pp. 635-671.

- [42] X. Cheng, M. Prehm, M. K. Das, J. Kain, U. Baumeister, S. Diele, d. Leine, A. Blume, C. Tschierske. *J. Am. Chem. Soc.* **2003**, *125*, 10977-10996.
- [43] M. Kölbel, T. Beyersdorff, X. Cheng, C. Tschierske, J. Kain, S. Diele. *J. Am. Chem. Soc.* **2001**, *123*, 6809-6818.
- [44] P. J. Collings, *Liquid Crystals: Nature's Delicate Phase of Matter*. (Princeton University Press, Princeton, **2002**). pp. 82-106.
- [45] S. T. Wu, D. Coates, E. Bartmann, *Liq. Cryst.* **1991**, *10*, 635-646.
- [46] I. C. Sage, in *Handbook of Liquid Crystals*, Vol. 1, D. Demus, J. Goodby, G. W. Gray, H.W. Spiess, V. Vill eds. (Wiley-VCH, Weinheim, **1998**), pp. 731-762.
- [47] J. Hoodboom, T. Rasing, A. E. Rowan, R. J. M. Nolte, *J. Mater. Chem.* **2006**, *16*, 1305-1314.
- [48] T. Uchida, H. Seki, in *Liquid Crystals, Applications and Users*, B. Bahadur ed. (World Scientific, London, **1990**), *Vol. 3*, p. 1.
- [49] M. Schadt, W. Helfrich, *Appl. Phys. Lett.* **1971**, *8*, 127-128.
- [50] T. J. Scheffer, J. Nehring, *J. Appl. Phys.* **1985**, *58*, 3022.
- [51] R. Kiefer, B. Webber, F. Windscheid, G. Baur, *Proc. Japan Displays* **1992**, *92*, 547-550.
- [52] Fergason, J. L. *SID Int. Symp. Dig. Technol.* **1985**, *16*, 68-70.
- [53] A. Takeda, S. Kataoka, T. Sasaki, H. Chida, H. Tsuda, K. Ohmuro, T. Sasabayashi, Y. Koike, K. Okamoto, *SID Digest.* **1998**, 1077-1100.
- [54] K.H. Kim, *SID Digest*, **2003**, *40*, 1208-1215.
- [55] Y. Tanaka, Y. Taniguchi, T. Sasaki, A. Takeda, Y. Koibe, K. Okamoto, *SID Digest.*, **1999**, 206-209.

- [56] Y. Koike, K. Okamoto, *Fujitsu Sci. Tech. J.* **1999**, *35*, 221-228.
- [57] S. Eustis, M. A. El-Sayed, *Chem. Soc. Rev.* **2006**, *35*, 209-217.
- [58] J. W. Mellor, *A Comprehensive Treatise on Inorganic and Theoretical Chemistry*, Longmans, Green and Co, London, **1923**.
- [59] M. Faraday, *Philos. Trans. Roy. Soc.* **1857**, *147*, 145-153.
- [60] J. Turkevitch, P. C. Stevenson, J. Hillier, *Discuss. Faraday Soc.* **1951**, *11*, 55-75.
- [61] G. Schmid, R. Pfeil, R. Boese, F. Bandermann, S. Meyer, G. H. M. Calis, J. W. A. Velden, *Chem. Ber.* **1981**, *114*, 3634-3642.
- [62] A. C. Templeton, W. P. Wuelfing, R. W. Murray, *Acc. Chem. Res.* **2000**, *33*, 27-36.
- [63] C. J. Murphy, T. K. Sau, A. M. Gole, C. J. Orendorff, J. Gao, L. Gou, S. E. Hunyadi and T. Li, *J. Phys. Chem. B* **2005**, *109*, 13857-13870.
- [64] C. Burda, X. Chen, R. Narayanan, M. A. El-Sayed, *Chem. Rev.* **2005**, *105*, 1025-1102.
- [65] Y. Xia, P. Yang, Y. Sun, Y. Wu, B. Mayers, B. Gates, Y. Yin, F. Kim, H. Yan, *Adv. Mater.* **2003**, *15*, 353-389.
- [66] M. Sastry, M. Rao, K. N. Ganesh, *Acc. Chem. Res.* **2002**, *35*, 847-855.
- [67] R. L. Whetten, M. N. Shafiqullin, J. T. Khoury, T. G. Schaaff, I. Vezmar, M. M. Alvarez, A. Wilkinson, *Acc. Chem. Res.* **1999**, *32*, 397-406.
- [68] A. N. Shipway, M. Lahav, I. Willner, *Adv. Mater.* **2000**, *12*, 993-998.
- [69] M. P. Pileni, *J. Phys. Chem. B* **2001**, *105*, 3358-3371.
- [70] C. N. R. Rao, G. U. Kulkarni, P. J. Thomas, *Chem. Soc. Rev.* **2000**, *29*, 27-35.
- [71] S. A. Maier, M. L. Brongersma, P. G. Kik, S. Meltzer, A. A. G. Requicha, H. A.

- Atwater, *Adv. Mater.* **2001**, *13*, 1501-1505.
- [72] M. De, P. S. Ghosh, V. M. Rotello, *Adv. Mater.* **2008**, *20*, 4225-4241.
- [73] D. W. Grainger, D. G. Castner, *Adv. Mater.* **2008**, *20*, 867-877.
- [74] N. L. Rosi, C. A. Mirkin, *Chem. Rev.* **2005**, *105*, 1547-1562.
- [75] R. Shenhar, V. M. Rotello, *Acc. Chem. Res.* **2003**, *36*, 549-561.
- [76] E. Katz, I. Willner, *Angew. Chem., Int. Ed.* **2004**, *43*, 6042-6108.
- [77] R. Narayanan, M. A. El-Sayed, *J. Phys. Chem. B*, **2005**, *109*, 12663-12676.
- [78] K. Kneipp, H. Kneipp, I. Itzkan, R. R. Dasari, M. S. Feld, *Chem. Rev.* **1999**, *99*, 2957-2976.
- [79] S. Chen, A. C. Templeton, R. W. Murray, *Langmuir* **2000**, *16*, 3543-3548.
- [80] Y.-S. Shon, C. Mazzitelli, R. W. Murray, *Langmuir* **2001**, *17*, 7735-7741.
- [81] M. K. Corbierre, R. B. Lennox, *Chem. Mater.* **2005**, *17*, 5691-5696.
- [82] M. Brust, J. Fink, D. Bethell, D. J. Schiffrin, C. J. Kiely, *Chem. Commun.* **1995**, 1655-1656.
- [83] M. J. Hostetler, S. J. Green, J. J. Stokes, R. W. Murray, *J. Am. Chem. Soc.* **1996**, *118*, 4212-4213.
- [84] G. Schmid, B. Corain, *Eur. J. Inorg. Chem.* **2003**, 3081-3098.
- [85] S. Link, M.A. El-Sayed, *J. Phys. Chem. B* **1999**, *103*, 8410-8426.
- [86] Y-Y. Yu, S. Chang, C. Lee, C. R. Wang, *J. Phys. Chem. B* **1997**, *101*, 6661-6664.
- [87] N. R. Jana, L. Gearheart, C. J. Murphy, *J. Phys. Chem. B* **2001**, *105*, 4065-4067.
- [88] Y. N. Xia, *Y. Science* **2002**, *298*, 2176-2179.
- [89] S. I. Stoeva, V. Zaikovski, B. L. V. Prasad, P. K. Stoimenov, C. M. Sorensen, K. J. Klabunde, *Langmuir* **2005**, *21*, 10280-10283.

- [90] E. Hao, R. C. Bailey, G. C. Schatz, J. T. Hupp, S. Li, *Nano Lett.* **2004**, *4*, 327-330.
- [91] J. P. Wilcoxon, B. L. Abrams, *Chem. Soc. Rev.* **2006**, *35*, 1162-1194.
- [92] Z. L. Wang, Y. Liu, Z. Zhang eds *Handbook of Nanophase and Nanostructured Materials*. Vol 2. (Kluwer Academic, Plenum, **2003**).
- [93] A. Dass, A. Stevenson, G. R. Dubay, J. B. Tracy, R. W. Murray, *J. Am. Chem. Soc.* **2008**, *130*, 5940-5946.
- [94] R.C. Rau, *Advances in X-ray Analysis*, vol. 5, Plenum Press, Inc., New York, **1962**, p. 104.
- [95] M. Hu, J. Chen, Z-Y. Li, L. Au, G. V. Hartland, X. Li, M. Marquese, Y. Xia, *Chem. Soc. Rev.* **2006**, *35*, 1084-1094.
- [96] M. Sastry, M. Rao, K. N. Ganesh, *Acc. Chem. Res.* **2002**, *35*, 847-855.
- [97] K. A. Willets, R. P. Van Duyne, *Ann. Rev. Phys. Chem.* **2007**, *58*, 267-297.
- [98] A. C. Templeton, M. J. Hostetler, C. T. Kraft, R. W. Murray, *J. Am. Chem. Soc.* **1998**, *120*, 1906-1911.
- [99] A. Badia, L. Cuccia, L. Demers, F. Morin, R. B. Lennox, *J. Am. Chem. Soc.* **1997**, *119*, 2682-2692.
- [100] A. Badia, L. Demers, L. Dickinson, F. G. Morin, R. Lennox, L. Reven, *J. Am. Chem. Soc.* **1997**, *119*, 11104-11105.
- [101] A. J. Kell, R. L. Donkers, M. S. Workentin, *Langmuir* **2005**, *21*, 735-742.
- [102] D. Bethell, M. Brust, D. J. Schiffrin, C. Kiely, *J. Electroanalytical Chem.* **1996**, *409*, 137-143.
- [103] C. Cheng Lin, Y. C. Yeh, C. Y. Yang, G. F. Chen, Y. C. Chen, Y. C. Wu, C. C. Chen, *Chem. Commun.* **2003**, 2920-2921.

- [104] B. Donnio, P. García-Vázquez, J-L. Gallani, D. Guillon, E. Terazzi, *Adv. Mater.* **2007**, *19*, 3534-3539.
- [105] D. V. Leff, P. C. Ohara, J. R. Heath, W. M. Gelbart, *J. Phys. Chem.* **1995**, *99*, 7036-7041.
- [106] M. Brust, C. J. Kiely, *Colloids and Surfaces A: Physicochem. Eng. Aspects* **2002**, *202*, 175-186.
- [107] R. L. Whetten, J. T. Khoury, M. Alvarez, S. Murthy, I. Vezmar, Z. L. Wang, P. W. Stephens, C. L. Cleveland, W. D. Luedtke, U. Landman, *Adv. Mater.* **1996**, *8*, 428-433.
- [108] R. L. Whetten, M. N. Shafiqullin, J. T. Khoury, T. G. Schaaff, I. Vezmar, M. M. Alvarez, A. Wilkinson, *Acc. Chem. Res.* **1999**, *32*, 397-406.
- [109] G. Schmid, W. Meyer-Zaika, R. Pugin, T. Sawitowski, J. P. Majoral, A. M. Caminade, C.O. Turrin, *Chem. Eur. J.* **2000**, *6*, 1693-1697.
- [110] W. D. Luedtke, U. Landman, *J. Phys. Chem.* **1996**, *100*, 13323-13325.
- [111] C. J. Kiely, J. Fink, J. G. Zheng, M. Brust, D. Bethell, D. J. Schiffrin, *Adv. Mater.* **2000**, *12*, 640-643.
- [112] M. P. Pileni, *Langmuir* **1997**, *13*, 3266-3276.
- [113] J. Fink, C. J. Kiely, D. Bethell, D. J. Schiffrin, *Chem. Mater.* **1998**, *10*, 922-926.
- [114] C. Vilain, F. Goettmann, A. Moores, P. L. Floch, C. Sanchez, *J. Mater. Chem.* **2007**, *17*, 3509-3514.
- [115] K. K. Caswell, J. N. Wilson, U. H. Bunz, C. J. Murphy, *J. Am. Chem. Soc.* **2003**, *125*, 13914-13915.
- [116] M. H. Zareie, X. Xu, M. B. Cortie, *Small* **2007**, *3*, 139-145.

- [117] J. Y. Chang, H. Wu, H. Chen, Y. C. Ling, W. Tan, *Chem. Commun.* **2005**, 8, 1092-1094.
- [118] S. T. Joseph, B. I. Ipe, P. Pramod, K. G. Thomas, *J. Phys. Chem. B* **2006**, 110, 150-157.
- [119] X. Hu, W. Cheng, T. Wang, E. Wang, S. Dong, *Nanotechnology* **2005**, 16, 2164-2169.
- [120] H. Nakashima, K. Furukawa, Y. Kashimura, K. Torimitsu, *Chem. Commun.* **2007**, 10, 1080-1082.
- [121] G. Schmid, U. Simon, *Chem. Commun.* **2005**, 8, 697-710
- [122] C. Guarise, L. Pasquato, P. Scrimin, *Langmuir* **2005**, 21, 5537-5541.
- [123] I. Hussain I, Z. Wang, A. I. Cooper, M. Brust, *Langmuir* **2006**, 22, 2938-2941.
- [124] G. A. DeVries, M. Brunnbauer, Y. Hu, A. M. Jackson, B. Long, B. T. Neltner, O. Uzun, B. H. Wunsch, F. Stellacci. *Science* **2007**, 315, 358-361.
- [125] R. P. Carney, G. A. De Vries, C. Dubois, H. Kim, J. Y. Kim, C. Singh, P. K. Ghorai, J.B. Tracy, R. L. Stiles, R. W. Murray, S. C. Glotzer, F. Stellacci. *J. Am. Chem. Soc.* **2008**, 130, 798-789.
- [126] A. C. Balazs, T. Emrick, T. P. Russell, *Science* **2006**, 314, 1107-1110.
- [127] D. Wyrwa, N. Beyer, G. Schmid, *Nano Lett.* **2002**, 2, 419-421.
- [128] T. Reuter, O. Vidoni, V. Torma, G. Schmid, L. Nan, M. Oleiche, L. Chi, H. Fuchs, *Nano Lett.* **2002**, 2, 709-711.
- [129] A. K. Boal, T. H. Galow, F. Ilhan, V. M. Rotello, *Adv. Funct. Mater.* **2001**, 11, 461-465.
- [130] R. Deans, F. Ilhan, V. M. Rotello, *Macromolecules* **1999**, 32, 4956-4960.

- [131] J. van Herrikhuyzen, R. A. J. Janssen, E. W. Meijer, S. C. J. Meskers, A. P. Schenning, *J. Am. Chem. Soc.* **2006**, *128*, 686-687.
- [132] J. van Herrikhuyzen, S. J. George, M. R. J. Vos, N.A. Sommerdijk, A. Ajayaghosh, S. C. Meskers, A. P. Schenning, *Angew. Chem., In. Ed.* **2007**, *46*, 1825-1828.
- [133] J.-Y. Lee, Q. Zhang, T. Emrick, A. J. Crosby, *Macromolecules* **2006**, *39*, 7392-7396.
- [134] H. Ozawa, M. Kawao, H. Tanaka, T. Ogawa, *Langmuir* **2007**, *23*, 6365-6371.
- [135] K. Norgaard, T. Bjornholm, *Chem. Commun.* **2005**, *14*, 1812-1823.
- [136] Y. Kondo, H. Fukuoka, S. Nakano, K. Hayashi, T. Tsukagoshi, M. Matsumoto, N. Yoshino, *Langmuir* **2007**, *23*, 5857-5860.
- [137] C. R. Hansen, F. Westerlund, K. Moth-Poulsen, R. Ravindranath, S. Valiyaveetil, T. Bjornholm, *Langmuir* **2008**, *24*, 3905-3910.
- [138] R. A. McMillan, C. A. Paavola, J. Howard, S. L. Chan, N. J. Zaluzec, J. D. Trent, *Nat. Mater.* **2002**, *1*, 247-252.
- [139] A. S. Blum, C. M. Soto, C. D. Wilson, J. D. Cole, M. Kim, B. Gnade, A. Chatterji, W. F. Ochoa, T. Lin, J. E. Johnson, B. R. Ratna, *Nano Lett.* **2004**, *4*, 867-870.
- [140] C. A. Mirkin, R. L. Letsinger, R. C. Mucic, J. J. Storhoff, *Nature* **1996**, *382*, 607-609.
- [141] A. P. Alivisatos, K. P. Johnsson, X. Peng, T. E. Wilson, C. J. Loweth, J. Bruchez, P. G. Schultz, *Nature* **1996**, *382*, 609-611.
- [142] C. M. Niemeyer, U. Simon, *Eur. J. Inorg. Chem.* **2005**, *18*, 3641-3655.
- [143] D. Nykypanchuk, M. Mathew, D. van der Lelie, O. Gang, *Nature* **2008**, *451*,

549-552.

- [144] Y. P. Sung, A. K. R. Lytton-Jean, B. Lee, S. Weigand, G. C. Schatz, C. A. Mirkin, *Nature* **2008**, *451*, 553-556.
- [145] C.-L. Chen, P. Zhang, N. L. Rosi, *J. Am. Chem. Soc.* **2008**, *130*, 13555-13557.

Chapter 2: Liquid crystal / nanoparticle composites

– A Review

Mutual benefits can be realized by the combination of LCs and NPs: (1) tuning the properties, especially the assembly behaviour of NPs using LCs (or using concepts of LCs), (2) modulating the properties such as defect formation or eletro-optic properties of LCs using NPs. As both aspects will be described in the thesis, this chapter will be used to review the relevant literature on LC/NP composites.

2.1 Tuning NP Properties Using LCs

2.1.1 NP Assembly

To use nanomaterials for macroscopic devices and for device integration, routes to organize them into one, two or three-dimensions with precise spatial control is the key issue [1, 2]. As indicated in Chapter 1, the most successful assembly methods include the use of polymers (particularly block copolymers) [3, 4], biomolecules like DNA [5-8] or proteins [9-11], organisms such as viruses [12, 13], and Langmuir-Blodgett films [14-16], among others. Using LC materials as an organizing host (or using the concept of liquid crystalline ordering) to assemble nanomaterials is still in its infancy [17]. Nevertheless, LCs are unique candidates due to the great variety of mesophase morphologies and fast response to external stimuli such as temperature and electric or magnetic fields [18]. Three parts will be included in this section: NPs forming LC phases, NPs with LC coatings, and assembly of NPs using LCs.

2.1.1.1 NPs Forming LC Phases

Onsager in the 1940s theoretically assessed the formation of LC phases by rigid-rod objects [19]. This theory predicts that a nematic phase can be formed in concentrated suspensions of rod-like materials above a certain threshold concentration, provided the aspect ratio of the rods is large enough. Indeed, a variety of rod-like nanomaterials can form nematic phases (or nematic-like ordering). Examples include gold nanorods [20], CdSe nanorods [21] (Fig. 2.1), and carbon nanotubes [22-24]. In all cases, nematic LC phases were verified by the observation of birefringent textures with typical disclinations using polarized optical microscopy. These LC-like structures (such as the disclinations seen in the texture) also remain visible after the solvent had been evaporated, and were in some cases also revealed by scanning electron microscopy [22, 24].

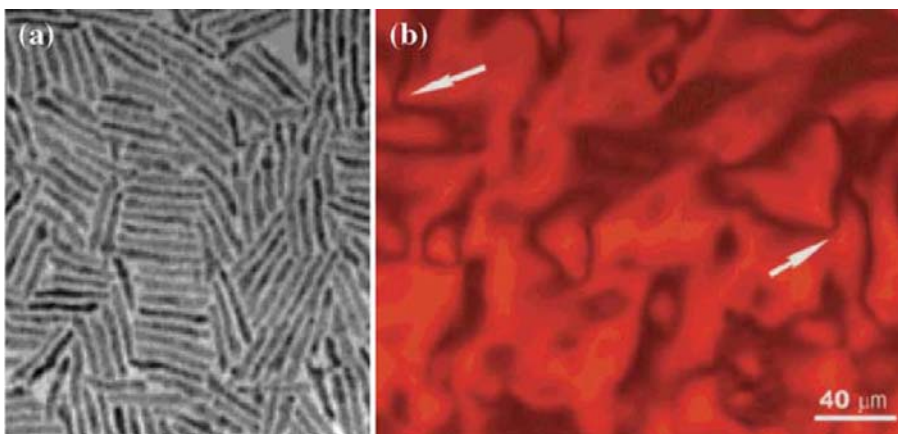


Fig. 2.1. (a) TEM image of CdSe nanorods with width of approximately 4.2 nm and length of 40 nm. (b) Image of liquid crystalline phase in concentrated solution of CdSe nanocrystals using a polarized light optical microscope. Disclinations of strength $1/2$ are clearly visible (the arrows point to the disclinations). Reprinted with permission from ref. [21]

Similar to the molecular shape variations of organic LC molecules, where different shapes of molecules can lead to LC behavior such as rod-like, disk-like or bent shaped, LC phase formation by NPs is not limited to rod-like nanomaterials. Other shapes of NPs

such as disk-shaped NPs can also exhibit LC ordering, and nematic as well as other LC phases can be formed. Examples include dispersions of submicrometer-sized colloidal disks of $\text{Al}(\text{OH})_3$, $\text{Ni}(\text{OH})_2$, and phosphoantimonate ($\text{H}_3\text{Sb}_3\text{P}_2\text{O}_{14}$) sheets forming in part nematic, smectic, and columnar type LC phases [25-29]. In most cases, LC phase formation is restricted to aqueous solutions. Properly modified nanomaterial surfaces also allow LC phase formation (or LC-like ordering) in organic solvents. One example is polymer-functionalized TiO_2 nanorods forming a nematic and a smectic phase using THF as solvent [30, 31].

2.1.1.2 NPs Decorated with LC Molecules

To introduce the anisotropic and self-assembly properties of organic LCs to NPs, the best approach seems to directly link NPs to LCs. The first example of Au NPs covered (protected) with an LC molecule was reported by Iketa and coworkers using the Brust-Schiffrin two-phase method [32]. As revealed by DSC, the prepared NPs showed a double melting that was associated by the authors with mesomorphic properties of the Au NPs, although a typical LC texture was not observed.

Mehl and Cseh using post-synthesis modified Au NPs (i.e., Au NPs modified using a place exchange reaction with a thiolated thermotropic LCs-side-on fashion) observed the formation of typical nematic marble and *schlieren* textures [33, 34], and discovered more recently 3-dimensional ordering of the NPs within this nematic phase [35]. With the assumption that liquid crystalline thiolates are not necessary to form Au NPs showing LC behavior, Terrazi *et al.* prepared dendrimer functionalized Au NPs, which were able to either self-assemble into a thermotropic cubic phase in the bulk or into a hexagonal lattice

on a flat surface [36]. Kim *et al.* synthesized Au NPs using cyanobiphenyl-based LC thiolates, and instead of finding an LC phase for the resulting Au NPs, a one dimensional arrangement of the Au NPs was observed upon heating the NPs in the mesomorphic temperature range for a certain time [37]. Using LCs containing aniline groups, which are known to reduce HAuCl_4 and form Au NPs, Ajayan and coworkers successfully demonstrated both in-situ synthesis and assembly of Au NPs in an LC host in one step [18].

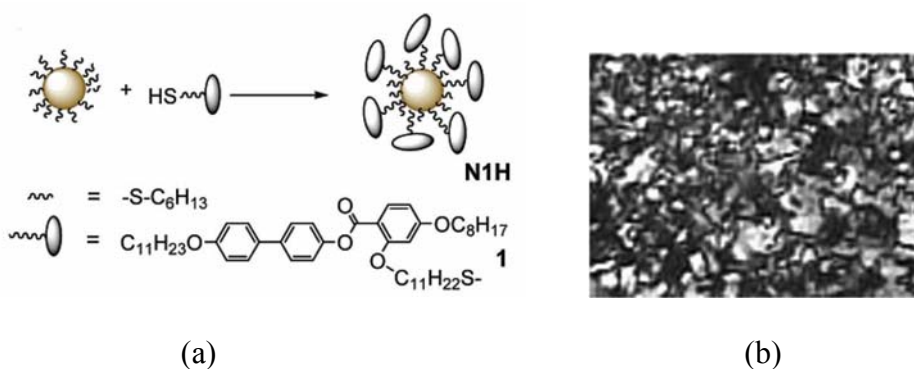


Fig. 2.2. (a) Schematic representation of the Au NP synthesis using LC thiols in a place exchange reaction, and (b) polarized light optical photomicrograph image of the Au NPs showing the typical nematic *Schlieren* texture. Reprinted with permission from ref. [33]

Aside from Au NPs, other, spherical NPs have also been investigated and studied for the ability to form LC phases. Goodby *et al.* synthesized C60-fullerene / LC hybrids by using twelve LC units that were symmetrically positioned around the C60 core, and the final decorated C60-LC hybrid formed a chiral nematic phase [38]. Using C60 as a functional part of its mesogen units, Nakamura *et al.* have shown that by attachment of five suitable aromatic groups to one pentagon of the C60 molecule, a columnar phase and a smectic phase can be formed [39, 40]. Self-assembly of Ag NPs has also been

demonstrated by Yoon and coworkers using LC phospholipid membranes [41]. Kanie *et al.* reported on the formation of thermotropic nematic and cubic phases by coating needle-shaped TiO₂ as well as α -Fe₂O₃ NPs with LC units [42, 43]. Covalent bonding of LC units to siloxane backbones followed by linking with dopamine-functionalized ferrite NPs produced transparent, flexible magnetic composites as reported by Song *et al.* [44].

With respect to applications for the above mentioned NP/LC hybrids, one potential use could originate from the control of the macroscopic alignment of these hybrids, which would be an important prerequisite to utilize the LCs' response to external stimuli such as electric or magnetic fields [45].

2.1.1.3 NPs Suspended in LC Hosts

Particles (not restricted to nano-size particles) doping into LC host has been broadly studied, starting with the formation of defects in the LC host and controlling the defect (i.e., NPs) location, over movement and assembly of NPs in LC phases, to altering of electro-optic properties of these composites. Published works describing these or related effects will be discussed in the next section. Several examples of the direct use of LC materials to assemble NPs without discussing electro-physical properties or defect formation will also be included here.

Patrick *et al.* demonstrated the first successful example of using thermotropic LCs for producing organized nanomaterial arrays on surfaces [46]. In this method, single and multi-walled carbon nanotubes were dispersed in a room temperature-nematic LC and oriented along with the LC in an electric or magnetic field on a grooved surface. Thereafter, the LC was drained through a porous membrane leaving an ordered nanotube

film behind.

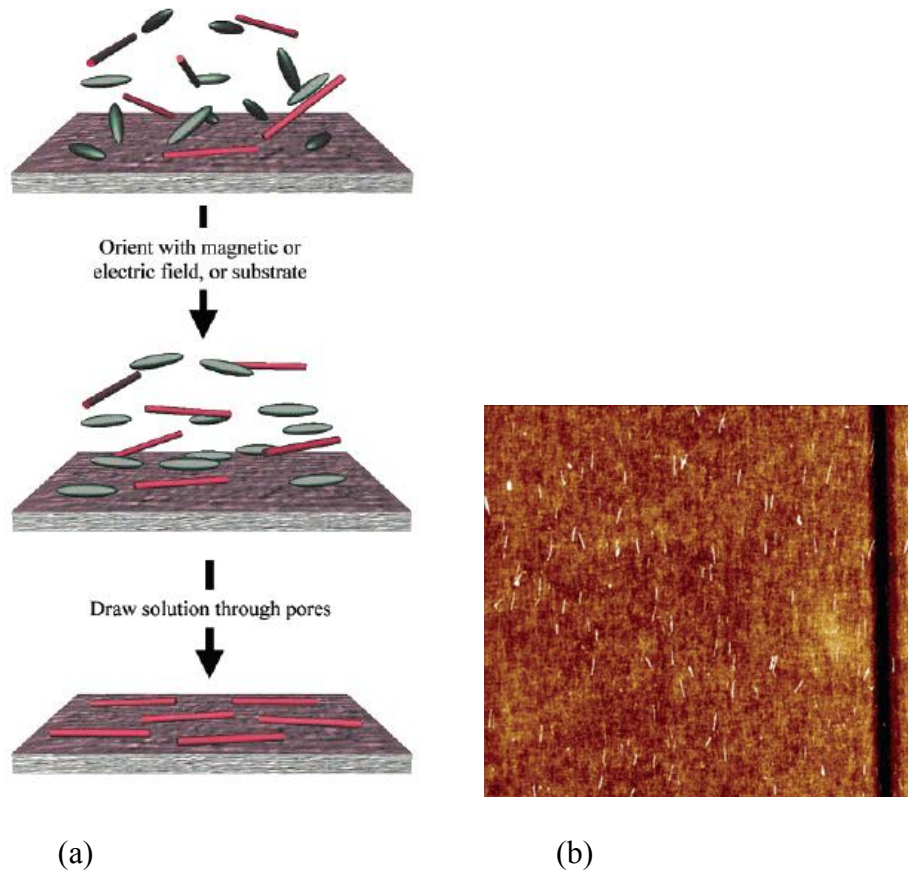


Fig. 2.3 (a) Scheme of organizing carbon nanotubes with an LC solvent: (1) a droplet of liquid crystal doped with carbon nanotubes is applied to a porous membrane substrate and then aligned using a grooved surface or an external field. (2) The LC is drained through the porous membrane leaving behind an ordered nanotube film. (b) An AFM image of aligned multi-walled carbon nanotubes. Reprinted with permission from ref. [46]

One limitation of using thermotropic LCs to align carbon nanotubes is the limiting low concentration of carbon nanotubes in the LC host due to their low solubility [46]. In contrast, using lyotropic LCs to separate and align carbon nanotubes can reach high concentrations, and using this technique, advanced research on carbon nanotube based devices could be achieved [47]. Two standard methods to prepare lyotropic LCs loaded with well-dispersed carbon nanotubes use either a suspension of carbon nanotubes in the

isotropic, low-surfactant-concentration regime (below the *cmc*), followed by adding more and more surfactant until an LC phase is formed [48, 49], or alternatively by adding carbon nanotubes to an already prepared lyotropic LC sample [50].

Patrick and coworkers also demonstrated that needle-shaped micron-sized SiC particles can be well aligned in nematic LCs, and the equilibrium orientation largely depends on the particle's surface modification and the structure of the LC host [51]. Talroze *et al.* studied the effect of H-bonded liquid crystal polymers on the alignment of CdSe quantum dots, and demonstrated that the alignment of the NPs can be tuned by varying the structure of the polymer and by varying the size of the CdSe quantum dot [52].

2.1.2 Other Properties of NPs

Liquid crystals can not only be used to guide (self)-assembly of NPs, but can also be employed to tune other NP properties such as the surface plasmon resonance (SPR) of Au NPs suspended in an LC matrix. Abbott and coworkers reported that the SPR of Au NPs immersed in LCs can be tuned by a change of the ordering of the LC molecules around the NPs (i.e., planar or homeotropic orientation or anchoring). This was achieved by sandwiching the LCs between two glass slides coated with alkanethiol-functionalized NPs. By tuning the temperature within the LC phase, the ordering (order parameter) of LCs is known to change, and the peak of SPR can be shifted accordingly [53]. The possibility of tuning the SPR of Au NPs in an LC matrix has also been studied by several other groups, and was also accomplished by changing of the orientation of LC molecules using an electric field [54-57]. Light-driven plasmonic switches were realized with Au

nanodisks using a photoresponsive LC [58]. Zhao *et al.* used an LC gel to modulate the luminescence intensity of core-shell CdSe/ZnS quantum dots [59].

2.2 Modulating LC properties using NPs

2.2.1 Defect formation via doping particles

Theoretical studies concerned with doping particles into an LC matrix can date back to the 1970's by Brochard and de Gennes with the aim of lowering the magnetic field intensities required for LC orientation [60]. In recent years, composite systems, i.e., an LC host doped with particles (in most cases, the particles being studied are not on the nano scale), have been extensively studied with respect to defect formation induced by the particles [61], and the majority of studies dealt with nematic LCs. A nematic LC possesses orientational ordering along a certain direction, and the vector along this direction is called the director. In a given domain without any perturbation, the director field is uniformly aligned in one direction. With the presence of particles, the director around the particles will change depending on the boundary conditions. The LC molecules can be normal (vertical) or parallel (planar) to the surface of the particles, depending on the chemical environment of the particle). In contrast, at a certain distance away from the particle, the bulk of the LC molecules are still uniformly aligned. Because of this mismatch, a topological defect and elastic distortions will be induced [62-65]. With strong normal anchoring of LC molecules to the particle surface, a defect called hedgehog is formed; with weaker anchoring strength, a Saturn ring defect is observed. For planar anchoring conditions, the formed defect is called a boojum [65]. Depending on the director configuration around the particle, a hedgehog defect behaves like a dipole,

whereas a Saturn ring and a boojum defect have quadrupolar symmetry. Because of the dipolar symmetry, the particle-hedgehog pair creates dipolar distortions of the director at long range along with short-range repulsion due to the dipolar defects, which leads to chain-like structures (arrays) of the dispersed particles. Saturn ring and boojum defects are shown to form anisotropic clusters or zigzag chains depending on the angles between the quadrupoles [63, 65]. All of these defects (hedgehog, Saturn ring and boojum) as well as the related chain-like arrays or anisotropic clusters have been theoretically studied and experimentally observed [60, 63, 66].

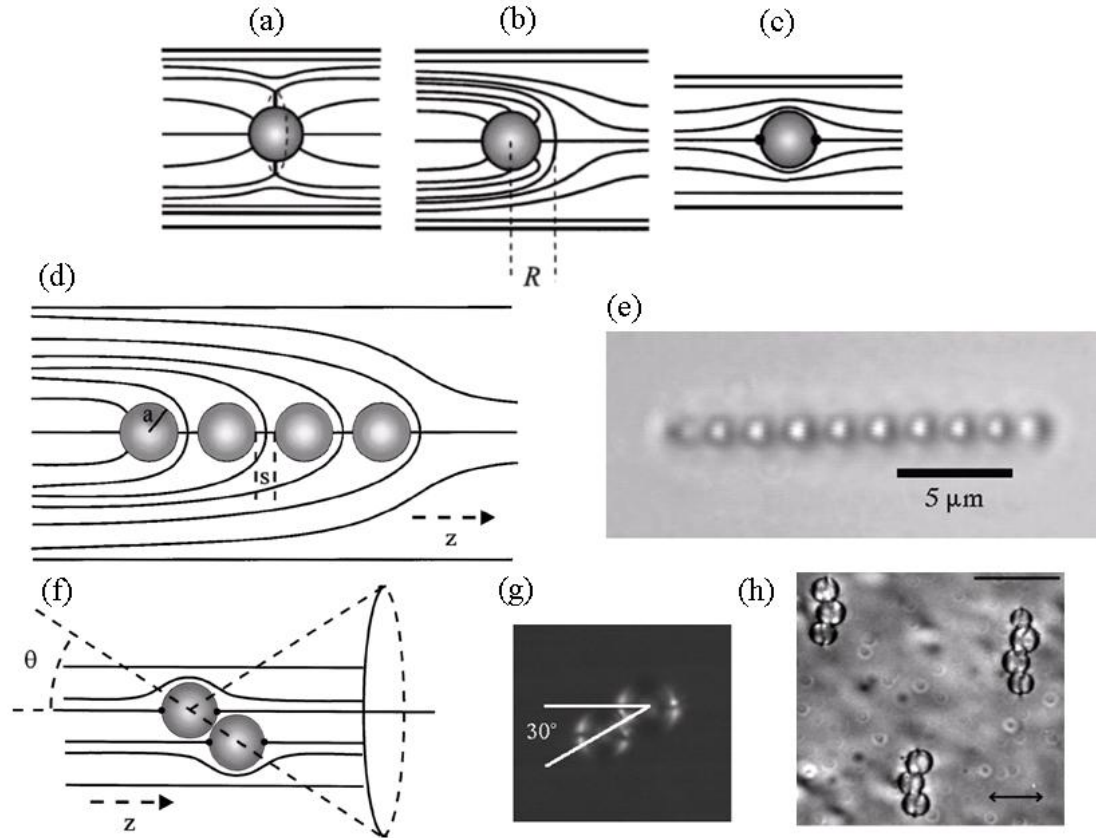


Fig. 2.4. Typical defects created by spherical particles in nematic LCs. Schematic of the director field: normal boundary conditions of (a) hedgehog, (b) Saturn ring and (c) planar boundary conditions with two surface defects known as boojums, (d) a chain of droplets formed by interaction between the topological dipoles with hedgehog types of defects. (e) Optical microscope picture of several water droplets forming a long chain with hedgehog type of defects, (f) the nematic director field for two particles with planar anchoring. The particles make an angle due to the quadrupoles. (g) Optical microscopy image of two particles and (h) zigzag chains of particles with planar anchoring conditions. Reprinted with permission from ref. [63] and ref. [65].

Particles showing these phenomena that have been studied include emulsions of water microdroplets [64, 65, 67-69], silicon oil [63, 70], gold-coated glass spheres [66], magnetic particles [67, 71], silica particles [72], and ZnS nanocrystals [73,74]. The LC phases were mostly nematic phases, but also include chiral nematic phases [75-77] and lyotropic LC phases [78-80]. Note that all particles mentioned above are in the micron-size regime, and there are only a very few studies with particles in the nano-size

regime [17].

Using the forces created by the formation of defects together with the tendency to minimize the LC's elastic distortion (approaching minima in the elastic energy landscape), particles of different size and shape have also been moved within LC host matrices. Examples for these particle motions in LCs include the levitation of metal nanowires and the electro-rotation of glass beads [81-83].

2.2.2 Electro-optical properties of LCs and emerging display related applications using nanoparticle doping

Contrary to the approach of using LC-decorated NPs for the assembly of NPs, the preparation of LC/NP nanocomposites by doping NPs into LC hosts has also been studied by a number of groups, with a particular focus on altering the display-related electro-optic properties of the LC host phase.

Two types of particles have been extensively studied so far, carbon nanotubes [84-93] and silica NPs [94-101]. Effects found for carbon nanotube doping include: reduced effective ion backflow effects due to the ion trapping by the carbon nanotubes [86, 88, 90, 91], increased dielectric anisotropy of the LC host phase [86, 87, 89], faster response time [84], and lower or higher driving voltages [86, 87, 89, 91]. There are also reports using carbon nanotube films to control the alignment of nematic LCs for flexible display applications [102-103]. One particular phenomenon, reported first for silica NP doped nematics, is the so-called memory effect, where the LC orientational state is retained after the field is switched off [100, 101] (not restricted to silica nanoparticles [104]). This memory effect can, for example, be used for bistable display modes. It was also shown

that silica NP-doped LCs can have bistable/multistable switching characteristics as well as reduced response times for the use in dynamic mode displays [101].

Ferroelectric NPs ($\text{Sn}_2\text{P}_2\text{S}_6$, BaTiO_3) have been studied by Reznikov *et al.* [104-110] as well as Reshetnyak and coworkers [111, 112]. Effects reported by both groups include increasing the order parameter of nematic LCs with increasing clearing temperature (from N phase to isotropic phase) and enhancement of the dielectric anisotropy. A recent erratum, however, shows that a better understanding of the composite system was necessary to interpret the observed results [113].

Kobayashi *et al.* described a frequency modulation electro-optic response with millisecond or sub-millisecond response time in twisted nematic LCDs as well as lower operating voltages in different LCD switching modes using particles such as Pd, Ag, Ag-Pd, Au, MgO, or SiO_2 [114-116]. Contrary to the broadly used the Brust-Schiffirin method for the preparation of metal (Au) NPs, the metal NPs used were synthesized by an alcoholic reduction method using UV irradiation of ethanol solutions of the relevant salts in the presence of the nematic liquid crystal [116]. Au NPs synthesized using the Brust-Schiffirin method have also been studied and the effects include increasing electrical conductivity, lower threshold voltages in nematic [117], ferroelectric [118] and discotic LCs [119], as well as a memory effect related to ferroelectric LCs [120].

Chen *et al.* showed that diamond powders could lead to a reduction of the ion concentration in the LC host. As a result, the transient currents and threshold voltage were drastically reduced [121]. Jeng *et al.* showed that NPs made of polyhedral oligomeric silsesquioxanes induce vertical alignment of LCs with applications in areas such as flexible LC displays and guest-host LC displays [122-124].

One could conclude that there is enough experimental evidence to believe that nanomaterials could have a profound impact on current and future LCDs. However, carefully designed materials and experiments are needed to fully exploit these NP-LC systems for device applications. For example, carbon nanotubes are always contaminated with impurities such as amorphous carbon or metal particles, and therefore it is crucial to examine the effects of such impurities to discern the contribution of the carbon nanotubes themselves to the electro-optic properties of the final composites [46]. There are only a limited number of studies that are concerned with the effects of surfactants as impurities [101] or side effects of ultrasonic synthesis [121], which are commonly used for some nanomaterial synthesis. And finally, a more detailed evaluation of structure-property relationships between the LC and the nanomaterials is needed. Such studies would focus on compatibility, miscibility, stability, size and shape effects of the nanomaterials dispersed in an LC host.

2.3 Concluding Remarks and Outline of the Thesis

It seems quite obvious that LC/NP composites have been extensively studied over the past decade. Numerous new phenomena, as well as applications, emerged from these studies. However, research in this field is ongoing and growing world-wide. More focused studies are needed to drive economical breakthroughs of LC/NP composites that would have to focus on such possibilities as macroscopic alignment of LC/NP hybrids, detailed structure-property relationship studies, theoretical investigations of defects in LCs with nano-sized particles and the prevention of NP aggregation in bulk LC phases.

In the present thesis, studies of the LC/Au NP composites have been pursued with two

general types of LC materials, one type forming primarily nematic phases and a second type forming smectic and columnar LC phases.

Chapter 4 studies the effect of different Au NP functionalizations (hydrophilic vs. hydrophobic) on the stability of the latter type of LC material forming either a smectic-A or a rectangular columnar LC phase depending on the length of a lateral hydrocarbon chain.

Chapters 5 to 10 describe effects/phenomena found for nematic LCs doped primarily with Au NPs. Chapter 5 introduces the phenomenon found for nematic LCs doped with non-chiral as well as chiral Au NPs, i.e., the formation of uniform stripe textures or patterns separated by areas of homeotropic alignment. Two scenarios are proposed to explain this phenomenon. One of the two scenarios has been proven experimentally, and the results of these experiments are discussed in chapter 6. The fascinating puzzle of the origin of chirality in Au NPs is first introduced in chapter 5. In chapter 7, using the same chiral Au NPs, the chirality of Au NPs has been further studied including chemical modifications of the NP corona. The regions of homeotropic alignment prompted the use of this phenomenon to control the alignment of LCs with suspended Au NPs. A dual alignment phenomenon was found, and associated electro-optic investigations will be described and discussed in chapter 8. Chapter 9 is then an extension study of these electro-optic studies introducing Ag and CdTe NPs. Starting with basic research to study defect formation and the role of chirality in chapter 5 to more LCD-oriented research in chapter 8, chapter 10 then discloses explorations of initial structure-property relationships in LC/NP composites comparing LC-decorated with ‘simple’ alkylthiol-capped Au NPs.

Conclusions and future work will be presented in the final chapter 11.

References

- [1] G. Schmid, U. Simon, *Chem. Commun.* **2005**, 697-710.
- [2] M. Sastry, M. Rao, K. N. Ganesh, *Acc. Chem. Res.* **2002**, 35, 847-855.
- [3] M. Mlller, J. P. Spatz, A. Roescher, *Adv. Mater.* **1996**, 8, 337-340.
- [4] R. Shenhar, T. B. Norsten, V. M. Rotello, *Adv. Mater.* **2005**.17, 657-669.
- [5] G. P. Mitchell, C. A. Mirkin, R. L. Letsinger, *J. Am. Chem. Soc.* **1999**, 121, 8122-8123.
- [6] C. A. Mirkin, R. L. Letsinger, R. C. Mucic, J. J. Storhoff, *Nature* **1996**, 382, 607-609.
- [7] A. P. Alivisatos, K. P. Johnsson, X. Peng, T. E. Wilson, C. J. Loweth, Jr., M. P. Bruchez, P. G. Schultz, *Nature* **1996**, 382, 609-611.
- [8] J. Zheng, P. E. Constantinou, C. Micheel, A. P. Alivisatos, R. A. Kiehl, N. C. Seeman, *Nano Lett.* **2006**, 6, 1502-1504.
- [9] Z. Li, S-W. Chung, J-M. Nam, D. S. Ginger, C. A. Mirkin, *Angew. Chem., Int. Ed.* **2003**, 115, 2408-2411.
- [10] S. Mann, W. Shenton, M. Li, S. Connolly, D. Fitzmaurice, *Adv. Mater.* **1999**, 12, 147-150.
- [11] S. R. Hall, W. Shenton, H. Engelhardt, S. Mann, *ChemPhysChem.* **2001**, 2, 184-186.
- [12] C. Flynn, *Acta Materialia* **2003**, 51, 5867-5880.
- [13] K. T. Nam, D-W. Kim, P. J. Yoo, C. Chiang, N. Meethong, P. Hamond, Y-M. Chiang, A. M. Belcher, *Science* **2006**, 312, 885-888.
- [14] I. Gascon, J.-D. Marty, T. Gharsa, C. Mingotaud, *Chem. Mater.* **2005**, 17, 5228

-5230.

- [15] R. Jin, Y. Cao, C. A. Mirkin, K. L. Kelly, G. C. Schatz, J. G. Zheng, *Science* **2001**, *294*, 1901-1903.
- [16] P. K. Vemula, G. John, *Chem. Commun.* **2006**, 2218-2220.
- [17] J. W. Goodby, I. M. Saez, S. J. Cowling, V. Gortz, M. Draper, A. W. Hall, S. Sia, G. Cosquer, S-E. Lee and E. P. Raynes, *Angew. Chem., Int. Ed.* **2008**, *47*, 2754-2787.
- [18] V. A. Mallia, P. K. Vemula, G. John, A. Kumar, P. M. Ajayan, *Angew. Chem., Int. Ed.* **2007**, *46*, 3269-3274.
- [19] L. Onsager, *Ann. N. Y. Acad. Sci.* **1949**, *51*, 627-659.
- [20] N. R. Jana, L. A. Gearheart, S. O. Obare, C. J. Johnson, K. J. Edler, S. Mann, C. J. Murphy, *J. Mater. Chem.* **2002**, *12*, 2909-2912.
- [21] L-S. Li, J. Walda, L. Manna, A. Paul. Alivisatos, *Nano Lett.* **2002**, *2*, 557-560.
- [22] W. Song, I. Kinloch, A. Windle, *Science* **2003**, *302*, 1363-1363.
- [23] S. Zhang, S. Kumar, *Small* **2008**, *4*, 1270-1283.
- [24] S. Zhang, I. Kinloch, A. Windle, *Nano Lett.* **2006**, *6*, 568-572.
- [25] A. B. D. Brown, S. M. Clarke, A. R. Rennie, *Langmuir* **1998**, *14*, 3129-3132.
- [26] F. M. Kooij, H. N. W. Lekker, *J. Phys. Chem. B* **1998**, *102*, 7829-7832.
- [27] F. M. Kooij, K. Kassapidou, H. N. W. Lekker, *Nature* **2000**, *406*, 868-871.
- [28] P. Davidson, J.-C. P. Gabriel, *Curr. Opin. Coll. Interf. Sci.* **2005**, *9*, 377-383.
- [29] J.-C. P. Gabriel, F. Camerel, B. J. Lemaire, H. Desvaux, P. Davidson, P. Batail, *Nature* **2001**, *413*, 504-508.
- [30] M. Zorn, S. Meuer, M. N Tahir, Y. Khalavka, C. Sonnichsen, W. Tremelb, R.

- Zentel, *J. Mater. Chem.* **2008**, *18*, 3050-3058.
- [31] S. Meuer, P. Oberle, P. Theato, W. Tremel, R. Zentel, *Adv. Mater.* **2007**, *19*, 2073-2078.
- [32] N. Kanayama, O. Tsutsumi, A. Kanazawa, T. Ikeda, *Chem. Commun.* **2001**, 2640-2641.
- [33] L. Cseh, G. Mehl, *J. Am. Chem. Soc.* **2006**, *128*, 13376-13377.
- [34] L. Cseh, G. Mehl, *J. Mater. Chem.* **2007**, *17*, 311-315.
- [35] Zeng, X. P.; Liu, F.; Fowler, A. G.; Ungar, G.; Cseh, L.; Mehl, G. H.; Macdonald, J. E. *Adv. Mater.* **2009**, *21*, 1746-1750
- [36] B. Donnio, P. García-Vázquez, J-L. Gallani, D. Guillon, E. Terazzi, *Adv. Mater.* **2007**, *19*, 3534-3539.
- [37] I. In, Y.-W. Jun, Y. J. Kim, S. Y. Kim, *Chem. Commun.* **2005**, 800-801.
- [38] S. Campidelli, C. Eng, I. M. Saez, J.W. Goodby, R. Deschenaux, *Chem. Commun.* **2003**, 1520-1521.
- [39] M. Sawamura, K. Kawai, Y. Matsuo, K. Kanie, T. Kato, E. Nakamura, *Nature*, **2002**, *419*, 702-705.
- [40] Y. W. Zhong, Y. Matsuo, E. Nakamura, *J. Am. Chem. Soc.* **2007**, *129*, 3052-3052.
- [41] N. Oh, J. H. Kim and C. S. Yoon, *Adv. Mater.* **2008**, *20*, 3404-3409.
- [42] K. Kanie, T. Sugimoto, *J. Am. Chem. Soc.* **2003**, *125*, 10518-10519.
- [43] K. Kanie, A. Muramatsu, *J. Am. Chem. Soc.* **2005**, *127*, 11578-11579.
- [44] H. M. Song, J. C. Kim, J. H. Hong, Y. B. Lee, J. Choi, J. I. Lee, W. S. Kim, J-H. Kim, N. H. Hur, *Adv. Funct. Mater.* **2007**, *17*, 2070-2076.
- [45] J. Hoogboom, T. Rasing, A. E. Rowan, R. J. M. Nolte, *J. Mater. Chem.* **2006**, *16*,

1305-1314.

- [46] M. D. Lynch, D. L. Patrick, *Nano Lett.* **2002**, *2*, 1197-1201.
- [47] J. P. F. Lagerwall, G. Scalia, *J. Mater. Chem.* **2008**, *18*, 2890-2898.
- [48] G. Scalia, C. von Buhler, C. Hagele, S. Roth, F. Giesselmann, J. P. F. Lagerwall, *Soft Matter* **2008**, *4*, 570-576.
- [49] J. P. F. Lagerwall, G. Scalia, M. Haluska, U. Dettlaff-Weglikowska, S. Roth, F. Giesselmann, *Adv. Mater.* **2007**, *19*, 359-364.
- [50] V. Weiss, R. Thiruvengadathan, O. Regev, *Langmuir* **2006**, *22*, 854-856.
- [51] M. D. Lynch, D. L. Patrick, *Chem. Mater.* **2004**, *16*, 762-767.
- [52] G. A. Shandryuk, E.V. Matukhina, R. B. Vasil'ev, A. Rebrov, G. N. Bondarenko, A. S. Merekalov, A. M. Gaskov, R. V. Talroze, *Macromolecules* **2008**, *41*, 2178-2185.
- [53] G. M. Koenig, M-V. Meli, J-S Park, J. J. de Pablo, N. L. Abbott, *Chem. Mater.* **2007**, *19*, 1053-1061.
- [54] J. Muller, C. Sonnichsen, H. Poschinger, G. Plessen, T. A. Klar, J. Feldmann, *Appl. Phys. Lett.* **2002**, *81*, 171-173.
- [55] W. Dickson, G. A. Wurtz, P. R. Evans, R. J. Pollard, A. V. Zayats, *Nano Lett.* **2008**, *8*, 281-286.
- [56] P. A. Kossyrev, A. Yin, S. G. Cloutier, D. A. Cardimona, D. Huang, P. M. Alsing, J. M. Xu, *Nano Lett.* **2005**, *5*, 1978-1981.
- [57] L-H. Hsu, K-Y Lo, S-A Huang, C-Y Huang, C-S. Yang, *Appl. Phys. Lett.* **2008**, *92*, 181112.
- [58] V. K. S. Hsiao, Y. B. Zheng, B. K. Juluri, T. J. Huang, *Adv. Mater.* **2008**, *20*,

3528-3532.

- [59] X. Tong, Y. Zhao, *J. Am. Chem. Soc.* **2007**, *129*, 6372-6373.
- [60] F. Brochard, P. G. de Gennes, *J. Phys. (Paris)* **1970**, *31*, 691-708.
- [61] H. Stark, *Physics Reports* **2001**, *351*, 387-474.
- [62] J. C. Loudet, P. Hanusse, P. Poulin, *Science* **2004**, *306*, 1525.
- [63] J. C. Loudet, P. Barois, P. Auroy, P. Keller, H. Richard, P. Poulin, *Langmuir* **2004**, *20*, 11336-11347.
- [64] P. Poulin, H. Stark, T. C. Lubensky, D. A. Weitz, *Science* **1997**, *275*, 1770-1773.
- [65] P. Poulin, D. A. Weitz, *Phys. Rev. E* **1998**, *57*, 626-637.
- [66] Y. Gu, N. L. Abbott, *Phys. Rev. Lett.* **2000**, *85*, 4719-4722.
- [67] P. Poulin, V. Cabuil, D. A. Weitz, *Phys. Rev. Lett.* **1997**, *79*, 4862-4865.
- [68] O. Mondain-Monval, J. C. Dedieu, T. Gulik-Krzywicki, P. Poulin, *Eur. Phys. J. B* **1999**, *12*, 167-170.
- [69] P. Poulin, *Curr. Opin. Colloid Interface Sci.* **1999**, *4*, 66-71.
- [70] J.-C. Loudet, P. Barois, P. Poulin, *Nature* **2000**, *407*, 611-613.
- [71] C. Da Cruz, O. Sandre, V. Cabuil, *J. Phys. Chem. B* **2005**, *109*, 14292-14299.
- [72] M. Kreuzer, T. Tschudi, W. H. De Jeu, R. Eidenshink, *Appl. Phys. Lett.* **1993**, *62*, 1712.
- [73] M. Adams, Z. Dogic, S. L. Keller, S. Fraden, *Nature* **1998**, *393*, 349-352.
- [74] S.-W. Lee, C. B. Mao, C. E. Flynn, A. M. Belcher, *Science* **2002**, *296*, 892-895.
- [75] M. Zapotocky, L. Ramos, P. Poulin, T. C. Lubensky, D. A. Weitz, *Science* **1999**, *283*, 209-212.
- [76] M. Mitov, C. Portet, C. Bourgerette, E. Snoeck, M. Verelst, *Nat.*

Mater. **2002**, *1*, 209-231.

- [77] M. Mitov, C. Bourgerette, F. de Guerville, *J. Phys.: Condens. Matter* **2004**, *16*, S1981-S1988.
- [78] O. Mondain-Monval, J. C. Dedieu, T. Gulik-Krzywicki, P. Poulin, *Eur. Phys. J. B* **1999**, *12*, 167-170.
- [79] P. Poulin, N. O. France's Mondain-Monval, *Phys. Rev. E* **1999**, *59*, 4384-4387.
- [80] V. A. Raghunathan, P. Richetti, D. Roux, *Langmuir* **1996**, *12*, 3789-3792.
- [81] C. Lapointe, A. Hultgren, D. M. Silevitch, E. J. Felton, D. H. Reich, R. L. Leheny, *Science* **2004**, *303*, 652-655.
- [82] C. Lapointe, D. H. Reich, R. L. Leheny, *Langmuir* **2008**, *24*, 11175-11181.
- [83] G. Liao, I. I. Smalyukh, J. R. Kelly, O. D. Lavrentovich, A. Jákli, *Phys. Rev. E* **2005**, *72*, 031704.
- [84] H. Chen, W. Lee, N. Clark, *Appl. Phys. Lett.* **2007**, *90*, 033510.
- [85] S. Y. Jeon, S. H. Shin, S. J. Jeong, S. H. Lee, S. H. Jeong, Y. H. Lee, H. C. Choi, K. J. Kim, *Appl. Phys. Lett.* **2007**, *90*, 121901.
- [86] W. Lee, C. Wang, Y. Shih, *Appl. Phys. Lett.* **2004**, *85*, 513-515.
- [87] C. Huang, C. Hu, H. Pan, K. Lo, *Jpn. J. Appl. Phys.* **2005**, *44*, 8077-8081.
- [88] I. S. Baik, S. Y. Jeon, S. H. Lee, K. A. Park, S. H. Jeong, K. H. An, Y. H. Lee, *Appl. Phys. Lett.* **2005**, *87*, 263110.
- [89] C. Huang, H. Pan, C. Hsieh, *Jpn. J. Appl. Phys.* **2006**, *45*, 6392-6394.
- [90] H. Chen, W. Lee, *Appl. Phys. Lett.* **2006**, *88*, 222105.
- [91] G. Scalia, J. P. F. Lagerwall, S. Schymura, M. Haluska, F. Giesselman, S. Roth, *Phys. Status Solidi B* **2007**, *244*, 4212-4217.

- [92] C. Huang, H. Pan, *Appl. Phys. Lett.* **2006**, *89*, 056101.
- [93] S. Y. Jeon, S. H. Shin, J. H. Lee, S. H. Lee, Y. H. Lee, *Jpn. J. Appl. Phys.* **2007**, *46*, 7801-7802.
- [94] L. Dolgov, O. Yaroshchuk, *Mol. Cryst. Liq. Cryst.* **2004**, *409*, 77-89.
- [95] O. Yaroshchuk, L. Dolgov, A. D. Kiselev, *Phys. Rev. E* **2005**, *72*, 051715.
- [96] L. Dolgov, O. Yaroshchuk, *Colloid Polym. Sci.* **2004**, *282*, 1403-1408.
- [97] M. Kreuzer, T. Tschudi, W. H. de Jeu, R. Eidenschink, *Appl. Phys. Lett.* **1993**, *62*, 1712-1715.
- [98] M. Kreuzer, T. Tschudi, R. Eidenschink, *Mol. Cryst. Liq. Cryst.* **1992**, *223*, 219-227.
- [99] R. Eidenschink, W. H. de Jeu, *Electron. Lett.* **1991**, *27*, 1195-1996.
- [100] C-Y Huang, C-C. Lai, Y-H. Tseng, Y-T. Yang, C-J. Tien, K-Y. Lo, *Appl. Phys. Lett.* **2008**, *92*, 221908.
- [101] D. Sikharulidze, *Appl. Phys. Lett.* **2005**, *86*, 033507.
- [102] A. Schindler, J. Brill, N. Fruehau, J. P. Novak, Z. Yaniv, *Physica E* **2007**, *37*, 119-123.
- [103] J. M. Russell, S. Oh, I. Larue, O. Zhou, E. T. Samulski, *Thin Solid Film* **2006**, *509*, 53-57.
- [104] G. Puchkovskaya, Y. Reznikov, A. Yakubov, O. V. Yaroshchuk, A. Glushchenko, *J. Mol. Struct.* **1997**, *404*, 121-128.
- [105] Y. Reznikov, O. Buchnev, O. Tereshchenko, V. Reshetnyak, A. Glushchenko, J. West, *Appl. Phys. Lett.* **2003**, *82*, 1917-1919.
- [106] E. Ouskova, O. Buchnev, V. Reshetnyak, Y. Reznikov, H. Kresse, *Liq. Cryst.*

- 2003**, *30*, 1235-1239.
- [107] O. Buchnev, C.-I. Cheon, A. Glushchenko, Y. Reznikov, J. L. West, *J. Soc. Inf. Disp.* **2005**, *13*, 749-754.
- [108] F. Li, J. West, A. Glushchenko, C.-I. Cheon, Y. Reznikov, *J. Soc. Inf. Disp.* **2006**, *14*, 523-527.
- [109] F. Li, O. Buchnev, C.-I. Cheon, A. Glushchenko, V. Reshetnyak, Y. Reznikov, T. J. Sluckin, J. L. West, *Phys. Rev. Lett.* **2006**, *97*, 147801.
- [110] O. Buchnev, A. Dyadyusha, M. Kaczmarek, V. Reshetnyak, Y. Reznikov, *J. Opt. Soc. Am. B* **2007**, *24*, 1512-1516.
- [111] V. Y. Reshetnyak, *Mol. Cryst. Liq. Cryst.* **2004**, *421*, 219-224.
- [112] V. Y. Reshetnyak, S. M. Shelestiuk, T. J. Sluckin, *Mol. Cryst. Liq. Cryst.* **2006**, *454*, 201-206.
- [113] F. Li, O. Buchnev, C.-I. Cheon, A. Glushchenko, V. Reshetnyak, Y. Reznikov, T. J. Sluckin, J. L. West, *Phys. Rev. Lett.* **2007**, *99*, 219901.
- [114] T. Miyama, J. Thisayukta, H. Shiraki, Y. Sakai, Y. Shiraishi, N. Toshima, S. Kobayashi, *Jpn. J. Appl. Phys.* **2004**, *43*, 2580.
- [115] S. Kobayashi, T. Miyama, N. Nishida, Y. Sakai, H. Shiraki, Y. Shiraishi, N. Toshima, *J. Display Technol.* **2006**, *2*, 121-129.
- [116] T. Miyama, H. Shiraki, Y. Sakai, T. Masumi, S. Kundu, Y. Shiraishi, N. Toshima, S. Kobayashi, *Mol. Cryst. Liq. Cryst.* **2005**, *433*, 29-40.
- [117] S. K. Prasad, K. L. Sandhya, G. G. Nair, U. S. Hiremath, C. V. Yelamaggad, S. Sampath, *Liq. Cryst.* **2006**, *33*, 1121-1125.
- [118] S. Kaur, S. P. Singh, A. M. Biradar, A. Choudhary, K. Sreenivas, *Appl. Phys. Lett.*

2007, *91*, 023120.

- [119] L. A. Holt, R. J. Bushby, S. D. Evans, A. Burgess, G. Seeley, *J. Appl. Phys.* **2008**, *103*, 063712.
- [120] J. Prakash, A. Choudhary, A. Kumar, D. S. Mehta, A. M. Biradar¹, *Appl. Phys. Lett.* **2008**, *93*, 112904.
- [121] P. S. Chen, C-C. Huang, Y-W. Liu, C. Chao, *Appl. Phys. Lett.* **2007**, *90*, 211111.
- [122] S-C. Jeng, C-W. Kuo, H-L. Wang, C-C. Liao, *Appl. Phys. Lett.* **2007**, *91*, 061112.
- [123] C-W. Kuo, S-C. Jeng, H-L. Wang, C-C. Liao, *Appl. Phys. Lett.* **2007**, *91*, 141103.
- [124] W-Y. Teng, S-C. Jeng, C-W. Kuo, Y-R. Lin, C-C. Liao, W-K. Chin. *Opt. Lett.* **2008**, *33*, 1663-1665.

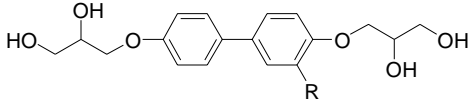
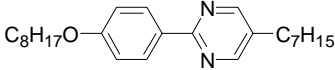
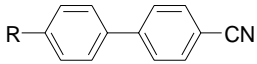
Chapter 3: Materials and Methods

3.1 Materials

3.1.1 LCs

Seven different LC hosts were used in this thesis. Their structure, phase transitions as well as source (if commercially available) are shown below:

Table 3.1 LC structure, phase transitions, phase transition temperatures and source.

LC structure and phase transition	Source
<p>Chapter 4</p>  <p>R=CH₃: Cr 105 SmA 230 Iso R=C₉H₁₉: Cr 72 Col_r (<i>c2mm</i>) 97 Iso</p>	Synthesized following ref. [1]
<p>Chapter 5, 8, 9</p>  <p>Cr 52 (SmA 45) N 70 Iso</p>	Commercially available from Hoechst.
 <p>Chapter 5, 6, 8, 10</p> <p>R=C₅H₁₁: Cr 25 N 35 Iso</p>	Commercially available from Merck KGaA
<p>Chapter 5, 8, 9, 10</p> <p>R=C₈H₁₇: Cr 22 SmA 32.5 N 40 Iso</p>	Commercially available from Merck KGaA
<p>Chapter 10</p> <p>R=OC₁₀H₂₀SH: Cr 62 N 72.5 Iso</p>	Synthesized following ref. [2]

3.1.2 Au NPs

All Au NPs were synthesized following the general Brust-Schiffrin method [3]. The exact ratio of the different reagents as well as the precise synthesis procedure followed the one reported by Shon and coworker [4], either using the two-phase method (toluene/water and use of TOAB) or the one-phase method using THF. Mixed-monolayer Au NPs (Au NPs protected with two types of thiols) were prepared in two different ways, either by in-situ synthesis or by post-synthesis NP modification using the place-exchange reaction [5]. The different types of Au NPs studied in this thesis are shown in Table 2.2. Details of the synthesis of the individual Au NPs can be found in the individual chapters, in which they are discussed.

In general, the synthesis of Au NPs is relatively easy to perform. The synthesis and all purification processes can be completed in one day. A critical requirement for Au NP synthesis is that all glassware was carefully cleaned using *aqua regia* and DI water, to prevent dust and other impurities acting as seeds during NP formation, which might give larger NP aggregates. Time is also critical. An example is the synthesis of hexanethiol or dodecanethiol protected NPs, where after addition of the thiol, the solution color should change from orange to almost colorless (pale yellow), which means Au^{3+} was reduced to Au^{1+} [4], and only thereafter should a freshly prepared solution of NaBH_4 be added. For other NPs such as for example an azo-benzene decorated thiol, because the thiol itself is yellow, it is difficult to observe this color change. Hence, the type of thiol has to be taken into consideration. The NaBH_4 solution should be freshly prepared, and added almost immediately to the reaction mixture. The formed Au NPs should stir for at least 2 hours before purification; partly because the Au NPs will ripen and change size during that time

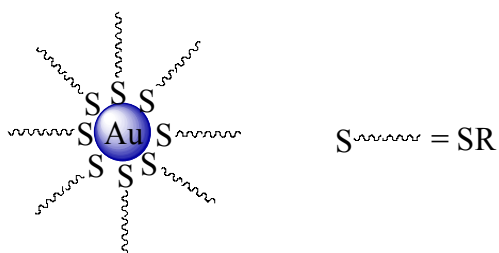
(i.e. better size uniformity). There is also procedure to reflux NPs in toluene overnight to get larger, but uniform Au NPs (narrow size distribution) [6]. Compared with synthesis of Au NPs, purification becomes sometimes a more delicate issue. Inorganic by-product from NaBH_4 can be washed out by water. Tetraoctylammonium bromide (TOAB) can also be easily washed by several organic solvents such as acetone, acetonitrile, hexane, ethyl acetate, etc. In contrast, removing the free extra thiol, in some case, can become a really critical problem. Based on the author's experience, thin layer chromatography (TLC) is a necessary step to decide which solvent (or mixture of solvent) is needed for washing. Because the as-synthesized Au NPs can also easily dissolve in certain solvents, choosing the right solvent with a good solubility for the free thiol only, and poor or no solubility for Au NPs is important. For these TLC tests, choosing a solvent with an R_f value of free thiol between 0.3 or 0.4, while the Au NPs do not move from the TLC baseline is best. This strategy has been successfully used for several Au NPs described in this thesis.

Two different methods have been used in this thesis for the synthesis of Au NPs: the one-phase method using THF/ H_2O and the two-phase method using toluene/ H_2O . There might be slight difference between these two methods, whereas in this thesis, it is difficult to differentiate these two methods regarding their performance of the final Au NPs for LC/Au NP composites. One drawback using the two-phase method is that there is always some small residue of TOAB in the final product, and studies showed that TOAB can reduce the stability of Au NPs [7], especially when the Au NPs are not stored properly (e.g. prolonged exposure to oxygen). For the one-phase, the THF method, the solvent must be freshly distilled to eliminate peroxides. THF used as received to

synthesize dodecane thiol protected Au NPs led to Au NPs aggregates that were insoluble in organic solvents after several weeks.

Proper storage of Au NPs is also critical. Au NPs can not be stored in a solution for prolonged time intervals. It is best to avoid extended exposure to air and light. Hence, the best way to store Au NPs is in a dry state under a protective atmosphere of N₂ and wrapped in aluminum foil to prevent exposure to light. Several Au NPs used for the work described in this thesis have been stored for three or four years using this method and still show similar size, solubility and purity as detected by TEM, XRD as well as UV-vis and NMR spectroscopy.

Table 3.2 Structures of the Au NPs.



-SR		
Chapter 4-10	SC_6H_{13}	
Chapter 5-10	$SC_{12}H_{25}$	
Chapter 4	$SC_6H_{11}(OC_2H_4)_3OH$	
Chapter 5-7		
Chapter 5-7	SC_6H_{13} /	Various ratios Details shown in Chapters 5-7
Chapter 5-7	$SC_{12}H_{25}$ /	Various ratios Details shown in Chapters 5-7
Chapter 10	SC_6H_{13} /	Ratio: 1:1
	$SC_{12}H_{25}$ /	Ratio: 9:1

3.2 Methods

3.2.1 Characterization of the Au NPs

The purity of the Au NPs and ratio of thiols in mixed-monolayer Au NPs were checked using ^1H NMR recorded with a Bruker Avance 300 spectrometer. Particle sizes were measured and evaluated by TEM, XRD and using UV-vis spectra. Transmission electron microscopy (TEM) images were obtained on a JEOL FX 2000 operating at an accelerating voltage of 160 kV. High-resolution transmission electron microscopy (HR-TEM) was carried out using JEOL FEG-T/STEM operating at an acceleration voltage of 200 kV. A drop (10 μl) of the isolated gold colloid solutions was drop-cast on carbon coated copper grids (400 mesh) and dried in air. Wide-angle powder x-ray diffraction (XRD) patterns of the gold nanoclusters were obtained on an MPD X'Pert system (PANalytical) using $\text{CuK}\alpha$ radiation (40 kV, 200 mA). UV-vis spectra were obtained using an Agilent 8453 spectrophotometer or a Cary 5000 UV-vis-NIR spectrophotometer (Varian). The ellipticity of the Au NPs was measured using a J-810 spectropolarimeter (Jasco Inc.) using a bandwidth of 2 nm, a scanning speed of 20 nm/min with 4 seconds response time, and a data pitch of 0.1 nm. All spectra are baseline corrected. The CD intensity and wavelength of the spectropolarimeter were calibrated using solutions of *d*-10-camphorsulphonic acid.

3.2.2 Characterization of LCs and LC/Au NP composites

The LC texture and phase transitions were observed using an Olympus BX51-P polarizing microscope in conjunction with a Linkam LS350 heating stage. Transition temperatures were measured with a Pyris Diamond DSC with Intra-cooler (Perkin-Elmer).

Some LCs and LC/Au NP composites (chapter 4) were also analyzed by small-angle x-ray scattering (SAXS) using a Bruker-Nonius FR591 rotating-anode generator with a copper anode operated at 3.4 kW. The beam was collimated and focused with mirror-monochromator optics and the scattered radiation was detected using a Bruker Hi-Star wire (area) detector (at the University of Pennsylvania, Department of Physics and Astronomy). The electro-optic tests were performed using an LCAS automated liquid crystal analyzer (LC Vision). The LC test cells used were planar 5.0 micron cells with antiparallel polyimide alignment layers and low pre-tilt (Displaytech Inc., purchased from Linkam Scientific Instruments) and planar 5.0 or 6.8 micron cells with parallel or antiparallel polyimide alignment layers and 1° to 3° pre-tilt (Instec, Inc.). The LC test cells were filled by capillary force with LCs or LC/NP composites in the isotropic liquid phase before investigation.

For more details regarding the electro-optic properties related to LC display of the LC/Au NP composites, readers are encouraged to consult the following references [8, 9]. One example is the pretilt angle of the liquid crystal cells. Although the pretilt angle is not directly related to the uniform alignment of the LC molecules, it shows that an appropriate pretilt angle is necessary for twisted nematic LCDs to prevent reverse tile disclinations. Thus, all commercially available LC cells have small pretilt angles [10].

Aside from the synthesis of the Au NPs, the preparation of LC/Au NP mixtures is another key issue for the results outlined in this thesis. It starts with preparing individually pure LC as well as Au NP solutions with a known concentration. Based on the aimed concentration of Au NPs in the LC host, a mixture the two solutions is then prepared, and finally the solvent is removed under a steady dtream of dry N₂ gas to

obtain the final LC/Au NP mixture. In principle, it is difficult for LC/Au NP mixtures to be completely homogeneous, and a certain solubility of the Au NPs in the LC host is critical. Controlling the evaporation rate of the solvent used, the use of different types of solvents, the temperature, the amount of LC, the size and functionalization of the Au NPs, the ways of filling the cells, heating and cooling rates, as well as the type of substrate (untreated microglass slides vs. rubbed polyimide coated cell), play important roles for the final performance of the LC/Au NP composites. In general, using non-chlorinated solvents such as ethyl acetate or hexane produce better results than chlorinated solvents, since free halogen in halogenated solvents can induce NP decomposition. Using N₂ gas to evaporate the solvent is also a way of preventing oxidation of the Au NPs during this process. Once the mixtures are sandwiched between glass slides or filled into cells, the prepared sample can be very stable for several years. A key difference between pure LCs and LC/NP mixtures is that for pure LCs it is recommended to fill the cell with the LC in the N phase to obtain the best possible alignment, whereas for LC/NP composites filling the cells with the LC/NP mixture in the isotropic phase is most critical to obtain the desired alignment and prevent Au NP aggregation.

References

- [1] M. Kölbl, T. Beyersdorff, X. Cheng, C. Tschierske, J. Kain, S. Diele, *J. Am. Chem. Soc.* **2001**, *123*, 6809-6818.
- [2] I. In, Y.-W. Jun, Y. J. Kim, S. Y. Kim, *Chem. Commun.* **2005**, 800-801.
- [3] M. Brust, M. Walker, D. Bethell, D. J. Schiffrin, R. Whyman, *Chem.*

Commun. **1994**, 801-802.

- [4] H. Choo, E. Cutler, Y. S. Shon, *Langmuir* **2003**, *19*, 8555-8559.
- [5] M. J. Hostetler, S. J. Green, J. J. Stokes, R. W. Murray, *J. Am. Chem. Soc.* **1996**, *118*, 4212-4213.
- [6] A. Shaffer, J. G. Wodern, Q. Huo, *Langmuir* **2004**, *20*, 8343-8351.
- [7] M. Dasog, R. W. J. Scott, *Langmuir* **2007**, *23*, 3381-3387.
- [8] I. C. Khoo, S. T. Wu, *Optics and Nonlinear Optics of Liquid Crystals* , World scientific, **1993**.
- [9] B. Bahadur, *Liquid Crystals: Applications and Uses*, World scientific, **1990**.
- [10] D-R. Chiou, L-J. Chen, *Langmuir* **2006**, *22*, 9403-9408.

Chapter 4: Effects of hydrophilic and hydrophobic gold nanoclusters on the stability and ordering of bolaamphiphilic liquid crystals*

This paper was reproduced with permission from J. Mater. Chem. 2007, 17, 2139-2144. Copyright 2007 - The Royal Society of Chemistry. It is co-authored with A. Lepp, P. A. Heiney and T. Hegmann. The text is a verbatim copy of the published paper.

Starting in 2004, different LC hosts doped with functionalized Au NPs have been systematically studied ranging from one dimensional ordered LCs (nematic), over two-dimensional (smectic) to three-dimensional (columnar) ordering. One particular type of LC host was chosen first, a so-called bolaamphiphilic LC. Earlier work by Tschierske and coworkers [16b] showed that a slightly changed length of the lateral alkyl chain of these molecules produces a different LC phase, along with different phase transition temperatures. The phases formed range from a smectic-A phase, over a rectangular columnar phase to a hexagonal columnar phase. Two kinds of LCs were chosen from this series, one forming a smectic-A phase and a second one forming a rectangular columnar phase. Using these two LC materials, the effects of hydrophilic and hydrophobic Au NP coatings on the stability and ordering of these two LC hosts were studied. Structure-property relationships in LC/NP composites are the core of this thesis and the basic principles behind all observed phenomena. This chapter is the linking chapter to show that proper functionalization of Au NPs is the key.

Note: Nanocluster and nanoparticle are regarded interchangeable words in this thesis.

Abstract: Electron microscopy, optical microscopy, and x-ray diffraction studies of dispersions of hydrophilic and hydrophobic thiolate-capped gold nanoclusters in bolaamphiphilic liquid crystals (LCs) indicate random inclusion of the nanoclusters in the LC matrix with a concentration- and monolayer-type-dependent effect on the mesophase stability of the LC host. Both types of nanoclusters show no effect on the thermal properties of the smectic-A phase of LCs **1**. In contrast, the rectangular columnar phase of LCs **2** is gradually destabilized with an increasing concentration of the hydrophobic hexane thiolate gold clusters **Au1**, and gradually stabilized with an increasing concentration of the hydrophilic ethyleneglycol protected gold nanoclusters **Au2**. In addition, structural characterization using small-angle x-ray scattering (SAXS) indicated no change in the lattice of the rectangular columnar phase of **2** in mixtures with both nanoclusters (*c2mm*), but provided evidence for a macroscopic phase separation into particle-rich and particle-poor domains with the same rectangular lattice but slightly different lattice parameters for mixtures with higher concentrations of **Au2** in **2**.

4.1 Introduction

A main challenge in the area of nanoscale (self-) assembly is to develop protocols for the organization of nanoparticles (NPs) wherein the separation between the NPs can be tailored. The ability to organize or align metallic, magnetic and semiconducting NPs into arrays, networks and circuits in a precise and controlled fashion is key to the fabrication of a variety of devices making use of the intriguing properties of nanoscale materials [1]. To produce periodic arrays of NPs, a variety of different self-assembly strategies have been developed over the past years, including: immobilization on solid supports [2],

Langmuir–Blodgett films [3], NP-filled polymer matrices [4], or the use of biomacromolecules such as DNA [5]. For example, the optical properties of metallic NPs (e.g., gold, silver, platinum) depend on whether they comprise periodic organized structures such as monolayer or multilayer films or are solutions of organized or randomly, highly dispersed entities [6]. Applications such as nanoscale electronics, functional coatings, optical memories and display devices, which are based on the collective properties of organized particles, require flexibility in controlling the architecture of NP arrays.

Recently, another approach using liquid crystalline phases to assemble or synthesize nanoscale materials has received enormous attention, to a large extent due to the intrinsic ability of liquid crystals (LCs) to combine order and mobility on the molecular (nanoscale) level. The majority of work in this area has focused on lyotropic LCs to fabricate or assemble metal NPs [7] or low-dimensional polymer structures [8], rarely on thermotropic LCs [9]. Considering the demonstrated strong impact of thermotropic LCs on existing device and display applications [10] as well as the richer mesomorphism (number of LC phases; e.g., tilted smectic, non-hexagonal columnar, and others), thermotropic LCs should be considered excellent candidates for NP assembly or for constructing LC-hybrid nanocomposites with great potential for use in a variety of optical applications.

The capability of orienting small particles using thermotropic liquid crystals was theoretically predicted more than 35 years ago [11]. So far, topological defects and the formation of particle aggregates as a result thereof have been most intensively studied for nematic liquid crystals [12], and much of the underlying physics has recently been

reviewed by Stark [13].

However, apart from a few rare examples of LC dendrimers for nanocluster preparation [14], and mixtures of gold clusters with discotic LCs [15], comparatively little is known about interactions of functionalized NPs with more complex LC phase morphologies formed by multi-block LC molecules (i.e., formation of defects or ordering).

The focus of this work is on the use of one particular type of thermotropic LC forming more complex supramolecular architectures, i.e., lateral substituted bolaamphiphiles [16], with the goal of creating ordered LC-nanocomposites based on functionalized gold nanoclusters. Extensive exploitation of this structural motif in series of such multi-block LC molecules by Tschierske *et al.* has shown that small structural variations such as increasing the length of the lateral hydrocarbon chain have a significant effect on the type and stability of the supramolecular assembly [16]. From this series, we selected two members, **1** and **2** (see Fig.4.1a), forming a lamellar (**1**; SmA) or a rectangular columnar phase [**2**; Col_r(*c2mm*)]. Out of the series, these two LC compounds appeared particularly useful to study structure–property relationships in mixtures with functionalized nanoclusters as they present an interesting transition from a lamellar to a columnar mesophase organization. To probe the possibility of organizing nanoscale gold clusters using these LC phase morphologies, we prepared mixtures of two types of gold particles functionalized with either a hydrophobic (hexane thiolate, **Au1**) or a hydrophilic monolayer protection (triethyleneglycol-terminated pentane thiolate, **Au2**), attempting to utilize attractive interactions between compatible molecular parts common to both the nanocluster and the LC molecule (i.e., van der Waals interaction between hydrocarbon

chains in the case of **Au1**, or H-bonding between hydroxy groups for **Au2**).

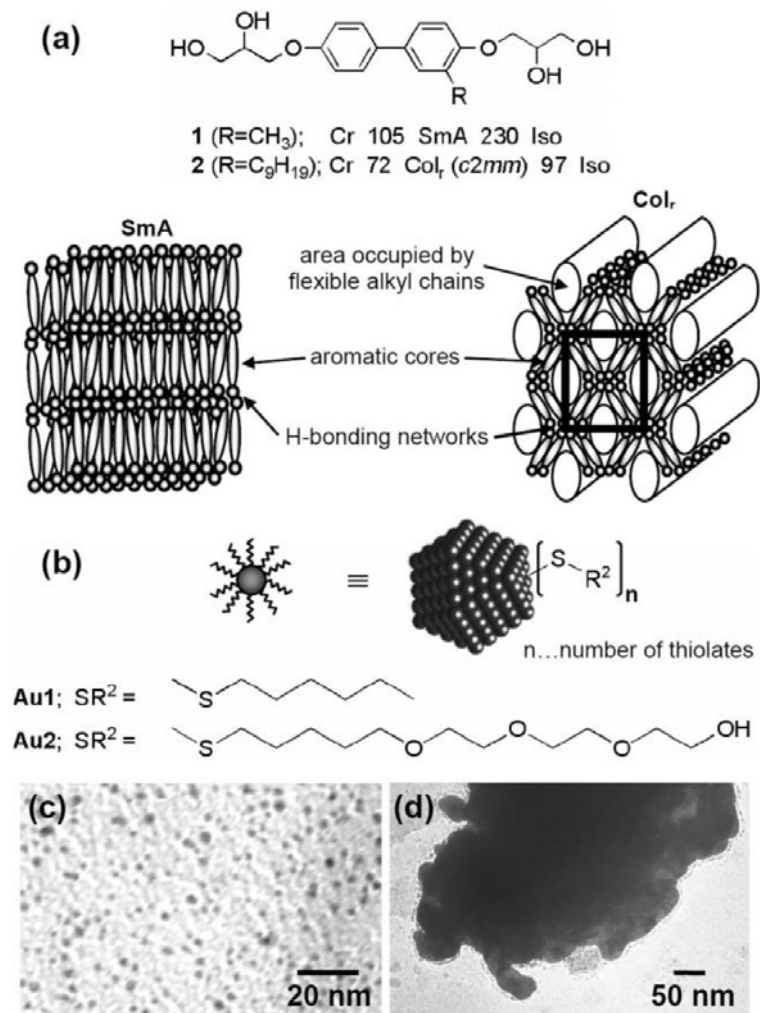


Fig. 4.1 (a) Structure and LC phase morphology of the SmA and Col_r (*c2mm*) phases formed by **1** and **2**[16] (abbreviations: SmA = smectic A phase, Col_r = rectangular columnar phase). (b) Gold nanoclusters **Au1** and **Au2** used in dispersions with the bolaamphiphilic liquid crystals **1** and **2**. (c, d) TEM images of the gold clusters: (c) **Au1**, and (d) **Au2**. Note that the **Au2** clusters strongly aggregate after drop-casting on the TEM grid. For a TEM image of some isolated **Au2** clusters see SI.

4.2 Experimental

4.2.1 General methods

All solvents used for the synthesis of the gold nanoclusters and the LCs were Aldrich Purification grade purified via a PureSolv solvent purification system (Innovative Tech.

Inc.). Wide-angle powder X-ray diffraction (XRD) patterns of the gold nanoclusters were obtained on an MPD X'Pert system (PANalytical) using CuK α radiation (40 kV, 200 mA). **Au1** was measured in reflection geometry using a zero-background flat sample holder, **Au2** using a 0.3 mm glass capillary in transmission geometry. UV-vis spectra were obtained using an Agilent 8453 spectrophotometer. ^1H and ^{13}C NMR spectra were recorded with a Bruker Avance 300 spectrometer. Transmission electron microscopy (TEM) images were obtained on a JEOL FX 2000 TEM instrument operating at an accelerating voltage of 160 kV. A 3 mL drop of the isolated gold colloid solution was dropcast on a carbon coated copper grid (400 mesh) and dried for 2 h (TEM image analysis of more than 1000 particles—Software: Scion Image Beta 4 and Image J). Polarized optical microscopy (POM) was performed using an Olympus BX51-P polarizing microscope in conjunction with a Linkam LS350 heating stage. DSC was done using a Pyris Diamond DSC with Intra-cooler (Perkin-Elmer). Samples were prepared as outlined below, tried in high vacuum and annealed under a stream of dry N_2 . Heating and cooling rates were set to $10\text{ }^\circ\text{C min}^{-1}$. Small-angle X-ray scattering (SAXS) measurements of the pure LCs and the nanocluster–LC mixtures employed a Bruker-Nonius FR591 rotating-anode generator with a copper anode operated at 3.4 kW. The beam was collimated and focused with mirror-monochromator optics and the scattered radiation was detected using a Bruker Hi-Star wire (area) detector [17]. Samples were sealed in 1 mm diameter glass capillaries. Measurements were made at fixed sample–detector distances of 11, 54, and 124 cm; the final refinement of the unit cell parameters was made using the data from the 54 cm configuration. In-situ temperature-dependent measurements employed a custom Linkam heating cell. Primary

data analysis was performed using Datasqueeze [18].

For the preparation of LC–nanocluster TEM specimens, solutions of the gold nanoclusters in mixtures with the LC were dropcast on carbon coated copper grids and heated above the clearing point of the LC for 20 min, cooled to the LC phase and annealed at constant temperature for 4 h under a steady stream of dry N₂. The 13 wt% **Au1** in sample **1** was annealed at 170 °C, all other samples at 80 °C.

4.2.2 Synthesis

1 and **2** were synthesized following the procedure reported by Tschierske and coworkers [16b] and displayed identical phase transition temperatures.

All glassware used for the preparation and storage of colloidal gold was treated with aqua regia, cleaned with piranha solution, and rinsed with DI water (Millipore, Resistivity 18.2 MΩ) and dried overnight at 100 °C. **Au1** clusters were prepared according to the Brust–Schiffrin procedure [19]. **Au2** were synthesized following a method reported by Shon and coworkers [20].

The final monolayer-protected nanoclusters, after exhaustive washing with different pure solvents and drying under high vacuum, were characterized by ¹H NMR (no free, nonbound thiol), TEM, powder XRD, and UV-vis. The size, size distribution, formula and molecular weight for both **Au1** and **Au2** are summarized in Table 4.1 (for details see SI). Following the protocol by Heath *et al.* [21], the average number of gold atoms per cluster (N_{Au}) was calculated using $N_{Au} = 4\pi r^3/3v_g$, where r is the radius (Å) measured by TEM and v_g the volume of a gold atom ($v_g = 17\text{Å}^3$) assuming a quasi-spherical particle. The average number of thiolates coating the gold cluster (n_{thiol}) was calculated using n_{thiol}

$$= 4\pi r^2/21.4 \text{ \AA}^2.$$

Table 4.1 Size, size distribution, formula, and molecular weight (average) of the gold nanoclusters **Au1** and **Au2**^a

	Size/nm		Formula ^b	Mol. wt./g mol ⁻¹
	TEM	XRD ^b		
Au1	2.15 ± 0.65	2.1 ± 0.6	Au ₃₆₁ (SC ₆ H ₁₃) ₇₂	79357
Au2	3.90 ± 0.60	7.6 ± 1.3 ^c	Au ₁₉₁₂ [SC ₅ H ₁₁ (OC ₂ H ₄) ₃ OH] ₂₄₅	435709

^a For exact size distribution, average number of gold atoms per cluster (N_{Au}), and number of thiolates see SI. ^b Calculated from the wide-angle powder XRD pattern using the Scherrer equation. ^c The larger size calculated from the FWHM is a result of particle aggregation.

4.3 Results and discussion

4.3.1 Thermal properties

To study the textural characteristics and thermal properties of **1** and **2** doped with different concentrations of both gold clusters, we first examined the mixtures by polarized optical microscopy (POM, Fig. 4.2) and DSC. For **1**, the phase transition temperatures and the texture of the SmA phase (focal-conic fan texture, Fig. 4.2a) remained largely unaffected by an increase of the concentration of **Au1** or **Au2** until ca. 20 wt%, when the gold clusters began to phase separate forming islands of agglomerated clusters in the LC that were clearly visible by optical microscopy with parallel (un-crossed) polarizers. Recently, we reported the observation of a similar phenomenon for gold nanoclusters doped into conventional, rod-like (calamitic) LCs [22]. In these

mixtures, gold clusters such as **Au1** produced quasi-periodic stripe domains (patterns) in the high-temperature nematic phase, but showed no effect on the low-temperature SmA phase.

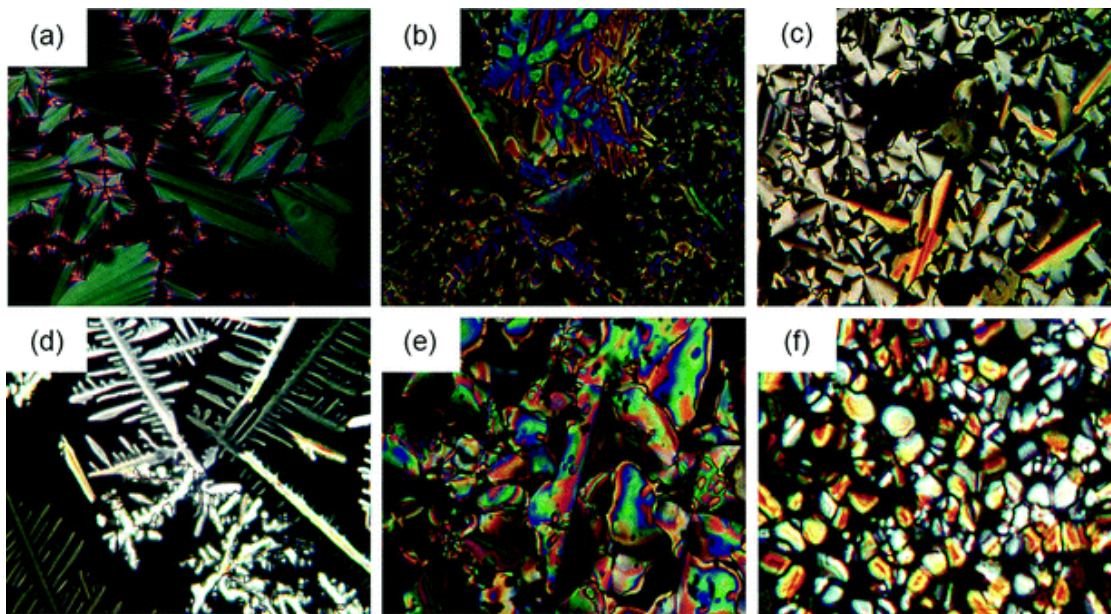


Fig. 4.2 Polarized optical photomicrographs of the NP-LC mixtures on cooling from the isotropic liquid phase: (a) 12 wt% **Au1** in **1** at 140 °C, (b) 1 wt% **Au1** in **2** at 93 °C, (c) 5 wt% **Au1** in **2** at 81 °C, (d) 1 wt% **Au2** in **2** at 99 °C, (e) 5 wt% **Au2** in **2** at 105 °C, and (f) 10 wt% **Au2** in **2** at 98 °C.

In contrast, the phase stability (LC phase range) of **2** forming a Col_r phase critically depends on both the type (**Au1** or **Au2**) and the concentration of the suspended gold nanoclusters. Fig. 4.3 shows the dependence of the clearing temperature of the columnar phase of **2** on the concentration of **Au1** and **Au2**.

As can be seen by comparison of both plots [Fig. 4.3(a) and (b)], an increasing concentration of the hydrophobic gold clusters **Au1** results in a gradual destabilization of the Col_r phase. At higher concentrations (about 10 wt%) aggregation of the gold clusters sets in as observed by POM with uncrossed (parallel) polarizers. In contrast, increasing

the concentration of the hydrophilic gold clusters **Au2** in **2** affords a stabilization of the phase with a maximum at *ca.* 9 wt%, after which the clearing temperature starts to drop again. All mixtures of **Au1** and **Au2** in **2** displays broader phase transitions in comparison to pure **2**, and the transitions become yet broader in mixtures of **Au2** in **2** at concentrations above 5 wt% (see DSC traces in the ESI). This observation is also in agreement with the POM investigations showing different phase transition temperatures (clearing temperatures, i.e., occurrence of birefringent domains) in different sample areas. This behavior is particularly pronounced for both the 9 wt% and the 10 wt% mixtures, giving a first hint of local concentration differences of the gold nanoclusters in the LC matrix of **2**.

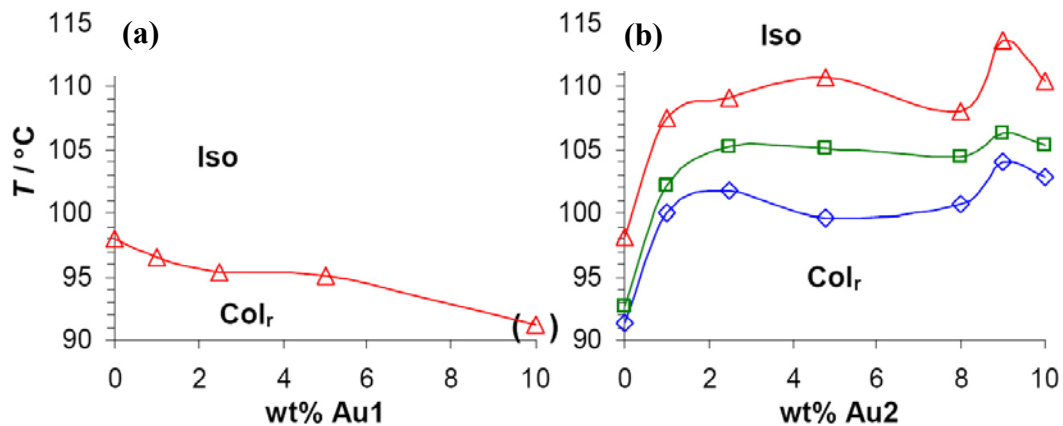


Fig. 4.3 Stability of the columnar phase of **2** vs. concentration of suspended nanoclusters obtained by DSC (for DSC traces see ESI); \blacktriangle : high- T onset of the phase transitions, 1st heating; \blacksquare : peak maximum, 1st heating; \blacklozenge : peak maximum, 1st cooling: (a) **Au1** in **2** (at around 10 wt%, the **Au1** nanoclusters phase-separate forming islands of aggregated particles in **2**), (b) **Au2** in **2** (for 10 wt% **Au2** in **2**, SAXS indicates the coexistence of two Col_r phases with slightly different lattice parameters, see Fig. 4.5).

While changes in the elastic properties and altered interactions with the glass surfaces of **2** in mixtures with the gold nanoclusters could account for the differences of the

thin-film texture of mixtures containing up to 8 wt% gold clusters in comparison to pure **2** [occurrence of dendritic domains, and disappearance of mosaic domains, compare Fig. 4.2(b)–(e)], mixtures of 9 to 10 wt% **Au2** in **2** showed no textural resemblance to pure **2** or to mixtures with lower particle content (no dendritic or pseudo-focal conic domains). These particular mixtures, however, over the entire LC phase range formed rather non-characteristic textures with birefringent domains forming a mosaic-type pattern (Fig. 4.2f).

4.3.2 Structural characterization

To characterize the LC phase structure and explore eventual long-range ordering of the gold clusters in the LC matrix of **2**, three selected mixtures were examined by small-angle x-ray scattering (SAXS) and some mixtures (including **Au1** in **1**) additionally by TEM. We note that TEM produces images that are merely 2D projections of 3-dimensional objects, and can therefore not always be used as the sole source for providing information on 3D assemblies [9c].

As can be seen in the TEM images after annealing (Fig. 4.4 and SI) both **Au1** and **Au2** clusters appear well dispersed in the LC matrix of **1** or **2**, while pure **Au2** readily aggregate. We interpret this as the result of attractive interactions between the amphiphilic LC with both nanoclusters. Judging from the mesophase stabilizing effect, these interactions appear more pronounced for the hydrophilic nanoclusters **Au2**.

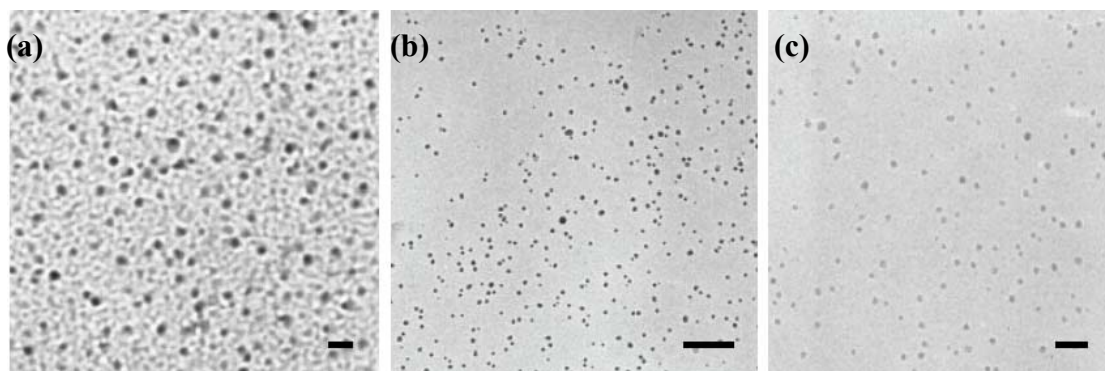


Fig. 4.4 TEM images of the gold clusters dispersed in the liquid crystal phases of **1** and **2**: (a) 13 wt% **Au1** in **1**, (b) 10 wt% **Au1** in **2**, and (c) 21 wt% **Au2** in **2**. Scale bar: 20 nm in (a), 100 nm in (b) and (c).

Although TEM images of **Au1** and **Au2** in **2** appear to show regions of uniformly spaced gold nanoclusters (Fig. 4.4(b) and (c), for larger images, see SI, X-ray scattering at very low angles ($2\theta = 0.3^\circ - 5.5^\circ$) did not reveal any periodic ordering on length scales less than 30 nm. However, an important fact we can deduce from the TEM images of the mixtures is that the gold nanoclusters are well dispersed in the LC host phases of **1** and **2**. This is further supported by the observation that all Au-containing samples are observed to strongly attenuate the X-ray beam. In some cases, depending on preparation conditions (SI), **2** can accommodate up to 21 wt% of **Au2** without aggregation and phase separation of the gold clusters (Fig. 4.4c) usually observed for TEM specimens prepared by drop-casting solutions of pure **Au2** in different solvents (Fig. 4.1d).

SAXS of pure **2** confirmed the phase assignment reported by Tschierske *et al.* [16a, 23]. The diffraction patterns of both 5 wt% mixtures of **2** with **Au1** and **Au2** indicate the same lattice ($c2mm$) with almost identical lattice parameters (Table 4.2). However, the mixture of **2** containing 10 wt% of **Au2** shows three diffraction maxima with $q_1 = 0.2691$, $q_2 = 0.37$, and $q_3 = 0.3753 \text{ \AA}^{-1}$ that are best interpreted as the coexistence of two Col_r phases with slightly different lattice parameters [see Fig. 4.5 (d, e) and Table 2].

Considering this macroscopic phase separation into two Col_r phases with *c2mm* lattice, which is quite remarkable on its own (one would expect complete miscibility), we re-examined mixtures with 9 and 10 wt% **Au2** in **2** by POM. Indeed, on slow cooling (1 °C min⁻¹) from the isotropic liquid phase, different sample areas of the same thin film texture showed the appearance of birefringent domains or features (onset of the Iso–Col_r phase transition on cooling) at different temperatures varying from *ca.* 94 °C to about 120 °C (see textural areas 1 to 11 in Fig. 4.6). Since the Col_r phase of **2** is gradually stabilized with an increasing concentration of **Au2**, this phenomenon is best explained with a spatial concentration difference, with particle-rich domains showing higher clearing temperatures (and different lattice parameters at higher cluster concentration) and particle-poor domains having lower clearing points. Such macroscopic separation into particle-poor and particle-rich domains has been reported for nematic phases containing gold nanoclusters [22], and is consistent with the TEM images of annealed binary mixtures of **Au2** in **2** (Fig. 4.4).

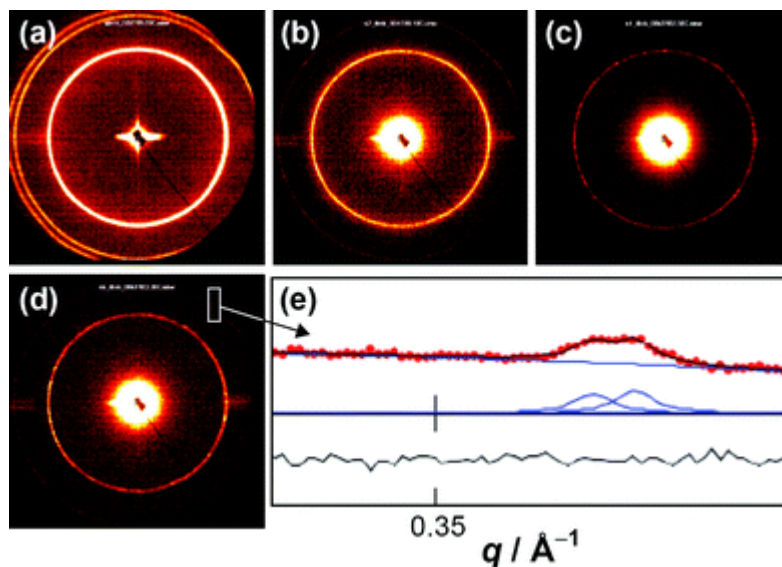


Fig. 4.5 SAXS of (a) pure **2** ($c2mm$) at 95 °C on heating, (b) 5 wt% **Au1** in **2** at 90 °C on cooling, (c) 5 wt% **Au2** in **2** at 105 °C on cooling, (d) 10 wt% **Au2** in **2** at 103 °C on cooling, and (e) least-square fits to diffractogram (d), (200) peak positions: $q_2 = 0.3700 \text{ \AA}^{-1}$, $q_3 = 0.3753 \text{ \AA}^{-1}$ indicating the coexistence of two CoI_r phases with slightly different lattice parameters.

Table 4.2 Small-angle powder diffraction data (q -values, Miller indices, and lattice parameters for **2** and of **Au1** and **Au2** in **2**)

wt% AuX in 2	$T/^\circ\text{C}$	$q_1, q_2, q_3/\text{\AA}^{-1}$	$a, b/\text{nm}$
5 wt% Au1	90, heating	0.2693 (110), 0.3702 (200)	3.22, 3.40
	90, cooling	0.2693 (110), 0.3700 (200)	3.22, 3.40
5 wt% Au2	105, heating	0.2700 (110), 0.3735 (200)	3.20, 3.40
10 wt% Au2	100, heating	0.2691 (110), 0.3700 (200), 0.3753 (200) ^a	3.22, 3.39; 3.26, 3.35 ^a
		Pure 2	95, heating
	95, cooling	0.2699 (110), 0.3715 (200)	3.21, 3.38

^a Coexistence of two phases with slightly different lattice parameters.

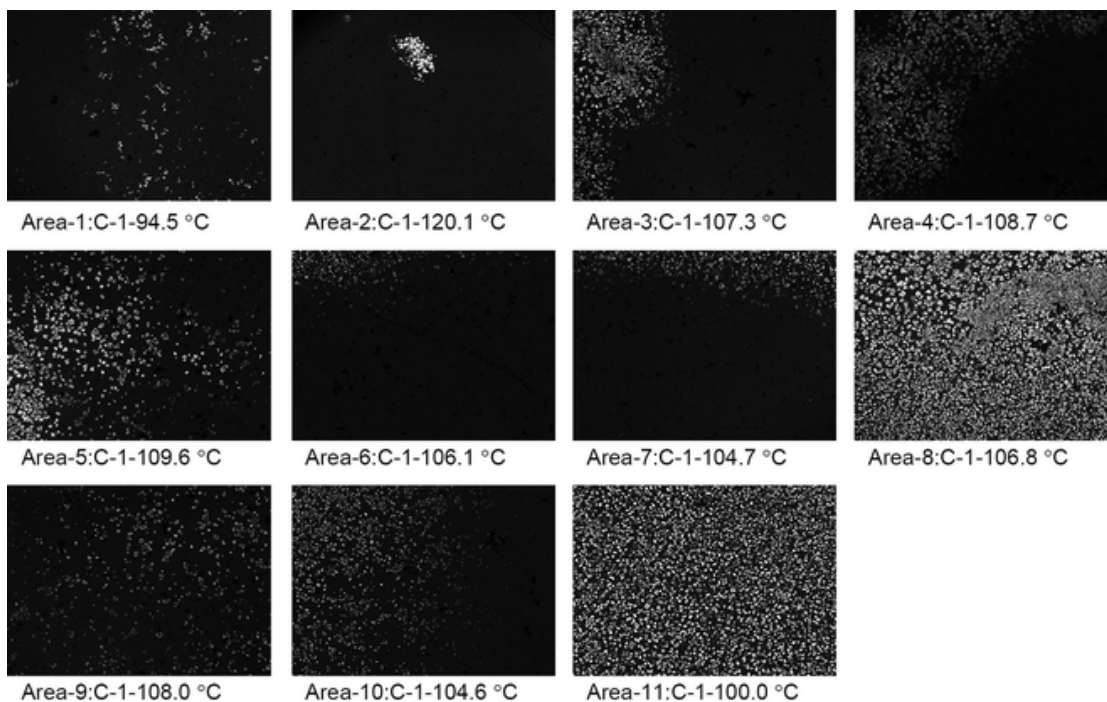


Fig. 4.6 POM micrographs of the 10 wt% **Au2** in **2** mixture. One can clearly see that different areas (1 to 11) of the thin film sample start to show birefringent textures on cooling from the isotropic liquid phase at different temperatures (C-1 indicates first cooling after sample preparation). Despite the vigorous preparation procedure to ensure sample homogeneity (dispersion of the gold clusters in the LC phase), this observation indicates local differences in nanocluster concentrations with areas of higher nanocluster concentration showing higher clearing temperatures according to the thermal characterization using DSC. (For a larger version of this figure with additional magnified sections see SI.)

4.4 Conclusions

In summary, the presented studies show that the thermal stabilities of the two bolaamphiphilic LC derivatives strongly depend on the size, the concentration and the surface functionalization of dispersed gold nanoclusters. Both types of gold cluster appear to have no effect on the stability and bulk ordering of the SmA phase of **1** indicating the formation of random defects with homeotropic anchoring of the LC molecules to the cluster surface [22]. In contrast, **2** shows a marked difference in the thermal behaviour in mixtures with the two different nanoclusters. While the hydrophobic

clusters are very likely randomly embedded by areas occupied by the flexible alkyl chains creating defects in the Col_r structure with only little effect on the thermal properties, the larger, hydrophilic clusters stabilize the Col_r phase (maximum at *ca.* 9 wt%) forming defects, due to the large particle size in comparison with the molecular dimensions of the LC, that initially do not affect the overall organization of the LC molecules in the bulk, until a further increase of the nanocluster concentration (at around 9–10 wt%) results in a phase separation into particle-poor domains with the same lattice parameters as pure **2** and particle-rich domains with the same lattice type but different lattice parameters. The mesophase stabilizing effect inherently connected to the macroscopic phase separation is particularly noteworthy considering defect formation and the extremely low concentration of the **Au2** nanoclusters (5 wt% **Au2**= 0.006 mol %) [24]. The mesophase stabilizing effect dominant in the particle-rich domains likely arises from the high concentration (density) of hydrophilic hydroxy groups surrounding the hydrophilic **Au2** clusters by participating in H-bonding interactions with the polar 2, 3-dihydroxypropyloxy groups of the LC (principally forming a new Col_r phase that coexists with the Col_r phase of the particle-poor domains with similar lattice parameters as pure **2** [25]. Similar mesophase stabilizing effects have been reported by Tschierske *et al.* for structurally related amphiphilic LCs in samples saturated with ethylene glycol or formamide [26].

Continuing efforts will focus on LC-decorated gold nanoclusters to enhance the compatibility between nanocluster and LC host to achieve long-range ordering of the nanoclusters. Future research will then tackle binary mixtures with amphiphilic LCs showing LC phase transitions such as $\text{SmA}-\text{Col}_r$ or $\text{Col}_r-\text{Col}_h$. In this respect, the current

work is an important step in this direction, and proves that interactions between nanoclusters and LC molecules strongly depend on the particular materials combination, the molecular structure and elastic properties of the LC, as well as the type and size of the nanocluster. Finally, we trust that the present work on gold nanocluster incorporation into mesophases formed by amphiphile multi-block LC molecules will stimulate future experimental and theoretical research focusing on NP assembly and synthesis in columnar LC phases, as well as defect formation in more complex LC phase morphologies.

Acknowledgements

This work was supported in part by Natural Sciences and Engineering Research Council (NSERC), the Canada Foundation for Innovation (CFI), and the University of Manitoba. Structural work at the University of Pennsylvania was supported by the MRSEC program of the National Science Foundation (Grant # DMR05-20020). We thank Dr Chaturvedi for assistance with the TEM imaging, and Dr Bieringer for access to powder XRD measurements.

References

- 1 (a) M. Brust, *Nat. Mater.* **2005**, *4*, 364-365; (b) A. C. Templeton, W. P. Wuelfing, R. W. Murray, *Acc. Chem. Res.* **2000**, *33*, 27-36.
- 2 M. K. Corbierre, J. Beerens, J. Beauvais, R. B. Lennox, *Chem. Mater.* **2006**, *18*, 2628-2631 and references therein.

- 3 See, for example: M. Fukuto, R. K. Heilmann, P. S. Pershan, A. Badia, R. B. Lennox, *J. Chem. Phys.* **2004**, *120*, 3446-3459.
- 4 For a review see: R. Shenhar, T. B. Norsten, V. M. Rotello, *Adv. Mater.* **2005**, *17*, 657-669.
- 5 S. W. Chung, D. S. Ginger, M. W. Morales, Z. F. Zhang, V. Chandrasekhar, M. A. Ratner, C. A. Mirkin, *Small* **2005**, *1*, 64-69 and references therein.
- 6 L. M. Liz-Marzán, *Mater. Today* **2004**, *2*, 26-31.
- 7 (a) Y. Yamauchi, T. Momma, T. Yokoshima, K. Kuroda, T. Osaka, *J. Mater. Chem.* **2005**, *15*, 1987-1994; (b) T. M. Dellinger, P. V. Braun, *Chem. Mater.* **2004**, *16*, 2201-2207; (c) P. S. Khiew, S. Radiman, N. M. Huang, Md. S. Ahamd, *J. Cryst. Growth* **2004**, *268*, 227-237; (d) R. Patakfalvi and I. Dékány, *Colloid Polym. Sci.* **2002**, *280*, 461-470; (e) J. H. Ding, D. L. Gin, *Chem. Mater.* **2000**, *12*, 22-24.
- 8 (a) W. Dobbs, J.-M. Suisse, L. Douce, R. Welter, *Angew. Chem., Int. Ed.* **2006**, *45*, 4179-4182; (b) A. Taubert, *Angew. Chem., Int. Ed.* **2004**, *43*, 5380-5382; (c) D. T. Cormick, Z. W. Fordham, J. Smith, P. J. McMullan, S. F. Thames, C. A. Guymon, *Polymer* **2003**, *44*, 2751-2759 and references therein; (d) R. C. Smith, W. M. Fischer, D. L. Gin, *J. Am. Chem. Soc.* **1997**, *119*, 4092-4093.
- 9 (a) L. Cseh, G. H. Mehl, *J. Mater. Chem.* **2007**, *17*, 311-315; (b) L. Cseh, G. H. Mehl, *J. Am. Chem. Soc.* **2006**, *128*, 13376-13377; (c) K. Kanie, A. Muramatsu, *J. Am. Chem. Soc.* **2005**, *127*, 11578-11579; (d) I. In, Y.-W. Jun, Y. J. Kim, S. Y. Kim, *Chem. Commun.* **2005**, 800-801; (e) N. Kanayama, O. Tsutsumi, A. Kanazawa, T. Ikeda, *Chem. Commun.* **2001**, 2640-2641.
- 10 J. Dijon, in *Liquid Crystals: Applications and Uses*, ed. B. Bahadur, World

Scientific, Singapore, **1990**, vol. 1, ch. 13.

- 11 F. Brochard, P. G. de Gennes, *J. Phys.* **1970**, *31*, 691-708.
- 12 (a) O. V. Kuksenok, R.W. Ruhwandl, S. V. Shiyankovskii, E. M. Terentjev, *Phys. Rev. E* **1996**, *54*, 5198-5203; (b) R.W. Ruhwandl, E. M. Terentjev, *Phys. Rev. E* **1997**, *56*, 5561-5565; (c) P. Poulin, V. Cabuil, D. A. Weitz, *Phys. Rev. Lett.* **1997**, *79*, 4862-4865; (d) P. Poulin, H. Stark, T. C. Lubensky, D. A. Weitz, *Science* **1997**, *275*, 1770-1773; (e) P. Poulin, D. A. Weitz, *Phys. Rev. E* **1998**, *57*, 626-637; (f) T. C. Lubensky, D. Pettey, N. Currier, H. Stark, *Phys. Rev. E* **1998**, *57*, 610-625; (g) M. Zapotocky, L. Ramos, P. Poulin, T. C. Lubensky, D. A. Weitz, *Science* **1999**, *283*, 209-212; (h) H. Stark, *Eur. Phys. J. B* **1999**, *10*, 311-321; (i) H. Stark, J. Stelzer, R. Bernhard, *Eur. Phys. J. B* **1999**, *10*, 515-529; (j) P. Poulin, N. France's, O. Mondain-Monval, *Phys. Rev. E* **1999**, *59*, 4384-4387; (k) O. Mondain-Monval, J. C. Dedieu, T. Gulik- Krzywicki, P. Poulin, *Eur. Phys. J. B* **1999**, *12*, 167-170; (l) Y. D. Gu, N. L. Abbott, *Phys. Rev. Lett.* **2000**, *85*, 4719-4722; (m) J.-C. Loudet, P. Barois, P. Poulin, *Nature* **2000**, *407*, 611-613; (n) D. Andrienko, G. Germano, M. P. Allen, *Phys. Rev. E* **2001**, *63*, 041701; (o) J.-C. Loudet, P. Poulin, P. Barois, *Euro phys. Lett.* **2001**, *54*, 175-181; (p) J.-C. Loudet, P. Poulin, *Phys. Rev. Lett.* **2001**, *87*, 165503; (q) J.-C. Loudet, O. Mondain-Monval, P. Poulin, *Eur. Phys. J. E* **2002**, *7*, 205-208; (r) B. I. Lev, S. B. Chernyshuk, P. M. Tomchuck, H. Yokoyama, *Phys. Rev. E* **2002**, *65*, 021709; (s) M. Mitov, C. Portet, C. Bourgerette, E. Snoeck, M. Verelst, *Nat. Mater.* **2002**, *1*, 229-231; (t) M. Mitov, C. Bourgerette, F. de Guerville, *J. Phys.: Condens. Matter* **2004**, *16*, 1981-1994; (u) J. J. Feng, C. Zhou, *J. Colloid Interface Sci.* **2004**, *269*, 72-78; (v) J. Fukuda, H. Yokoyama, M. Yoneya, H. Stark, *Mol.*

- Cryst. Liq. Cryst.* **2005**, *435*, 723-734; (w) M. Svetec, S. Kralj, Z. Bradac, S. Žumer, *Eur. Phys. J. E* **2006**, *20*, 71-79; (x) P. Kossyrev, M. Ravnik, S. Žumer, *Phys. Rev. Lett.* **2006**, *96*, 048301.
- 13 (a) H. Stark, *Phys. Rev. E* **2002**, *66*, 032701; (b) H. Stark, *Phys. Rep.* **2001**, *351*, 387-474.
- 14 S. Kumar, V. Lakshminarayanan, *Chem. Commun.* **2004**, 1600-1602.
- 15 G. Lattermann, L. Torre Lorente, M. Grudzev, M. Krekhova, N. V. Usoltseva, *21st International Liquid Crystal Conference*, Keystone (CO), Book of Abstracts, 2006, p. 218.
- 16 (a) X. Cheng, M. Prehm, M. K. Das, J. Kain, U. Baumeister, S. Diele, D. Leine, A. Blume, C. Tschierske, *J. Am. Chem. Soc.* **2003**, *125*, 10977-10996; (b) M. Kölbel, T. Beyersdorff, X. Cheng, C. Tschierske, J. Kain, S. Diele, *J. Am. Chem. Soc.* **2001**, *123*, 6809-6818; (c) M. Kölbel, T. Beyersdorff, I. Sletvold, C. Tschierske, J. Kain, S. Diele, *Angew. Chem., Int. Ed.* **1999**, *38*, 1077-1080.
- 17 See <http://www.lrsm.upenn.edu/lrsm/facMAXS.html> for additional details.
- 18 See <http://www.datasqueezesoftware.com> for more details.
- 19 M. Brust, M. Walker, D. Bethell, D. J. Schiffrin, R. Whyman, *Chem. Commun.* **1994**, 801-802.
- 20 H. Choo, E. Cutler, Y. S. Shon, *Langmuir* **2003**, *19*, 8555-8559.
- 21 D. V. Leff, P. C. Ohara, J. R. Heath, W. M. Gelbart, *J. Phys. Chem.* **1995**, *99*, 7036-7041.
- 22 H. Qi, T. Hegmann, *J. Mater. Chem.* **2006**, *16*, 4197-4205.
- 23 For reasons that are not understood, but consistent with ref. 16a, the (200) reflection

was observed both on heating and cooling but the (020) reflection was seen only on heating.

- 24 A recent report by West *et al.* reported a dramatic increase in the N–Iso phase transition temperature (clearing temperature) by up to 40 °C by doping 1 wt% BaTiO₃ NPs into one specific nematic LC (MLC-6609) via an increase of orientational ordering: J. L. West, F. Li, Y. Reznikov, O. Buchnev, C. I. Cheon, A. Glushchenko, V. Y. Reshetnyak, T. J. Sluckin, Book of Abstracts, *21st International Liquid Crystal Conference ILCC*, Keystone (CO), 2006, p. 193. Other types of LCs were not affected, and most nematic LCs are commonly destabilized by the addition of different types of nanoparticles: C. Da Cruz, O. Sandre, V. Cabuil, *J. Phys. Chem. B* **2005**, *109*, 14292-14299.
- 25 As with most amphiphilic compounds, we have taken all possible precautions to avoid contamination of the LCs, gold nanoclusters and binary mixtures with water during handling and sample/ specimen preparation (DSC, SAXS, POM, TEM, etc.). For more details see ref. 22 of: B. Chen, U. Baumeister, G. Pelzl, M. K. Das, X. Zeng, G. Ungar, C. Tschierske, *J. Am. Chem. Soc.* **2005**, *127*, 16578-16591. In addition to the precautions outlined there, we have used drying agents and high vacuum to dry all samples, and used a flow of dry N₂ for the sample handling.
- 26 C. Sauer, S. Diele, N. Lindner, C. Tschierske, *Liq. Cryst.* **1998**, *25*, 109-116.

Appendix A

Supplementary Information for Chapter 4

Synthesis of LCs

1 and **2** were synthesized based on a procedure reported by Tschierske and coworkers [S1].

1: ^1H NMR (300 MHz, DMSO- D_6 , δ , ppm): 7.53 (d, 2H, $3J=8.7\text{Hz}$, Ar-H), 7.39 (m, 2H, Ar-H), 6.96 (m, 3H, Ar-H), 4.95 (d, 1H, $3J=5.1\text{Hz}$, CHOH), 4.92 (d, 1H, $3J=5.1\text{Hz}$, CHOH), 4.66 (m, CH_2OH), 4.05- 3.78 (m, 6H, ArOCH_2 , CHOH), 3.54-3.44 (m, 4H, CH_2OH), 2.22 (s, 3H, CH_3). ^{13}C NMR (75MHz, DMSO- D_6 , δ , ppm): 157.8, 156, 132.4, 131.8, 128.2, 127.1 (2C), 126.3, 124.4, 114.8 (2C), 111.7, 70.0 (2C), 69.9, 69.6, 62.8, 62.7, 16.1.

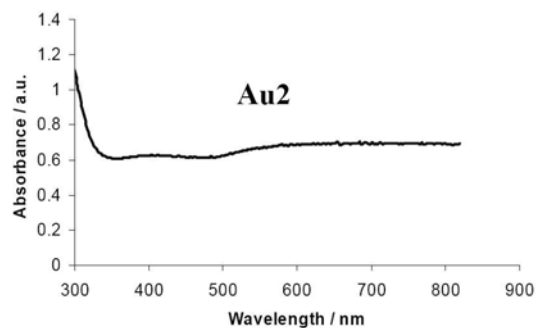
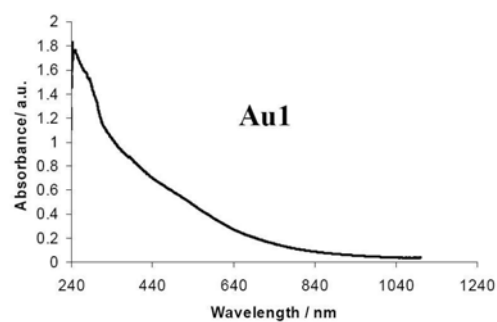
2: ^1H NMR (300 MHz, DMSO- D_6 , δ , ppm): 7.52 (d, 2H, $3J=8.85\text{Hz}$, Ar-H), 7.38-7.35 (m, 2H, Ar- H), 6.99-6.95 (2d, 3H, Ar-H), 4.91 (br, 1H, CHOH), 4.65 (br, 1H, CHOH), 4.05-3.85 (m, 6H, ArOCH_2 , CHOH), 3.51-3.45 (m, 4H, CH_2OH), 2.61 (t, 2H, $3J=7.2\text{Hz}$, Ar- CH_2), 1.57 (m, 2H, ArCH_2CH_2), 1.30- 1.24 (m, 12H, CH_2), 0.85 (t, 3H, $3J=6.6\text{Hz}$, CH_3). ^{13}C NMR (75MHz, DMSO- D_6 , δ , ppm): 158, 156, 132.4, 131.8, 130.9, 129, 127.2, 126.0, 114.8, 111.7, 70.0, 69.9, 69.6, 62.8, 62.7, 31.3, 29.0, 28.9, 28.7, 28.5, 28.1, 22.1, 14.0. MS m/z (rel. int., %): 460 (28) $[\text{M}]^+$, 386 (20), 312 (45), 273 (6), 213 (7), 199 (50), 149 (26).

Thiol for Au2: 2-{2-[2-(5-Mercaptopentyloxy)ethoxy]ethoxy}ethanol was prepared according to a published procedure. [S2] ^1H NMR (300 MHz, acetone- D_6 , δ , ppm): 6.2 (br, 1H, CH_2OH), 3.61 (m, $\text{OCH}_2\text{CH}_2\text{O}$, 12H), 3.45 (t, 2H, $3J=6.2\text{Hz}$, $\text{CH}_2\text{OCH}_2\text{CH}_2$),

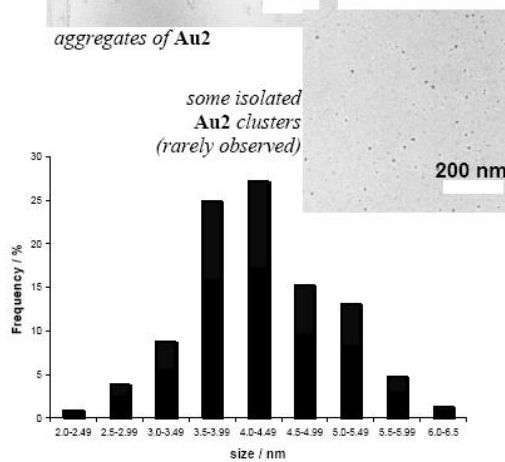
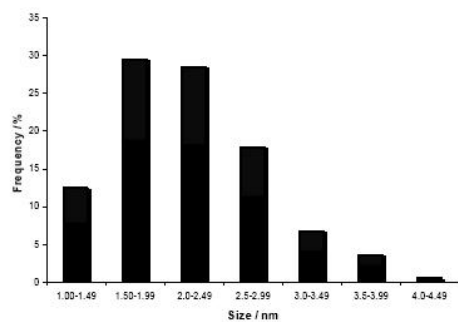
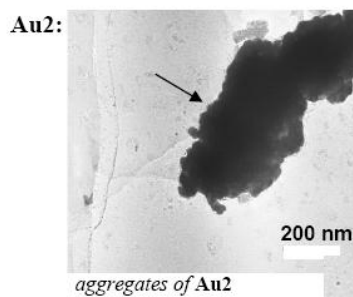
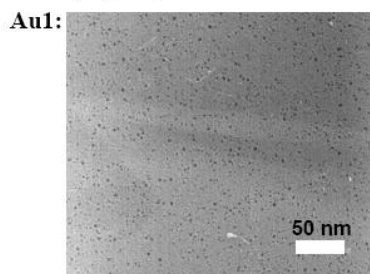
2.53 (q, 2H, CH_2SH), 1.60 (m, 6H, CH_2). ^{13}C NMR (75 MHz, acetone- D_6 , δ , ppm): 72.8, 71.1, 70.73, 70.5, 70.3, 61.3, 34.2, 33.7, 29.6, 26.1. MS m/z (rel. int., %): 252 (0.1) $[M]^+$, 133 (1.85), 119 (1.79), 103(1.76), 89 (22.73).

Gold nanoclusters characterization:

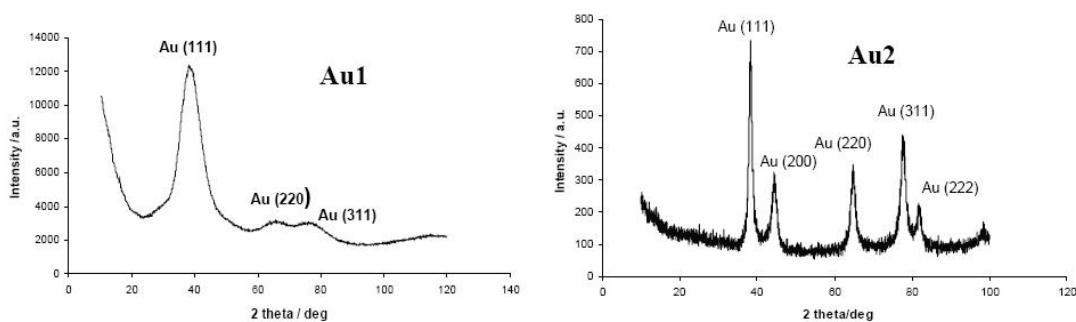
UV-vis (Fig. S4.1)



TEM (Fig. S4.2)



Wide-angle Powder XRD of Au1 and Au2 (Fig. S4.3)

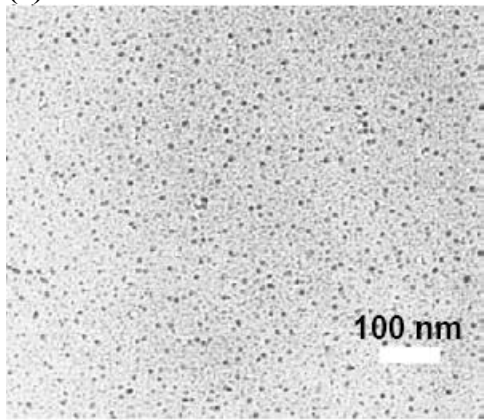


TEM of annealed mixtures (more detailed and larger images):

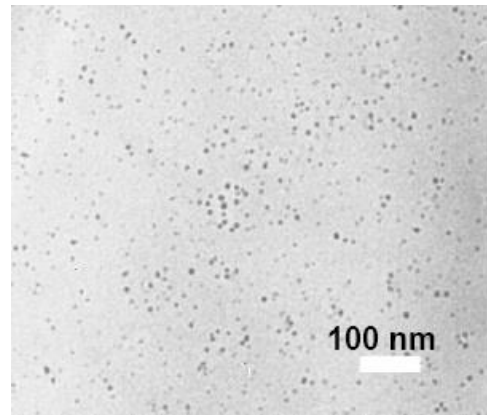
Although some areas in the TEM images appear to show organization of the nanoclusters over shorter length scales [two examples are shown in Figs. S4(b) and (d)], and one could argue about self-assembly on such shorter length scales, x-ray scattering at low and ultra-low angles did not reveal any bulk, long range periodic ordering of the gold nanoclusters. The original size of the **Au1** is about 2 nm, but increases upon heating to ca. 4 nm. For the **Au2** clusters, no change in size was observed. Hence, in the final mixtures with **2**, both nanoparticles are similar in size, and effects on the LC ordering are primarily a result of interactions with the hydrophilic or hydrophobic monolayers. The reason for the difference of this size-effect between the larger (**Au2**) and the smaller clusters (**Au1**) was explained by the fact that smaller nanoclusters have larger chemical potentials and, as a result thereof, have a greater tendency to sinter and change size [S3].

TEM image of mixture of gold nanoclusters in LCs (Fig. S4.4)

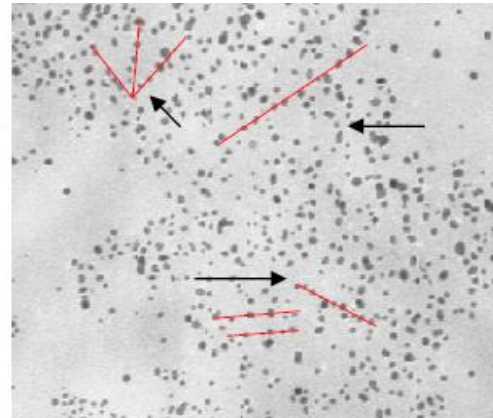
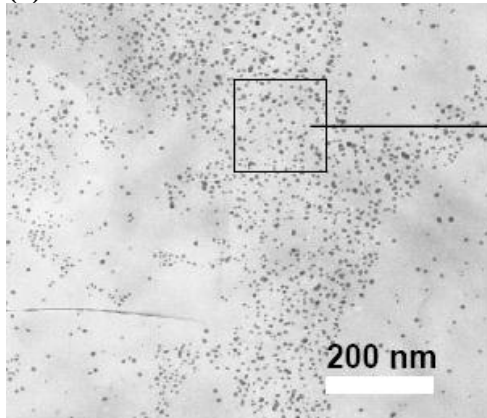
(a) 13wt% Au1 in 1



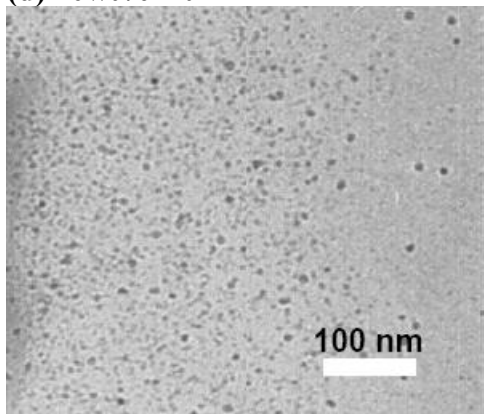
(b) pure Au1 (heated to annealing T)



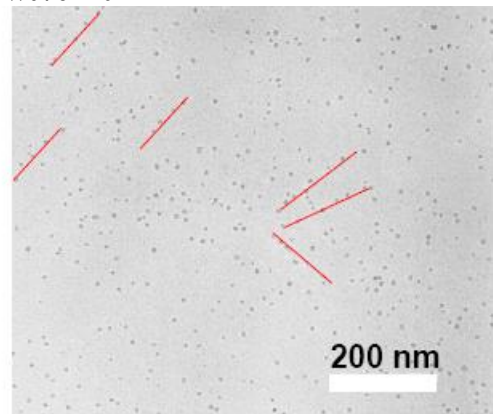
(c) 10wt% Au1 in 2



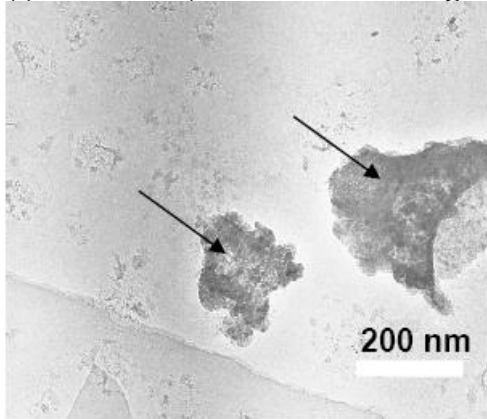
(d) 10wt% Au2 in 2



(e) 21wt% Au2 in 2

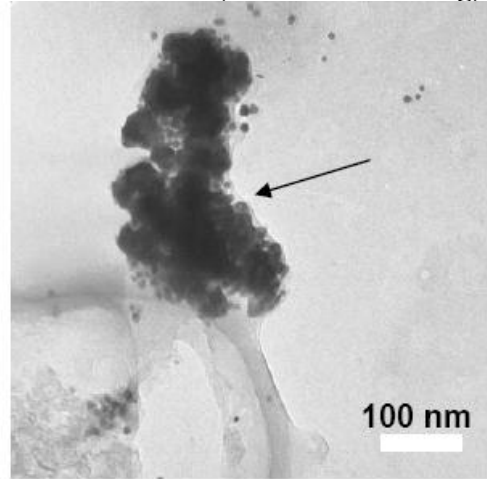


(f) Pure Au₂ (heated to annealing T)



(Notice particle aggregates)

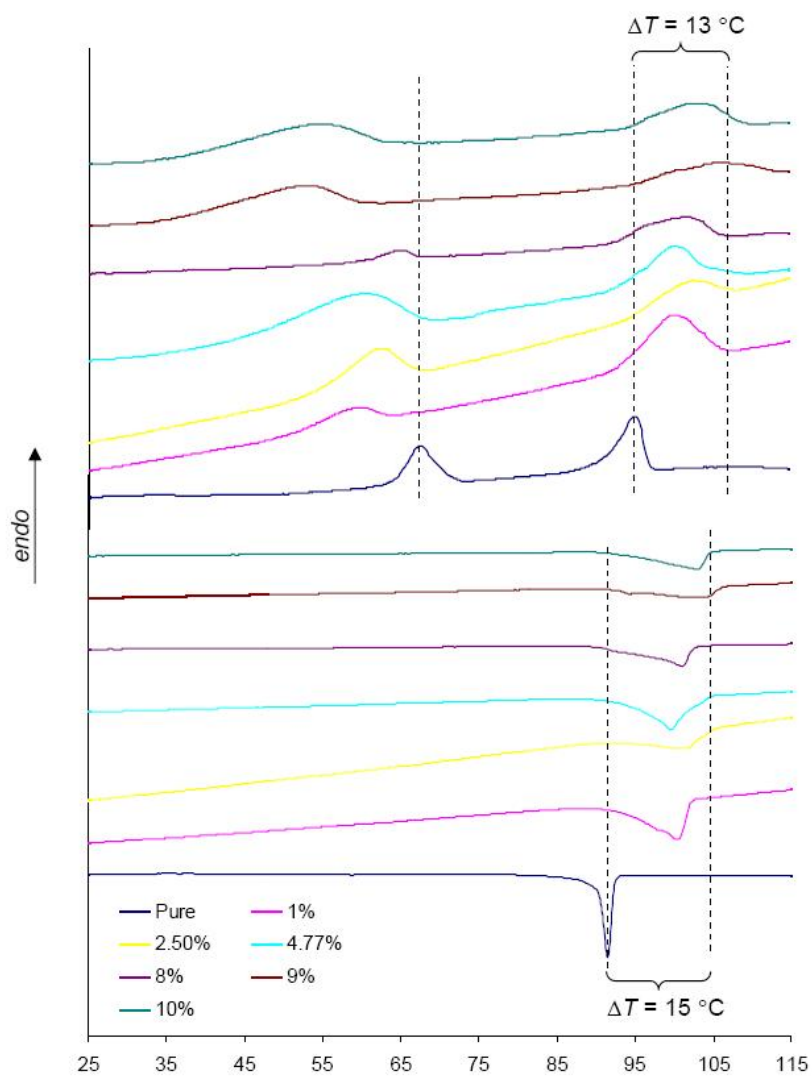
(g) 10wt% Au₂ in 2 (without annealing)



(Notice particle aggregates)

DSC for Au2 in 2 (Fig. S4.5)

Preparation of the samples requires annealing of the mixtures under a steady stream of dry N₂. Therefore, the DSC traces shown represent the second heating and second cooling run. As can be seen in the cooling runs by DSC, the samples do not crystallize over shorter periods of time, in some cases not for days. To ensure a measurable melting point in the second heating scan (first in the DSC instrument), ready, filled and closed sample pans were left in a desiccator to crystallize prior to DSC measurements.



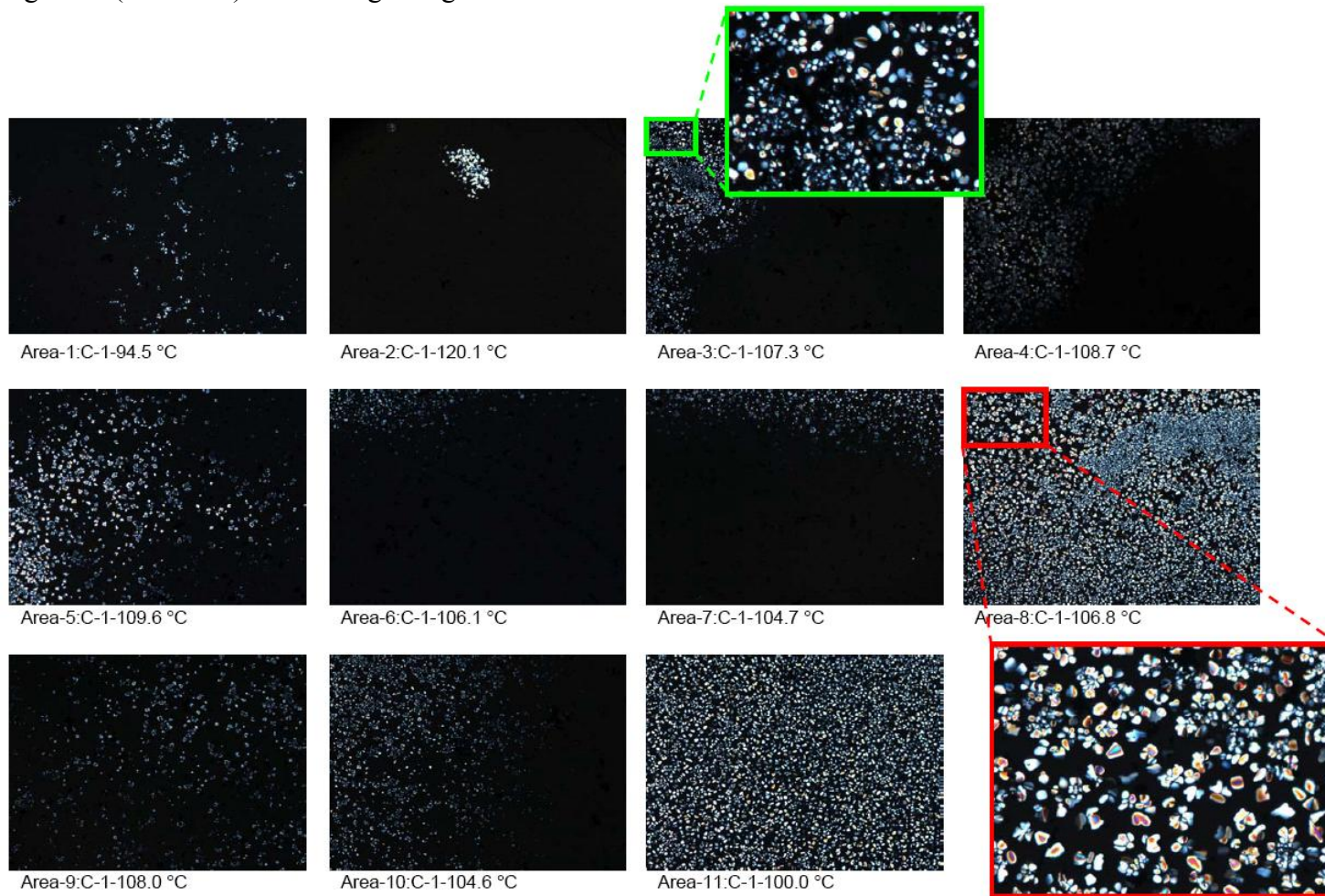
NP Stability

Recent studies on the stability of thiolate-protected gold nanoparticles showed that thiols with a carbon chain longer than C6 begin to desorb from the gold nanoparticle surface above a threshold of 160 °C.[S4] Therefore, we assume that during all mixing experiments with **2** no changes in the nanoparticle composition (surface) *via* desorption of thiolate takes place.

References

- (S1) M. Kölbl, T. Beyersdorff, X. Cheng, C. Tschierske, J. Kain, S. Diele, *J. Am. Chem. Soc.* **2001**, *123*, 6809-6818.
- (S2) P. Chirakul, V. H. Perez-Luna, H. Owen, G. P. Lopez, *Langmuir* **2002**, *18*, 4324-4330.
- (S3) M. M. Maye, W. Zheng, F. L. Leibowitz, N. K. Ly, C. Zhong, *Langmuir* **2000**, *16*, 490-497.
- (S4) M. Büttner, T. Belser, P. Oelhafen, *J. Phys. Chem. B* **2005**, *109*, 5464-5467.

Fig. S4.6 (main text) with enlarged segments



Chapter 5: Formation of periodic stripe patterns in nematic liquid crystals doped with functionalized gold nanoparticles

This paper was reproduced with permission from J. Mater. Chem. 2006, 16, 4197-4205.

Copyright 2006 - The Royal Society of Chemistry. It is co-authored with T. Hegmann.

The text is a verbatim copy of the published paper.

The previous chapter (chapter 4) began to establish that the nanoparticle surface functionalization can have a profound effect not only on the stability but also on the ordering of bolaamphiphilic LC block molecules. It was found that both hydrophilic and hydrophobic Au NPs at concentrations up to 5 wt% have no effect on the ordering as well as the thermal properties of the lamellar smectic-A LC phase, but a tremendous effect on the rectangular columnar phase of the bolaamphiphile with a longer lateral hydrocarbon chain. This study provided the first data pointing to the critical role of the nanoparticle capping agent in mixtures with LC phases of different symmetry. The following chapters will build on this observation and now focus on the least-ordered nematic phase, which has great significance for LC information displays. Chapters 6 to 10 will continue to establish structure-property relationships between LCs and dispersed nanoparticles and investigate in more detail the role of the nanoparticle capping agent. A new phenomenon will be introduced, namely the formation of birefringent stripe patterns and the induction of homeotropic alignment of the LC molecules in contact with surfaces known to induce planar alignment of the nematic LCs used.

Abstract: Mixtures of nematic liquid crystals (LCs) were produced by doping small quantities of gold nanoparticles coated with non-chiral hexane- (**Au1**), dodecane- (**Au2**) or chiral Naproxen-functionalized dodecane thiolates (**Au3**, **Au4**). Circular dichroism (CD) spectroscopy confirmed the optical activity for both Naproxen-functionalized gold nanoclusters. The small CD measured for **Au1** and **Au2** as well as the weak CD above 400 nm measured for **Au3** and **Au4** is attributed to scattering artifacts of dense particles aggregating in solution. For all mixtures, characterization of the nanoparticle doped nematic phase by polarized optical microscopy revealed the formation of uniform stripe textures or patterns separated by areas of homeotropic alignment due to a spatial separation of particle-rich and particle-poor domains. Similar characteristic textures were also observed for mixtures of the chiral nematic phase produced by doping either only the Naproxen-functionalized thiol **3b** or Naproxen and additionally dodecane thiolate-protected gold nanoparticles **Au2**. On the basis of these findings, observed for the first time for alkane thiolate-capped gold nanoclusters doped into nematic LCs, two different scenarios are suggested. In the first scenario, the optically active gold nanoparticles **Au3** and **Au4** transfer chirality to the non-chiral nematic LC host. In the second scenario, all functionalized gold nanoclusters **Au1–Au4** form topological defects resulting in chain-like particle aggregates, separated by areas of homeotropic alignment due to particles residing at the LC–glass interface.

5.1 Introduction

Nematic liquid crystals (N-LCs) are one-dimensionally ordered fluids commonly formed by rod-shaped molecules. Dispersed colloidal particles disrupt the nematic order, and minimization of the elastic energy leads to the formation of anisotropic colloidal structures [1].

Sufficiently large particles, depending on the strength and direction of the nematic anchoring on the particle surface, can form various types of topological defects such as Saturn rings, hyperbolic hedgehogs, and boojums in agreement with theoretical considerations [2-7]. Past experimental studies focused on dispersions of water microdroplets [1, 8 9], ferrofluids [10], gold coated glass spheres [11], or silicon oil [12-15] in nematic LCs as well as latex particles in lyotropic LCs [9, 16].

For most particles, if the nematic LC molecules are strongly and perpendicularly anchored at the surface of a spherical particle, the particles act like a radial hedgehog carrying a topological charge. Placed in a uniformly aligned nematic solvent to satisfy the boundary conditions at infinity, the particle should nucleate a further defect in its nematic environment. As theoretically predicted [17, 18], the dipole is the preferred configuration for large particles and sufficiently strong anchoring, although quadrupoles are also observed [11]. The topological dipole formed by one quasi-spherical particle and an accompanying topological defect, known as a hyperbolic hedgehog, generate elastic forces that lead to the formation of chain-like particle aggregates [19]. However, the interactions between colloidal particles and the nematic LC molecules strongly depend on the particular combination of the two materials, the molecular structure and elastic

properties of the LC, as well as on the type and likely the size and shape of the colloidal particle used.

The work reported here had two main objectives. First, we were interested how functionalized gold nanoclusters (chiral and non-chiral) in the size-regime of the N-LCs used interact with the nematic solvent, and if the expected topological defects can be used to organize the colloidal gold particles in one or more dimensions. Secondly, we were intrigued by the possibility of inducing a chiral nematic phase by doping small quantities of gold colloids coated with common chiral dopant structures such as (*S*)-Naproxen.

For the latter, it has been known for a long time that doping nematic phases with chiral, non-racemic compounds (chiral additives or dopants) transforms them into chiral nematic phases [20], characterized by a helical spatial arrangement of the director. Polarizing optical microscopy (POM) commonly provides direct evidence of the chirality induced by a chiral dopant in a non-chiral nematic LC. Characteristic textures and defect structures clearly reveal the difference between chiral and non-chiral nematic phases. Depending on the boundary conditions (planar, homeotropic), between crossed polarizers nematic LCs such as **LC1** usually produce so-called *schlieren* [Fig.5.1a], marble or thread-like textures, whereas the chiral nematic phase induced by doping 5 wt% of a chiral dopant such as (*S*)-Naproxen into **LC1** can display so-called oily-streak, fan-like, fingerprint [Fig. 5.1b] or cholesteric finger textures [21] (for a better comparison, most of the LC textures discussed in this paper are combined in Fig. 5.1).

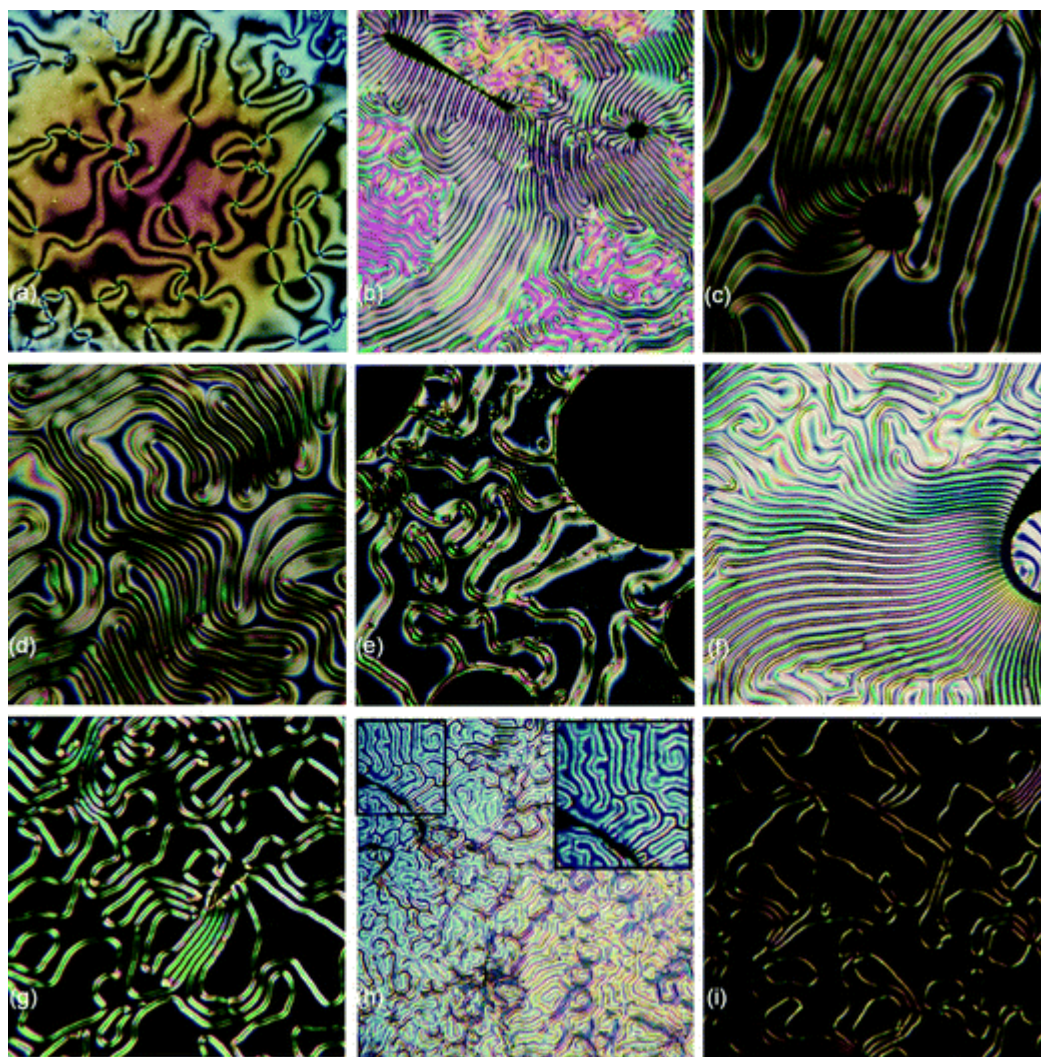


Fig. 5.1 POM micrographs (crossed polarizers) of the N phase taken on cooling from just below the Iso–N phase transition (T_{NI}): (a) *schlieren* texture of **LC1** (68 °C); (b) fingerprint texture of the N* phase of **LC1** doped with 5 wt% Naproxen (44 °C); (c) stripe texture of the N phase of 5 wt% **Au2** in **LC1** (64 °C); stripe texture and coexisting areas with homeotropic alignment: (d) 5 wt% **Au2** in **LC1** (61 °C); (e) **Au3** in **LC1** (51 °C, large circular areas are air-bubbles in the LC film); (f) fingerprint texture of the N* phase of **LC1** doped with 5 wt% of **3b** (54 °C); (g) cholesteric finger texture [21] of the N* phase of **LC1** doped with 5 wt% of **3b** (56 °C, different area); (h) finger-like texture of the N* phase of 5 wt% **Au2** in **LC1** doped with 5 wt% Naproxen (55 °C, inset: magnified area); (i) stripe pattern of the N phase of 5 wt% **Au2** in **LC1** in rubbed polyimide ITO glass cell (cell gap: 5 μm , no electric field applied).

With this in mind, we investigated mixtures consisting of pure N-LCs (**LC1–LC3**) doped with small quantities (≤ 5 wt%) of gold nanoclusters coated with a monolayer of

alkyl thiolates functionalized with (*S*)-Naproxen as a chiral dopant moiety ('true' monolayer **Au3**, mixed monolayer **Au4**; see Fig. 5.2), and, for comparison, with gold clusters capped with non-chiral, straight alkyl thiolates (hexane thiolate-capped **Au1**, dodecane thiolate-capped **Au2**, see Fig. 5.2).

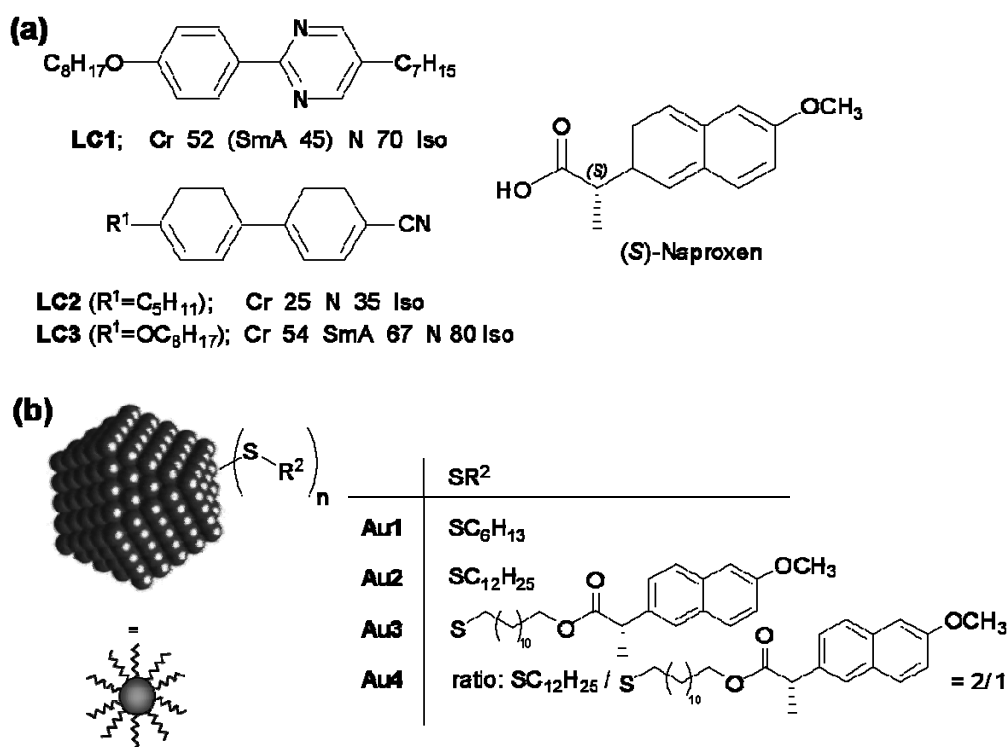


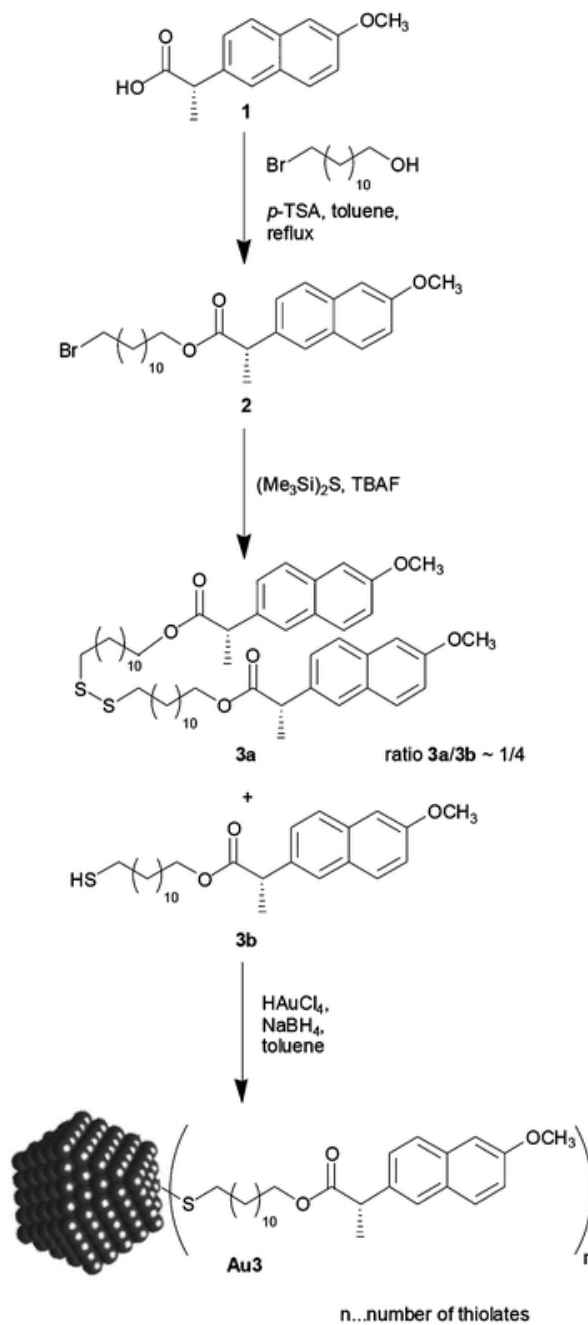
Fig. 5.2 (a) Structures and phase transition temperatures ($^{\circ}C$) of **LC1–LC3**. Cr = crystalline solid, SmA = smectic-A phase, N = nematic phase, and Iso = isotropic liquid phase. (b) General (truncated) cuboctahedral shape of the gold colloids, and structures of thiolate capping agents.

5.2 Experimental

5.2.1 General methods

HAuCl₄·3H₂O (99.999%), (*S*)-Naproxen, *p*-toluenesulfonic acid, NaBH₄, hexamethyldisilathiane (Me₃Si)₂S, hexan-1-thiol, dodecan-1-thiol, tetraoctylammonium bromide, 12-bromododecan-1-ol, and tetrabutylammonium fluoride (TBAF, 1.0M in THF) were purchased from Aldrich and used as received. All solvents used for the synthesis of **3b** and the gold nanoclusters were Aldrich Purification grade purified *via* a PureSolv solvent purification system (Innovative Technology Inc.). X-Ray diffraction (XRD) patterns were obtained on an MPD X'Pert system (PANalytical) using CuK_α radiation (40 kV, 200 mA). **Au1**, **Au3** and **Au4** were measured in reflection geometry using a zero-background flat sample holder, **Au2** using a 0.3 mm glass capillary in transmission geometry. UV-vis spectra were obtained using an Agilent 8453 spectrophotometer. ¹H and ¹³C NMR spectra were recorded with a Bruker Avance 300 spectrometer. Transmission electron microscopy (TEM) images were obtained on a JEOL FX 2000 TEM instrument operating at an accelerating voltage of 160 kV. A 3 μL drop of the isolated gold colloid solutions was drop cast on carbon coated copper grids (400 mesh) and dried for 2 h. Circular dichroism (CD) spectra were recorded on a J-810 spectropolarimeter (Jasco Inc.) using a bandwidth of 2 nm (accumulation of three spectra, circular quartz cuvettes with 1 cm path length). Solvents for CD spectroscopy were CHCl₃ Spectroanalyzed[®] and THF Optima[®] (HPLC, Spectrophotometry grade) from Fisher Scientific. POM was performed using an Olympus BX51-P polarizing microscope in conjunction with a Linkam LS350 heating/cooling stage.

The Naproxen-functionalized thiol **3b** was synthesized in two steps by an esterification with 12-bromododecanol, followed by treatment with hexamethyldisilathiane to produce a mixture of disulfide **3a** and thiol **3b** in a ratio of approximately 1/4 according to a procedure reported by Hu and Fox (see Scheme 1 and SI for details) [22]. Although the disulfide **3a** could have been used for the gold nanoparticle synthesis as well, column chromatography was used to separate the thiol **3b** before the synthesis of **Au3**.



Scheme 1. Synthesis of thiol **3b** and corresponding gold nanoclusters **Au3**. Assuming full coverage, the number of thiolates coating the gold cluster (n) scales with the size of the individual gold particle and varies within the sample depending on the size distribution.

5.2.2 Synthesis of Au nanoclusters (Au1–Au4)

All glassware used for the preparation and storage of colloidal gold was treated with *aqua regia*, cleaned with piranha solution, and rinsed with DI water (Millipore, resistivity 18.2 M Ω) and dried overnight at 100 °C. **Au1** nanoparticles were synthesized according to a method reported by Shon and coworkers [23]. **Au2** and **Au3** were prepared according to the Brust–Schiffrin procedure [24]. All nanoparticle samples were characterized by ^1H NMR, UV-vis, TEM (see Fig. 5.3) and XRD. The **Au4** clusters are mixed monolayer protected gold nanoparticles as shown in Fig. 5.2. Note that only the Naproxen-functionalized clusters are decorated with thiolate groups having asymmetric carbon atoms. The average sizes of the gold colloids as determined by TEM and XRD are summarized in Table 5.1.

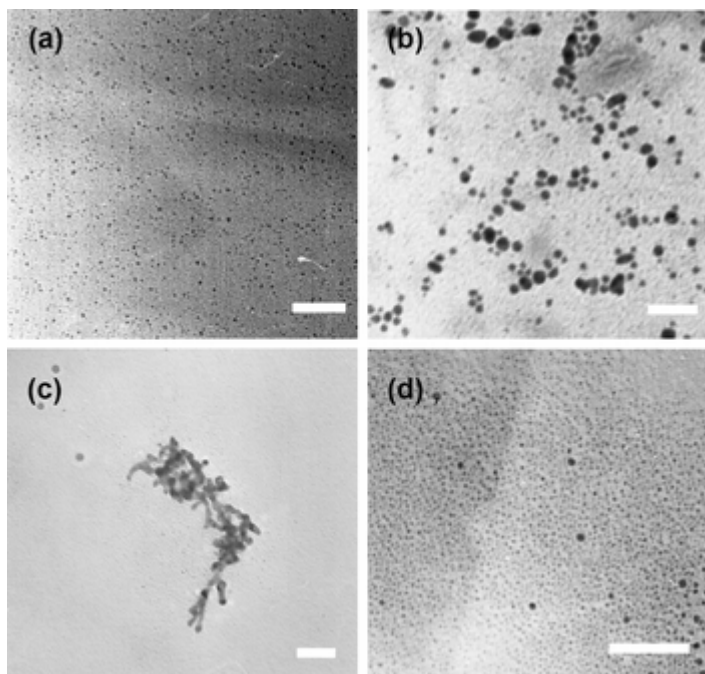


Fig. 5.3 TEM micrographs of the gold nanoclusters: (a) **Au1**, (b) **Au2**, (c) **Au3**, and (d) **Au4** (micrograph scale bars = 50 nm).

Table 5.1 Average particle size (nm) of the gold nanoparticles **Au1–Au4**^a

Cluster	Particle size/nm	
	TEM ^b	XRD ^c
Au1	2.1 ± 0.6	1.3
Au2	7.4 ± 2.3	5.9
Au3	3.5 ± 0.8	6.2
Au4	1.4 ± 0.3	— ^d

^a For exact size distribution see ESI. ^b TEM image analysis of more than 1000 particles (Software: Scion Image Beta 4 and Image J). ^c Calculated from the powder XRD pattern using the Scherrer equation. ^d Due to the small cluster size, the completely overlapping Au(111) and Au(200) diffraction peaks could not be separated, preventing measurement of the FWHM of these diffraction peaks.

Briefly, for **Au3**, 12-sulfanyldodecyl (2*S*)-2-(6-methoxy-2-naphthyl) propanoate **3** (1.16 mmol, 0.5 g) and HAuCl₄·3H₂O (0.58 mmol, 0.2 g) were dissolved in freshly distilled, dry THF (20 ml). The resulting solution was stirred for 10 min, after which a freshly prepared solution of NaBH₄ (0.22 g) in DI water (10 ml) was added at once. The mixture was stirred for an additional 2 h. The solvent was evaporated under reduced pressure, and the black precipitate was collected and exhaustively washed with DI water and hexane. The purity of the nanoparticles (removal of unreacted thiol) was checked by ¹H NMR.

Au4 was prepared by using a mixture of thiols **2** and **3** in a ratio of 1:1. The resulting gold nanoparticles (**Au4**) are capped with both thiols in a ratio of approximately 2:1 as determined by ¹H NMR (ratio determined by integration over characteristic CH₃-peak of dodecanethiol and OCH₃-peak of the Naproxen-functionalized thiol **3b**).

5.2.3 LC–nanoparticle mixtures

All glass vials and Teflon-coated spatulas were rinsed with *aqua regia* prior to all mixture preparations. Mixtures of **LC1** doped with **Au1–Au4** were then prepared by mixing solutions of both components in a common, pure, and dry solvent (*e.g.*, ethyl acetate). The resulting solutions were sonicated or stirred (agitated) for at least 3 min, and the solvent was evaporated by a steady stream of dry N₂ over the open glass vials. Thereafter, all mixtures were dried under vacuum for 24 h. prior to the preparation of the thin films sandwiched between non-treated microscope glass slides, unless otherwise noted, all mixtures were heated just below the isotropic–nematic phase transition (T_{NI}) and continuously mixed (stirred or occasionally mildly sonicated).

In this context some comments on gold nanocluster stability should be made. Recent studies on the stability of thiolate-protected gold nanoparticles showed that thiols with a carbon chain longer than C6 begin to desorb from the gold nanoparticle surface above a threshold of 160 °C [25]. Therefore, we assume that during all mixing experiments no changes in the nanoparticle composition (surface) *via* desorption of thiolate takes place. To verify this assumption, we performed test experiments by heating the nanoparticle samples in toluene to 70 °C overnight (temperature of the LC phase transitions) followed by evaporation of the solvent under reduced pressure. ¹H NMR spectra before and after heating in toluene were identical with broadened signals indicating no dissociated thiol.

5.3 Results and discussion

5.3.1 Optical activity and circular dichroism

To obtain additional information on the optical activity of the gold nanoclusters, CD spectra of each particle sample were measured in solution over a range extending from 240 to 600 nm (Fig. 5.4 and SI).

At this point, a short discussion of gold nanoparticle chirality, and observations of chiral gold nanoparticles by CD in the literature seems relevant. Circular dichroism is observed when optically active matter absorbs left and right handed circularly polarized light with a different extinction coefficient. Recent theoretical studies on the structural properties of gold nanoclusters have shown that the most stable (lowest energy) isomers of bare Au₂₈, Au₅₅ as well as thiol-protected clusters (*e.g.*, Au₂₈(SCH₃)₁₆) correspond to chiral nanostructures [26]. These findings provided theoretical support for the existence of chirality in noble metal clusters suggested by the intense optical activity measured in the metal-based electronic transitions of size-separated glutathione-protected gold particles in the size range of 20 to 40 atoms [27]. Further theoretical work, based on quantifying chirality *via* the Hausdorff chirality measure [26, 28], predicts that strong structural distortions in a gold cluster upon thiol protection could induce chirality in an achiral unprotected cluster [26].

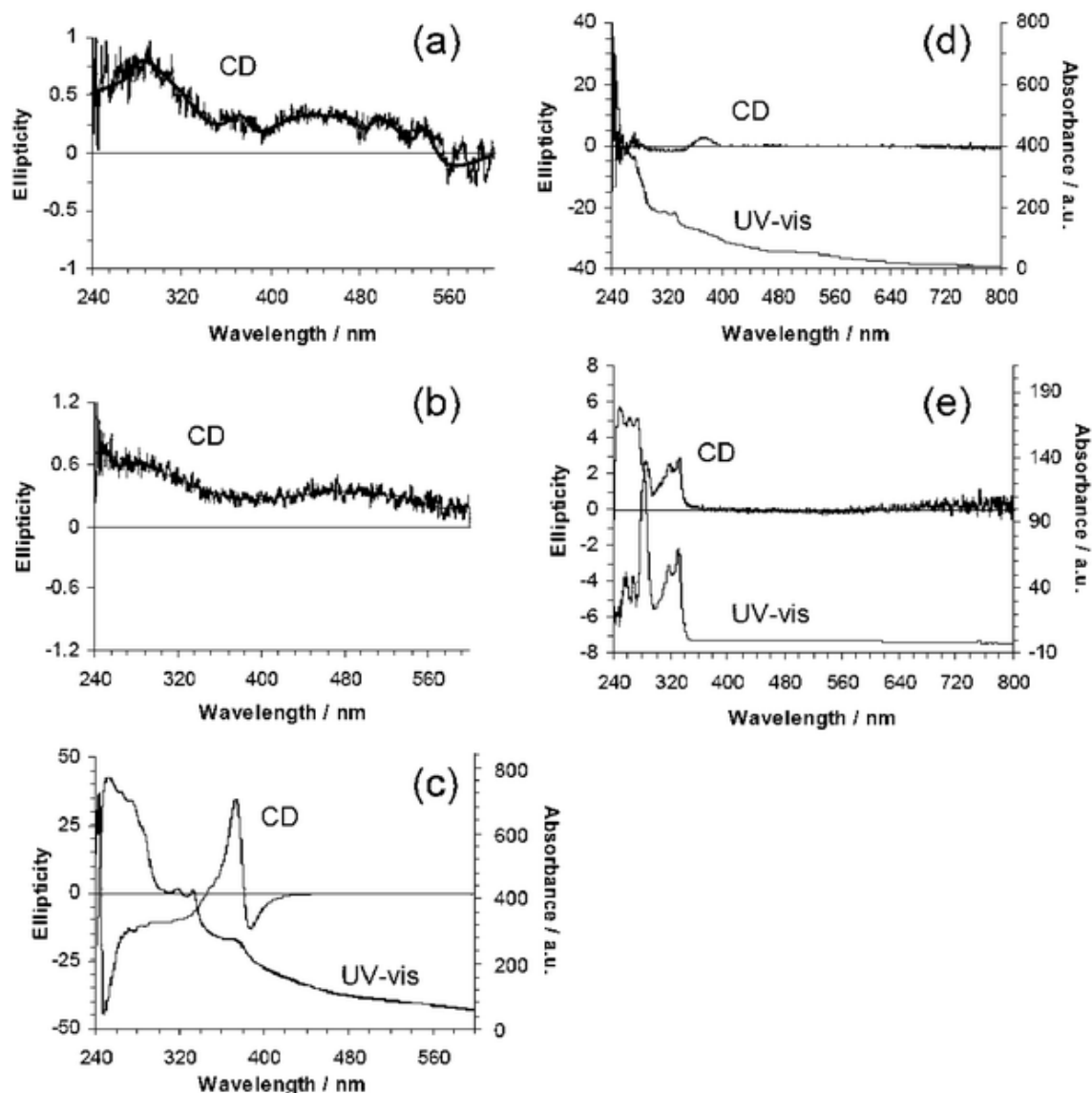


Fig. 5.4 CD spectra of (a) Au1, and (b) Au2. CD and UV-vis spectra of: (c) Au3, (d) Au4, and (e) 3b. (For more detailed images and concentrations see SI.)

In addition to the work of Whetten and Schaaf on glutathione-capped gold nanoparticles [27], the groups of Fujihara and Yao both reported on the syntheses of optically active nanoclusters protected with chiral (*R*)- and (*S*)-BINAP [29] or penicillamines [30] (D-Pen, L-Pen, and racemate). It is important to note that all three groups used enantiomeric species as the capping agent for the synthesis of their gold nanoparticles resulting in enantiopure particles with an optical activity that was identified

by circular dichroism (CD) spectroscopy. However, the complexity of the CD spectra in the UV regions as well as CD signals at wavelengths where the used protecting agent does not absorb could not be explained by the chirality of the capping agent itself. Hence, the structured CD spectra are likely to arise from quantized electronic transitions and their interactions in the cluster, which indicate, as theory predicts [26], that nanoparticles can indeed form well-defined stereostructures as 'normal' chiral molecules do.

The CD spectra of hexane thiolate and dodecane thiolate-protected gold clusters show very weak and diffuse signals with uncharacteristic features centered at 285 and 475 nm [Fig. 5.4(a,b)]. The scattering observed for the ellipticity of the alkane thiolate clusters (**Au1**, **Au2**) is likely due to the size distribution of the present nanoparticles as observed by TEM and XRD [31]. In contrast, the natural CD spectra of both Naproxen functionalized gold nanoparticles (**Au3**, **Au4**) show well-defined Cotton effects centered around 340 and 380 nm, where the Naproxen-functionalized thiol **3b** does not exhibit an absorption maximum [Fig. 5.4(c–e) and SI]. Hence, only the **Au3** and **Au4** nanoparticles appear to be optically active as indicated by the non-zero CD signals.

As summarized by Beratan *et al.* [32], there are currently three proposed mechanisms for chiroptic signatures of chiral monolayer protected gold clusters assuming: (i) a chiral core due to thiolate-passivated lattice distortions [26], (ii) an achiral core with chirality induced by a chiral adsorption pattern, or (iii) an achiral adsorption pattern of chiral adsorbates [32]. For a given cluster ensemble with achiral adsorbates such as **Au1** and **Au2**, and given that one or both of the first two mechanisms is valid, the net influence should average to zero resulting in racemic mixtures for both **Au1** and **Au2**. Hence, a plausible explanation for the observed weak CD (concentration dependent $\Delta\epsilon_{\max}$, see SI)

are scattering artifacts (or circular differential scattering of anisometric particle aggregates) [33] of the **Au1** and **Au2** gold clusters aggregating in solution. The same effect likely also responsible for the large CD ($\Delta\epsilon_{\max}$) values below 400 nm observed for **Au3** and the weak CD above 400 nm observed for both **Au3** and **Au4** [33c]. In addition, the largest contribution to the CD at 380 nm for **Au3** corresponds to an absorption maximum in the UV-vis spectrum that is due to intermolecular interactions of the Naproxen cores within one and the same cluster as well as between Naproxen units of neighboring clusters forming particle aggregates in solution. Lower $\Delta\epsilon_{\max}$ values measured at around 380 nm for the mixed monolayer **Au4** clusters confirmed this assumption (see SI for all detailed CD spectra) [34]. Hence, only the **Au3** and **Au4** nanoclusters should be considered chiral. The CD measurements confirmed that chirality is only located at the chiral center of the surrounding Naproxen moieties and not, in contrast to previous reports on chiral gold clusters [27, 29, 30], in the particle core.

5.3.2 Mixtures with nematic LCs

To probe the propensity of the Naproxen-functionalized gold clusters to induce chiral nematic phases upon dispersion in the non-chiral nematic LC hosts, we initially prepared mixtures of 5 wt% **Au3** and **Au4** in **LC1**, and investigated phase transition temperatures and texture formation for thin films sandwiched between untreated (no alignment layers or coatings), cleaned microscopy glass slides by polarized optical microscopy. For comparison, we also prepared mixtures of 5 wt% of pure Naproxen, thiol **3b**, gold colloids **Au1** and **Au2** in **LC1**. In addition, to study eventual effects of the LC host structure, we also investigated mixtures of all four nanoclusters in **LC2** and **LC3**.

Between untreated glass slides, on cooling from just below the nematic to isotropic phase transition (T_{NI}), **LC1** doped with 5 wt% of each of the nanoclusters, **Au1–Au4**, in each case shows reproducible formation of stripe textures consisting of coloured, birefringent stripes separated by dark domains [see Fig. 5.1(c–e) for **Au2** and **Au3**; for **Au1** and **Au4** in **LC1** see SI]. The streaks or line domains appear at the transition from the isotropic liquid phase to the nematic phase, right after the initially formed nematic droplets merge to form the thin nematic film, and do not disappear in the N phase over time or with decreasing temperature. However, these stripes disappear upon further cooling at the transition to the low-temperature SmA phase of **LC1**, but reappear upon heating to the N phase.

At first glance, these textures closely resemble textures commonly observed for chiral nematic liquid crystals with long helical pitch, so-called cholesteric finger textures. For example, **LC1** doped with 5 wt% of the Naproxen-thiol **3b** shows two characteristic textures depending on the area of the sample viewed between crossed polarizers. Some areas show typical fingerprint textures [Fig. 5.1(f)], whereas other areas show cholesteric finger textures [Fig. 5.1(g)]. No change in the appearance of these textures is observed by rotating the samples between crossed polarizers. The stripe domains display no obvious change in birefringence, and the dark domains remain dark indicating homeotropic alignment of the nematic LC molecules within these domains. For lower concentrations of nanoclusters two important changes were observed: (i) the number of stripes is reduced with decreasing particle content, and (ii) areas showing homeotropic alignment for higher concentrations of clusters now display *schlieren* textures [see Fig. 5.5(a) for a mixture of 1 wt% **Au2** in **LC1**].

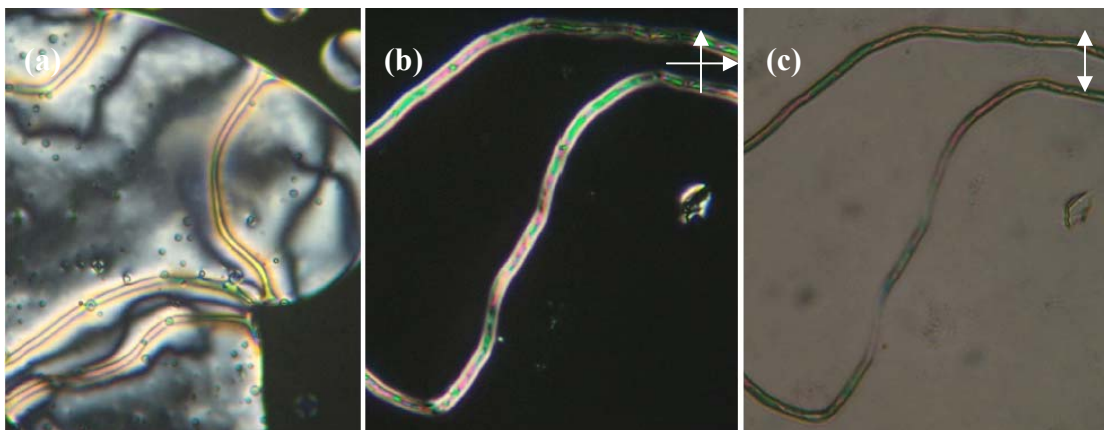


Fig. 5.5 POM micrographs of the N-phase taken on cooling from just below the Iso–N phase transition (T_{NI}). (a) Coexisting stripe domains and fingerprint texture of 1 wt% **Au2** in **LC1** (68 °C). 5 wt% **Au3** in **LC1** at 44 °C (b) crossed polarizers, and (c) parallel polarizers.

On the contrary, higher concentrations of all gold clusters in **LC1** as well as **LC2** and **LC3** (commonly above *ca.* 10 wt%) could not be prepared without significant amounts of the gold clusters precipitating out of the nematic solvent.

It is also interesting to note that the stripe domains remain coloured (birefringent) with un-crossed (parallel) polarizers [see Fig. 5.5(b,c)]

The same textures were also observed for mixtures of **Au1–Au4** in **LC2** and **LC3**. As a general observation for all nanoparticle–LC mixtures, the cooling rate plays a significant role in the formation of the observed stripe textures.

Faster cooling rates ($>1 \text{ } ^\circ\text{C min}^{-1}$) commonly result in stripe textures with some areas between the stripes displaying *schlieren* textures [similar to Fig. 5.5(a)], which disappear upon further cooling into the nematic phase and are replaced by the previously described homeotropic domains commonly about 5 °C below the Iso–N phase transition.

On the other hand, slower cooling rates ($<1\text{ }^{\circ}\text{C min}^{-1}$) eventually result in textures showing exclusively stripe domains and no homeotropic domains or areas with *schlieren* texture (see Fig. 5.6).

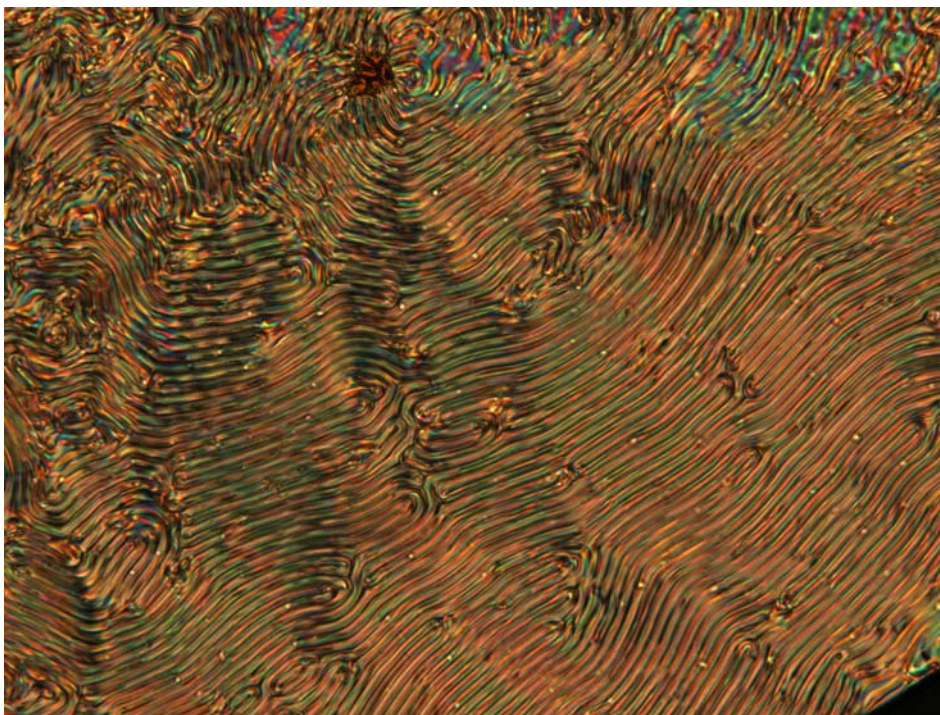


Fig. 5.6 POM micrographs (crossed polarizers) of the N phase of 5 wt% **Au1** in **LC1** taken on cooling from just below the Iso–N phase transition (cooling rate $< 1\text{ }^{\circ}\text{C min}^{-1}$).

However, a mixture of **LC1** initially doped with 5 wt% (*S*)- Naproxen to produce a chiral nematic phase and then doped with 5 wt% **Au2** [Fig. 5.1(h)] displayed a texture similar to typical fingerprint textures commonly observed for chiral N-LCs. However, a closer look at magnified areas of these textures [*e.g.*, inset in Fig. 5.1(h)] actually reveals quite a similarity to the stripe domain textures observed for mixtures of **LC1** with the gold nanoclusters or of **LC1** doped with **3b**. Assuming a fingerprint texture for both the ternary mixture **LC1**–(*S*)-Naproxen–**Au2** and **LC1** doped only with 5 wt% Naproxen, a major difference is the temperature-dependent change in helical pitch. The helical pitch of **LC1** doped with 5 wt% (*S*)-Naproxen is $4.9\text{ }\mu\text{m}$ at $44\text{ }^{\circ}\text{C}$, and for the ternary mixture

8.9 μm at 42 $^{\circ}\text{C}$ (measured as twice the distance between dark fringes [35]). A similar observation was recently reported by Mitov *et al.* for platinum nanoparticles suspended in a chiral nematic polysiloxane LC oligomer [36]. Surprisingly, at higher temperatures the helical pitch of the ternary mixture decreases significantly to 3.4 μm at 54 $^{\circ}\text{C}$ as compared to 4.2 μm for the **LC1**–5 wt% (*S*)-Naproxen mixture at the same temperature.

To further investigate the observed texture phenomena, we also looked at the nanoparticle–LC mixtures in rubbed polyimide ITO (indium tin oxide) glass cells favoring parallel alignment of nematic LCs. Surprisingly, the same textures were observed under these surface (alignment) conditions [see for example Fig. 5.1(i)]. Despite the polyimide alignment layers, the dark domains remain dark upon sample rotation between crossed polarizers indicating a homeotropic alignment of the N-LC molecules in these domains.

To explain the observed texture formation we consider two possible scenarios. In the first scenario, the optically active gold nanoparticles **Au3** and **Au4** would act as chiral dopants and transfer their chirality to the non-chiral LC. Here, it is important to note that the thiolate ligands do not dissociate from the gold core at temperatures of the LC phase transitions as discussed earlier.

To assess the validity of this scenario we attempted to measure the helical pitch also for the **Au3** and **Au4** mixtures, which did not display fingerprint textures. In principle, there are two well-established techniques to measure the helical pitch in chiral nematic phases, the Grandjean–Cano technique [37, 38] and the Cano wedge method [39]. Both techniques require a uniform alignment of the chiral nematic phase on (Grandjean–Cano) or between (Cano wedge) glasses slides coated with alignment layers (*e.g.*, rubbed

polyimide or nylon). As can be seen, for example, in Fig. 5.1(i), we were unable to produce uniform aligned samples of the gold nanoparticle (**Au3**, **Au4**)–**LC1** mixtures. Even driving the cell with an electric field does not change the initially formed stripe texture [40].

In the second scenario, coating the gold clusters **Au1**–**Au4** with either aliphatic (**Au1**, **Au2**) and/or aromatic thiolates (**Au3**, **Au4**) promotes homeotropic anchoring of the nematic LC molecules to the particle surface (splay-like deformation). As a result, the particles form a topological defect or dipole. These topological dipoles formed by the gold colloids and the accompanying topological defect (hyperbolic hedgehog) generate elastic forces in the N-LC that lead to the formation of chain-like particle aggregates, as described by Žumer and coworkers [19]. These aggregates are then responsible for the birefringent stripe domains visible in the textures (see Fig. 5.7). We consider these domains particle-rich, since lower concentrations of particles for all LC–nanoparticle combinations produce a lower area density of birefringent stripes. The homeotropic domains are then particle-poor with particles residing at either one or both of the glass–N-LC interfaces (top and/or bottom). This arrangement of randomly dispersed functionalized gold nanoclusters appears as the only possible explanation for the homeotropic domains observed for both untreated glass slides as well as cells coated with polyimide alignment layers (see Fig. 5.8, proposed model) [41, 42]. This would also explain the occurrence of common *schlieren* textures for mixtures with lower particle concentration. This separation into particle-rich and particle-poor domains could initially be driven by a drag of gold clusters along the Iso–N interface during the formation of the nematic droplets at the phase transition as discussed by West and coworkers [43]. If,

however, **Au3** and **Au4** would act, locally, as chiral dopants introducing a chiral twist, a combination of both scenarios, a chirality transfer from the Naproxen-thiols coating the gold nanoclusters to the nematic LC phase and the formation of chain-like particle aggregates (topological defect networks) should be considered to explain the observed texture phenomena for **Au3** and **Au4** in **LC1**.

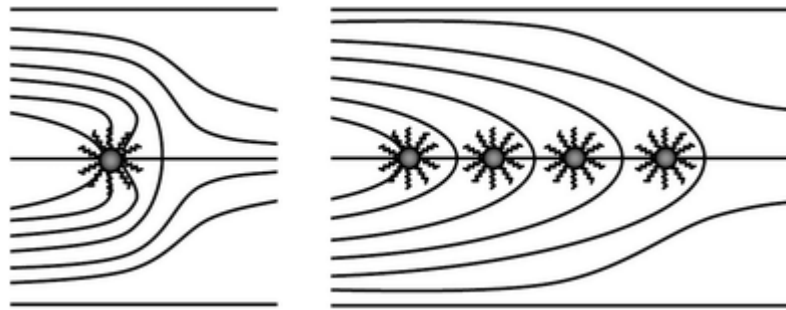


Fig. 5.7 (a) Formation of a hyperbolic hedgehog produced by a particle with homeotropic anchoring conditions; (b) schematic representation of a chain-like particle aggregate formed by interaction of topological dipoles (adapted from ref. 8).

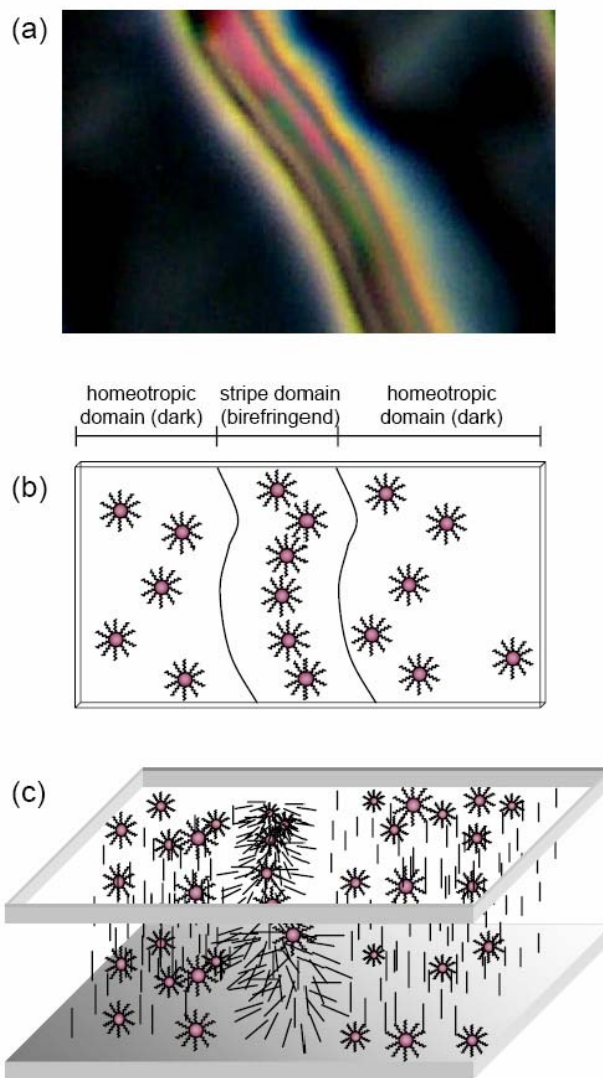


Fig. 5.8 Simplified model for the organization of the gold nanoparticles in the N-LCs (not to scale). (a) Isolated stripe domain (center) between two homeotropically aligned domains (left and right); (b) top view indicating particle-rich (stripe domain) and particle-poor areas (homeotropic domains)—LC molecules are omitted for clarity; and (c) 3D model with gold nanoclusters residing at both glass–N-LC interfaces in the homeotropic domains.

5.4 Conclusions

In summary, gold nanoparticles capped with alkyl thiolates and/or alkyl thiolates functionalized with (*S*)-Naproxen as a chiral dopant moiety were prepared, and mixtures of these particles with N-LCs were investigated by polarized optical microscopy.

All gold nanoparticle–LC mixtures show strikingly similar textural characteristics between untreated glass slides as well as in cells coated with polyimide alignment layers. On cooling from the isotropic liquid phase, patterns of birefringent stripes occur separated by areas of homeotropic alignment despite surfaces commonly promoting parallel alignment of N-LC molecules. While the specific combination of the gold nanoclusters and the used N-LCs produces significant changes in the topological (defects, dipoles, and chain-like particle aggregates) and rheological properties (qualitatively increased viscosity), other properties such as phase transition temperatures and phase stability are only mildly affected. For example, the Iso–N phase transition temperatures of **LC1–LC3** decrease only slightly (1–2 °C), and the phase transitions remain sharp [44]. Although the contribution of the chiral Naproxen moieties remains somewhat unclear, the specific interactions between the N-LCs and the gold colloids, the formation of topological defects, homeotropic anchoring of the LC molecules to the colloid surface, and the elastic properties of the N-LC all play integral roles in the spontaneous assembly of the gold nanoparticles into chain-like aggregates similar to other quasi-spherical particles [11, 19].

Future work including experiments with different (chiral) adsorbates as well as size-separated gold clusters will focus on determining the contributions and local effects of chiral moieties on the formation of the observed stripe texture. These and other experiments will also help clarifying if the unique size-dependent electronic properties of the gold nanoparticles or nanoparticle aggregates are responsible for the large size discrepancy between the width of the birefringent stripe domains (~2–5 μm depending on the type of nanoparticle used) and the nanoparticle size (1–7 nm).

Ultimately, the combination of nanoscale particles and liquid crystals as presented here will lead to the discovery of new or improved LC mixtures with tunable properties for a variety of applications in the information display sector, or find use as waveguides or bandgap materials if periodic domains can be produced over large enough areas.

Acknowledgements

This work was supported by NSERC and the University of Manitoba. We thank M. C. Chaturvedi and J. van Dorp for assistance with the TEM imaging, M. Bieringer and J. O'Neil for providing XRD and access to CD measurements.

References and notes

- 1 P. Poulin, H. Stark, T. C. Lubensky, D. A. Weitz, *Science* **1997**, *275*, 1770-1773.
- 2 O. V. Kuskenok, R. W. Ruhwandl, S. V. Shiyankovskii, E. M. Terentjev, *Phys. Rev. E* **1996**, *54*, 5198-5203.
- 3 R.W. Ruhwandl, E. M. Terentjev, *Phys. Rev. E* **1997**, *56*, 5561-5565.
- 4 T. C. Lubensky, D. Petey, N. Currier, H. Stark, *Phys. Rev. E* **1998**, *57*, 610-625.
- 5 H. Stark, *Eur. Phys. J. B* **1999**, *10*, 311-321.
- 6 H. Stark, J. Stelzer, R. Bernhard, *Eur. Phys. J. B* **1999**, *10*, 515-523.
- 7 D. Andrienko, G. Germano, M. P. Allen, *Phys. Rev. E* **2001**, *63*, 041701.
- 8 P. Poulin, D. A. Weitz, *Phys. Rev. E* **1998**, *57*, 626-637.
- 9 O. Mondain-Monval, J. C. Dedieu, T. Gulik-Krzywicki, P. Poulin, *Eur. Phys. J. B* **1999**, *12*, 167-170.

- 10 P. Poulin, V. Cabuil, D. A. Weitz, *Phys. Rev. Lett.* **1997**, *79*, 4862-4865.
- 11 Y. D. Gu, N. L. Abbott, *Phys. Rev. Lett.* **2000**, *85*, 4719-4722.
- 12 J.-C. Loudet, P. Barois, P. Poulin, *Nature* **2000**, *407*, 611-613.
- 13 J.-C. Loudet, P. Poulin, P. Barois, *Europhys. Lett.* **2001**, *54*, 175-181.
- 14 J.-C. Loudet, P. Poulin, *Phys. Rev. Lett.* **2001**, *87*, 165503.
- 15 J.-C. Loudet, O. Mondain-Monval, P. Poulin, *Eur. Phys. J. E* **2002**, *7*, 205-208.
- 16 P. Poulin, N. France`s, O. Mondain-Monval, *Phys. Rev. E* **1999**, *59*, 4384-4387.
- 17 (a) J. Fukuda, H. Yokoyama, M. Yoneya, H. Stark, *Mol. Cryst. Liq. Cryst.* **2005**, *435*, 723-734; (b) H. Stark, *Phys. Rev. E*, **2002**, *66*, 032701.
- 18 J. J. Feng, C. Zhou, *J. Colloid Interface Sci.* **2004**, *269*, 72-78.
- 19 (a) M. Svetec, S. Kralj, Z. Bradac, S. Žumer, *Eur. Phys. J. E* **2006**, *20*, 71-79; (b) P. Kossyrev, M. Ravnik, S. Žumer, *Phys. Rev. Lett.* **2006**, *96*, 048301.
- 20 For an overview see: *Chirality in Liquid Crystals* (Partially Ordered Systems), ed. H.-S. Kitzerov and C. Bahr, Springer, Heidelberg, **2001**.
- 21 I. Dierking, *Textures of Liquid Crystals*, Wiley-VCH, Weinheim, **2003**.
- 22 J. Hu, M. A. Fox, *J. Org. Chem.* **1999**, *64*, 4959-4961.
- 23 H. Choo, E. Cutler, Y. S. Shon, *Langmuir* **2003**, *19*, 8555-8559.
- 24 (a) M. Brust, M. Walker, D. Bethell, D. J. Schiffrin, R. Whyman, *Chem. Commun.* **1994**, 801-802; (b) M. Brust, J. Fink, D. Bethell, D. J. Schiffrin, C. Kiely, *Chem. Commun.* **1995**, 1655-1656.
- 25 M. Büttner, T. Belser, P. Oelhafen, *J. Phys. Chem. B* **2005**, *109*, 5464-5467.
- 26 (a) I. L. Garzón, J. A. Reyes-Nava, J. I. Rodríguez-Hernández, I. Sigal, M. R. Beltrán, K. Michaelian, *Phys. Rev. B: Condens. Matter Mater. Phys.* **2002**, *66*,

- 073403; (b) I. L. Garzón, M. R. Beltrán, G. González, I. Gutierrez-González, K. Michaelian, J. A. Reyes-Nava, J. I. Rodríguez-Hernández, *Eur. Phys. J. D* **2003**, *24*, 105-109; (c) C. E. Román-Velázquez, C. Noguez, I. L. Garzón, *J. Phys. Chem. B* **2003**, *107*, 12035-12038.
- 27 G. T. Schaaf, R. L. Whetten, *J. Phys. Chem. B* **2000**, *104*, 2630-2641.
- 28 (a) A. B. Buda, K. Mislow, *J. Am. Chem. Soc.* **1992**, *114*, 6006-6012; (b) L. Coffey, J. Drapala, T. Erber, *J. Phys. A: Math. Gen.* **1999**, *32*, 2263-2284.
- 29 M. Tamura, H. Fujihara, *J. Am. Chem. Soc.* **2003**, *125*, 15742-15743.
- 30 H. Yao, K. Miki, N. Nishida, A. Sasaki, K. Kimura, *J. Am. Chem. Soc.* **2005**, *127*, 15536-15543.
- 31 In contrast to the work of Whetten and Schaaf [27] and Kimura *et al.*[30], **Au1–Au4** are not monodisperse. Therefore, the CD measured represents the average over all particle sizes in the sample. The weak CD, attributed to artifacts, measured for **Au1** and **Au2**, however, are reproducibly positive for different preparations (prepared on different days with the same set of starting materials). For example, the CD spectra of **Au1** and the CD spectra of the concentration dependence were measured for different preparations of **Au1** (see Fig. S2 and S3 in SI). We are currently trying to determine the nature of these artifacts, and the contributions from multiple scattering of particle aggregates in solutions.
- 32 M.-R. Goldsmith, C. B. George, G. Zuber, R. Naaman, D. H. Waleck, P. Wipf, D. N. Beratan, *Phys. Chem. Chem. Phys.* **2006**, *8*, 63-67.
- 33 (a) C. Bustamante, D. Keller and M. Kim, Theory of absorption and circular dichroism of large inhomogeneous molecular aggregates, in *Polarized spectroscopy*

- of ordered systems*, ed. B. Samori and E. W. Thulstrup, Nato ASI Series C: Mathematical and Physical Sciences, **1987**, 242, pp. 357–380; (b) M. F. Maestre, The effect of anisotropic properties of randomly oriented particles on polarized light: An operational calculus for spatially heterogeneous distributions, in *Polarized spectroscopy of ordered systems*, ed. B. Samori and E. W. Thulstrup, Nato ASI Series C: Mathematical and Physical Sciences, **1987**, 242, pp. 381–390; (c) C. Bustamante, I. Tinoco, Jr., M. F. Maestre, *Proc. Natl. Acad. Sci. U. S. A.* **1983**, *80*, 3568-3572.
- 34 These interactions would also facilitate aggregation of particles in solution. Contributions from circular differential scattering due to the formation of cluster aggregates were not discussed in previous experimental reports 27, 29, 30 on chiral gold nanoparticles.
- 35 For an example, see: E. Grelet, S. Fraden, *Phys. Rev. Lett.* **2003**, *90*, 198302.
- 36 (a) M. Mitov, C. Portet, C. Bourgerette, E. Snoeck, M. Verelst, *Nat. Mater.* **2002**, *1*, 229-231; (b) M. Mitov, C. Bourgerette, F. De Guerville, *J. Phys.: Condens. Matter* **2004**, *16*, S1981.
- 37 (a) F. Grandjean, *C.R. Hebd. Seances Acad. Sci.* **1921**, *172*, 71-74; (b) R. Cano, *Bull. Soc. Fr. Mineral.* **1968**, *91*, 20-27.
- 38 G. Heppke, F. Oestreicher, *Mol. Cryst. Liq. Cryst.* **1977**, *41*, 245-249.
- 39 (a) G. Gottarelli, B. Samori, C. Stremmenos, G. Torre, *Tetrahedron.* **1981**, *37*, 395-399; (b) For an illustration of the Cano wedge method see: K. Akagi, S. Guo, T. Mori, M. Goh, G. Piao, M. Kyotani, *J. Am. Chem. Soc.*, **2005**, *127*, 14647-14654.
- 40 Further electro-optical investigations will be reported in due course.

- 41 Alkylthiols used in self-assembled monolayers (SAMs) are known to promote homeotropic anchoring of N-LCs such as 5CB (here LC2): R. A. Drawhorn, N. L. Abbott, *J. Phys. Chem.* **1995**, *99*, 16511-16515.
- 42 The sharp boundaries between birefringent and homeotropic areas appear similar to textures shown for patterned surfaces reported by Clark and Lee—a result of chiral symmetry breaking at the interface between parallel and homeotropically aligned domains in the absence of a chiral phase. See: B.-W. Lee, N. A. Clark, *Science* **2001**, *291*, 2576-2580.
- 43 J. L. West, K. Zhang, A. Glushchenko, D. Andrienko, M. Tasinkevych, Y. Reznikov, *Eur. Phys. J. E* **2006**, *20*, 237-242.
- 44 A recent report by West *et al.* reported a dramatic increase in the N–Iso phase transition temperature by up to 40 °C for some LCs doped with BaTiO₃ nanoparticles: J. L. West, F. Li, Y. Reznikov, O. Buchnev, C. I. Cheon, A. Glushchenko, V. Y. Reshetnyak, T. J. Sluckin, Book of Abstracts, *21st International Liquid Crystal Conference*, Keystone, Colorado, USA, 2006, p. 193.

Appendix B

Supplementary Information for Chapter 5

Synthesis of 12-sulfanyldodecyl (2*S*)-2-(6-methoxy-2-naphthyl) propanoate (**3b**)

12-bromododecyl (2*S*)-2-(6-methoxy-2-naphthyl) propanoate was synthesized according to a published procedure [S1] using (*S*)-Naproxen (7.8 mmol, 1.8 g), 12-bromo-dodecan-1-ol (7.8 mmol, 2.0 g) and *p*-toluenesulfonic acid (9.8 mmol, 1.7 g) in toluene (50 ml). The mixture was refluxed for about 10 h under N₂ in a round bottom flask using a Dean-Stark trap. The reaction progress was monitored by TLC (hexane:ethyl acetate = 8:2). After the reaction was complete, the reaction mixture was cooled to room temperature, and then washed with water (3×). The organic layer was separated, dried (Na₂SO₄), and the solvent evaporated under reduced pressure. The crude residue was purified by column chromatography (hexane:ethyl acetate = 8:2) to afford 3.6 g (97%). ¹H NMR (300 MHz, CDCl₃) δ (ppm): 1.22 (m, br, 16H, CH₂), 1.44 (m, H, CH₂CH₂O), 1.62 (d, 3H, J=7.2Hz, CH₃CH), 1.88 (m, 2H, CH₂CH₂Br), 3.43 (t, 2H, J=6.8Hz, CH₂Br), 3.83 (m, 1H, CHCH₃), 3.93 (s, 3H, CH₃O), 4.10 (t, 2H, J=6.6Hz, OCH₂CH₂), 7.18 (m, 2H, Ar-H), 7.46 (d, 1H, J=8.5Hz, Ar-H), 7.70 (d, 2H, J=3.6Hz, Ar-H), 7.74 (s, 1H, Ar-H). ¹³C NMR (75 MHz, CDCl₃): δ 129.66, 128.63, 127.46, 126.31, 125.70, 119.32, 105.98, 65.28, 55.69, 45.95, 34.43, 33.25, 29.89, 29.17, 28.58, 26.19, 18.91. MS m/z (rel. int., %): 478 (7.1) [M]⁺, 396 (9.3), 185 (100), 170 (5.9), 141 (7.5).

3b was synthesized according to a procedure reported by Hu and coworkers [S2]. Briefly, 12-bromododecyl (2*S*)-2-(6-methoxy-2-naphthyl) propanoate (2.5 mmol, 1.2g) was dissolved with freshly distilled dry THF (5 ml) and then cooled to -10 °C using an

acetone/ice bath. To the resulting solution, hexamethyldisilathiane (3.0 mmol, 0.63ml) and TBAF (1M in THF, 2.76mmol, 2.76ml) were added under an inert-gas atmosphere. After the reaction was complete (TLC, hexane:ethyl acetate = 8:2), the mixture was allowed to warm to room temperature. Thereafter, the solution was partitioned between diethyl ether (100 ml) and saturated aqueous ammonium chloride (100 ml), the layers were separated, and the organic phase washed with water (50 ml). After evaporation of the solvent under reduced pressure, the crude residue was purified by column chromatography (hexane:ethyl acetate = 8:2) to yield 1.95 g of **3b** (60 %). R_f (hexane:ethylacetate = 9:1) 0.46 (disulfide **3a**: R_f (hexane:ethylacetate = 9:1) 0.2). $[\alpha]_D^{20} +26.5^\circ$, (in comparison to (*S*)-Naproxen: $[\alpha]_D^{20} 66 \pm 2^\circ$, c 0.01 in chloroform source: Sigma-Aldrich). ^1H NMR (300 MHz, CDCl_3) δ (ppm): 1.21-1.37 (m, br, 20H, CH_2 , and overlapped 1H, SH), 1.58 (d, 3H, $J=7.2\text{Hz}$, CH_3CH), 2.53 (q, 2H, $J=7.5\text{Hz}$, CH_2SH), 3.88 (q, 1H, $J=6.2\text{Hz}$, CHCH_3), 3.93 (s, 3H, CH_3O), 4.08 (t, 2H, $J=6.8\text{Hz}$, CH_2O), 7.18 (m, 2H, Ar-H), 7.46 (d, 1H, $J=1.8\text{Hz}$, Ar-H), 7.70 (d, 2H, $J=4.4\text{Hz}$, Ar-H), 7.73 (s, 1H, Ar-H). ^{13}C NMR (75 MHz, CDCl_3): δ 129.65, 127.45, 126.68, 126.30, 119.30, 105.97, 65.28, 55.68, 45.94, 34.45, 29.92, 29.47, 28.77, 26.31, 26.19, 25.05, 18.91. MS m/z (rel. int., %): 432 (3.4) $[\text{M}]^+$, 230 (3.2), 212 (5.3), 185 (100), 171 (2.7), 155 (2.0), 141 (8.8).

Gold nanoparticle characterization (Au1-Au4)

UV-vis

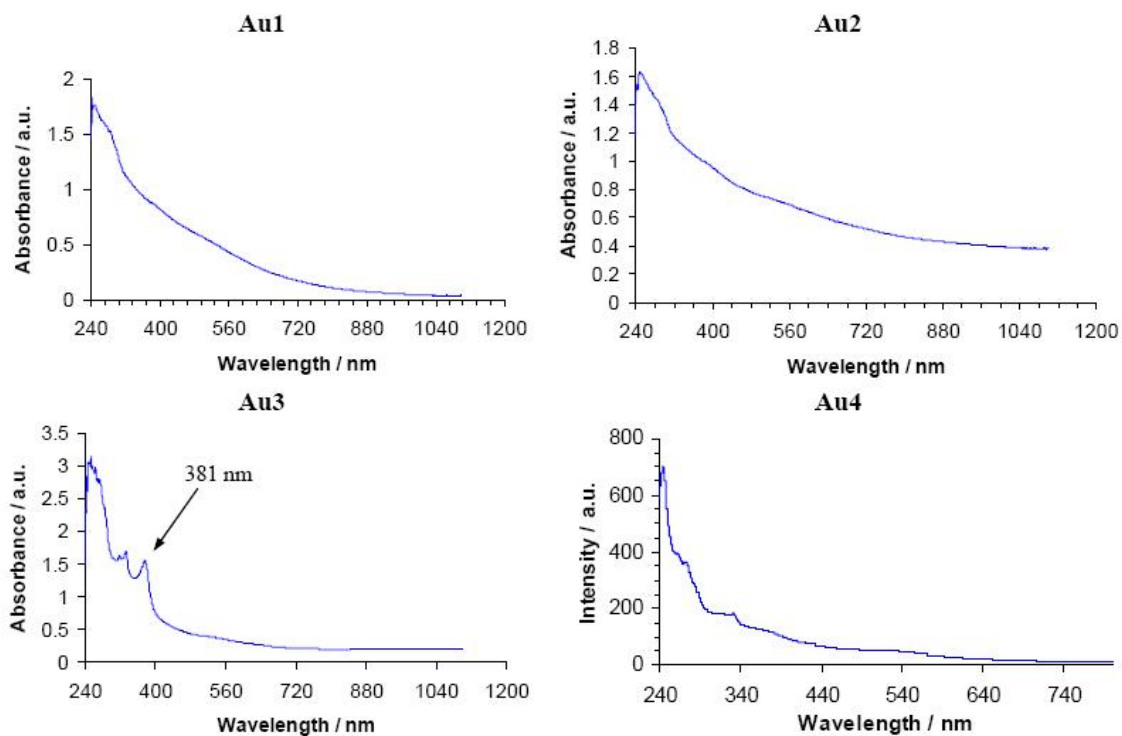
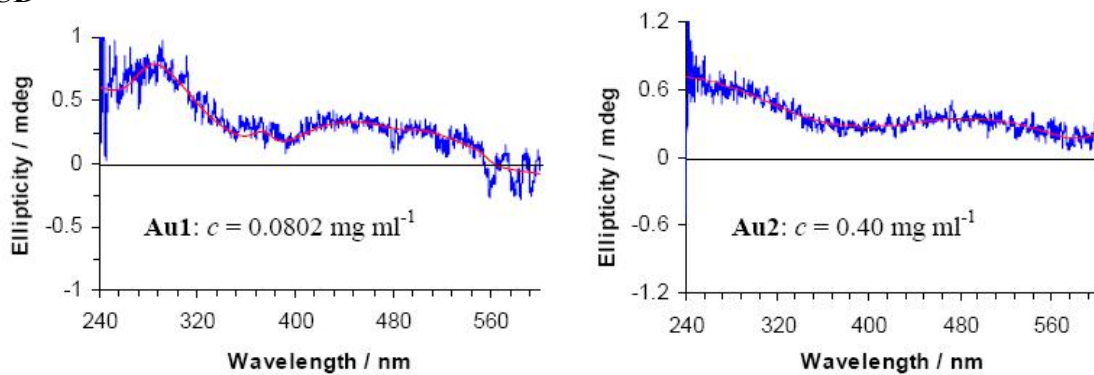
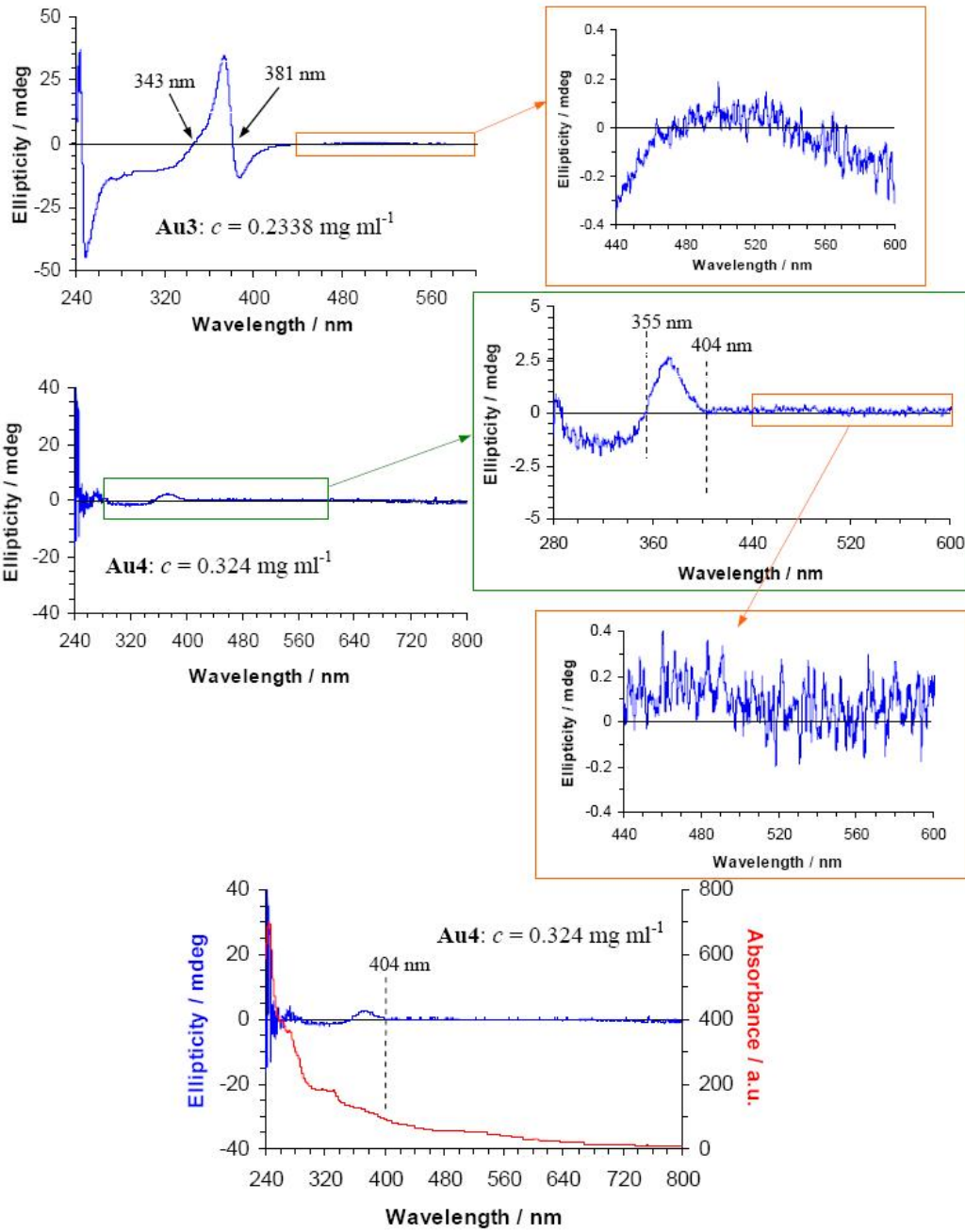


Fig. S5.1. UV-vis spectra of Au1-Au4.

CD





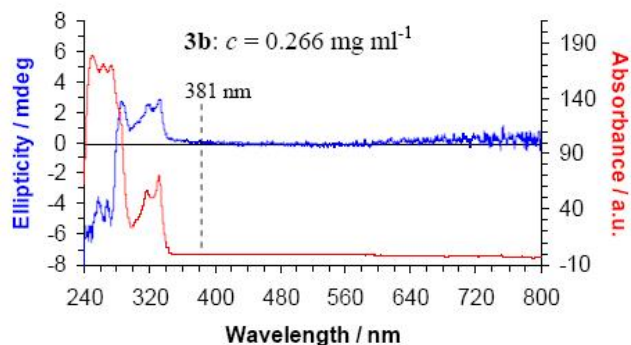


Fig. S5.2 CD spectra of **Au1-Au4** and thiol **3b** in chloroform.

CD - Concentration Dependence for **Au1** in CHCl_3

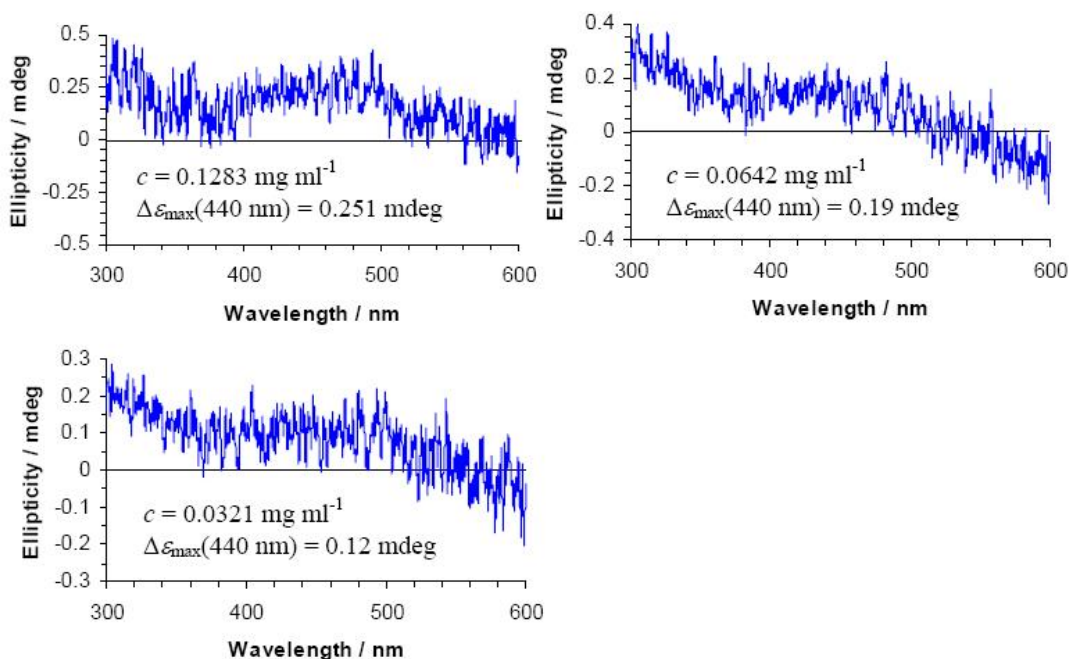


Fig. S5.3 CD spectra of **Au1** in chloroform at three different concentrations.

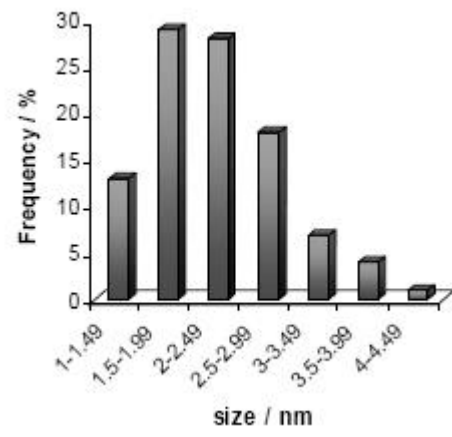
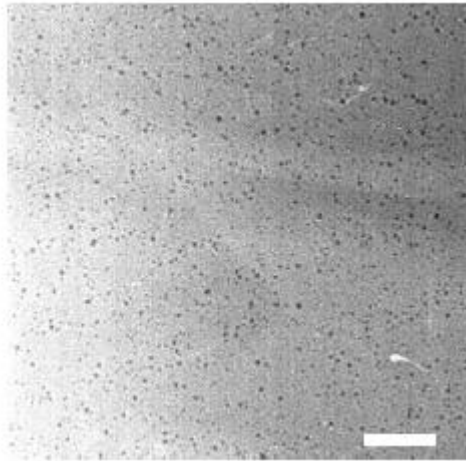
Comment regarding CD

Since no chiral bias is present during the synthesis, both **Au1** and **Au2** should be obtained as a racemate, if the gold nanocluster core was chiral. The two different scenarios: (i) a chiral core due to thiolate induced lattice distortions, and (ii) a chiral adsorption pattern would average to zero in an ensemble of cluster adsorbates (parity

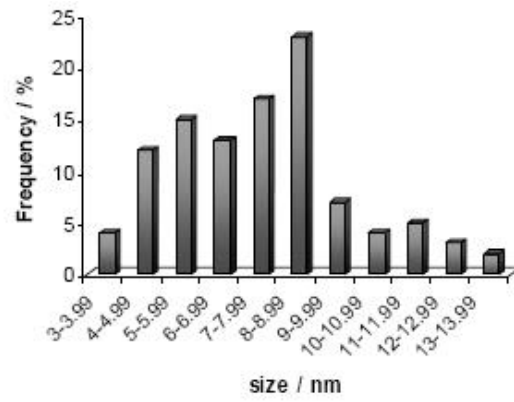
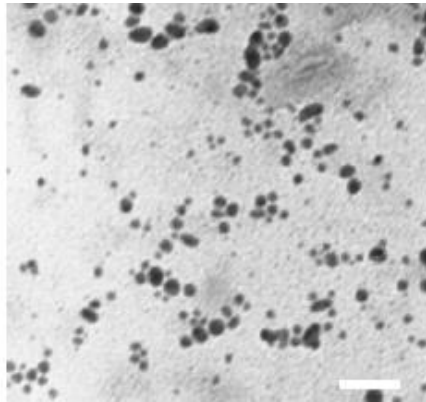
conservation) [S3]. The most reasonable explanation for the observed concentration-dependent CD at longer wavelength (where the thiol does not absorb) as well as for the higher $\Delta\varepsilon_{\max}$ values for **Au3** in comparison to **Au4** draws from results of CD experiments on bio-macromolecules such as DNA aggregates, chloroplast, proteins, or viruses for which similar ‘anomalies’ were reported in the past [S4]. This is that scattering (circular differential) and differential absorption both contribute to circular dichroism. However, scattering becomes increasingly important for particles/entities whose dimensions are greater than $1/20^{\text{th}}$ the wavelength of light [S5]. A higher concentration of particles in solution will naturally produce a higher number of particle aggregates or larger aggregates contributing to CD. In this way, the anomalous CD signals (so-called CD ‘artifacts’) are likely due to multiple scattering and dipole-dipole interactions of the dense particles [S6], which, in addition, continuously assemble into randomly shaped (anisometric) cluster aggregates. Yet again, this effect should average to zero, and one has to take into account that the measured CD is very weak. There are two more, but rather unlikely explanations for the observed CD. One would represent a parity violation (amplification of electro-weak forces due to the unique properties of gold nanostructures), and another one the presence of trace amounts of a chiral impurity during the cluster synthesis [S7].

TEM

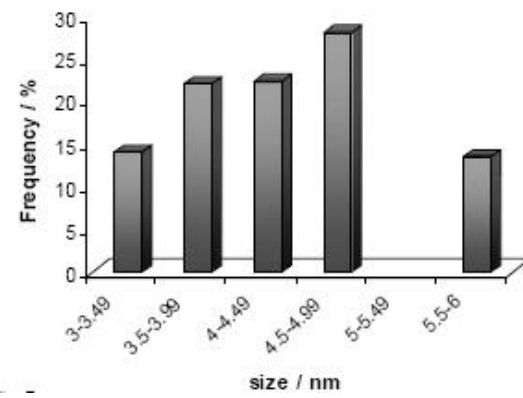
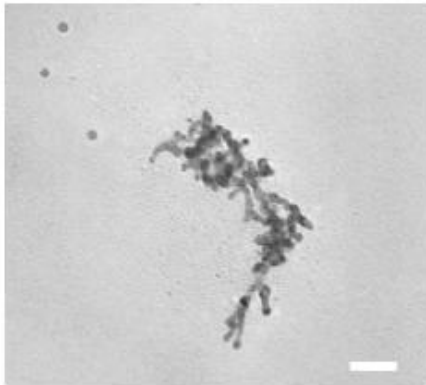
Au1



Au2



Au3



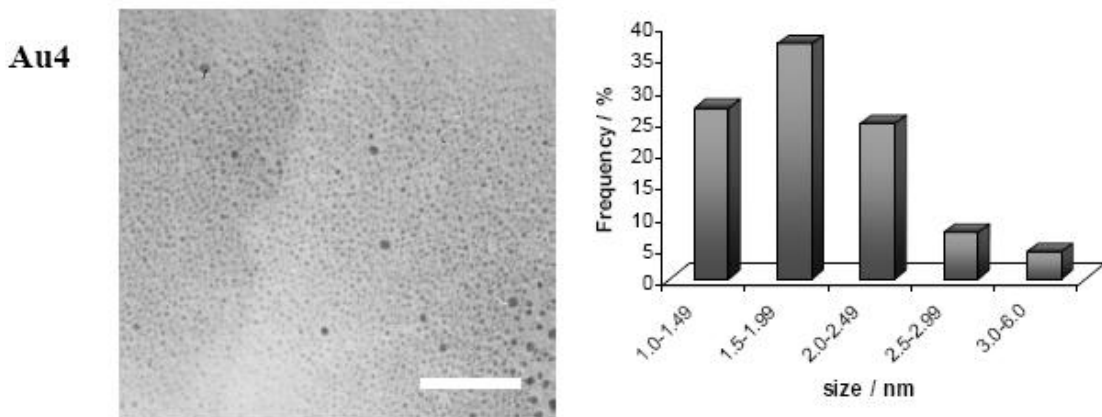
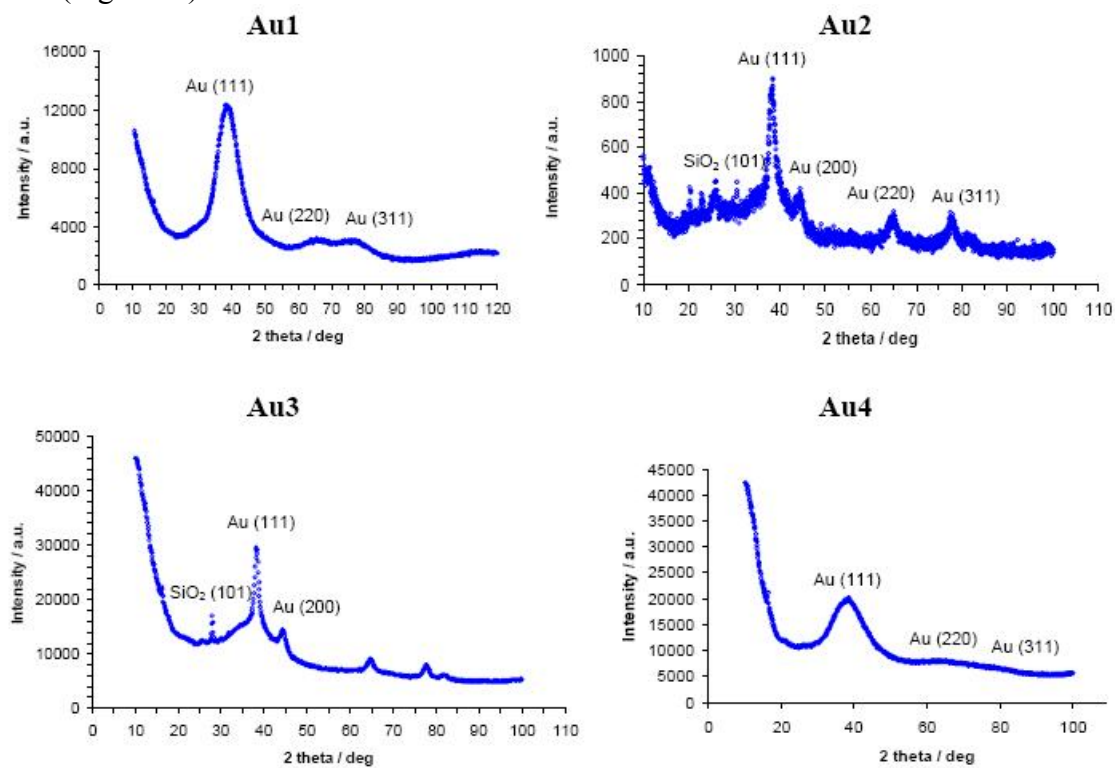


Fig. S5.4 TEM micrographs and size distribution of **Au1-Au4** (micrograph scale bars = 50 nm)

XRD (Fig. S5.5)



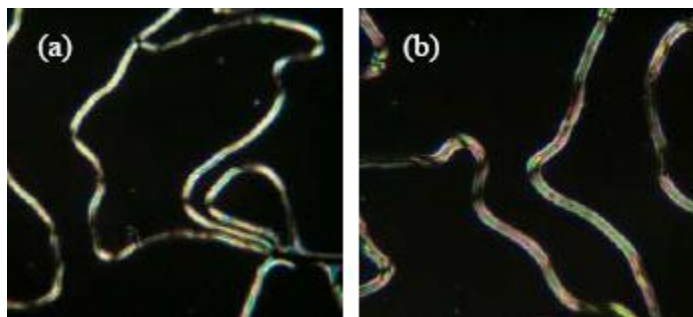


Fig. S5.6 POM micrographs of stripe pattern texture of the N phase of: (a) 5wt% **Au1** in **LC1** (64 °C), and (b) 5wt% **Au4** in **LC1** (56 °C) taken on cooling from the isotropic liquid phase.

References

- (S1) M. Kazemkaite, A. Bulovas, Z. Talaikyte, E. Butkus, V. Railaite, G. Niaura, A. Palaima, V. Razumas, *Tetrahedron Lett.* **2004**, *45*, 3551-3556.
- (S2) J. Hu, M. A. Fox, *J. Org. Chem.* **1999**, *64*, 4959-4961.
- (S3) M.-R. Goldsmith, C. B. George, G. Zuber, R. Naaman, D. H. Waldeck, P. Wipf, D. N. Beratan, *Phys. Chem. Chem. Phys.* **2006**, *8*, 63-67.
- (S4) O'Neil, J., personal communication.
- (S5) C. Bustamante, I. Tinoco Jr., M. F. Maestre, *Proc. Natl. Acad. Sci. USA.* **1983**, *80*, 3568-3572, and additional references [33a,b] in main text.
- (S6) C. Bustamante, M. F. Maestre, D. Keller, I. Tinoco Jr., *J. Chem. Phys.* **1984**, *80*, 4817-4823.
- (S7) In a test experiment, alkane thiolate capped nanoparticles synthesized in the presence of a chiral 'impurity' (we added one equivalent of **2**) gave the same CD and texture in **LC1** as alkane thiolate gold particles synthesized without the additional chiral component.

Chapter 6: Chirality transfer in nematic liquid crystals doped with (S)-naproxen-functionalized gold nanoclusters: an induced circular dichroism study

This paper was reproduced with permission from J. Mater. Chem. 2008, 18, 374-380.

Copyright 2008 - The Royal Society of Chemistry. It is co-authored with J. O'Neil and T. Hegmann. The text is a verbatim copy of the published paper.

In Chapter 5, thin film texture effects induced by ‘simple’ alkylthiol as well as chiral dopant-functionalized Au NPs in nematic LCs were introduced and discussed. Two scenarios have been suggested to explain the observed texture formation. In this chapter, the second scenario, i.e., the transfer of chirality from chiral Au NPs to the nematic LC host will be investigated in more detail using induced circular dichroism experiments. These tests should help clarify if chiral-dopant-decorated Au NPs are capable of a chiral perturbation in the nematic environment, and if the formation of identical thin film textures observed for non-chiral alkylthiol-capped Au NPs has a related origin.

Abstract: In a recent study, we found that nematic liquid crystals (N-LCs) doped with chiral (*S*)-naproxen-functionalized dodecane thiolate protected gold nanoclusters (**Au2**, **Au3**) or non-chiral alkyl thiolate protected Au clusters (**Au1**) produce thin film textures with characteristic uniform stripe patterns separated by areas of homeotropic alignment. While these textures closely resemble textures commonly observed for chiral nematic (N*-) phases with large helical pitch, so-called cholesteric finger textures, they originate from local concentration differences of the nanoclusters in the N-LC solvent. While areas with higher particle content form linear particle aggregates (stripe domains) due to the surface anchoring of the N-LC molecules to the cluster surface, areas of lower particle concentration give homeotropic alignment as a result of particles residing at the glass–N-LC interfaces. To elucidate and confirm a chirality transfer from the chirally modified gold clusters to the non-chiral N-LC, despite the complex thin film textures, we here present detailed induced circular dichroism (ICD) studies of thin films of 5CB doped with the three different Au clusters. These experiments revealed that the chiral Au nanoclusters (**Au2**, **Au3**) successfully transfer chirality to the N-LC host producing a chiral nematic phase (N*) with the opposite helical sense in comparison to the pure, organic chiral dopant dispersed in the same N-LC host. Thus, these results provide the first experimental proof for the usefulness of gold nanoclusters as chiral dopants for N-LCs. In contrast, for the non-chiral Au cluster, at a macroscopic level, no relationship between the cholesteric finger-like textures and chirality was found.

6.1 Introduction

Optically active (chiral) materials can be classified into two classes: intrinsically chiral materials (on a molecular level) and extrinsically chiral materials. Extrinsically chiral materials are based on a chiral molecular organization, which does not require chiral constituents or molecules [1]. In N-LCs (as well as tilted smectic LCs), induced circular dichroism (ICD) is the extrinsic circular dichroism due to the helical arrangement of the molecules. There are two main types of ICD: the first type includes chiral LCs doped with non-chiral molecules showing CD signals at the absorption wavelength of the non-chiral dopant molecules due to the induced helical arrangement through interactions with the LC (mimicking the helical organization) [2], and the second type includes chiral LC phases induced by a chiral dopant [3] (or mechanically induced by using a twisted cell) showing CD signals at the LC host absorption band [4]. Both types of ICD have been widely studied over the past several years [1, 4-10].

Two main textures can be found for N*-LCs using alignment layers: focal conic fingerprint texture, with the helical axes parallel to the surface, and Grandjean (planar) texture, with the helical axes perpendicular to the surface [11]. The focal conic texture shows birefringence but is optically inactive, whereas the Grandjean texture exhibits optical effects of the chiral mesophase and is suitable for CD measurements [12, 13]. One of the most interesting properties related to the Grandjean texture is the selective reflection of circularly polarized light at a wavelength commensurate with the helical pitch by the equation $\lambda = np$, where n is the mean refractive index, and p is the helical pitch [14]. The reflection is related to the handedness, i.e., right-handed N*-LCs only reflect right-circularly polarized light and show no effect on left-circularly polarized light,

and *vice versa* for left-handed N*-LCs [14]. As a result, both a circular reflection band and a circular adsorption band can be measured as a result of the chirality of the N*-LCs [5]. In some cases, a decreasing ICD intensity was observed during the transformation of the Grandjean texture into a focal conic fingerprint texture [8, 14]. Without surface alignment or other special treatment, N*-LCs commonly form multi-domains, and a signal in the CD-spectra related to selective reflection can be observed even in the absence of a planar texture. Additionally, the CD-band shape in these cases is commonly quite broad indicating the random distribution of the chiral domains [15]. In the absorption region, the apparent CD signal is a combination of the real CD signal, linear dichroism (LD), and birefringence. LD and birefringence effects, however, can be cancelled out by rotating the cell through 360° normal to the incident light beam [16, 17]. In similar experiments, aside from the described optical characteristics (textures) of N*-LC phase, CD spectropolarimetry has shown to be a powerful technique to prove LC phase chirality, and has successfully been utilized for chiral nematic (N*), chiral smectic-C (SmC*), and bent-core (bow or banana-shaped) LC phases [1-26].

In an attempt to combine the unique size-dependent properties of nanoscale materials and chirality by creating chirally decorated gold nanoclusters as dopants for N-LCs, we have recently shown that N-LCs upon doping with chiral (*S*)-naproxen-functionalized alkyl thiolate coated gold clusters produce thin film textures characterized by periodic stripe domains separated by dark areas showing no birefringence. These textural characteristics closely resemble textures commonly observed for N*-phases with large helical pitch, termed cholesteric finger textures [11]. Surprisingly, the same texture was

also found for mixtures containing non-chiral dodecane or hexane thiolate protected Au clusters [27].

Considering the strong homeotropic anchoring of the N-LC molecules to the nanocluster surface (dispersion, van der Waals interactions), the formation of linear particle aggregates as a result of the formation of topological defects (dipole, and hyperbolic hedgehog), and particles residing at the glass–N-LC interfaces producing homeotropic alignment in the domains separating the stripes were discussed as the main driving forces for this texture formation. At that point, we were unable to confirm whether the chiral Au nanoclusters transfer chirality to N-LCs, or not, solely based on the texture. In addition, given the formation of the described defects we were unable to produce uniform aligned samples between polyimide-coated glass slides (LC test cells with polyimide alignment layers) for these N-LC/nanocluster mixtures [27], making it impossible to use non-spectroscopic methods such as the Grandjean–Cano technique [28] or the Cano wedge method [29] to measure the helical pitch.

To provide experimental evidence for a chirality transfer (induction) in the N-LC–gold nanocluster mixtures, and to study the differences between N-LC–chiral Au cluster (gold nanocluster chiral dopants) and N-LC–non-chiral Au cluster mixtures, we here present detailed induced circular dichroism (CD) studies of thin films of a N-LC (5CB) doped with Au nanoclusters. Thin films of 5CB doped with the three different Au nanoclusters (one non-chiral: **Au1**, and two chiral; **Au2** and **Au3**) were first observed by polarized optical microscopy (POM), and characterized by UV-vis absorption, followed by ICD spectroscopy.

6.2 Experimental

Details of the synthesis of the gold nanoclusters, their characterization, and preparation of the mixtures with N-LCs were reported previously [27]. In this study, we use 5CB as the host LC, as 5CB shows an N phase at room temperature, which is convenient for CD measurements. The structures of 5CB, (*S*)-naproxen and the gold nanoclusters used are shown in Fig. 6.1. Thin films of 5CB–Au1–Au3 mixtures were prepared as follows. One quartz plate and one smaller square quartz plate were separated by Mylar spacers of a nominal thickness of 12 μm^* , and epoxied at four points [Fig. 6.1(a)] [30]. These cells were then filled with the mixtures at a temperature above the clearing point of 5CB (*ca.* 40 °C), and then slowly cooled down to the N phase at a cooling rate of 1°C min⁻¹. CD spectra were recorded on a J-810 spectropolarimeter (Jasco, Inc.) using a bandwidth of 2 nm, medium sensitivity with a maximum of 200 mdeg (except for specifically indicated samples). During the CD measurement, each cell was rotated normal to the light beam in 45° intervals from 0° to 315° to differentiate the intrinsic CD from linear dichroism and birefringence. UV-vis absorption spectra were measured using a Cary 5000 UV-vis-NIR spectrophotometer (Varian), and POM was performed using an Olympus BX51-P polarizing microscope in conjunction with a Linkam LS350 heating/cooling stage.

* Minor variations in cell thickness, due to the preparation of the sandwiched quartz cells using Mylar spacers and epoxy, cannot be excluded. The resulting variations in the LC film thickness will contribute to a difference in signal intensity. While this could likely have been avoided to some degree by using a room temperature LC mixture with lower aromatic content, contributions of linear dichroism and birefringence, particularly for mixtures with lower particle content, seem to play a more critical role (although they do not affect the observed sign of the CD signal).

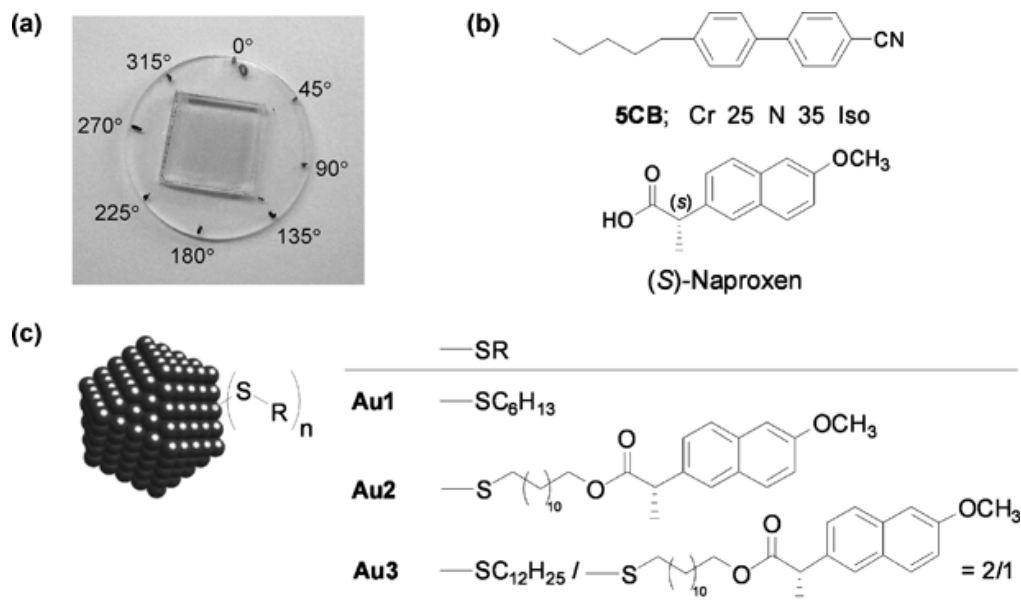


Fig. 6.1 (a) Photo of prepared sample; (b) structure and phase transition temperature (°C) of 5CB and (*S*)-naproxen. Cr = crystalline solid, N = nematic phase and Iso = isotropic phase; (c) gold nanoclusters and structure of thiolate protecting agents (n = number of thiolates coating the nanocluster; n depends on the nanocluster size).

6.3 Results and discussion

Pure 5CB and 5CB doped with (*S*)-naproxen were both tested first allowing us to compare the obtained CD spectra with the spectra of the 5CB–Au nanocluster mixtures. As observed by POM, the pure 5CB cell shows a typical nematic marble texture as shown in the Fig. 6.2a. Absorbance and CD spectra of 5CB are also collected in the Fig. 6.3a and b]. 5CB shows two absorption peaks at 200 and 280 nm, respectively [31]. However, the LC film must be very thin to display a real peak without saturation of the detector. For example, in a paper published by Hird and coworkers [31], suitable thin films of 5CB with 0.2–0.4 μm nominal thickness prepared using pulsed laser deposition show the related 280 nm absorption peak. As demonstrated by Hird and coworkers, a typical LC texture cannot be observed with such thin films [31].

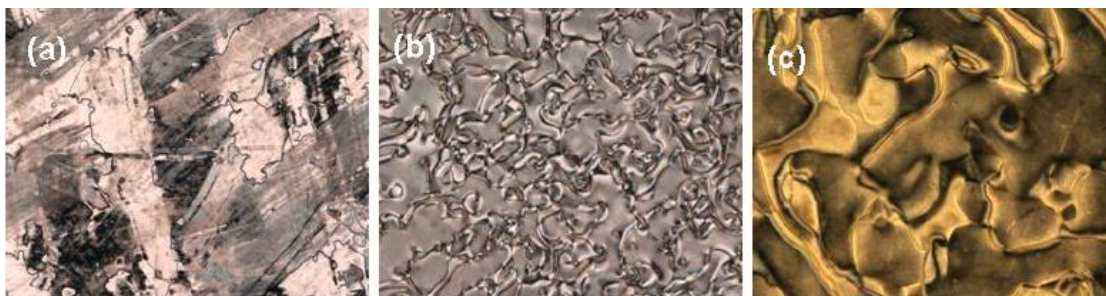


Fig. 6.2 POM micrographs of the N or N* phases at room temperature after cooling from the isotropic liquid phase at a cooling rate of 1°C/min: (a) marble texture of the N phase of pure 5CB; (b) oily-streak texture of the N* phase of 5CB doped with 0.1 wt% (*S*)-Naproxen, and (c) doped with 0.01wt% (*S*)- Naproxen.

In the present study, we did not attempt to produce sub-micron thin films showing no characteristic textures, since we were focusing on measuring the CD spectra of the binary N-LC–Au nanocluster mixtures showing the described textures that would allow us to examine possible relationships between the two components and the potential of inducing chirality. However, due to the thickness of these films, the absorbance is quite strong resulting in a saturation of the absorbance up to 318 nm. Therefore, only the edge above 318 nm of the 280 nm absorbance peak is shown in all CD spectra (real signal), and used in the discussion of induced chirality from the various dopants to the N-LC. This also applies to the 0° CD spectrum in Fig. 6.3b (included for comparison).

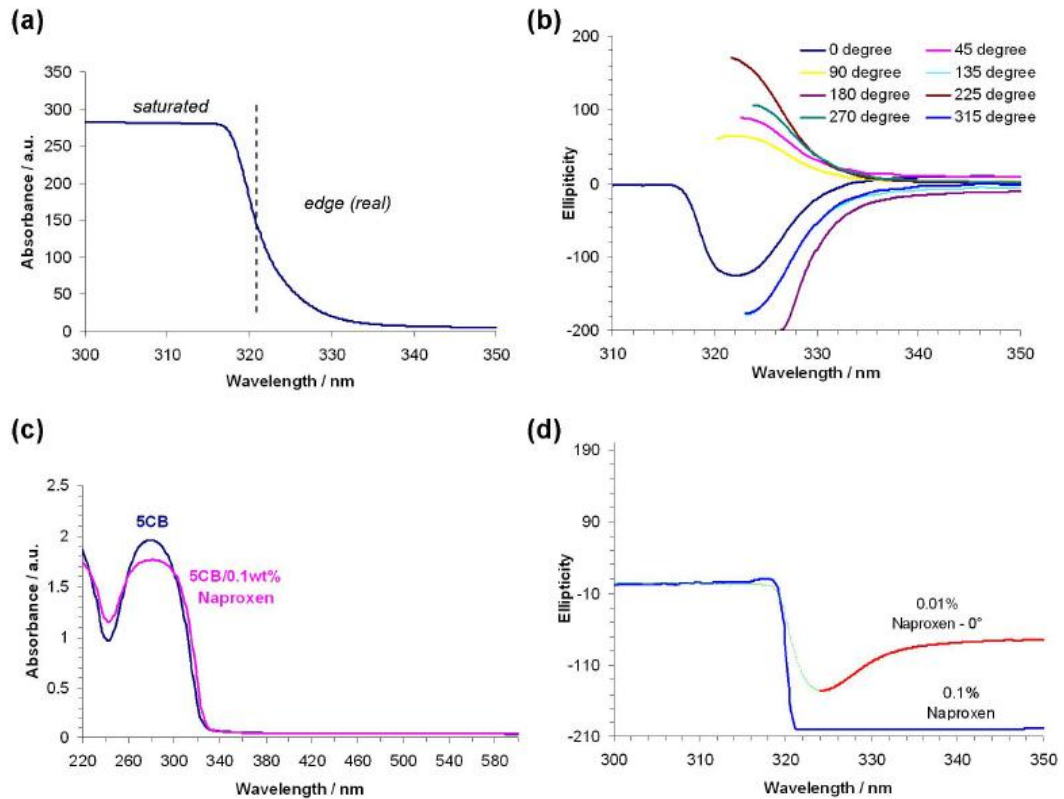


Fig. 6.3 (a) UV-vis absorption spectrum of a 12 μm thin film of pure 5CB. (b) CD spectra of a 12 μm thin film of pure 5CB at different rotating angles. (c) UV-vis absorption spectra of thin films of 5CB and 5CB doped with 0.1wt% (*S*)-Naproxen prepared by drop-casting on Quartz. (d) CD spectra of 12 μm thin film of 5CB doped with 0.1wt% and 0.01wt% (*S*)-Naproxen. Rotation of the LC film around its normal did not change the shape (sign, intensity) of the spectrum. All measurements were taken at room temperature.

CD spectroscopy measures the difference in absorbance of left- and right-handed circularly polarized light by a given specimen. In the presented experiments, if the absorbance is saturated due to the film's thickness, the zero CD signal in the saturated part of the spectrum below 320 nm only means that there is no light passing through the cell. The CD signal is saturated up to *ca.* 320 nm and decreases to zero at shorter wavelengths due to the saturated absorbance. In effect, only the edge shown in all spectra

should be regarded as a true CD signal. For the same reason, not the intensity but the sign of the CD signals is discussed and related to chirality, as pointed out by Green *et al.* [9] As expected for pure, non-chiral 5CB (see Fig. 6.3b), rotating the cell produced CD spectra showing regularly positive or negative signals due to linear dichroism and birefringence.

To measure a true CD of the N*-phase formed by doping a chiral dopant such as (*S*)-naproxen into a non-chiral N phase, we first need to know whether the CD signal is due to the induced chiral arrangement of the N-LC host, or due to the dopant's absorption itself. To exclude this, sub-micron thin films of pure 5CB and 5CB doped with 0.1 wt% (*S*)-naproxen were prepared by drop-casting solutions on one quartz plate, followed by evaporation of the solvent, heating the samples above the clearing point, and subsequent cooling to room temperature. The two UV-vis absorption spectra (see Fig. 6.3c) are quite similar, both showing an absorption maximum at 280 nm for 5CB indicating only a very minor contribution from (*S*)-naproxen to the spectrum. Hence, all CD spectra of the 12 μm thick films are showing signals with the major contribution arising from 5CB as the chromophore. Similarly, the absorption spectra of 12 μm thick cells of 5CB doped with both 0.1 wt% and 0.01 wt% (*S*)-naproxen are almost identical to the spectrum of pure 5CB (Fig. 6.3a) with minor differences in absorbance at longer wavelengths starting at 330 nm (both spectra are saturated below 320 nm).

Another point one has to take into consideration is that only low concentrations of a chiral dopant can be used. As can be seen from the CD spectrum of 5CB doped with 0.1 wt% (*S*)-naproxen (Fig. 6.3d), higher chiral dopant concentrations produce stronger CD reflection signals out of the measurable range of the CD instrument [even at low

sensitivity no changes in the spectral shape are apparent (maximum 2000 mdeg)]. Similar to the experiments described by Harkness and Gray using unmodified surfaces [15], the reflection band is quite broad as a result of multi-domain formation. However, a tenfold decrease in the (*S*)-naproxen concentration (0.01 wt%) produces a CD spectrum with the edge at a longer wavelength (red color in Fig. 6.3d) considered to be the real part of the CD signal. Between 350 and 330 nm, the negative CD signal arises from the selective reflection of the induced N*-phase. At shorter wavelengths starting at *ca.* 330 nm, the observed increasing negative intensity of the CD spectrum is related to the absorption, which is further modified by contributions of the linear dichroism and birefringence. As expected for an N*-phase, rotating the sample did not change the shape and the sign of the CD-band.

While it seems logical to assume that Au nanoclusters decorated with the same enantiomerically-enriched chiral dopant moiety [i.e., (*S*)-naproxen] would serve as chiral dopants for LC phases inducing an N*-phase with the same handedness, the unexpected similarity of the textures for both (*S*)-naproxen decorated Au clusters (**Au2**, **Au3**) and hexane thiolate (**Au1**) and dodecane thiolate protected Au nanoclusters warranted caution in making this conclusion simply based on textural observations. In addition, a bulk chiral induction in a N-phase by a minute amount of chirally decorated gold nanoclusters (5 wt% ~0.04 mole% depending on the nanocluster size) would provide evidence that nanoclusters in the few-nanometre size regime can influence or change the nematic environment on a macroscopic level, and are therefore not “invisible” to the N-LC host.

Depending on the LC host structure and the Au nanocluster concentration, fingerprint-like or cholesteric finger-like textures can be observed, or birefringent stripes

can co-exist beside domains displaying non-chiral nematic schlieren textures. The commonly observed texture with stripe domains resulting from linear particle aggregates of 5CB doped with 5 wt% **Au2** is shown in Fig. 6.4a. For 5CB doped with the nanoclusters, further cooling at higher cooling rates, or lower particle concentrations, sometimes produces 'normal' *schlieren* textures, which are not indicative of an N*-phase. For example, reducing the concentration of **Au2** to 1 wt% produced *schlieren* textures as shown in Fig. 6.4c. However, despite the formation of a typical non-chiral *schlieren* texture for the 5CB–**Au2** mixture, the CD absorption spectra [Fig. 6.5(a) and (b)] clearly show the chirality of the system. As can be seen from Fig. 6.5(b), although there are obvious linear dichroism and birefringence effects on the apparent CD signal, always positive CD signals for all sample rotation angles were observed, although the intensity at different angles varies, and provides clear evidence for induced chirality from the chiral gold nanocluster to the N-LC host. This result is distinctly different from the CD spectra obtained for 5CB doped with (*S*)-naproxen (see Fig. 6.3(d)), for which all CD-bands showed a negative sign. For 5CB doped with 5 wt% **Au2**, a higher concentration of chiral (*S*)-naproxen units (higher intensity in the CD spectra) reduces the relative contribution of linear dichroism and birefringence; the negative sign and the intensity of the CD signal are again independent of rotation angle. Aside from the lack of a clear CD reflection signal in the 5CB–**Au2** spectra, which is likely the result of a larger helical pitch of the 5CB–**Au2** mixture because of the overall lower concentration of (*S*)-naproxen (concentration-dependent helical pitch), the difference in sign was found to be the major difference between the CD spectra of 5CB–**Au2** and 5CB doped 0.1 wt% or 0.01 wt% (*S*)-naproxen.

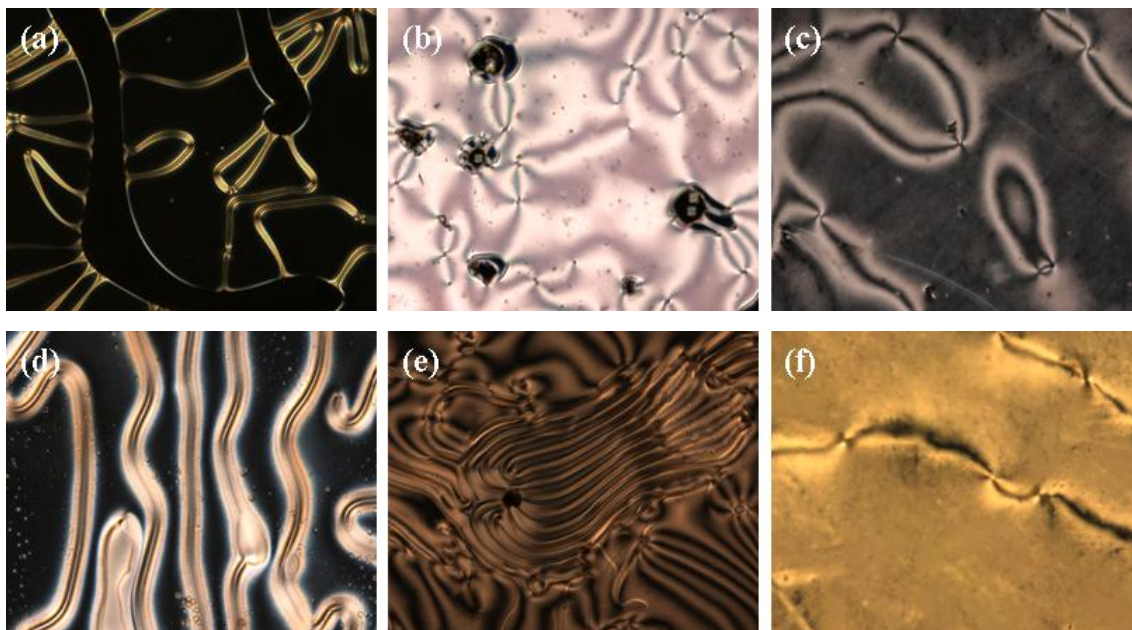


Fig. 6.4 POM micrographs of (a) 5CB doped with 5 wt% **Au2** at the transition from the isotropic liquid to the N*-LC phase (34.6 °C), (b) 5CB doped with 5 wt% **Au2** at room temperature, (c) 5CB doped with 1 wt% **Au2** at room temperature, (d) 5CB doped with 5 wt% **Au3** at 33.9 °C on cooling, (e) 5CB doped with 5 wt% **Au3** at room temperature, and (f) 5CB doped with 0.5 wt% **Au3** at room temperature.

Similar results were also obtained for mixtures of 5CB doped with **Au3**. Fig. 6.4(d) and (e) show the textures of 5CB doped with 5 wt% **Au3**. Likely due to the smaller size of **Au3** (1.4 nm for **Au3** vs. 3.5 nm for **Au2**), slightly different textural characteristics are observed. Upon cooling from the isotropic liquid phase, 5CB doped with **Au3** initially formed birefringent stripes separated by homeotropic domains that turn into *schlieren* texture domains at room temperature. Similar to 5CB doped with (*S*)-naproxen, 5CB doped with 5 wt% **Au3** displays a strong CD reflection signal out of the measurable range of the CD instrument. Most importantly, the real part of the CD spectrum (edge) has again a positive sign for each rotation angle. This is also true for the same mixture with lower **Au3** content (0.5 wt% **Au3**) showing a typical *schlieren* texture by POM

because of the lower particle concentration. These results support our assumption that the chirally decorated gold nanoclusters transfer chirality to the N-LC host. Similar to the CD spectra of the pure, isolated gold nanoclusters **Au2** and **Au3** in comparison to the CD spectrum of pure (*S*)-naproxen [27], 5CB doped with (*S*)-naproxen produces negative CD signals, and 5CB–**Au2** and 5CB–**Au3** constantly positive signals at all measured sample rotation angles [Figs. 6.5(c) and (d)]. This sign reversal must then be the result of a reverse rotation of N-LC molecules in these two systems, one left- and one right-handed. Such variation in chirality from the free (*S*)-naproxen to (*S*)-naproxen moieties tethered to the gold nanocluster surface *via* hydrocarbon chains can be expected, and related effects have previously been reported for side-chain LC polymers [32]. In fact, chiral inversions in nematic and smectic-C liquid crystals are a common phenomenon, and have been reported by a number of groups [33].

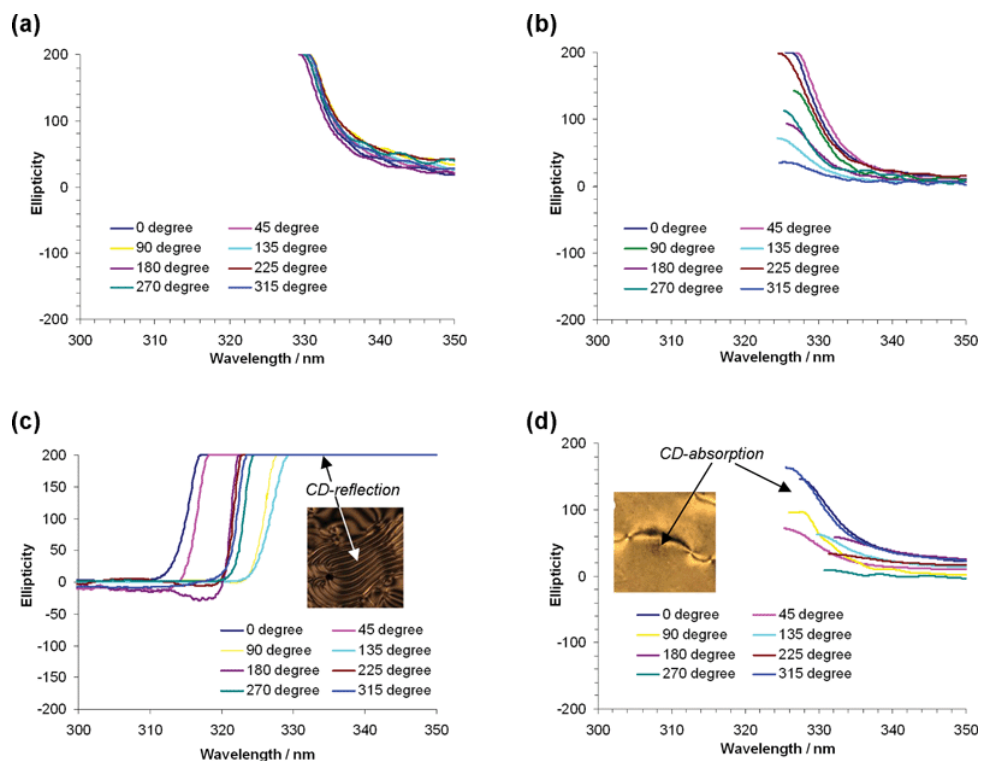


Fig. 6.5 CD spectra at different sample angular rotation angles of (a) 5CB doped with 5 wt% **Au2**, (b) 5CB doped 1 wt% **Au2**, (c) 5CB doped with 5 wt% **Au3**, and (d) 5CB doped with 0.5 wt% **Au3**. All measurements were taken at room temperature.

While it seems impossible, because of size and local (*S*)-naproxen concentration differences, to quantify the propensity of **Au2** and **Au3** to induce chirality in the N-LC host based on texture observations and CD spectra, a clear trend can be observed. As for commonly used organic chiral dopants, a higher concentration of **Au2** or **Au3** in 5CB results in a shorter helical pitch [34], and more intense CD signals are observed as a result thereof. Relevant factors such as the impossibility to obtain homogenous planar textures for the chirally decorated clusters along with the larger film thickness make it impossible to measure perfect CD reflection and absorption spectra. However, from the edge of the CD absorption and broad reflection spectra (here only **Au3**) we can conclude

that **Au2** and **Au3** successfully transfer chirality to the non-chiral N-LC host with the opposite helical sense as the pure, organic chiral dopant in the same N-LC [32, 33].

The last step was to study the finger-like texture formed by 5CB doped with hexane thiolate protected Au nanoclusters (**Au1**). The chirality of Au nanoclusters is still an open question [35]. The existence of local chirality of related silver nanoparticle aggregates, which can be regarded as a racemic mixture at the macroscopic level, was recently proposed by Drachev *et al.* using experiments such as photon scanning tunneling microscopy [36]. Although theoretical studies point out that the most stable isomers of bare Au₂₈, Au₅₅, and thiolate protected gold clusters can be chiral [37-41], no related experimental results proving chiral or macroscopic racemic properties of bare or non-chiral, thiol-protected Au nanoclusters *via* a chirality transfer and amplification' in a condensed phase have been reported so far.

To clarify the origin of the textural similarities (linear particle aggregates) we observed for chiral and non-chiral modified gold nanoclusters, and their relationship to possible local or macroscopic chirality of the N-LC mixtures, we further studied ICD of thin films of 5CB doped with **Au1**.

Fig. 6.6(a) shows the texture of 5CB doped with 1 wt% **Au1** at the transition from the isotropic liquid phase to the nematic phase on cooling, which appears quite similar to textures observed for **Au2** and **Au3** in 5CB shown in Fig. 6.4(a) and (d). With a slow cooling rate (<1 °C/min), even though most stripes disappear upon further cooling, several birefringent stripes remain clearly visible [Fig. 6.6(b)] at room temperature. In contrast, for faster cooling rates (achieved by opening the cover of the heating stage to increase the cooling rate), in some cases, all stripes disappear for the **Au1** clusters in 5CB,

and exclusively homeotropic alignment of the N-LC molecules is obtained [Fig. 6.6(c)]. These are excellent samples to study eventual chiral effects in these mixtures (related to the stripes or not). For the 5CB–1 wt% **Au1** mixture with roughly the same or higher area density of stripes as observed for **Au3** in 5CB, if the stripes are a result of local chirality, i.e., the alignment or orientation of the N-LC molecules adopts a helical arrangement, a constant positive or negative sign of the CD spectra will not be affected by rotating the sample about different sample rotation angles. The homeotropic domains as shown in Fig. 6.6(b), and the homeotropically aligned film in Fig. 6.6(c) should not give rise to any CD signal. The CD spectra of 5CB doped with 1 wt% **Au1** with birefringent stripe domains [linear particle aggregates as in Fig. 6.6(a) and (b)] is shown in Fig. 6.7.

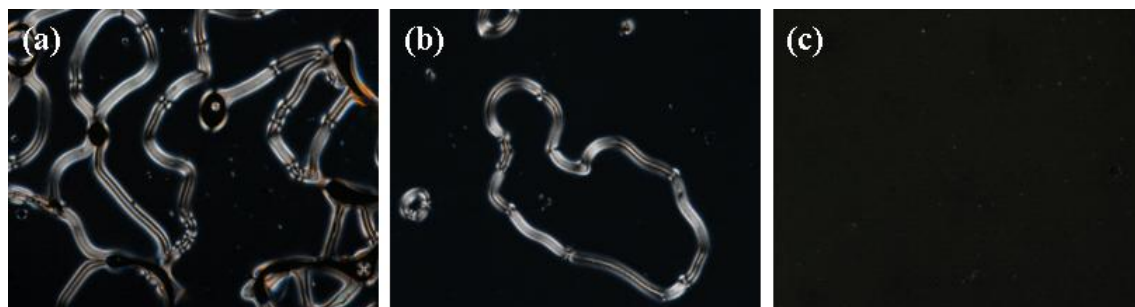


Fig. 6.6 POM micrograph of 5CB doped with 1 wt% **Au1**: (a) at 33.4 °C, (b) at room temperature (slow cooling), and (c) at room temperature showing no-stripes after rapid cooling.

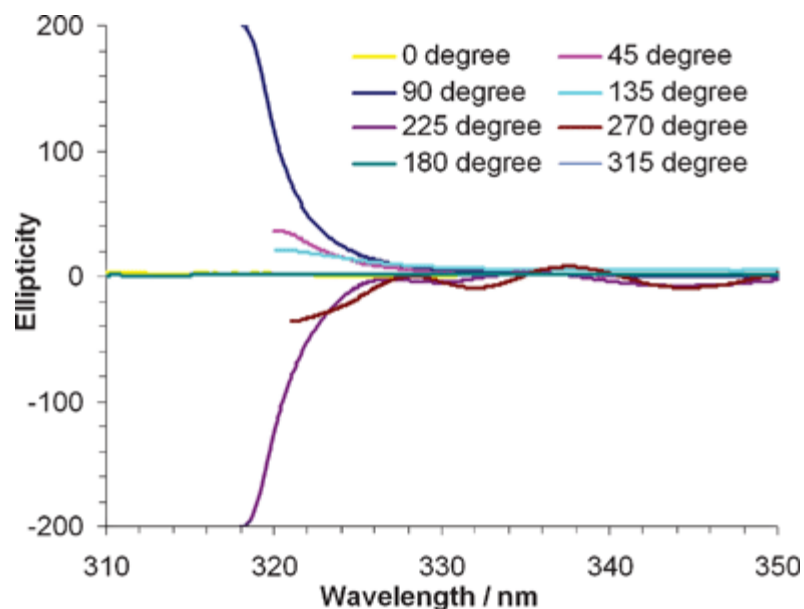


Fig. 6.7 CD spectra of 5CB doped with 1 wt% Au1 showing birefringent stripes at different sample rotation angles.

One can clearly see that the CD signal shows either negative or positive signs at different sample rotation angles, with several angles showing no (0° , 180°) or very weak CD signals (315°) (zero ellipticity). The similarity of these CD spectra with the CD spectra obtained for pure 5CB clearly demonstrates that there is no macroscopic chirality associated with the birefringent stripes. As expected then, the spectra of the complete homeotropically aligned film did not show any CD signal for any rotation angle (not shown). Based on these measurements, although local chiral distortions or a twist in the director configuration can not be completely excluded (since the birefringent stripes remain visibly colored even with uncrossed (parallel) polarizers [27], macroscopically no chirality is induced in the non-chiral N-phase by ‘simple’ alkyl thiolate capped gold nanoclusters.

6.4 Conclusions

To summarize, ICD measurements of 5CB doped with chiral Au nanoclusters (**Au2**, **Au3**) prove the successful transfer of chirality from the chirally capped Au nanoclusters to the non-chiral nematic LCs with a sign inversion (opposite helical sense) [32, 33, 42] from the pure, organic chiral dopant to chiral dopant decorated Au nanoclusters. To the best of our knowledge, this is the first example of induced LC chirality by Au nanoparticles. As nematic LCs doped with chiral additives are widely used in liquid crystal display (LCD) technologies, we foresee the possibility of using chiral Au nanoclusters in such and related applications by combining the chiral dopant capabilities reported here with the unique size and shape-dependent properties of alkylthiol capped nanoscale gold clusters such as, optical and electronic properties [43], room temperature magnetism [44], or luminescent blinking [45]. In addition, gold nanoparticle–N-LC mixtures were used for electrically controlled light scattering (near-field spectral tuning) [46], a proof-of-concept device capable of voltage-dependent color tuning (far-field spectral tuning) [47], and nematic mixtures with higher conductivity [48].

Finally, we have also shown that alkyl thiolate protected gold nanoclusters, despite similar textural effects in N-LCs, and theoretical as well as experimental indications of chirality of bare and thiolate protected metal (Au, Ag) nanoclusters, do not give rise to macroscopically detectable chiral effects, conformations, or aggregates in N-LCs.

Acknowledgements

This work was supported by the Natural Sciences and Engineering Research Council (NSERC) of Canada, the Canada Foundation for Innovation (CFI), the Manitoba Research and Innovations Fund (MRIF), and the University of Manitoba (Demonstration Project Grant).

References

- 1 F. D. Saeva, in *Liquid Crystals, the Fourth State of Matter*, ed. F. D. Saeva, Marcel Dekker, New York, **1979**, pp. 249-273.
- 2 F. D. Saeva, J. J. Wysocki, *J. Am. Chem. Soc.* **1971**, *93*, 5928-5929.
- 3 For an overview see: (a) *Chirality in Liquid Crystals (Partially Ordered Systems)*, ed. H.-S. Kitzerov and C. Bahr, Springer, Heidelberg, 2001; (b) G. Solladie, R. G. Zimmermann, *Angew. Chem., Int. Ed. Engl.*, **1984**, *23*, 348-362.
- 4 F. D. Saeva, *Mol. Cryst. Liq. Cryst.* **1973**, *23*, 171-177.
- 5 G. P. Spada, G. Proni, *Enantiomer* **1998**, *3*, 301-314.
- 6 F. D. Saeva, *J. Am. Chem. Soc.*, **1972**, *94*, 5135-5136.
- 7 J. Lee, Y. Ouchi, H. Takeze, A. Fukuda, J. Watanabe, *J. Phys.: Condens. Matter* **1990**, *2*, 271-274.
- 8 X. M. Dong, D. G. Gray, *Langmuir* **1997**, *13*, 3029-3034.
- 9 A similar situation was discussed by Green *et al.* In their paper, because of the strong optical density of the sample, only the CD at the absorbance band edge was measured; M. M. Green, S. Zanella, H. Gu, T. Sato, G. Gottarelli, S. K. Jha, G. P. Spada, A. M. Schoevaars, B. Feringa, A. Teramoto, *J. Am. Chem. Soc.* **1998**, *120*,

- 9810-9817.
- 10 S. Fireman-Shoresh, S. Marx, D. Avnir, *J. Mater. Chem.* **2007**, *17*, 536-544.
 - 11 I. Dierking, *Textures of Liquid Crystals*, Wiley-VCH, Weinheim, **2003**, pp. 51-70.
 - 12 H. W. Gibson, in *Liquid Crystals, the Fourth State of Matter*, ed. F. D. Saeva, Marcel Dekker, New York, **1979**, pp. 99-162.
 - 13 G. Gottarelli and G. P. Spada, in *Circular Dichroism – Principles and Applications*, ed. K. Nakanishi, N. Berova and R. W. Woody, VCH, New York, **1994**, pp. 547-561.
 - 14 F. D. Saeva, P. E. Sharpe, G. R. Olin, *J. Am. Chem. Soc.* **1973**, *95*, 7656-7659.
 - 15 B. R. Harkness, D. G. Gray, *Macromolecules* **1991**, *24*, 1800-1805.
 - 16 F. D. Saeva, G. R. Olin, *J. Am. Chem. Soc.* **1976**, *98*, 2709-2711.
 - 17 C. Spitz, S. Dahne, A. Quart, H. W. Abraham, *J. Phys. Chem. B* **2000**, *104*, 8664-8669.
 - 18 J. M. Ribo, J. Crusats, F. Sagues, J. Claret, R. Rubire, *Science* **2001**, *292*, 2063-2066.
 - 19 J. Yuan, M. Liu, *J. Am. Chem. Soc.* **2003**, *125*, 5051-5056.
 - 20 S.-W. Choi, S. Kang, Y. Takanishi, K. Ishikawa, J. Watanabe, H. Takezoe, *Angew. Chem., Int. Ed.* **2006**, *45*, 6503-6506.
 - 21 D. Katsis, P. H. M. Chen, J. C. Mastrangelo, S. H. Chen, *Chem. Mater.* **1999**, *11*, 1590-1598.
 - 22 J. Yoshida, H. Sato, A. Yamagishi, N. Hoshimo, *J. Am. Chem. Soc.* **2005**, *127*, 8453-8456.
 - 23 Y. Takanishi, G. J. Shin, J. C. Jung, S.-W. Choi, K. Ishiwawa, J. Watanabe, H.

- Takezoe, P. Toledano, *J. Mater. Chem.* **2005**, *15*, 4020-4024.
- 24 N. Hoshino, Y. Matsuoka, K. Okamoto, A. Yamagishi, *J. Am. Chem. Soc.* **2003**, *125*, 1718-1719.
- 25 T. Mitsuoka, H. Sato, J. Yoshida, A. Yamagishi, Y. Einaga, *Chem. Mater.* **2006**, *18*, 3442-3447.
- 26 C. Nuckolls, T. J. Kata, *J. Am. Chem. Soc.* **1998**, *120*, 9541-9544.
- 27 H. Qi, T. Hegmann, *J. Mater. Chem.* **2006**, *16*, 4197-4205.
- 28 (a) F. Grandjean, C. R. Hebd. *Seances Acad. Sci.* **1921**, *172*, 71-74; (b) R. Cano, *Bull. Soc. Fr. Mineral*, **1968**, *91*, 20-27; (c) G. Heppke, F. Oestreicher, *Mol. Cryst. Liq. Cryst.* **1978**, *41*, 245-249.
- 29 (a) G. Gottarelli, B. Samori, C. Stremmenos, G. Torre, *Tetrahedron* **1981**, *37*, 395-399; (b) For an illustration of the Cano wedge method see: K. Akagi, S. Guo, T. Mori, M. Goh, G. Piao, M. Kyotani, *J. Am. Chem. Soc.* **2005**, *127*, 14647-14654.
- 30 J. F. Li, K. A. Crandall, P. W. Chu, V. Percec, R. G. Petschek, C. Rosenblatt, *Macromolecules* **1996**, *29*, 7813-7819.
- 31 J. Gonzalo, P. E. Dyer, M. Hird, *Appl. Phys. Lett.* **1997**, *71*, 2752-2754, and references cited therein.
- 32 For effects in chiral LC polymers (side-chain and main-chain) and chiral LC polymer mixtures see: (a) M. Goh, T. Matsushita, M. Kyotani, K. Akagi, *Macromolecules* **2007**, *40*, 4762-4771; (b) D. B. Amabilino, J. L. Serrano, T. Sierra, J. Veciana, *J. Polym. Sci., Part A: Polym. Chem.* **2006**, *44*, 3161-3174; (c) M. M. Green, C. Khatri, *Macromol. Symp.* **1994**, *77*, 277-282; (d) I. Rusig, M. H. Godinho, L. Varichon, P. Sixou, J. Dedier, C. Filliatre, A. F. Martins, *J. Polym. Sci. Part B:*

- Polym. Phys.* **1994**, *32*, 1907-1914; (e) V. Percec, M. Kawasumi, *Macromolecules* **1993**, *26*, 3917-3928; (f) J. C. Mastrangelo, S. H. Chen, *Macromolecules* **1993**, *26*, 6132-6134; (g) R. A. Lewthwaite, J. W. Goodby, K. J. Toyne, *J. Mater. Chem.* **1993**, *3*, 241-245; (h) M. Radianguenebaud, P. Sixou, *Mol. Cryst. Liq. Cryst.* **1992**, *220*, 53-62; (i) P. Sixou, J. M. Gilli, A. Tenbosch, F. Fried, P. Maissa, L. Varichon, M. H. Godinho, *Phys. Scr.* **1991**, *35*, 47-52; (j) L. Varichon, A. Tenbosch, P. Sixou, *Liq. Cryst.* **1991**, *9*, 701-709; (k) J. M. G. Cowie, H. W. Hunter, *Macromol. Chem. Phys.* **1991**, *192*, 143-151.
- 33 For examples of chirality inversion in LC phases see: (a) C. Y. Li, S. Jin, X. Weng, J. J. Ge, D. Zhang, F. Bai, F. W. Harris, S. Z. D. Cheng, D. H. Yan, T. B. He, B. Lotz, L. C. Chien, *Macromolecules* **2002**, *35*, 5475-5482; (b) B. P. Huff, J. J. Krich, P. J. Collings, *Phys. Rev. E* **2000**, *61*, 5372-5378; (c) A. V. Emelyanenko, M. A. Osipov, D. A. Dunmur, *Phys. Rev. E* **2000**, *62*, 2340-2352; (d) D. J. Photinos, E. T. Samulski, *Science* **1995**, *270*, 783-786; (e) I. Dierking, F. Giesselmann, P. Zugenmaier, K. Mohr, H. Zschke, W. Kuczynski, *Z. Naturforsch. A* **1994**, *49*, 1081-1086; (f) K. Radley and N. McLay, *J. Phys. Chem.* **1994**, *98*, 3071-3072; (g) P. Styring, J. D. Vuijk, I. Nishiyama, A. J. Slaney, J. W. Goodby, *J. Mater. Chem.* **1993**, *3*, 399-405; (h) A. J. Slaney, I. Nishiyama, P. Styring, J. W. Goodby, *J. Mater. Chem.* **1992**, *2*, 805-810.
- 34 D. J. Broer, I. Heynderickx, *Macromolecules* **1990**, *23*, 2474-2477.
- 35 M. Bieri, C. Gautier, T. Burgi, *Phys. Chem. Chem. Phys.* **2007**, *9*, 671-685.
- 36 V. P. Drachev, W. D. Bragg, V. A. Podolskiy, V. P. Safonov, W. T. Kim, Z. C. Ying, R. L. Armstrong, V. M. Shalaev, *J. Opt. Soc. Am. B* **2001**, *18*, 1896-1903.

- 37 I. L. Garzón, J. A. Reyes-Nave, J. I. Rodriguez-Hernández, I. Sigal, M. R. Beltrán, K. Michaelian, *Phys. Rev. B: Condens. Matter* **2002**, *66*, 0734031-4.
- 38 I. L. Garzón, M. R. Beltrán, G. González, I. Gutierrez-González, K. Michaelian, J. A. Reyes-Nava, J. I. Rodriguez-Hernández, *Eur. Phys. J. D* **2003**, *24*, 105-109.
- 39 C. E. Román-Velázquez, C. Noguez and I. L. Garzón, *J. Phys. Chem. B* **2003**, *107*, 12035-12038.
- 40 X. López-Lozano, L. A. Pérez and I. L. Garzón, *Phys. Rev. Lett.* **2006**, *97*, 233401.
- 41 A. Lechtken, D. Schooss, J. R. Stairs, M. N. Blom, F. Furche, N. Morgner, O. Kostko, B. V. Issendorff, M. M. Kappes, *Angew. Chem., Int. Ed.* **2007**, *46*, 2944-2948.
- 42 A related effect was reported for dendrimers with a chiral periphery: J. F. G. A. Jansen, H. W. I. Peerlings, E. M. M. de Brabander van den Berg, E. W. Meijer, *Angew. Chem., Int. Ed.* **1995**, *34*, 1206-1209.
- 43 (a) M. Brust, *Nat. Mater.* **2005**, *4*, 364–365; (b) A. C. Templeton, W. P. Wuelfing, R. W. Murray, *Acc. Chem. Res.* **2000**, *33*, 27-36.
- 44 (a) J. de la Venta, A. Pucci, E. Fernández Pinel, M. A. García, F. de Julián, P. Crespo, P. Mazzoldi, G. Ruggeri, A. Hernando, *Adv. Mater.* **2007**, *19*, 875-877; (b) Y. Yamamoto, H. Hori, *Rev. Adv. Mater. Sci.* **2006**, *12*, 23-32.
- 45 C. D. Geddes, A. Parfenov, I. Gryczynski, J. R. Lakowicz, *Chem. Phys. Lett.* **2003**, *380*, 269-272.
- 46 J. Müller, C. Sönnichsen, H. von Poschinger, G. von Plessen, T. A. Klar and J. Feldmann, *Appl. Phys. Lett.* **2002**, *81*, 171-173.
- 47 P. A. Kossyrev, A. Yin, S. G. Cloutier, D. A. Cardimona, H. Danhong, P. M. Alsing,

J. M. Xu, *Nano Lett.* **2005**, *5*, 1978-1981.

48 S. K. Prasad, K. L. Sandhya, G. G. Nair, U. S. Hiremath, C. V. Yelamaggad, S.

Sampath, *Liq. Cryst.* **2006**, *33*, 1121-1125.

Chapter 7: Postsynthesis Racemization and Place Exchange Reactions: Another Step to Unravel the Origin of Chirality for Chiral Ligand-Capped Gold Nanoparticles

This paper was reproduced with permission from J. Am. Chem. Soc. 2008, 130, 14201-14206. Copyright 2008 - The American Chemical Society. It is co-authored with T. Hegmann. The text is a verbatim copy of the published paper.

The concepts of chirality originating in chiral ligand-capped Au NPs were first introduced in Chapter 5. In Chapter 6, the transfer of chirality from such chiral ligand-capped Au NPs to a nematic LC host was successfully demonstrated, and such studies might well pave the way for the use of such chiral nanomaterials as chiral dopants for electro-optical LC applications. In this chapter the quest to understand the origin of chirality and metal-based electronic transitions in CD experiments will continue. Using a series of (*S*)-naproxen-decorated Au NPs (identical to the ones described in Chapters 5 and 6), this Chapter will investigate the validity of different mechanisms proposed for Au NP chirality. A powerful strategy was developed to assess the chirality of Au NPs based on post-synthesis Au NP modifications such as hydrolysis and racemization.

Abstract: We examine how postsynthesis nanoparticle ligand shell modifications as a general approach can help in the understanding of currently proposed mechanisms for gold nanoparticle chirality. We compare the CD response of chirally decorated mixed-monolayer-protected gold nanoparticles synthesized in situ with quasi-identical gold nanoparticles either prepared by place exchange reactions or subjected to an aqueous base, resulting in partial hydrolysis and simultaneous partial racemization. We find that the CD response at wavelengths where the free chiral ligand does not absorb strongly depends on the preparation conditions, i.e., in situ synthesis vs place exchange, and that postsynthesis racemization of the chiral ligand produces racemic nanoparticles with no CD response, i.e., no induction of a chiral bias during reductive nanoparticle formation. Considering all experimental results for the described gold nanoparticle system with a C₁₂H₂₄ spacer between the nanoparticle surface and chiral center, the so-called “vicinal effect” with the formation of a supramolecular assembly of the chiral moieties seems to be active. Finally, we argue that postsynthesis nanoparticle ligand shell modifications such as racemization and/or place exchange reactions are very powerful tools to unravel contributions of the different gold nanoparticle chirality mechanisms.

7.1 Introduction

The origin of chirality in gold nanoparticles (Au NPs) is still an open question, despite extensive theoretical and experimental studies in recent years [1-12]. Three possible mechanisms have been proposed by Whetten *et al.* [1] in their early paper on glutathione-protected Au NPs: (1) the metal core is chiral, as in the asymmetric structure found in Ni₁₃₉ clusters; (2) the core is achiral, but the thiol groups bound to the Au atoms

are in a chiral pattern; (3) the adsorption pattern of the head groups and the core are achiral; only the chiral adsorbate influencing the electronic structure of the metal core contributes to chirality. The first mechanism can find support from theoretical studies of Garzón *et al.* [2] and calculations of Beratan *et al.* [3] support the second mechanism, i.e., the chiral adsorption pattern. Enlightened by metal surface chirality, a related chiral footprint model was proposed by Bürgi *et al.* [4]. In contrast, Yao *et al.* prepared penicillamine-capped Au NPs[5], and more recently penicillamine-capped Ag NPs [6], and the vicinal effect related to the third mechanism was discussed as the main effect for the origin of chirality of Au NPs (although other possibilities were not ruled out in the discussion and in follow-up studies [8,9]. More recently, the intrinsic chiral properties of Au NPs have been experimentally demonstrated in a landmark paper by Kornberg *et al.* [13] The authors, using high-resolution x-ray diffraction studies, found that the overall symmetry of the discrete nonchiral *p*-mercaptobenzoic acid-protected Au NPs was chiral (5-fold decahedral symmetry) and that the sulfur atoms bound to the surface Au atoms were chiral centers. Because the capping thiol was achiral (no chiral bias), both enantiomers were found to coexist, making the whole system racemic. This result is similar to the second mechanism proposed by Whetten *et al.* and related work by other groups [1, 3, 4, 11]. The emerging questions are now the following: (i) Is it possible to favor the formation of one Au NP enantiomer over the other using chiral protecting groups in situ during synthesis? (ii) Is it possible to form a chiral core upon adsorption of a chiral group postsynthesis (either in situ or via place exchange)?

To help answer these questions and disentangle contributions from the three mechanisms, surface ligand reactions could provide some insight. To distinguish between

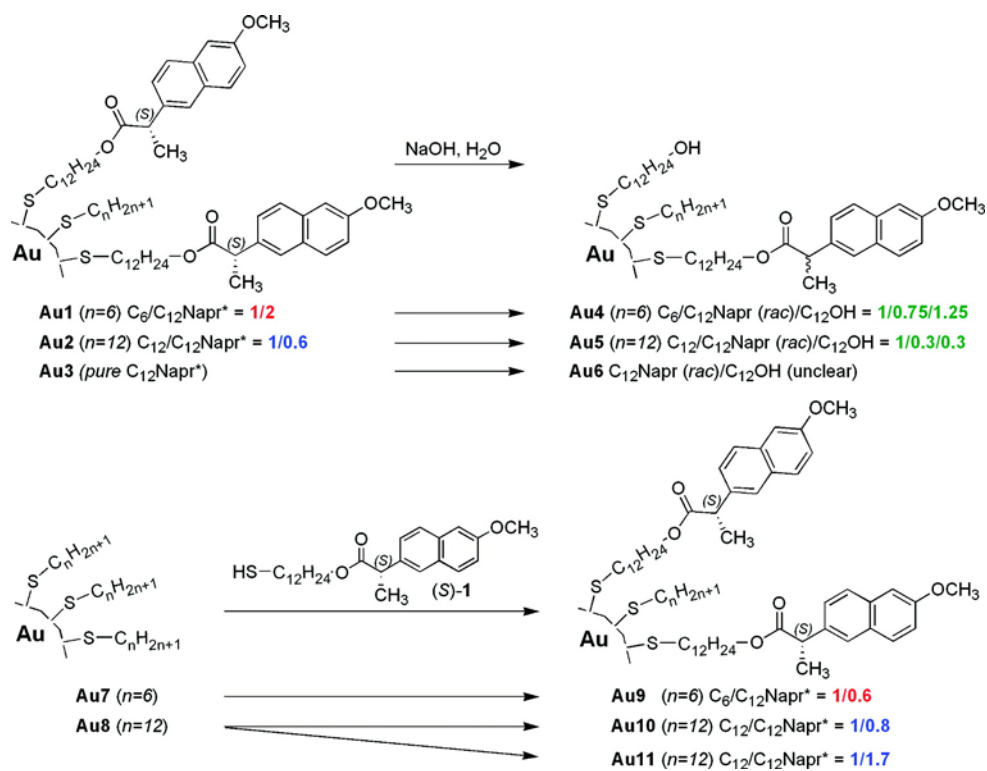
the first and second mechanisms, it is necessary to remove the possible chiral pattern by breaking the Au–S bond without affecting the core (postsynthesis NP modification) and compare the (chir)optical properties before and after. To discern the third mechanism from the other two, the strategy should be to remove the chiral centers without any effect on the surface (Au–S bond) and core. In this way, one should be able to differentiate the three possibilities and clarify major contributions in a given Au NP system. One such strategy has been used by Markovich *et al.* [7]. In their study, Ag NPs synthesized using DNA as the template showed optical activity (CD response at longer wavelengths), but NPs adsorbed postsynthesis onto DNA did not (no CD response). The authors suggested an active chiral core mechanism, although the helical DNA structure, setting this system apart from other chiral thiolate-protected Au NPs, could play a more complex role. Comparable strategies were also described for flat chiral metal surfaces [14, 15].

Initially interested in the transfer of chirality from Au NPs to liquid crystals [16], we developed chiral dopant-capped Au NPs, i.e., (*S*)-naproxen-functionalized alkanethiol [(*S*)-**1**]-capped Au NPs (**Au1–Au3**) [17], as shown in Scheme 1. In analogy to other studies, **Au1–Au3** NPs show a CD response at wavelengths where the free thiol (*S*)-**1** does not absorb (no related CD).

We here report on post-NP synthesis ligand modifications and place exchange reactions [18] to evaluate contributions of the different gold NP chirality models. First, considering the chemical structure of the (*S*)-**1** (ester with α -acidic H), hydrolysis reactions to remove chiral moieties and simultaneously racemize the chiral center [19] at the NP would give two possibilities: (i) identical CD response, meaning the Au core is chiral and/or the thiolate binding to the Au atoms is in a chiral pattern, or (ii) no CD

response, supporting the third mechanism of Whetten *et al.*[1] and Yao *et al.* [5, 6] that only the influence of the metal core's electronic structure plays a role. In a second set of experiments we introduced chiral centers to nonchiral (racemic [13]) alkanethiol-capped Au NPs (**Au7**, **Au8**) using place exchange reactions and tested the CD response, similar to the experiments by Markovich *et al.*,[7] but without the likely contributions of a helical arrangement. These methods are schematically summarized in Scheme 1, and the obtained size distributions as determined by TEM are collected in Table 1.

Scheme 1



7.2 Experimental

A description of the synthesis and characterization of **Au2** and **Au3** can be found in an earlier paper [17]. **Au1** was prepared under conditions similar to those of **Au2**, i.e., in situ synthesis of mixed-monolayer-protected Au NPs [20]. Briefly, for **Au1**, a mixture of 0.25 g (0.58 mmol) of (*S*)-**1** thiol, 0.08 mL (0.58 mmol) of hexanethiol, and 0.2 g (0.58 mmol) of $\text{HAuCl}_4 \cdot 3\text{H}_2\text{O}$ was dissolved in freshly distilled, dry, and, at least initially, peroxide-free THF (70 mL). The resulting solution was stirred for 10 min, after which a freshly prepared solution of 0.22 g (5.8 mmol) of NaBH_4 in DI water (10 mL) was added at once. The mixture was stirred for an additional 2 h, and then the solvent was evaporated under reduced pressure. The black precipitate was collected and exhaustively washed with ethanol. The purity of the nanoparticles was checked by ^1H NMR. Although for both **Au1** and **Au2** a 1:1 ratio of thiols was used during synthesis, the final NPs show different ratios (1:2 for **Au1** vs 1:0.6 for **Au2**), most probably due to (*S*)-**1** binding more easily to Au and the formation of Au NPs in the presence of the shorter hexanethiol.

The hydrolysis of the ester linkages and simultaneous racemization of the (*S*)-naproxen units (ratio \sim 1:1) for **Au1–Au3** was achieved by dissolving 10 mg of Au NPs in 40 mL of THF and addition of 20% aqueous NaOH (w/v). The solution was stirred at room temperature under an inert gas atmosphere. The amphipathic **Au6** NPs were extremely difficult to purify and unfortunately impossible to isolate, but **Au4** and **Au5** were isolated and characterized after evaporation of THF, exhaustive washing with water and ethanol, and drying under vacuum. The isolated yield of the NPs after hydrolysis/racemization (**Au4–Au6**) was about 75% (based on the average molecular weight of the gold nanoparticles assuming a spherical shape). The purity and optical activity were examined

by ^1H NMR and CD, respectively. Racemization of the (*S*)-naproxen unit under basic conditions was also pursued in control experiments using free (*S*)-**1** under identical conditions.

For the second set of reactions, **Au7** and **Au8** were first prepared using the same method as that described for **Au1–Au3**. For the place exchange reaction, 10 mg of **Au7** or **Au8** and 0.1 g of (*S*)-**1** were dissolved in 40 mL of freshly distilled, dry, and, at least initially, peroxide-free THF, and the resulting solution was stirred at room temperature for 4 days. After evaporation of the solvent, the NPs were purified by repeated washing with CH_3CN . For a second batch of **Au8**, the exchange reaction was done with twice the amount of chiral (*S*)-**1**. The isolated yield of the NPs after place exchange with (*S*)-**1** (**Au9–Au11**) was about 79% (based on the average molecular weight of the gold nanoparticles assuming a spherical shape). Purity was checked by ^1H NMR before performance of CD measurements.

Using the iodine decomposition method, the ratios between the two or three thiolates (i.e., disulfides after decomposition/oxidation) attached to the surface of all Au NPs before and after hydrolysis/racemization were determined by ^1H NMR (ratios of characteristic peaks) as described in detail by Murray *et al.* [21], and are detailed in Scheme 1 (for a collection of all ^1H NMR and UV–vis absorption spectra see the Supporting Information (SI)).

Table 7.1. Sizes (nm) and Size Distributions^a of the Investigated Au NPs **Au1–Au11**^b

Au NP	size distribution \pm SD (nm)
Au1	1.65 \pm 0.39
Au2	1.54 \pm 0.38
Au3	3.50 \pm 0.81
Au4	1.20 \pm 0.23
Au5	1.75 \pm 0.40
Au6	– ^c
Au7	1.58 \pm 0.44
Au8	1.93 \pm 0.47
Au9	1.31 \pm 0.29
Au10	1.57 \pm 0.43
Au11	1.61 \pm 0.42

^a TEM image analysis of all particles in each image was performed with the following software: Scion Image Beta 4 (Scion Corp.) and/or Image J. ^b Note that there will always be a difference in size as well as size distribution for NPs originating from a reaction of a pre-existing NP sample (e.g., Au4 from Au1) as a different NP population is imaged with (HR)-TEM. ^c Could not be isolated in pure form due to amphiphilicity of the resulting mixed-monolayer-protected Au NPs.

7.3 Results and Discussion

7.3.1 In-Situ-Synthesized Chiral Mixed-Monolayer Au NPs

Similar to other reports on chirally decorated Au NPs, **Au1–Au3** show a CD response (i.e., apparent Cotton effects) at wavelengths where the free thiol (*S*)-**1** does not absorb

light (Fig. 1c for **Au1**, Fig. 1e for **Au2**, and Fig. 1g for **Au3**). In Yao's paper [7] and in related work by other authors [3, 22], detailed discussions of the Au nanocluster electronic states are presented based on experiments by UV-vis, vis, and near-IR absorption spectroscopy. In a more recent paper by Huang *et al.* [23], two absorption maxima (bands) were detected for Au NPs in UV-vis experiments at wavelengths of 367 and 383 nm. The authors discussed these bands as originating from metal-centered (Au $5d^{10}$ to $6sp$ interband transitions) and/or ligand-metal charge-transfer transitions. Similarly for our systems presented here, the absorption peak around 380 nm (e.g., for **Au1** and **Au2**) linked to a chiral response is due to these interband and/or charge-transfer transitions. An important difference between our system and other chiral Au NPs reported in the literature is the distance of the chiral center from the Au NP surface. Arguments of whether this distance is too far to affect the electronic states of the Au NPs need to be addressed. Initial support comes from the obtained CD spectra. The CD response of **Au1–Au3** at wavelengths where the free thiol (*S*)-**1** does not absorb is one point. The second point builds on a recent paper by Rotello *et al.* [24] describing the use of chiral phenylalanine (Phe)-protected Au NPs. In their system, because the chiral center is more remote from the Au NP surface (C24 spacer), the CD response of the Au NPs is rather similar to that of the free thiol at similar wavelengths, despite the possibility of H-bonding and π - π interaction between the Phe moieties. Hence, the Au NPs in the present study should not be regarded as “simple” chiral ligand-protected Au NPs.

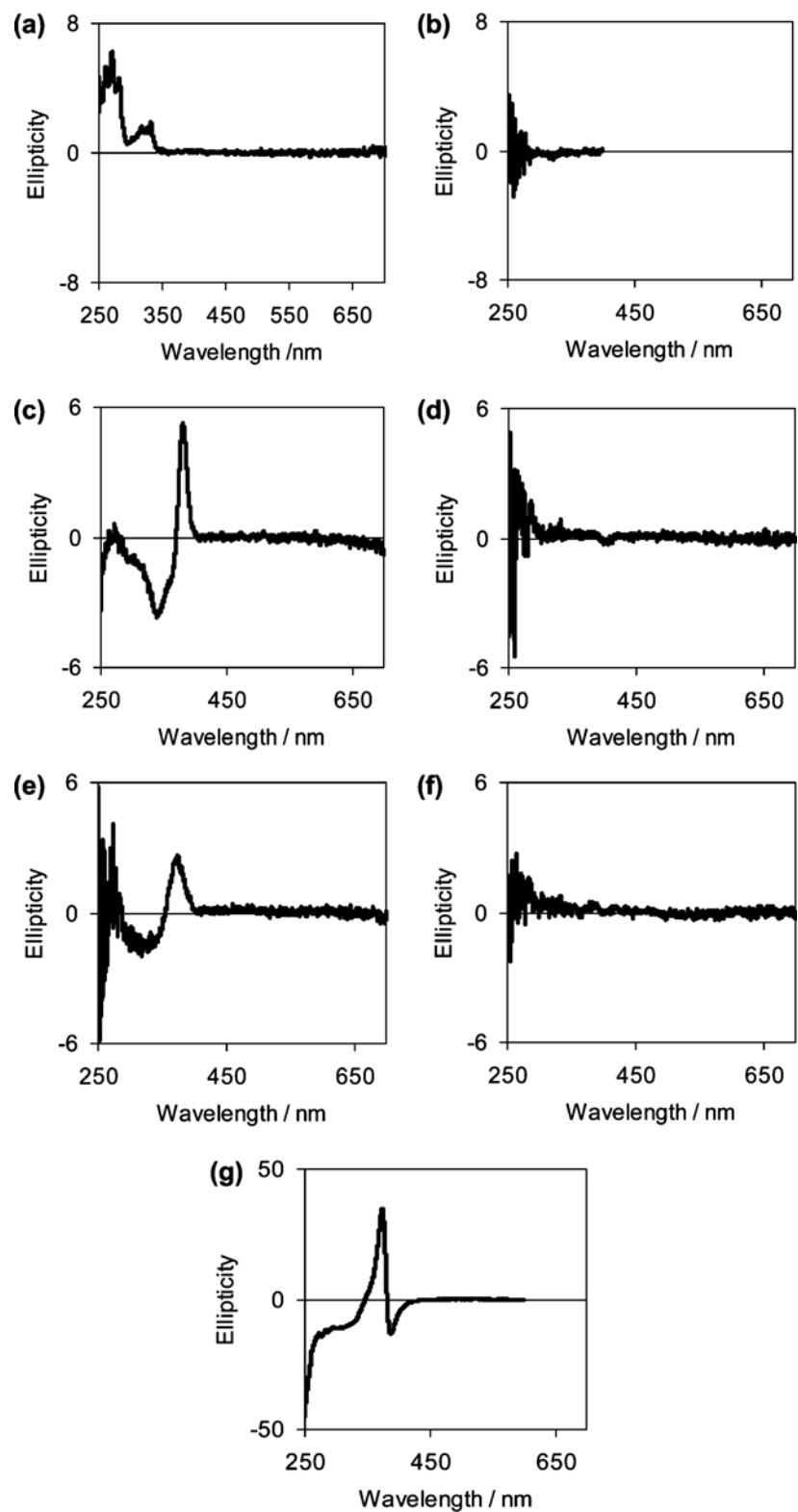


Fig. 7.1. CD spectra of (a) *(S)*-**1**, (b) (\pm) -**1** (after racemization), (c) **Au1**, (d) **Au4**, (e) **Au2**, (f) **Au5**, and (g) **Au3**.

7.3.2 Postsynthesis Racemization

As indicated above, the first step of our strategy was to racemize the chiral centers introduced during in situ mixed-monolayer-protected Au NP synthesis. The ^1H NMR spectra of both **Au4** and **Au5** (see the SI) after treatment with aqueous NaOH still show broad peaks related to the (*S*)-naproxen aromatic ring, indicating only partial removal of the chiral moiety (60% for **Au4** and 50% for **Au5**). In control experiments using free (*S*)-**1**, though much less pronounced, partial survival of the ester linkage of naproxen under these basic conditions was confirmed by NMR and TLC (matching R_f), and almost complete racemization was proven by a close to zero CD response (see Fig. 1b) in comparison to pure (*S*)-**1** with a nonzero CD spectrum with several absorption maxima below 340 nm (see Fig. 1a). Although a slight difference in reactivity between the Au NPs such as **Au1–Au3** and free (*S*)-**1** cannot be entirely excluded [25], these control experiments confirm the partial racemization/partial removal of the chiral moieties on the Au NP surface.

After hydrolysis / racemization, both **Au4** (Fig. 1d) and **Au5** (Fig. 1f) show virtually no CD response in comparison to the clearly observable Cotton effects at longer wavelength for the parent **Au1**, **Au2** (and **Au3**). These CD results confirm that postsynthesis partial removal and simultaneous racemization of the outer protective layer of the Au NPs synthesized in the presence of a chiral thiol result in macroscopic racemization of these Au NP systems. Hence, for the system presented here based on the results before and after hydrolysis and racemization, the only explanation for the CD response at longer wavelengths for **Au1–Au3** is that the chiral adsorbate influences the

electronic structure of the metal core during the reductive NP formation; i.e., the so-called “vicinal effect” [5] is active.

To rule out significant contributions of structural changes of the NP core, HR-TEM images were taken for all NPs (see Fig. 2). Considering the NPs’ small size ($\sim 1\text{--}2$ nm), the fact that TEM in this size regime is a generally unsatisfying experiment because uncertainties can be larger than the NP size distributions [26], the instrument’s resolution (~ 0.8 nm), and the limited number of NPs we can actually measure from the various images of all investigated TEM grids, no easy detectable difference of the NP shape and surface morphology before and after hydrolysis indicates that the dramatic change in CD response occurs predominantly as a result of the modification of the outer ligand shell of these Au NPs under mild basic conditions.

As can be seen from the TEM images, the as-synthesized and ligand-shell-modified Au NPs are not discrete or highly monodisperse. The hydrophobic nature of these mixed-monolayer-capped Au NPs and the impossibility to charge these NPs prevent us from using polyacrylamide gel electrophoresis (PAGE) to size separate the Au NPs (separation into batches with narrower size distribution) as described for other systems [1, 4-6, 8-11].

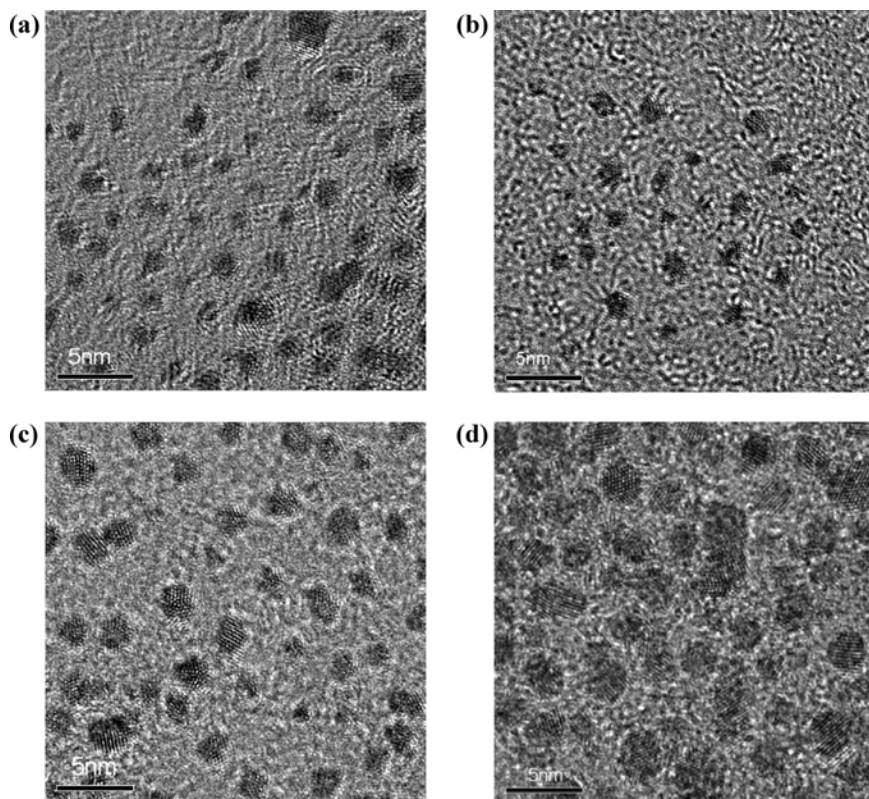


Fig. 7.2. HR-TEM images of (a) **Au1**, (b) **Au4**, (c) **Au2**, and (d) **Au5** (scale bars 5 nm). For size distributions see Table 1, and for larger images of **Au2** and **Au5** see the SI.

The obtained CD spectra are the result of mixtures of different sizes of Au NPs, although the size distributions are fairly narrow (around ± 0.35 nm). It is well-documented that different sizes of Au NPs show slightly different optical activities [6], but that chirally decorated metal NPs with related (similar) sizes commonly exhibit similar wavelengths, intensities, and signs of their CD responses. While some reports, analogous to the present investigation, deal with chiral Au NPs without size separation [7, 12], we also noticed that PAGE separation to narrow the size distribution does not necessarily produce discrete NPs [4, 6] as used in Kornberg's X-ray diffraction studies [13]. Considering the difference in CD response of **Au1** vs **Au4** and **Au2** vs **Au5** and that Whetten's third mechanism is the major contribution to the chirality of Au NPs, the size

distribution may not be the major concern, but rather the size itself. All NPs described so far (**Au1–Au5**) fall into the range of 1–2 nm, as in most other reports, and the effects of a narrower or wider size distribution across different protective ligand systems are likely difficult to assess.

7.3.3 Place Exchange Reaction

To further evaluate the validity of our findings, we also performed place exchange reactions which introduced chiral centers to nonchiral (racemic [13]) 1-hexanethiol- and 1-dodecanethiol-capped Au NPs (**Au7, Au8** → **Au9–Au11**; see Scheme 1). All ¹H NMR spectra can be found in the SI, and TEM/HR-TEM images are collected in Fig. 3.

After the place exchange reaction, **Au9** and **Au10** with less or an almost equal amount of chiral thiolate attached to the NP core (in comparison to **Au1** and **Au2**; for ratios see Scheme 1) showed almost no CD response at longer wavelengths. The obtained CD spectra appear similar to the CD spectrum of the free thiol (*S*)-**1** (CD response below 290 nm in Fig. 4a). Note here that **Au2** and **Au10** have almost identical size and size distribution. This is surprising as, for example, **Au10** is characterized by a slightly higher ratio of (*S*)-**1** attached to the NPs as compared to the in situ synthesized **Au2** (C₁₂:C₁₂Napr* = 1:0.8 for **Au10** vs 1:0.6 for **Au2**). This result clearly shows the difference between a chiral bias being present during NP formation in in situ mixed-monolayer-protected Au NP syntheses and introduction of a chiral bias after nanoparticle formation in place exchange reactions. The second batch with a C₁₂:C₁₂-(*S*)-naproxen thiolate ratio of 1:1.7 (**Au11**), however, exhibits CD response similar to that of **Au2**, which is characterized by an about 2.8-times lower (*S*)-naproxen

content (see Fig. 4b). Comparing **Au10** and **Au11** with **Au2**, or **Au9** with **Au1**, leads to an important finding, which is that the CD response at longer wavelengths is not related to single chiral adsorbates, but to a supramolecular assembly formed during nanoparticle formation and growth due to π - π stacking of (*S*)-naproxen moieties, contributing to the vicinal effect giving the related CD signal. Not clear, however, is the extent of π - π stacking involved in the supramolecular assembly that contributes to the CD response especially for **Au2**. Only about 1/3 of all thiolate protecting groups are (*S*)-naproxen-functionalized, so a “continuous network” of π - π -stacked naproxen moieties is not expected given the surface curvature of the Au NPs. However, it appears as the most reasonable explanation so far. This is also emphasized by the rather large optical activity of the true monolayer (*S*)-1-capped **Au3** NPs (see Fig. 1g), for which a complete coverage with π - π stacked naproxen moieties can be assumed. The space between the Au core and chiral center and the propensity of the ligand group to π - π stack are also critical. In the system reported by Rotello *et al.* [24] a near-quantitative place exchange led to Au NPs exclusively protected with chiral phenylalanine with no Au-related CD signal. This result was observed despite complete coverage with phenylalanine groups that could potentially participate in H-bonding interactions or π - π stacking, but would participate in the latter much less effectively than the naphthalene-derived (*S*)-naproxen.

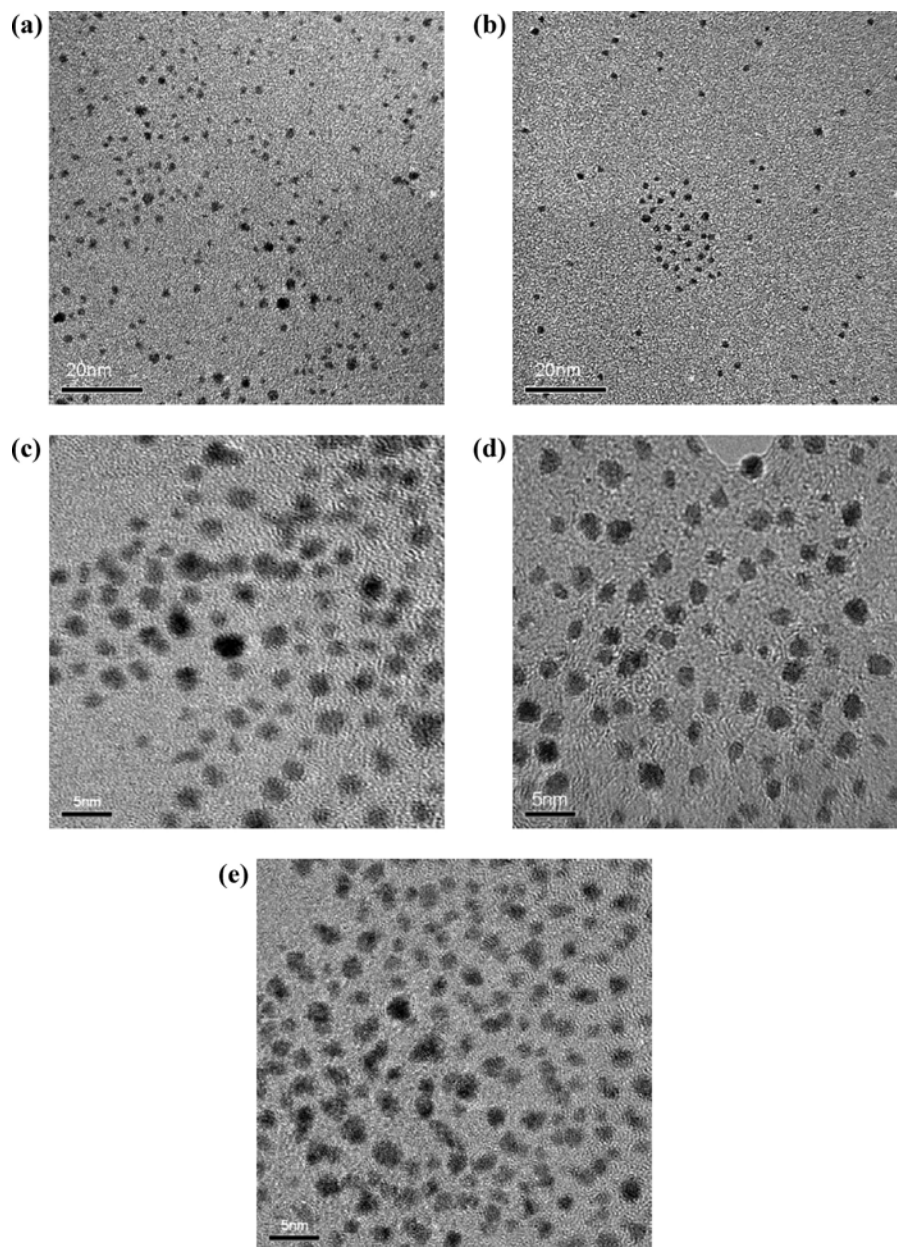


Fig. 7.3. TEM images of (a) **Au7** and (b) **Au9** (scale bars 20 nm) and HR-TEM images of (c) **Au8**, (d) **Au10**, and (e) **Au11** (scale bars 5 nm). For size distributions see Table 1.

The comparison between the **Au2/Au10** and **Au2/Au11** couples also reveals that a significantly lower amount of chiral thiol molecules on the NP surface is needed for in-situ-synthesized mixed-monolayer Au NPs to form a supramolecular assembly that

gives rise to a clear CD response at longer wavelengths. This appears to lend support to Murray's "edge and vertex" model for place exchange reactions (i.e., if place exchange reactions occur more easily at edges and vertices compared to terraces, formation of these supramolecular assemblies on NP terrace sites would require larger amounts of exchange thiols in place exchange reactions [27]. Related work by Bovet *et al.* supports the idea of a chiral supramolecular assembly resulting in a two-dimensional chiral Au surface [28].

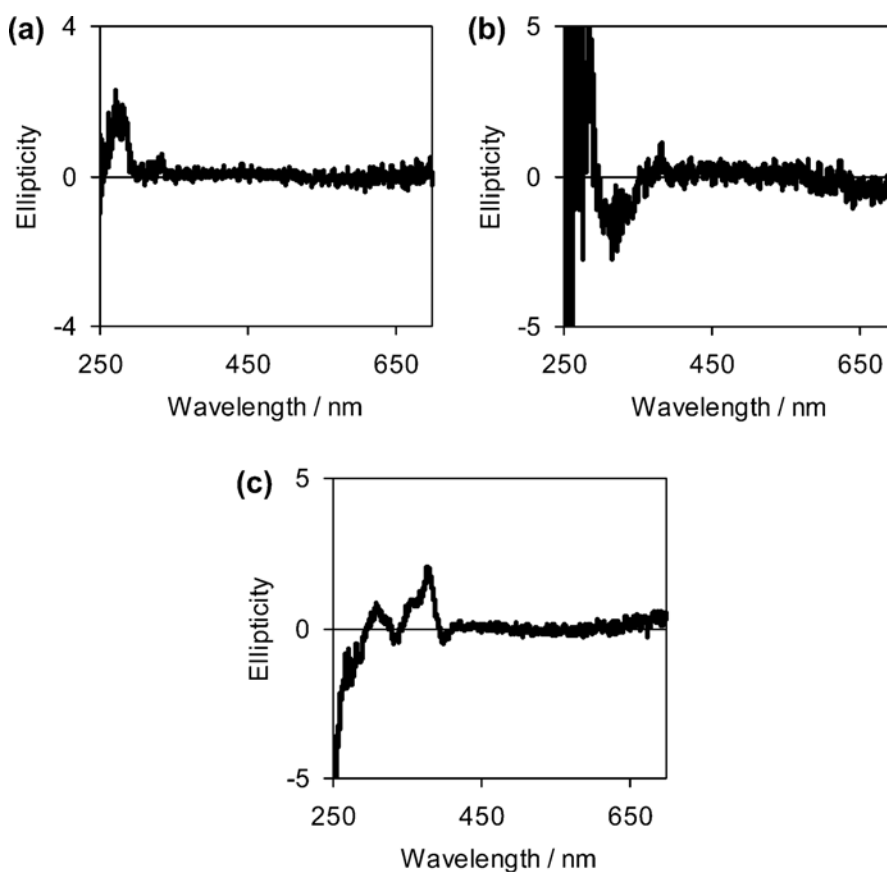


Fig. 7.4. CD spectra of (a) Au9, (b) Au10, and (c) Au11.

Despite numerous attempts to unequivocally elucidate the mechanism for metal NP place exchange reactions, some aspects of this ligand exchange remain uncertain [29-31]. Murray *et al.* showed that the place exchange reaction is inhibited under a protective

atmosphere of N₂ [29b] but more recently Bürgi *et al.* [11] using chiral thiolates, demonstrated that a place exchange reaction did occur in the absence of O₂ with the reaction completed within about 5 min, much shorter compared to previous reports. [27, 31] Hence, we foresee that chiral Au NPs could potentially serve as probes to study and better understand the mechanism of place exchange reactions.

The result of the present work, comparing the CD response of mixed-monolayer Au NPs along with the ratio of two different thiols, highlights the difference of in situ preparation vs place exchange reaction, yet the mobility of thiolates on the NP surface, as described in several studies,[29, 32] could play a key factor too. If the mobility of thiolates is high (fast distribution or segregation of different thiolates across the NP surface in solution), the initial locations of two different thiolates introduced either by in situ synthesis or via place exchange (given the edge and vertex model [27] is active) should give no difference for the chiroptical response of a bulk NP sample if the ratio of the two thiols is similar (as for **Au2** and **Au10**), because a high thiolate mobility would quickly equalize both systems. However, this is not what we observed. Other studies dealt with an inhomogeneous reactivity at different locations of the Au NP surface including the edge and vertex model [27] and other similar models and experiments. [24, 33] A possible slow migration of the thiolates (which could also lead to segregation of different thiolates on the NP surface) appears to have little effect on the chiral response we measured for the Au NP. On the basis of our current results, we consider the location (or distribution) of the two thiols on the Au NP surface to be somewhat different for the two synthesis methods. A more even distribution of the chiral thiolates during in situ synthesis appears to allow for an easier formation of a chiral supramolecular assembly

that can affect the electronic structure of the Au core. This model would also explain the amplified chiral induction of a chiral nematic liquid crystalline phase with opposite helical sense (compared to that of the free thiol (*S*)-**1**) using **Au2** or **Au3** as described in earlier studies. [16, 17] In the place exchange reactions, however, the chiral thiolates would dominate at edge and vertex sites and not at terraces (though less significant for smaller NPs), and hence, formation of such a supramolecular assembly seems less likely at lower overall chiral thiolate coverage.

7.4 Conclusion

Postsynthesis NP surface ligand reactions (i.e., racemization and hydrolysis) and place exchange reactions were pursued to elucidate the origin of chirality in chiral thiolate-protected Au NPs. In our model, on the basis of a chiral thiolate with a remote chiral center ($C_{12}H_{24}$ spacer), the formation of a supramolecular array in the NP ligand corona most strongly contributes to the so-called vicinal effect in Au NPs. For the given system, this appears to be the only effect for the observed chirality. We are currently pursuing studies on related chiral moieties with less or no aromatic content in an attempt to understand contributions from π - π stacking or other intermolecular attractive interactions such as H-bonding to the chiral response. In addition, studies at elevated temperatures as well as long-term CD experiments, given the Au NPs are stable long enough in solution as well as at higher temperatures without alteration of their size and composition (e.g., via ripening), will provide useful information with respect to thiolate mobility and its impact on the formation of a supramolecular assembly as well as the bulk chiroptic properties of such Au NPs.

Hence, we admit that the present study is not the sole answer to solving the Au NP chirality puzzle, that different mechanisms may be involved for other chiral ligand systems, and that the distance as well as the type of chiral center is critical. Far more important, from our point of view, is the presented methodology of using surface ligand reactions (racemization in particular) and the ligand place exchange reaction to remove or introduce chiral centers from or to the Au NP and at the same time avoiding significant changes to the NP core and/or the Au–S bond. The presented method has proven to be a powerful strategy to discriminate between the proposed mechanisms for Au NP chirality in our system. We therefore believe that this tactic should be a valuable tool for other chiral Au NPs and, in addition, highlights the use of chiral molecules as probes for studying molecular assemblies around Au NPs as well as investigating the edge and vertex model for place exchange reactions.[27]

Acknowledgements

This work was supported by the Natural Sciences and Engineering Research Council (NSERC) of Canada, the Canada Foundation for Innovation (CFI), and the University of Manitoba. We thank Prof. M. C. Chaturvedi, Dr. B. Tang, and Dr. H. R. Zhang for access and assistance with HR-TEM imaging and Prof. J. O’Neil for access to and valuable help with the CD measurements.

References:

1. T. G. Schaaff, R. L. Whetten, *J. Phys. Chem. B* **2000**, *104*, 2630-2641.
2. C. E. Román-Velázquez, C. Noguez, I. L. Garzón, *J. Phys. Chem. B* **2003**, *107*,

- 12035-12038.
3. M. R. Goldsmith, C. B. George, G. Zuber, R. Naaman, D. H. Waldeck, P. Wipf, D. N. Beratan, *Phys. Chem. Chem. Phys.* **2006**, *8*, 63-67.
 4. C. Gautier, T. Bürgi, *J. Am. Chem. Soc.* **2006**, *128*, 11079-11087.
 5. H. Yao, K. Miki, N. Nishida, A. Sasaki, K. Kimura, *J. Am. Chem. Soc.* **2005**, *127*, 15536-15543. Note: a detailed explanation of the vicinal effect can be found in this paper.
 6. N. Nishida, H. Yao, T. Ueda, A. Sasaki, K. Kimura, *Chem. Mater.* **2007**, *19*, 2831-2841.
 7. G. Shemer, O. Krichevski, G. Markovich, T. Molotsky, I. Lubitz, A. B. Kotlyar, *J. Am. Chem. Soc.* **2006**, *128*, 11006-11007.
 8. H. Yao, T. Fukui, K. Kimura, *J. Phys. Chem. C* **2007**, *111*, 14968-14976.
 9. N. Nishida, H. Yao, K. Kimura, *Langmuir* **2008**, *24*, 2759-2766.
 10. C. Gautier, R. Taras, S. Gladiali, T. Bürgi, *Chirality* **2008**, *20*, 486-493.
 11. C. Gautier, T. Bürgi, *J. Am. Chem. Soc.* **2008**, *130*, 7077-7084.
 12. T. Li, H. G. Park, H. -S. Lee, S. -H. Choi, *Nanotechnology* **2004**, *15*, S660-663.
 13. P. D. Jadzinsky, G. Calero, C. J. Ackerson, D. A. Bushnell, R. D. Kornberg, *Science* **2007**, *318*, 430-433.
 14. X. Zhao, *J. Am. Chem. Soc.* **2000**, *122*, 12584-12585.
 15. A. Mulligan, I. Lane, G. B. D. Rousseau, S. M. Johnston, D. Lennon, M. Kadodwala, *Angew. Chem., Int. Ed.* **2005**, *44*, 1830-1833.
 16. (a) H. Qi, J. O'Neil, T. Hegmann, *J. Mater. Chem.* **2008**, *18*, 374-380, b) H. Qi, T. Hegmann, *J. Mater. Chem.* **2008**, *18*, 3288-3294.

17. H. Qi, T. Hegmann, *J. Mater. Chem.* **2006**, *16*, 4197-4205.
18. M. J. Hostetler, S. J. Green, J. J. Stokes, R. W. Murray, *J. Am. Chem. Soc.* **1996**, *118*, 4212-4213.
19. (a) H.-Y. Lin, S. W. Tsai, *J. Molecular Catal. B* **2003**, *24-25*, 111-120, (b) S. W. Tsai, H. Wei, *J. Biocatalysis* **1994**, *11*, 33-45.
20. H. Choo, E. Cutler, Y. S. Shon, *Langmuir* **2003**, *19*, 8555-8559.
21. A. C. Templeton, M. J. Hostetler, C. T. Kraft, R. W. Murray, *J. Am. Chem. Soc.* **1998**, *120*, 1906-1911.
22. K. Nobusada, *J. Phys. Chem. B* **2004**, *108*, 11904-11908.
23. C. C. Huang, Z. Yang, K. -H. Lee, H. T. Chang, *Angew. Chem., Int. Ed.* **2007**, *46*, 6824-6828.
24. C. C. You, S. S. Agasti, V. M. Rotello, *Chem Eur. J.* **2008**, *14*, 143-150.
25. A. J. Kell, R. L. Donkers, M. S. Workentin, *Langmuir* **2005**, *21*, 735-742.
26. A. Dass, A. Stevenson, G. R. Dubay, J. B. Tracy, R. W. Murray, *J. Am. Chem. Soc.* **2008**, *130*, 5940-5946.
27. M. J. Hostetler, A. C. Templeton, R. W. Murray, *Langmuir* **1999**, *15*, 3782-3789.
28. N. Bovet, N. McMillan, N. Gadegaard, M. Kadodwala, *J. Phys. Chem. B* **2007**, *111*, 10005-10011.
29. (a) Y. Song, R. W. Murray, *J. Am. Chem. Soc.* **2002**, *124*, 7096-7102.
(b) Y. Song, T. Huang, R. W. Murray, *J. Am. Chem. Soc.* **2003**, *125*, 11694-11701.
30. (a) P. Ionita, B. C. Gilbert, V. Chechik, *Angew. Chem., Int. Ed.* **2005**, *44*, 3720-3722; (b) P. Ionita, A. Caragheorgheopol, B. C. Gilbert, V. Chechik, *Langmuir* **2005**, *20*, 11536-11544.

31. A. Kassam, G. Bremner, B. Clark, G. Ulibarri, R. B. Lennox, *J. Am. Chem. Soc.* **2006**, *128*, 3476-3477.
32. (a) R. S. Ingram, M. J. Hosteler, R. W. Murray, *J. Am. Chem. Soc.* **1997**, *119*, 9175-9178; (b) A. Centrone, Y. Hu, A. M. Jackson, G. Zerbi, F. Stellacci, *Small* **2007**, *3*, 814-817; (c) A. K. Boal, V. M. Rotello, *J. Am. Chem. Soc.* **2000**, *122*, 734-735.
33. (a) H. S. Mandal, H. B. Kraatz, *J. Am. Chem. Soc.* **2007**, *129*, 6356-6357; (b) G. A. Devries, M. Brunnbauer, Y. Hu, A. M. Jackson, B. Long, B. T. Neltner, O. Uzun, B. H. Wunsch, F. Stellacci, *Science* **2007**, *315*, 358-361.

Appendix C

Supplementary Information for Chapter 7

1. Instrumentation and Measurements

CD spectra were recorded on a J-810 spectropolarimeter (Jasco Inc.) using a bandwidth of 2 nm. Solvents for CD spectroscopy were CHCl_3 and THF (HPLC, Spectrophotometry grade) from Fisher Scientific. THF for synthesis was dried with Na/benzophenone and freshly distilled under N_2 . ^1H NMR spectra were recorded with a Bruker Advance 300 spectrometer. Transmission electron microscopy (TEM) images were obtained on a JEOL FX 2000 instrument (accelerating voltage 160 kV). High-resolution transmission electron microscopy (HR-TEM) was carried out using JEOL FEG-T/STEM operating at an acceleration voltage of 200 kV. A drop (10 μl) of the isolated gold colloid solutions was drop-cast on carbon coated copper grids (400 mesh) and dried in air.

2. CD and UV-vis spectra (collected)

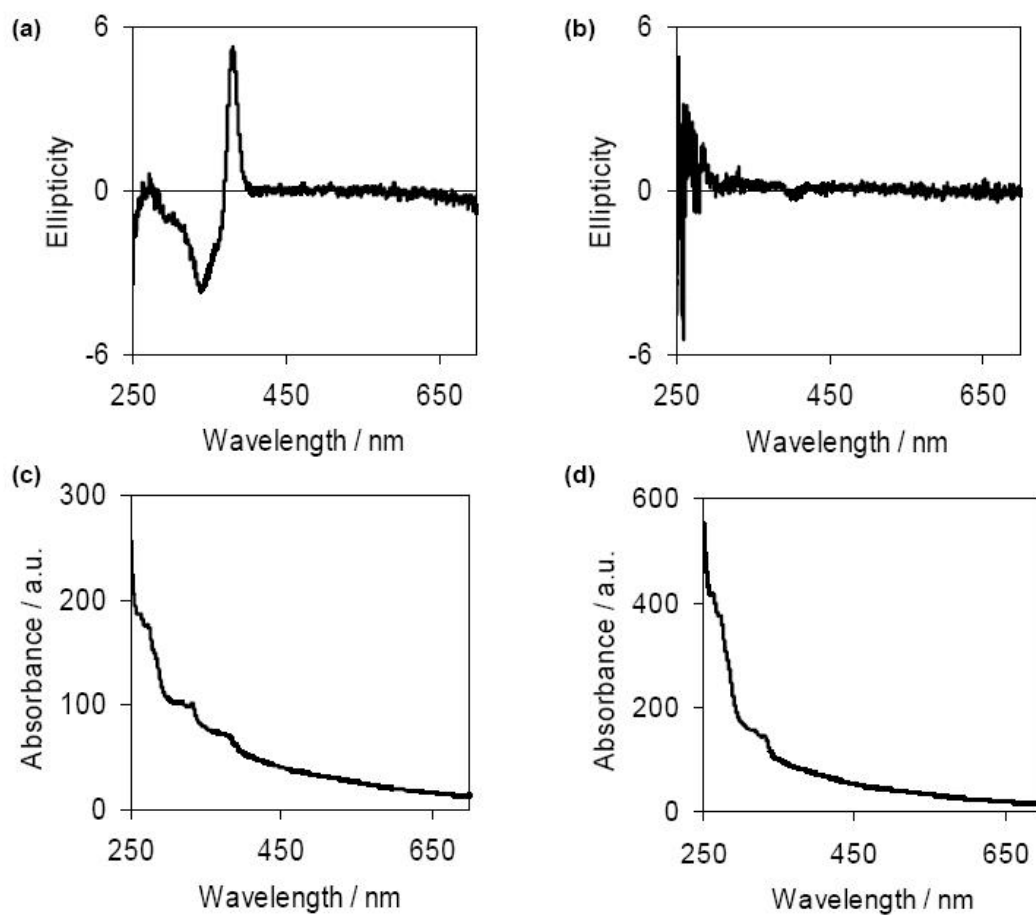


Fig. S7.1. CD spectra of: (a) **Au1**, (b) **Au4**. Absorption spectra from CD measurements of: (c) **Au1**; (d) **Au4**.

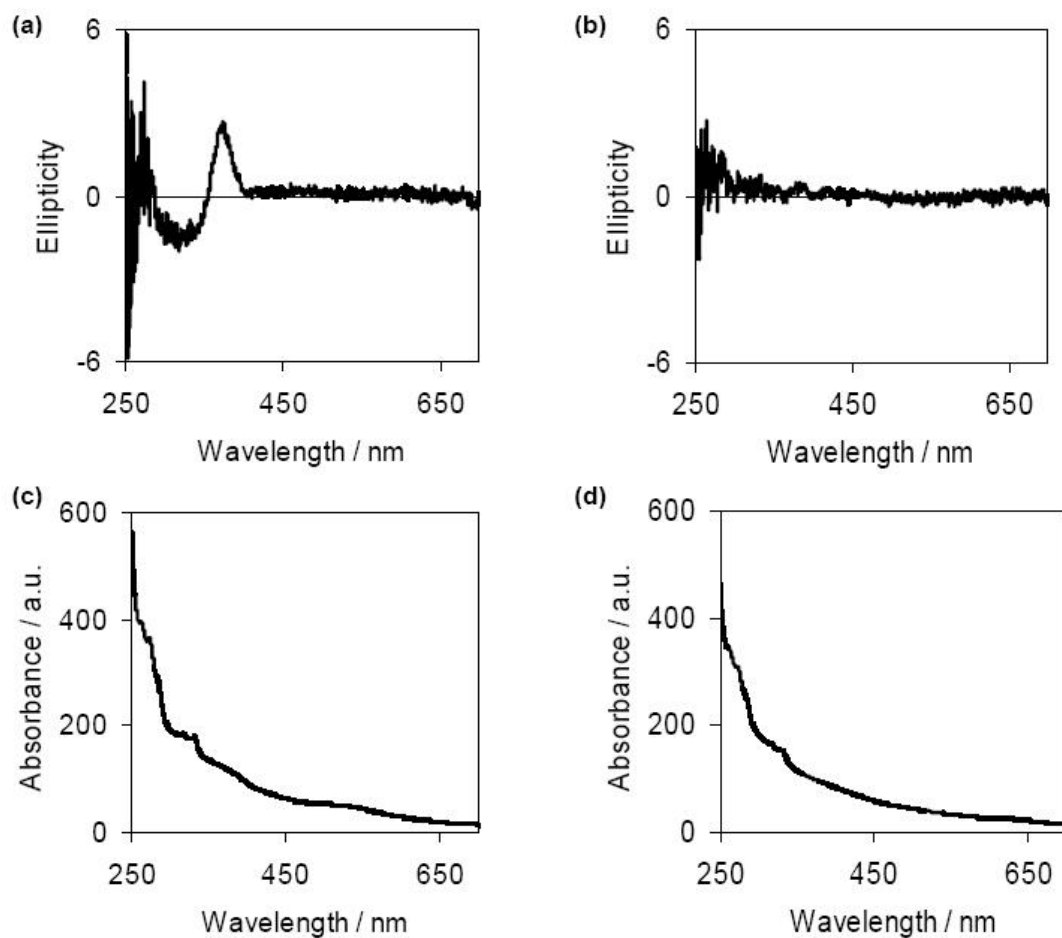


Fig. S7.2. CD spectra of: (a) **Au2**, (b) **Au5**; Absorption spectra from CD measurements of: (c) **Au2**, (d) **Au5**.

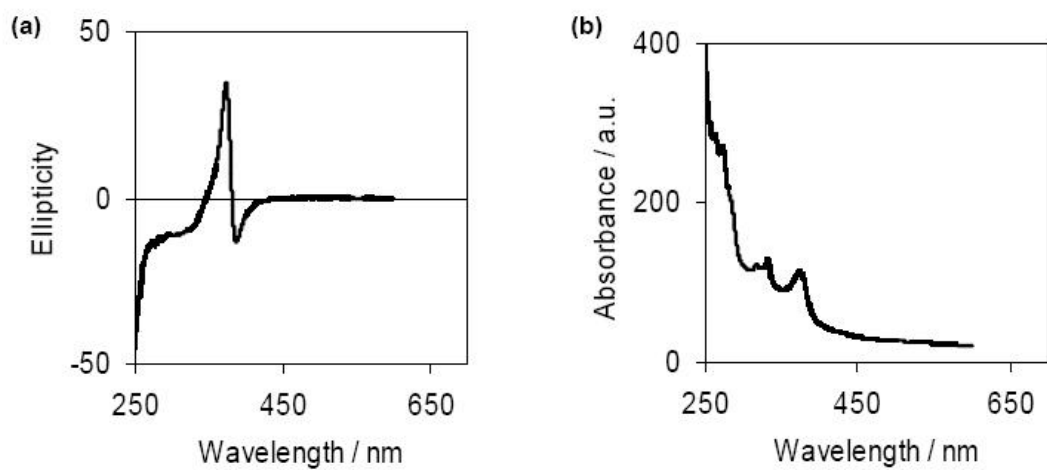


Fig. S7.3. (a) CD spectrum of **Au3**. (b) Absorption spectrum from CD measurement of **Au3**.

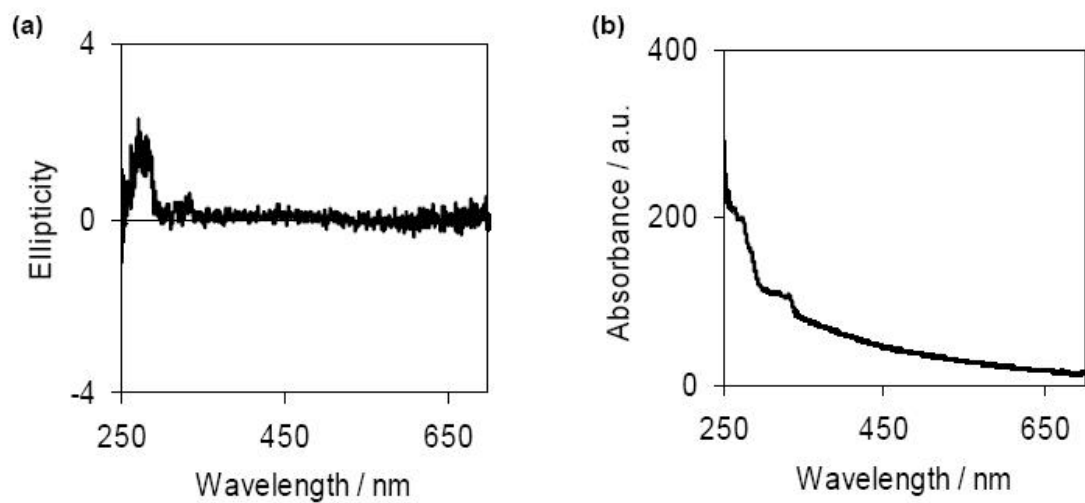


Fig. S7.4. (a) CD spectrum of **Au9**. (b) Absorption spectrum from CD measurement of **Au9**.

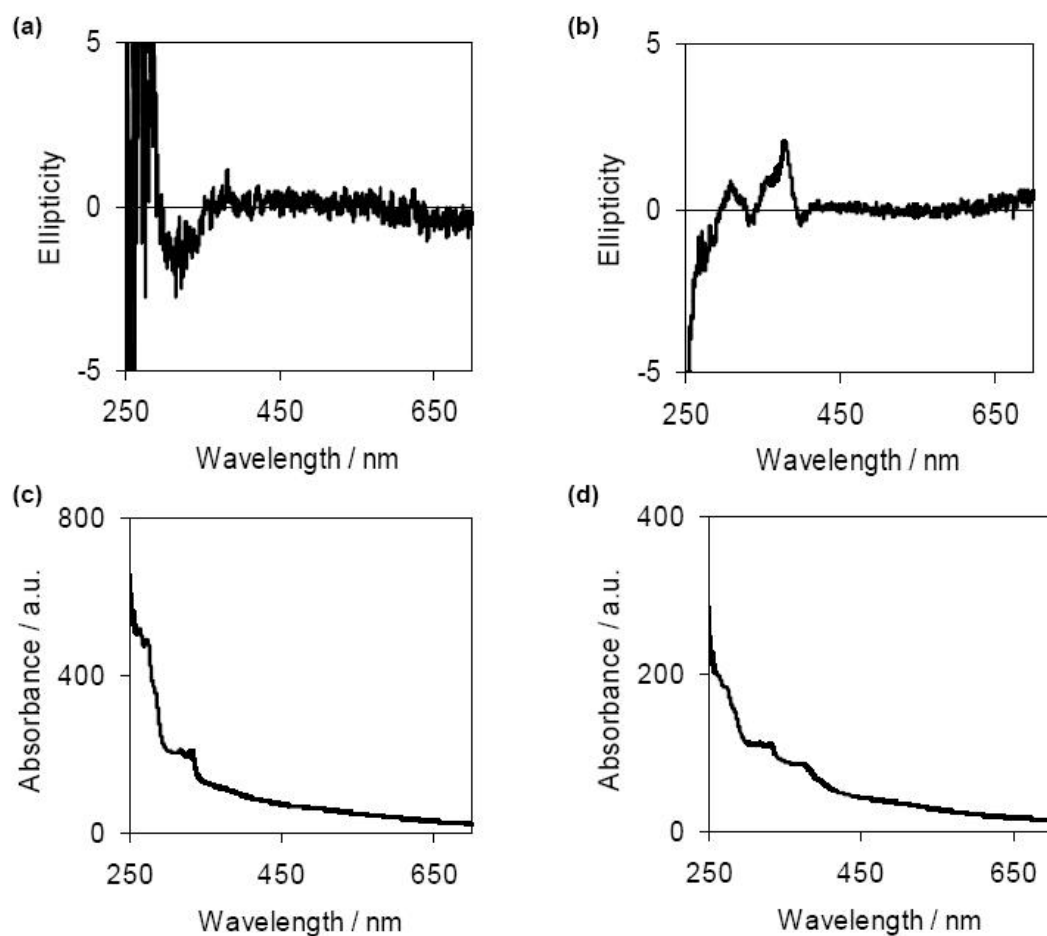


Fig. S7.5. CD spectra of: (a) **Au10**, (b) **Au11**. Absorption spectra from CD measurements of: (c) **Au10**, (d) **Au11**.

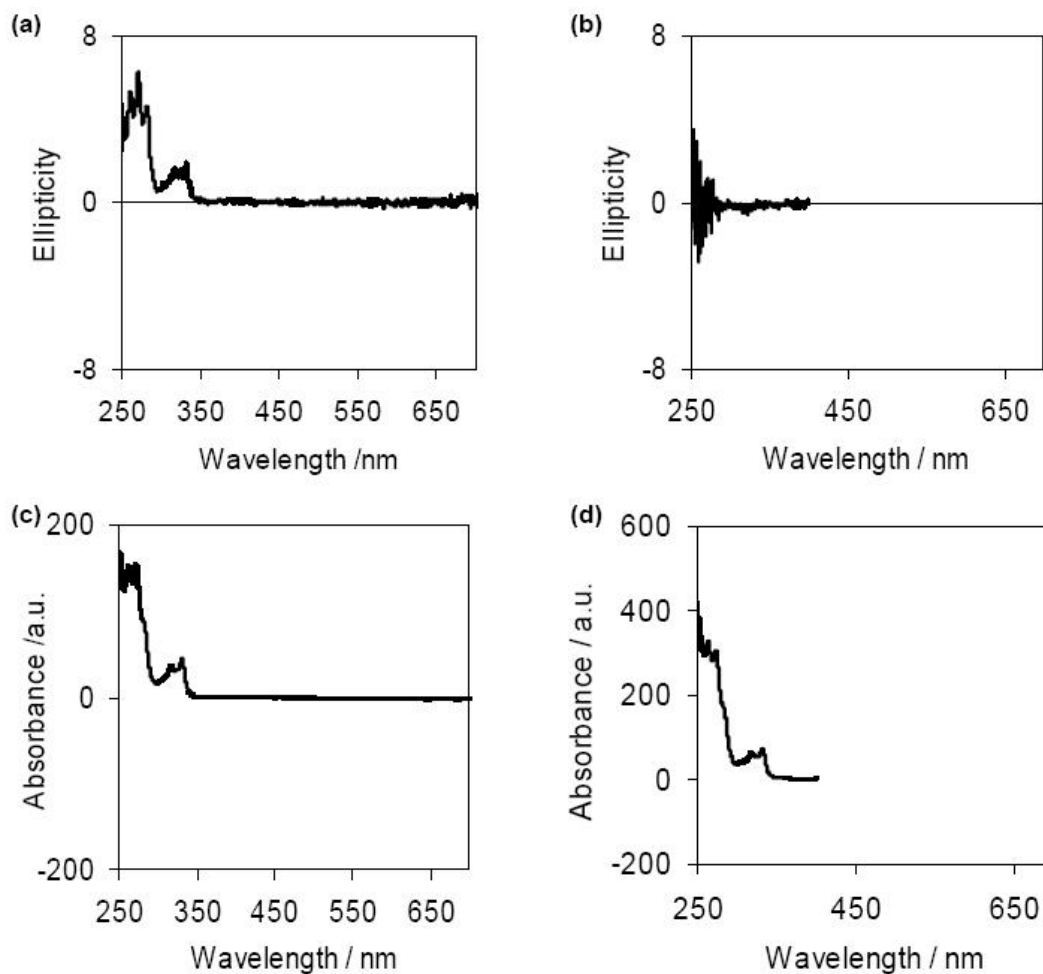
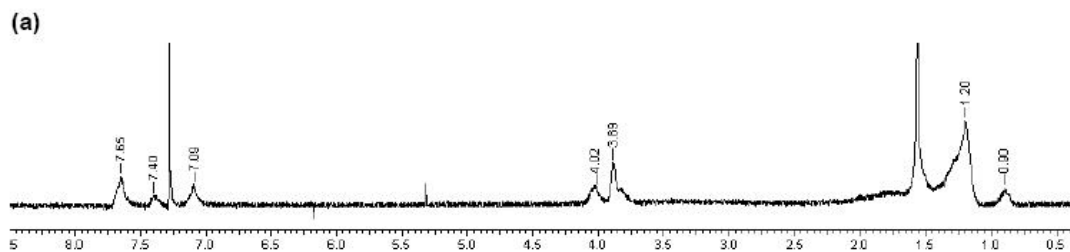


Fig. S7.6. CD spectra of: (a) (*S*)-**1**, (b) (*S*)-**1** after racemization. Absorption spectra from CD measurements (HT) of: (c) (*S*)-**1**; (d) (*S*)-**1** after racemization.

3. ^1H NMR spectra of (*S*)-**1** and the Au NPs before and after Murray's I_2 decomposition



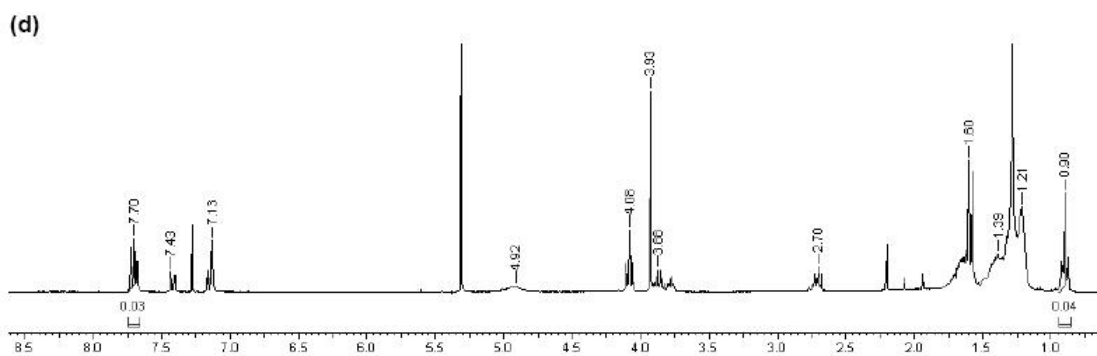
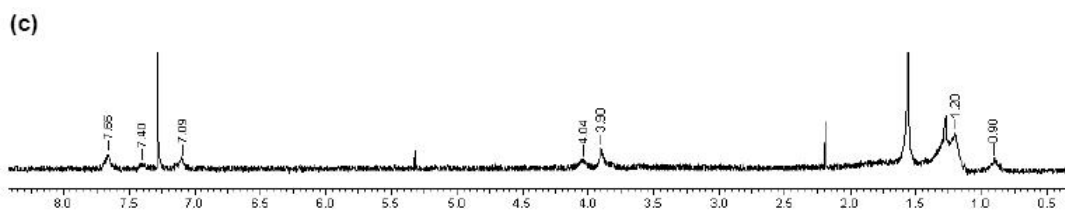
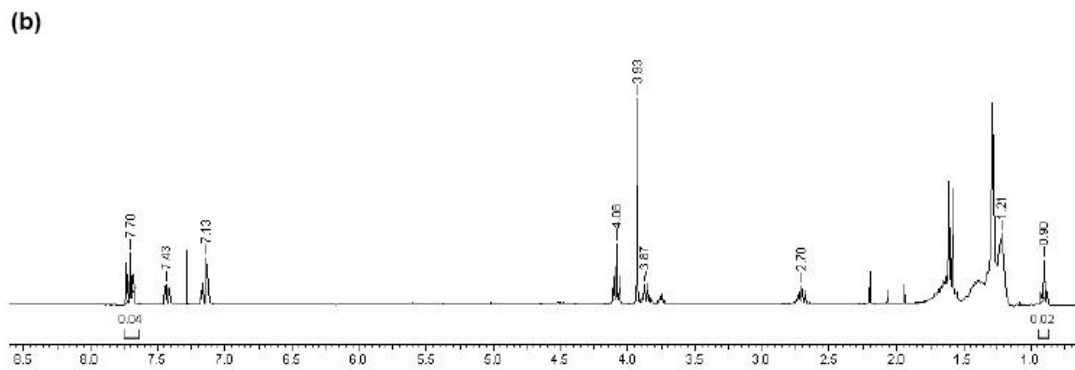
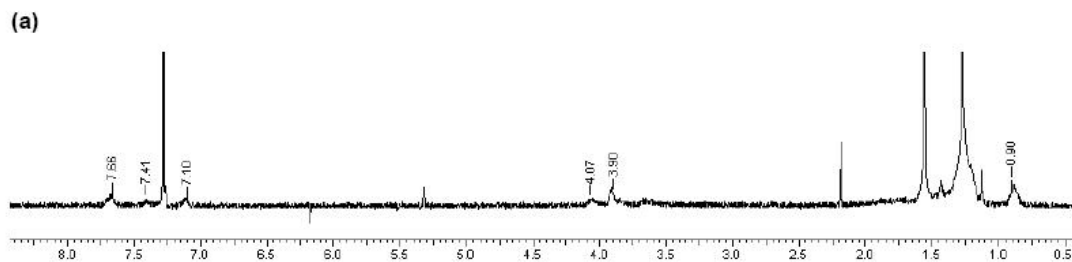


Fig. S7.7. ^1H NMR spectra of: (a) **Au1**; (b) **Au1** after I_2 induced NP decomposition.; (c) **Au4**; (d) **Au4** after I_2 induced NP decomposition.



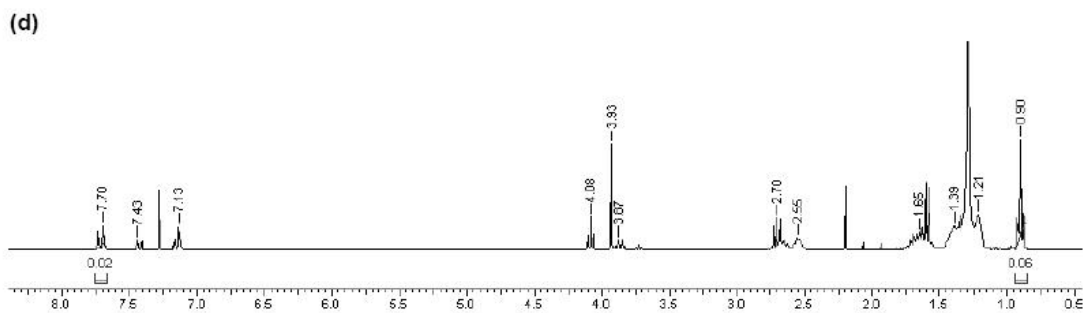
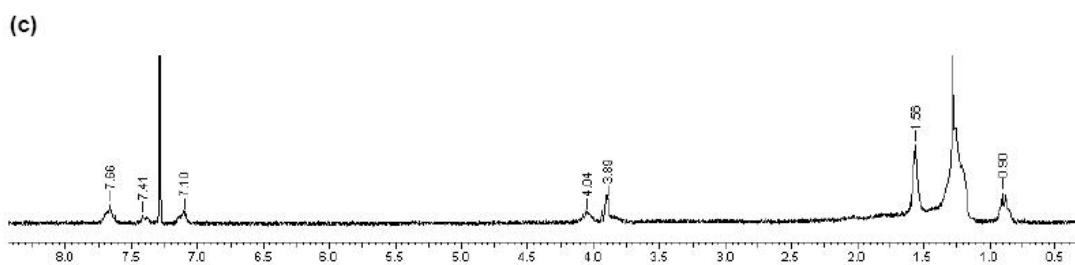
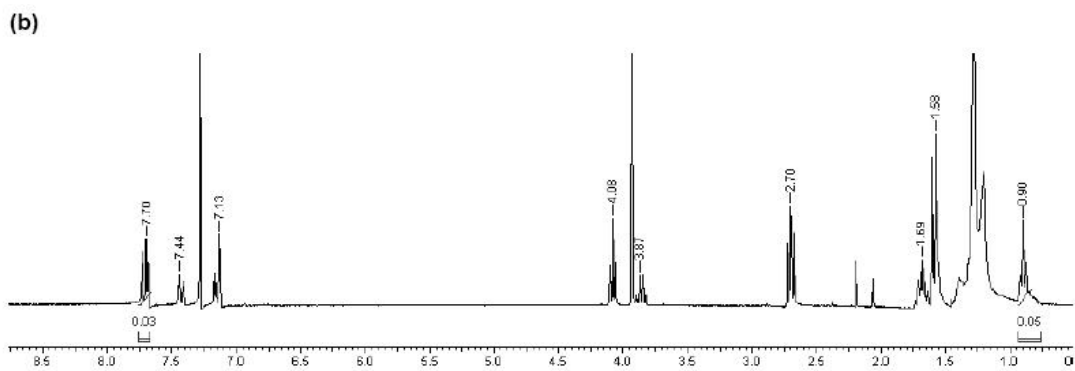
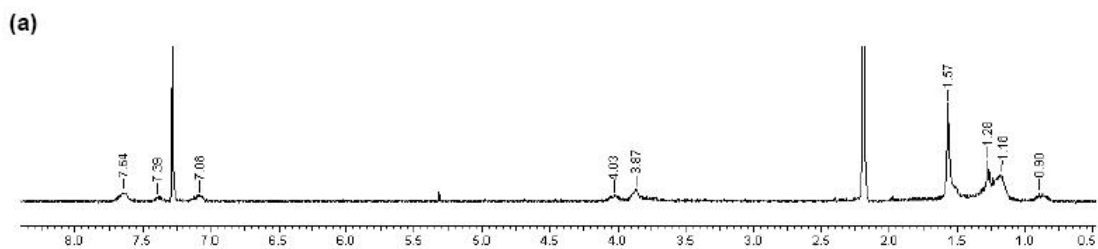


Fig. S7.8. ^1H NMR spectra of: (a) **Au2**, (b) **Au2** after I_2 induced NP decomposition, (c) **Au5**; (d) **Au5** after I_2 induced NP decomposition.



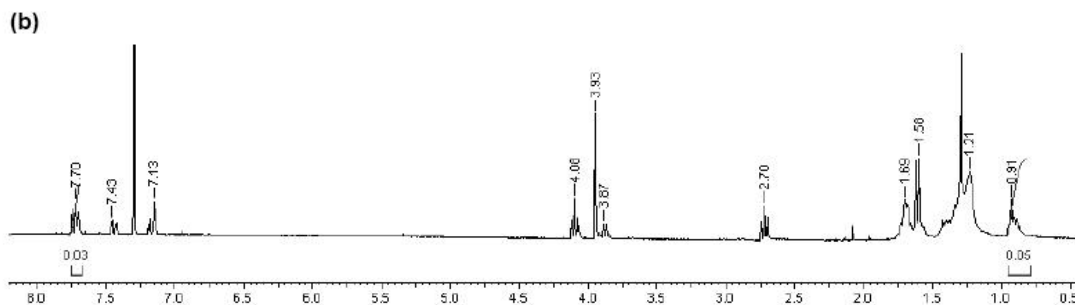


Fig. S7.9. ^1H NMR spectrum of (a) **Au9**; (b) **Au9** after I_2 induced NP decomposition.

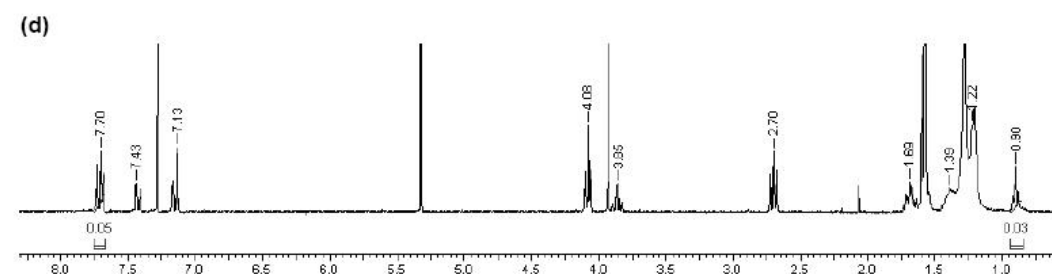
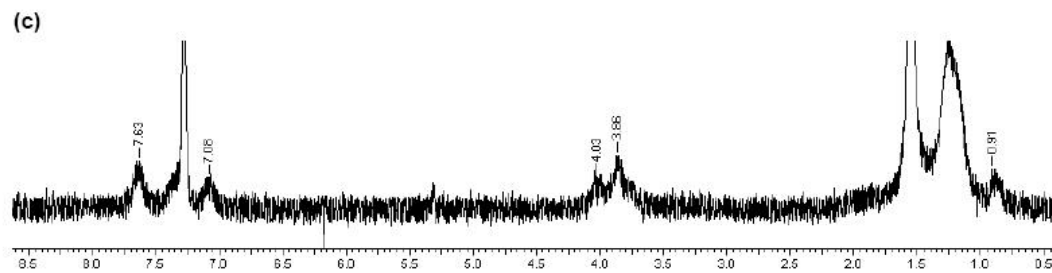
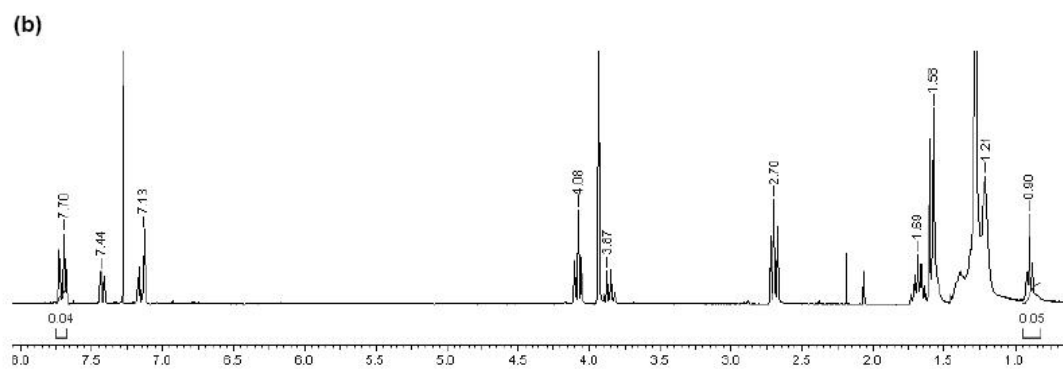
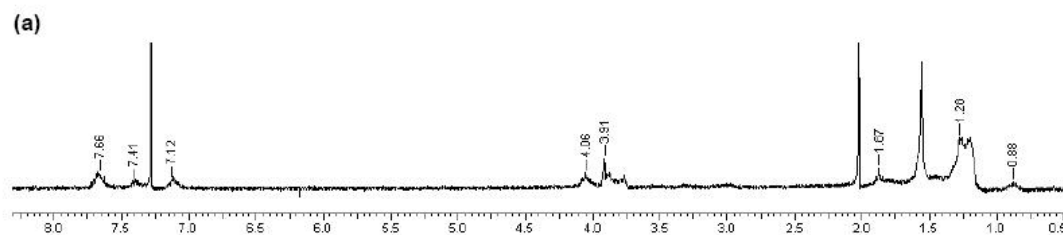


Fig. S7.10. ^1H NMR spectra of: (a) **Au10**; (b) **Au10** after I_2 induced NP decomposition, (c) **Au11**; (d) **Au11** after I_2 induced NP decomposition

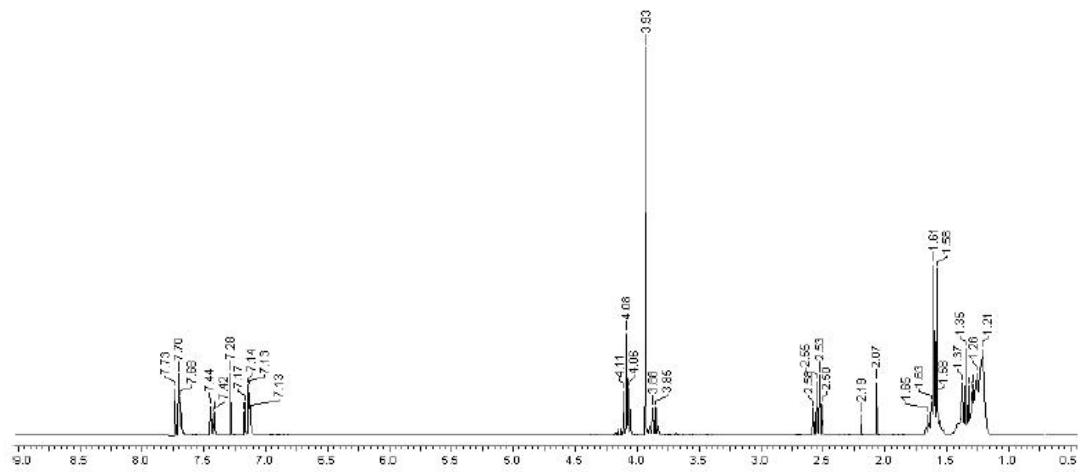
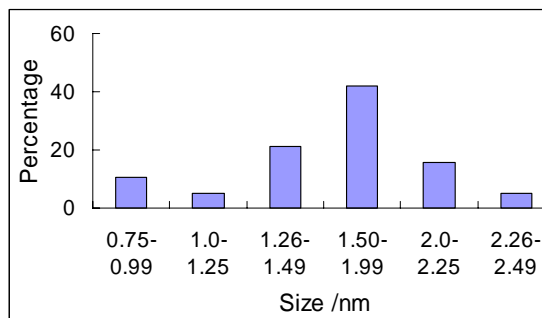
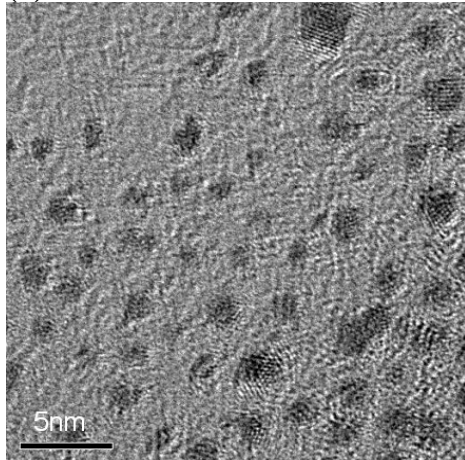


Fig. S7.11. ¹H NMR spectrum of (S)-1.

4. TEM/HR-TEM images of the Au NPs and size distribution histograms

(a)



(b)

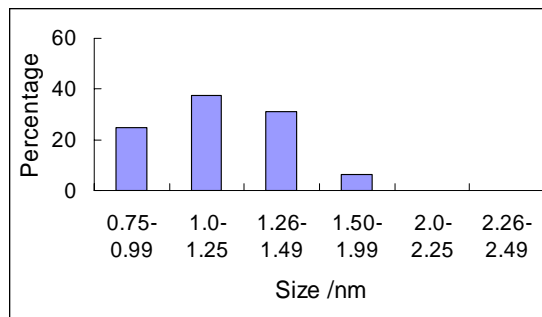
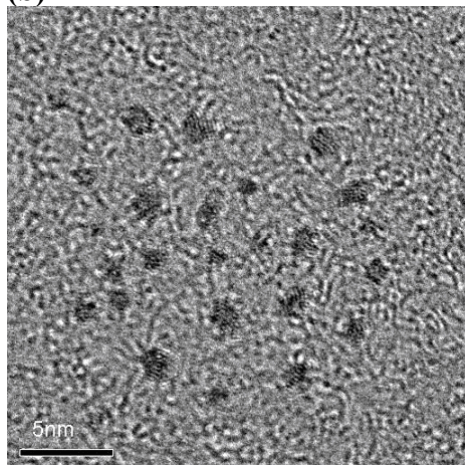


Fig. S7.12. HR-TEM images and size distribution histograms: (a) **Au1**; (b) **Au4** (scale bars: 5 nm).

Note: A TEM image of the **Au3** NPs was published in H. Qi, T. Hegmann, *J. Mater. Chem.* **2006**, *16*, 4197-4205 (Chapter 5).

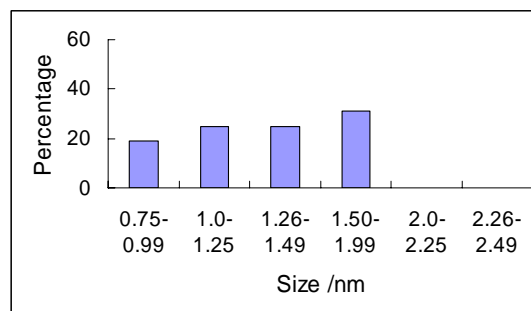
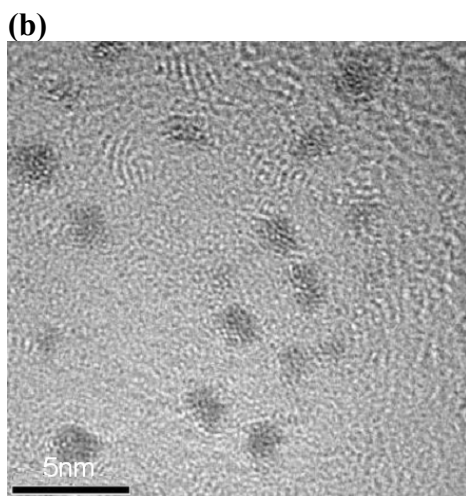
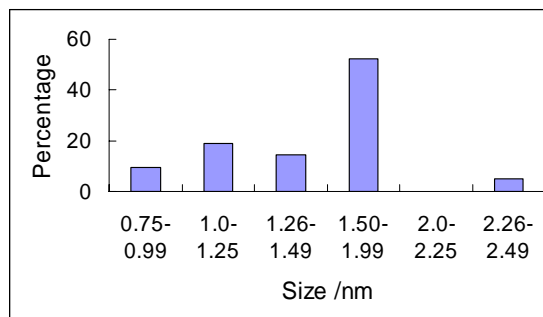
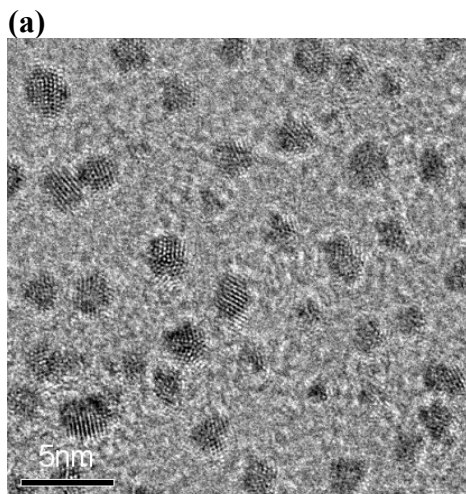


Fig. S7.13. HR-TEM images and size distribution histograms of: (a) **Au2**; (b) **Au5** (scale bars: 5 nm).

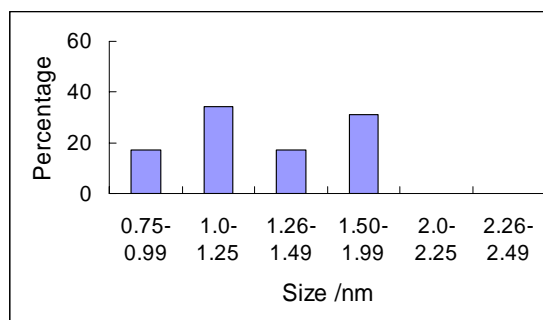
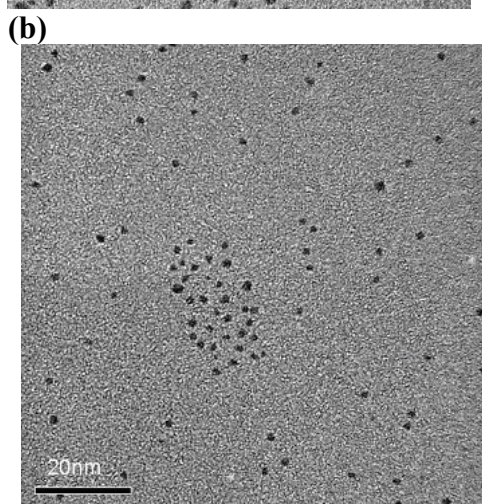
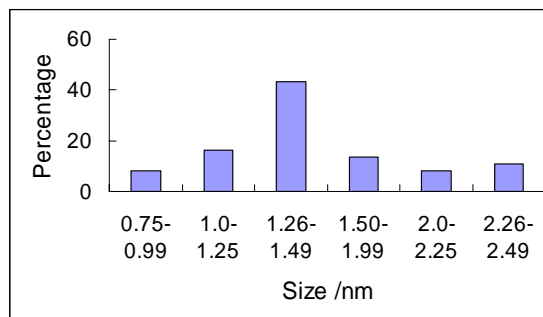
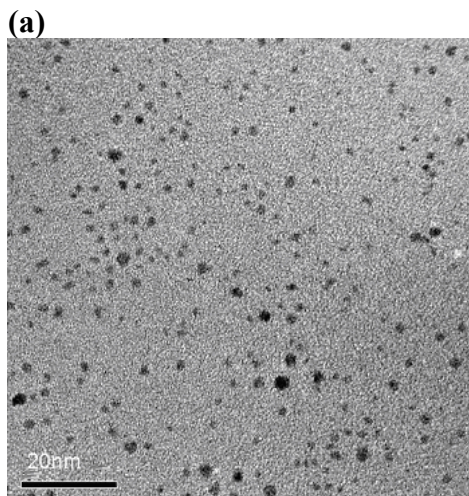


Fig. S7.14. TEM images and size distribution histograms of: (a) **Au7**, (b) **Au9** (scale bars: 20 nm).

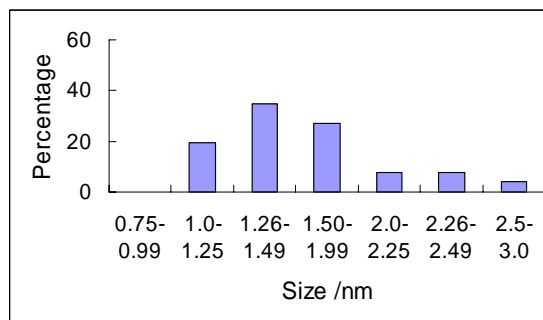
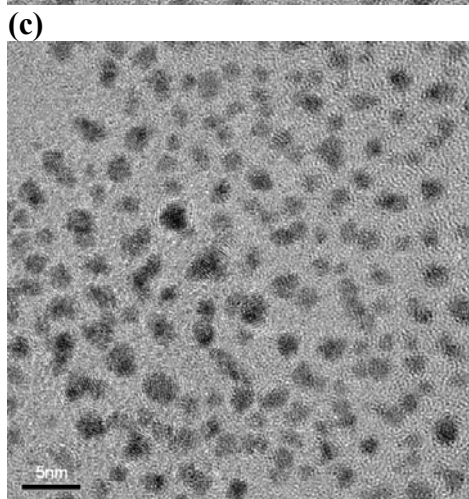
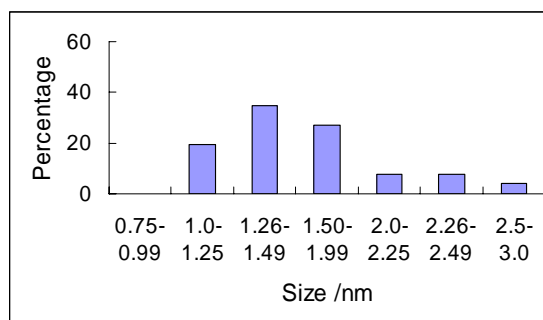
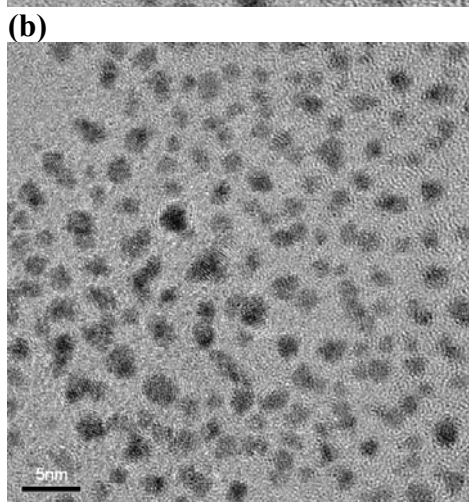
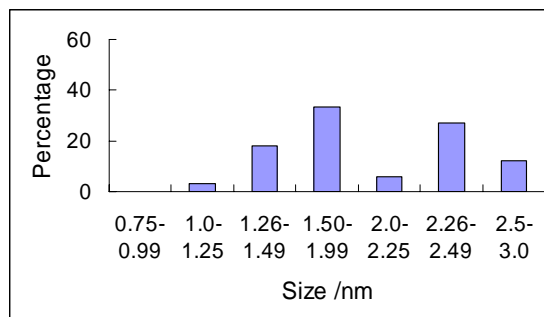
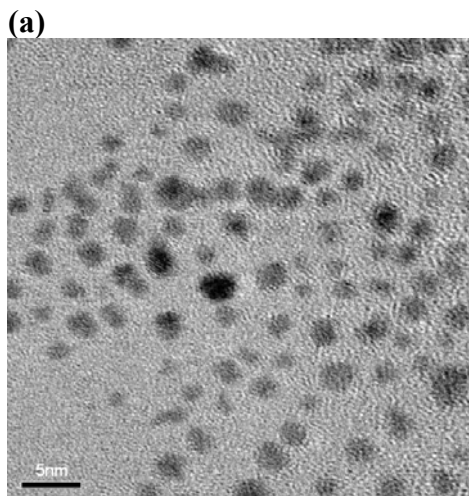
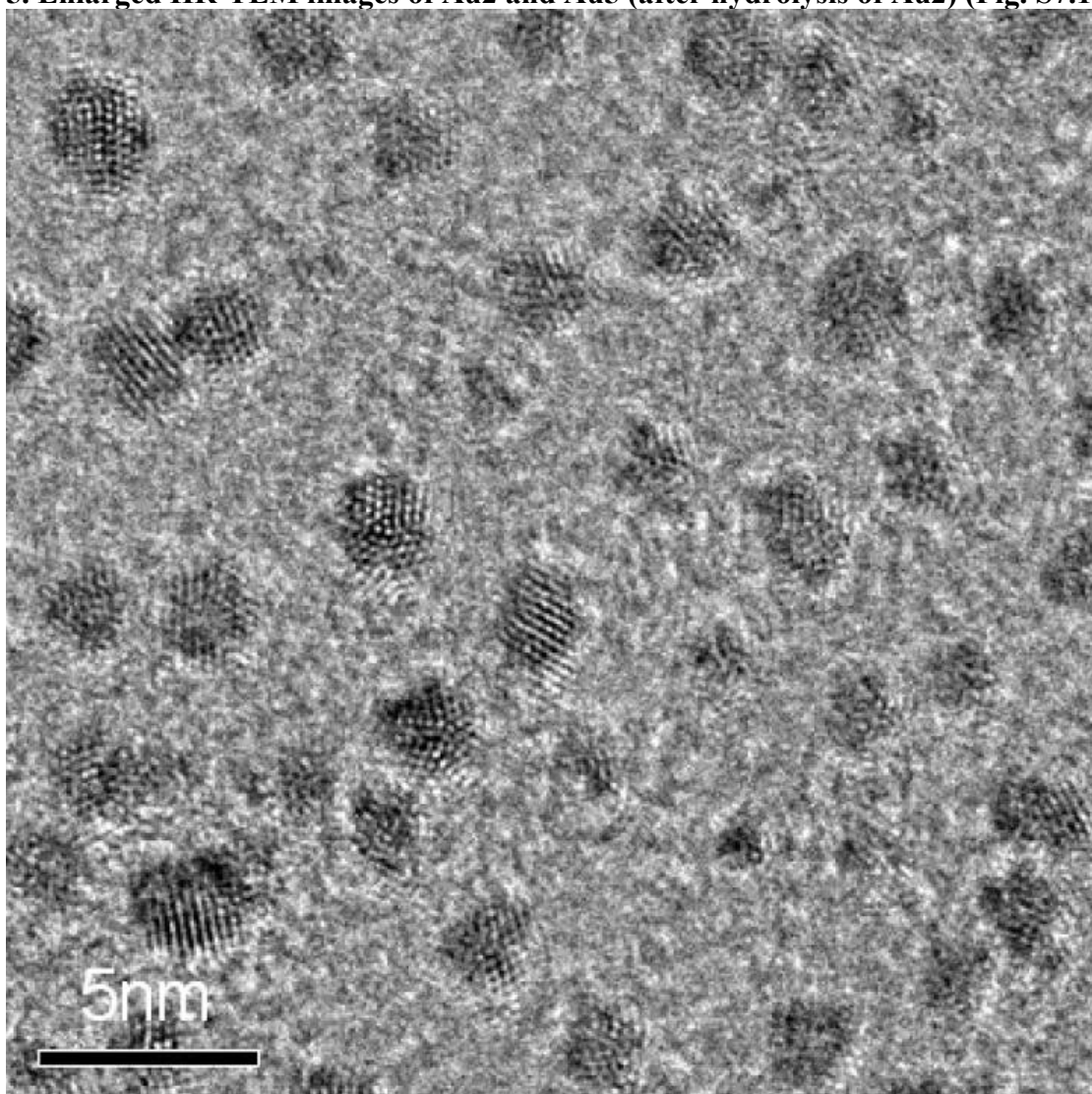
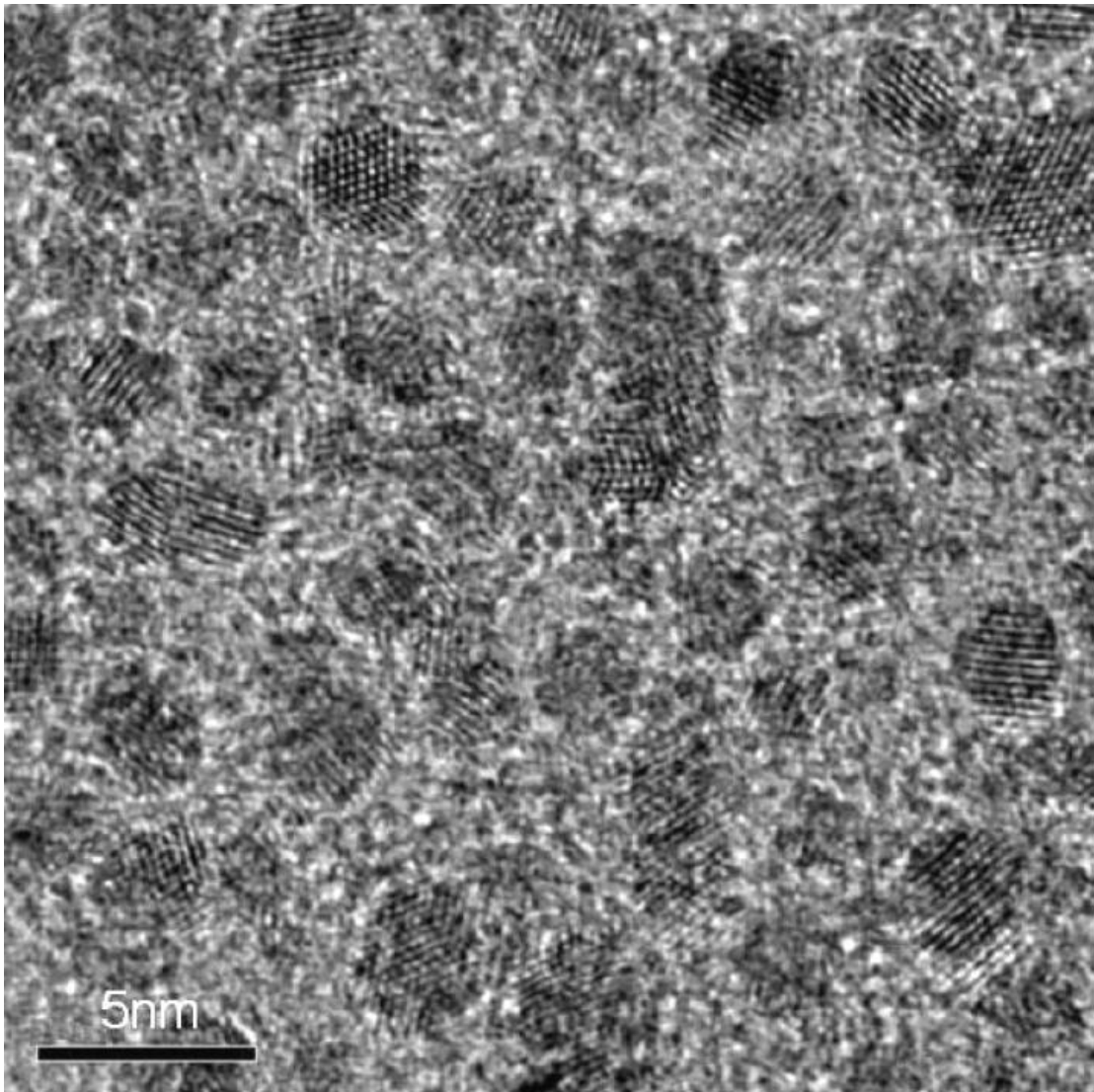


Fig. S7.15. HR-TEM images and size distribution histograms of: (a) **Au8**; (b) **Au10**; (c) **Au11** (scale bars: 5 nm).

5. Enlarged HR-TEM images of Au2 and Au5 (after hydrolysis of Au2) (Fig. S7.16)





Chapter 8: Unprecedented Dual Alignment Mode and Freedericksz Transition in Planar Nematic Liquid Crystal Cells Doped with Gold Nanoclusters

This paper was reproduced with permission from Adv. Funct. Mater. 2008, 18, 212-221.

Copyright - 2008 WILEY-VCH Verlag GmbH & Co. KGaA, Weinheim. It is co-authored with B. Kinhead and T. Hegmann. The text is a verbatim copy of the published paper.

In Chapter 5, the origin of periodic birefringent stripes separated by domains with homeotropic alignment was described and discussed. The similarity of these textures with chiral nematic textures featuring a long helical pitch promoted additional investigations using circular dichroism spectropolarimetry (Chapter 6). These investigations successfully proved one of the two scenarios proposed in Chapter 5 (i.e., the transfer of chirality from chiral ligand-capped Au NPs to the nematic LC host). Chapter 8 will now focus on the domains showing homeotropic alignment of the nematic LCs. It will be demonstrated that this phenomenon can be exploited to promote and control the alignment of nematic LC molecules via NP doping. In due course, we found a unique dual alignment and electro-optical switching mechanism in planar LC cells. Detailed electro-optic studies of these cells also revealed new insights into the beneficial effects of nanoparticle doping of nematics with respect to display applications.

Abstract: We demonstrate that alkylthiol-capped gold nanoclusters doped into nematic liquid crystals (N-LCs) with positive dielectric anisotropy give rise to an unprecedented dual alignment mode and electro-optical response, which has a potential impact on current liquid crystal (LC) display technologies and N-LC optical-biosensor design. By fine-tuning experimental conditions (temperature, electric field, and alignment), N-LCs doped with gold nanoclusters can be aligned and electrically reoriented either like N-LCs with a positive dielectric anisotropy in a planar cell or, alternatively, as N-LCs with a negative dielectric anisotropy in a homeotropic cell, both at lower threshold voltages than the pure N-LC.

8.1. Introduction

The response of a nematic liquid crystal (N-LC) to an applied electric field is an important property used in many device and display applications [1]. The ability of the director (parallel to the long molecular axis for a rodlike N-LC) to align along an external field results from the electric nature of the molecules. In the absence of external perturbations, the director of an N-LC is free to assume any orientation, but can be forced to point in a specific direction using planar [2] or homeotropic alignment layers [3]. Depending on initial alignment conditions, sign of the dielectric anisotropy, as well as electric field direction and strength, different director configurations can be induced [4,5].

The N-LC phase is characterized by molecules that have no positional order but tend to orient, when averaged over time, in the same direction (along the director, \mathbf{n}). Two major types of N-LCs can be distinguished that are currently used in different LC display technologies. N-LC molecules can possess a permanent or induced dipole either along

(used in twisted nematic (TN) cells [6] or in-plane switching (IPS) mode [7] displays) or across the long molecular axis (used in vertical alignment (VA) mode displays) [8].

Upon applying an electric field above a certain threshold ($E > E_{th}$), if the dipole moment is parallel (or almost parallel) to the long molecular axis, the N-LC possesses a positive dielectric anisotropy, $\Delta\epsilon > 0$ ($\epsilon_{||} > \epsilon_{\perp}$), and the director tends to orient along the electric field E direction (Fig. 8.1a and c and Supporting Information (SI)). If the dipole moments of the molecules are more or less normal to the long molecular axis, the N-LC possesses a negative dielectric anisotropy, $\Delta\epsilon < 0$ ($\epsilon_{||} < \epsilon_{\perp}$), and the director tends to orient perpendicular to E (Fig. 8.1b and d). The orientational order of the N-LC molecules does not change in an applied electric field, but the collective response to E causes a director reorientation (distortion). Hence, the larger $\Delta\epsilon$ is, the smaller electric field that is needed to reorient the molecules. The occurrence of such a change from an aligned to a deformed state, which can also be produced by applying a magnetic field of sufficient strength, is termed Freedericksz transition [9] and led to the discovery of so-called quasi-Freedericksz-type displays [10].

Just as interactions between N-LCs and surfaces can be manipulated to control the molecular alignment of N-LC molecules, interactions between N-LCs and suspended colloidal particles can be used to influence the orientation and assembly of colloids with different aspect ratios [11-15]. Dispersed colloidal particles disrupt the nematic order, and minimization of the elastic energy leads to the formation of anisotropic colloidal structures.

Depending on the strength and direction of the nematic anchoring on the particle surface (planar, homeotropic), sufficiently large or appropriately functionalized particles

can form various types of topological defects, such as Saturn rings, hyperbolic hedgehogs, and boojums. The formation of topological defects, and the formation of linear particle aggregates as a result thereof, have been most intensively studied for nematic and chiral nematic LCs, and much of the underlying physics has recently been reviewed by Stark [16,17]. Experimental studies focused on dispersions of water microdroplets [11], ferrofluid [18], gold-coated glass spheres [19], or silicon oil in N-LCs [13,20] as well as latex particles [21] in lyotropic N-LCs. For most particles, if the N-LC molecules are strongly and perpendicularly anchored at the surface of a spherical particle, the particles form a radial hedgehog carrying a topological charge (dipole). The topological dipole formed by the quasispherical particle and an accompanying topological defect, known as a hyperbolic hedgehog, generate elastic forces that lead to the formation of chainlike particle aggregates [11,13,16]. This also occurs when the system is confined in microcapillaries [22]. Another interesting example of nanoparticles in cholesteric LCs has been presented by Mitov *et al.*[23] The authors showed that Pt nanoclusters are capable of mimicking the typical fingerprint textures of chiral siloxane N*-LC oligomers, with the majority of the nanoclusters positioned at N-LC–air interfaces [23a].

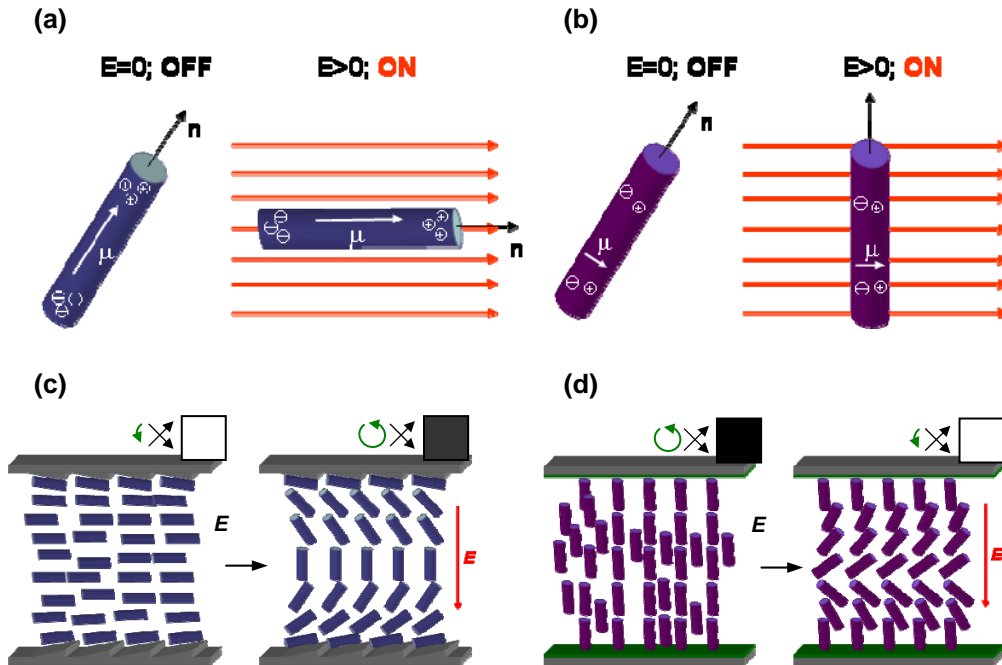


Fig. 8.1. Schematic representation of the response of an N-LC to an applied electric field. (a) Director reorientation of an N-LC with $\Delta\epsilon > 0$, and (b) of an N-LC with $\Delta\epsilon < 0$. (c) Schematic illustration of the electric Fredericksz effect of an N-LC with $\Delta\epsilon > 0$ in a planar cell. In the field-OFF state uniform planar alignment is observed (due to rubbing induced anisotropic dispersion interactions between N-LC molecules and oriented polyimide polymer chains [2]). Applying an electric field above the threshold field ($E > E_{th}$) results in collective reorientation to a bulk homeotropic orientation. (d) Illustration of the electric Fredericksz effect of an N-LC with $\Delta\epsilon < 0$ in a homeotropic cell. In the field-OFF state uniform homeotropic alignment is found (due to interactions with surfactant molecules on the glass surface). In the field-ON state with $E > E_{th}$ collective reorientation gives rise to bulk planar or tilted (splay) orientation. The cartoon above each model demonstrates the optical output through crossed polarizers: black square = homeotropic, white square = birefringent; the round, green arrows show if the particular N-LC orientation can be brought into an extinction position (director parallel to either polarizer) by rotating the sample between crossed polarizers (a full 360° arrow indicates continuous extinction, or no change in birefringence).

Inspired by the possibility to assemble gold nanoclusters into linear arrays using thermotropic LCs, we recently demonstrated the formation of the aforementioned linear particle aggregates in N-LCs with $\Delta\epsilon > 0$ for suspended nanosized thiolcapped gold clusters (diameter = 2–5 nm) via homeotropic anchoring of the N-LC molecules (i.e., the director) to the particle surface (interactions between hydrocarbon chains) [24]. Above a

certain gold nanocluster concentration (~ 5 wt%) for all of the N-LCs used, on moderately slow cooling from the isotropic liquid phase (at $1\text{ }^{\circ}\text{C min}^{-1}$), we observed the reproducible formation of thin film textures consisting of birefringent stripe domains because of the formation of linear nanoparticle aggregates.

For all mixtures containing the alkyl thiolate-capped Au nanoclusters (hexane- and dodecane thiolate) at the indicated cooling rate, these striped domains, which are likely to be located in near interface areas of the LC film, are separated by dark domains with homeotropic alignment of the N-LC molecules (slower cooling rates can produce exclusively striped domains [24]). The homeotropic alignment in the dark domains was easily identified by polarized microscopy because rotating the sample through 180° between the crossed polarizers produced no birefringent state.

The energetically preferred planar alignment of rodlike N-LCs on untreated glass surfaces meant that these domains were the result of the gold nanoclusters residing at the N-LC–glass interfaces in a similar way to the fingerprint-mimicking effect of surfactant-coated Pt nanoclusters mentioned earlier, with the majority of the Pt nanoclusters residing at the LC–air interface [23].

We report here the results of detailed optical and electro-optical studies using the same alkyl thiolate-capped gold nanoclusters for which we detected identical textural features between commercial indium tin oxide (ITO) coated glass cells (LC test cells, cell gaps: 5 or $6.8\text{ }\mu\text{m}$) with parallel and with antiparallel polyimide alignment layers that commonly favor planar orientation of the N-LC molecules (with respect to the director).

8.2 Experimental

The N-LCs used were commercially available pure LCs Felix-2900- 03 (Hoechst); 5CB and 8CB (Merck KGaA)]. The gold nanoclusters (hexane thiolatecapped (**Au1**) and dodecane thiolatecapped (**Au2**)) used for these experiments were prepared with a similar procedure as described in an earlier paper [24] and followed a modified Brust–Schiffrin approach [47] using tetrahydrofuran (THF) and an aqueous solution of NaBH₄ and no phase transfer agent such as tetraoctylammonium bromide (TOAB) [48] (see comment in Supporting Information). High-resolution transmission electron microscopy (HR-TEM) images were obtained on a Jeol ultrahigh resolution FEG-T/STEM operating at an accelerating voltage of 200 kV. A 10 μL drop of the cluster solution was drop-cast on a carbon-coated copper grid (400-mesh) and dried for 1 h. Details (references, HR-TEM images, size distribution) for the hexane thiolate-capped Ag and CdTe nanoclusters are given in the Supporting Information. All particles were stored as dry solids under a protective atmosphere of dry nitrogen in the dark, and could be repeatedly dispersed in and isolated from common organic solvents without change in size (no aggregation or ripening). All glass vials and Teflon-coated spatulas were rinsed with aqua regia prior to all mixture preparations.

Mixtures were then prepared by combining solutions of both components in a common, pure, and dry solvent (e.g., ethyl acetate). The resulting solutions were stirred (agitated) for at least 10 min, and the solvent was evaporated by a steady stream of dry N₂ over open glass vials. Thereafter, all mixtures were dried in vacuum for 24 h. prior to filling the LC test cells by capillary forces with the LC in the isotropic liquid phase; all mixtures were heated just below the isotropic-nematic phase transition ($T_{\text{Iso-N}}$) and continuously

mixed again.

Polarized optical microscopy (POM) was performed using an Olympus BX51-P polarizing microscope in conjunction with a Linkam LS350 heating and cooling stage. Electro-optical tests were done using an LCAS automated liquid crystal analyzer (LC Vision). The LC test cells used were planar 5.0 μm cells with antiparallel polyimide alignment layers and low pre-tilt (Displaytech Inc., purchased from Linkam Scientific Instruments) and planar 5.0 or 6.8 μm cells with parallel or antiparallel polyimide alignment layers and 1° to 3° pretilt (Instec, Inc.). The reproducibility of the alignment effects was checked on over 120 cells overall. The detailed quantitative electro-optical measurements were obtained using three cells (Displaytech, purchased from Linkam Scientific Instruments) for each mixture and a series of ten measurements each (3×10 to obtain standard deviations for each data point).

Representative high-resolution transmission electron microscopy (HR-TEM) images together with the structure and phase transition temperatures of the main LC used (Felix-2900-03) are given in Fig. 8.2.

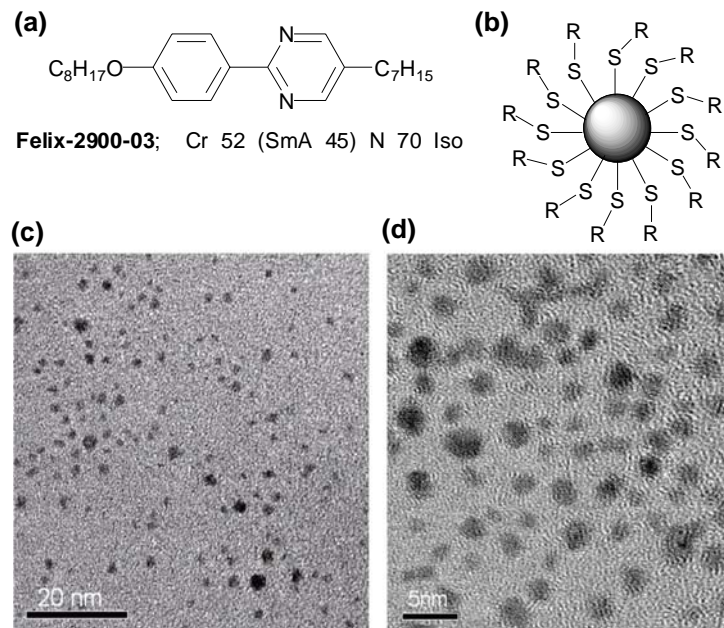


Fig. 8.2. a) Structure and phase transition temperatures of Felix-2900-03 (with a dielectric anisotropy $\Delta\epsilon = +0.62$ at $T_{\text{Iso-T}} = 10^\circ\text{C}$). b) Schematic representation of the alkyl thiolate-capped gold clusters. HR-TEM images of: c) hexane thiolate-capped **Au1** (size: 1.9 ± 0.5 nm) and d) dodecane thiolate-capped **Au2** (size: 2.1 ± 0.7 nm).

In Fig. 8.3a and b, it can be seen that the two most common planar cell types (parallel and antiparallel) essentially gave rise to the same texture phenomena when filled with the N-LC doped with 5 wt% of the gold clusters. The antiparallel cell (test cells from different supplier: Displaytech) had more defined stripe features and a higher number, as well as area density, of birefringent stripes. For both cells, all of the dark domains remained dark upon sample rotation between crossed polarizers indicating that there was homeotropic alignment in these domains.

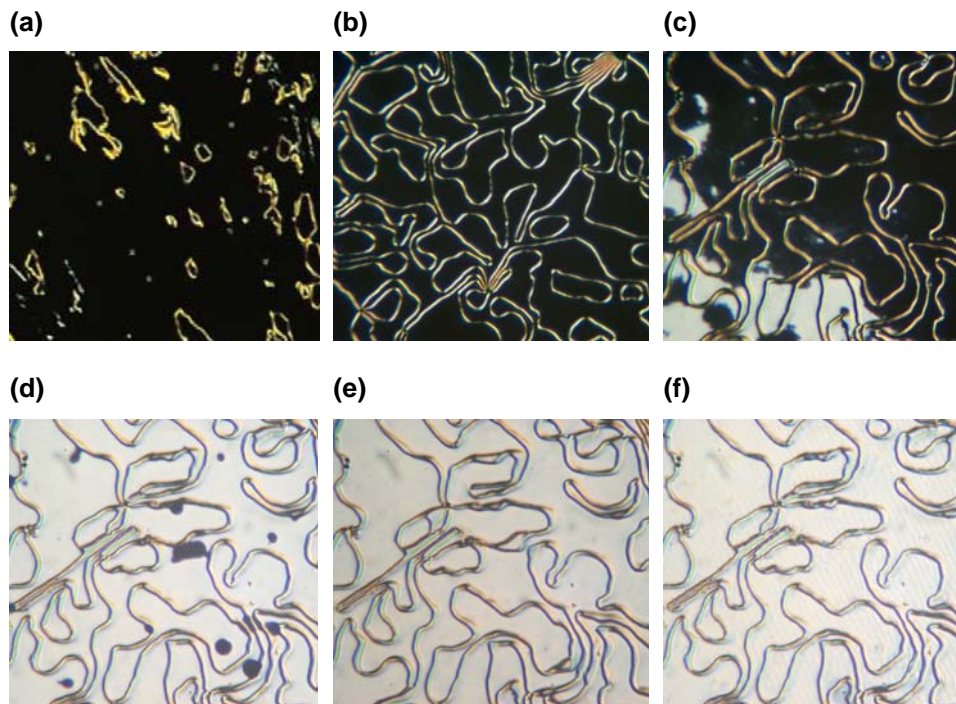


Fig. 8.3. Polarized optical photomicrographs of Felix-2900-03 N-LC (mixtures containing 5 wt% dodecane thiolate-capped gold nanoclusters (**Au2**) after filling the cell at field-OFF. a) Planar cell (cell gap: 5.0 μm) with parallel rubbed polyimide alignment layers (source: Instec) showing coexistence of birefringent stripes and homeotropic domains. b–f) Planar cell (cell gap: 5.0 μm) with antiparallel rubbed polyimide alignment layers (source: Displaytech Inc.) showing coexistence of birefringent stripes and, initially, domains that reorient by applying an electric field across the cell. a–b) $E = 0 \text{ V}\mu\text{m}^{-1}$, c) $E = 0.6 \text{ V}\mu\text{m}^{-1}$, d) $E = 1.0 \text{ V}\mu\text{m}^{-1}$, e) $E = 1.6 \text{ V}\mu\text{m}^{-1}$, and f) $E = 2.0 \text{ V}\mu\text{m}^{-1}$. Upon applying an electric field the number of birefringent stripes decreases.

8.3 Results and Discussion

8.3.1 Qualitative Alignment and Electro-optics

Armed with the knowledge that we could effectively reverse the alignment conditions set out by the planar alignment layers of the cell using small quantities of alkyl thiolate-capped gold nanoclusters, we were now motivated to study the electro-optical response of these planar cells filled with the different N-LC/gold nanocluster mixtures and investigate the effects of temperature, nanocluster type, and concentration, as well as

the cell gap.

In the first set of qualitative experiments, increasing the voltage of an applied dc electric field in both cell types (with parallel and antiparallel planar alignment) resulted in a reorientation of the nematic director from homeotropic orientation in the field-OFF state to a birefringent (planar or at least strongly tilted) orientation in the field-ON state. Considering the N-LC that had $\Delta\varepsilon > 0$ in a planar cell, this unexpected switching process sets in at $E = 0.6 \text{ V } \mu\text{m}^{-1}$ (Fig. 8.3c), and eventually extended to all homeotropic domains in the entire field-addressed area of both cell types when the applied field is increased to $E = 2.0 \text{ V } \mu\text{m}^{-1}$ and above (up to $6.0 \text{ V } \mu\text{m}^{-1}$). It is noteworthy that rotating the sample through 90° between crossed polarizers in both directions in the field-ON state revealed slight changes in the birefringence, but did not produce an extinction orientation in which the nematic director aligns parallel to either polarizer. This fact will prove to be important in the discussion of the observed phenomenon later in this paper. Interestingly, while some of the birefringent stripe domains did disappear initially on the application of an electric field of up to $E = 2.0 \text{ V } \mu\text{m}^{-1}$, a significant number of the linear nanoparticle aggregates responsible for the stripes neither disappeared nor participated in the switching process (Fig. 3c–f). On removal of the applied field, both cells reoriented again and the original homeotropic alignment in the dark domains recovered. At a field strength between $E = 1.0 \text{ V } \mu\text{m}^{-1}$ and $E = 6.0 \text{ V } \mu\text{m}^{-1}$, the cell could effectively be driven between the two orientations with an ac electric field (triangular waveform) acting, in fact, as a quasi-Freedericksz-type display cell of an N-LC, with $\Delta\varepsilon < 0$ in a homeotropic cell.

In the previous set of experiments, all planar cells were prepared by filling the cell with the N-LC–nanocluster mixtures in the isotropic liquid state using capillary forces,

followed by slow cooling to the N-phase (at $1\text{ }^{\circ}\text{C min}^{-1}$) with no field applied.

In the second set of qualitative experiments, we were interested to discover if we could influence the switching or reorientation behavior and the formation, or the area density, of the birefringent stripes by heating the filled cells above the clearing point ($T_{\text{N-Iso}}$) and then cooling them to a nematic (N) phase in the field-ON state (at $E = 2.0\text{ V}\mu\text{m}^{-1}$, because this field strength showed complete reorientation in the first experiment). Cells with either Au nanocluster (**Au1** or **Au2**) in the N-LC treated with this field-ON cooling approach showed the exact reverse switching phenomenon in the domains surrounding the birefringent stripes. In the field-ON state, the texture was again characterized by the aforementioned stripe domains surrounded by larger domains with homeotropic alignment of the director (as determined by sample rotation between crossed polarizers). On the other hand, in the field-OFF state these homeotropic domains reoriented forming stable birefringent domains with homogeneously planar alignment of the nematic director (or slightly tilted with respect to the cell surface). In a similar way to the case with the first experiment, increasing the applied field above $E > 2.2\text{ V}\mu\text{m}^{-1}$ resulted in a disappearance of most of the linear particle aggregates (stripes) as shown in Figs. 8.4a–c.

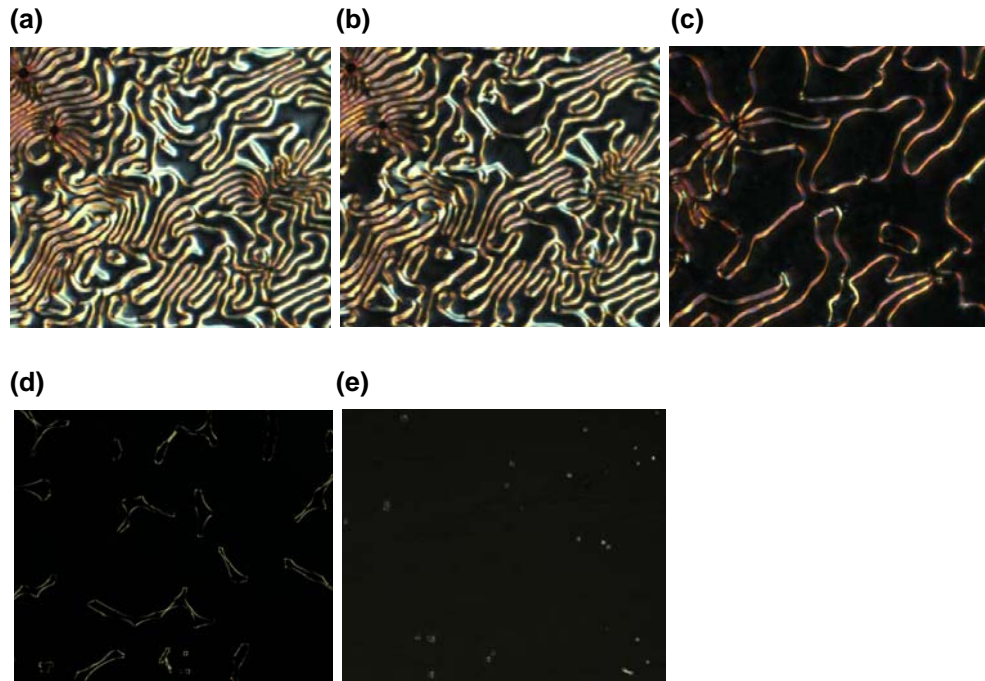


Fig. 8.4. Decreasing the number of chainlike particle aggregates (birefringent stripes). a–c) Polarized optical photomicrographs of Felix-2900-03 containing 5 wt% **Au2** after heating the cell to the isotropic liquid phase followed by cooling to the N-phase at field-ON (cell gap: 5.0 μm); a) at $E = 1.4 \text{ V } \mu\text{m}^{-1}$, b) at $E = 2.2 \text{ V } \mu\text{m}^{-1}$, and c) at $E = 3.2 \text{ V } \mu\text{m}^{-1}$. d) Polarized optical photomicrograph of Felix-2900-03 containing 5 wt% **Au2** (cell gap: 6.8 μm). e) Felix-2900-03 containing 10 wt% **Au2** after filling the cell at field-OFF (the entire cell shows uniform homeotropic alignment).

To summarize the second qualitative experiment, the same cell switching as a Freedericksz-type cell of an N-LC with $\Delta\varepsilon < 0$ in a cell with homeotropic alignment, can now be electrically driven with an ac electric field as a quasi-Freedericksz type display of an N-LC with $\Delta\varepsilon > 0$ in a cell with planar alignment. In both experiments, both field-OFF and field-ON states were stable and did not change over time, and the field-ON states quickly reoriented back to their previous state as soon as the field was turned off. It is rather surprising that cells, once treated with the cooling under the field-ON protocol,

could not be reversed back to their original state, with homeotropic domains, by heating above the clearing point in the field-OFF state and cooling to the N-phase at field-OFF.

The observed thermal history-dependent, dual alignment mode and the qualitative electro-optical effects were reproducible for Felix-2900-03 containing 5 or 10 wt% of **Au1** or **Au2** in planar cells (more than 20 cells for each concentrations of both nanoclusters in both parallel and antiparallel cell types) with a cell gap of ca. 5.0 μm (the batches of the commercial cells used had cell gap deviations of ca. $\pm 0.5 \mu\text{m}$). For cells with larger cell gaps (i.e., 6.8 μm ; source: Instec), however, not all tested cells showed uniform homeotropic alignment (as in Fig. 8.4d) in the domains surrounding the birefringent stripes at 5 wt% of the Au nanoclusters in the N-LC. For these (6.8 \pm 0.5) μm cells, we eventually succeeded, in most cases, in obtaining uniform homeotropic alignment in these domains by increasing the nanocluster concentration above 5 wt% (commonly 10 wt%, Fig. 8.4e). We attribute the occasional lack of uniform homeotropic alignment in these thicker cells, for the 5 wt% **Au1** or **Au2** in Felix-2900-03, to an increase of the bulk-to-interface ratio of the cells with larger cell gaps. In other words, when more particles were trapped in the bulk of the cell because they had interacted with the LC molecules, fewer particles were available to induce homeotropic alignment at the LC–alignment-layer interface. Increasing the nanocluster concentration to 10 wt% not only helped overcome this partial alignment problem, but also led to another very beneficial effect; in some cases, and more so for cells with smaller cells gaps (i.e., 5.0 μm), the higher particle content produced uniform homeotropic alignment over the entire cell area without formation of birefringent stripes (i.e., chain-like particle aggregates). This is the exact reverse phenomenon of that previously observed for untreated glass

slides, for which an increasing particle concentration produced a higher area density of birefringent stripes (Fig. 8.4e) [24].

Driving these cells with a *dc* or an *ac* field resulted in exactly the same electro-optical characteristics as those described for both experiments above in cells with lower particle concentration.

Another critical observation with respect to the reproducibility of this dual alignment mode, and the quality of the alignment in both modes in particular, was made by substituting the nematic host Felix-2900-03 (flanked by two hydrocarbons chains) with 5CB [25] or 8CB [26] (for structures, phase transition temperatures, and $\Delta\epsilon$ values, see Fig. 8.5). The lower solubility (inferior compatibility) of the alkylthiol-capped nanoclusters in the two polar cyanobiphenyl N-LCs (having only one hydrocarbon chain) complicated the formation of uniform homeotropic alignment for a number of cells.

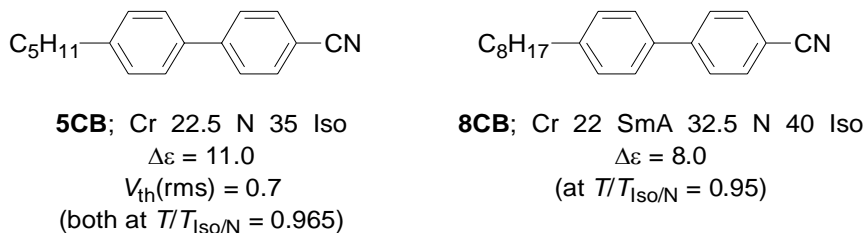


Fig. 8.5. Structures of 5CB and 8CB together with phase transition temperatures as well as literature values of the dielectric anisotropy and threshold voltage (5CB only) [25, 26].

Driving the homeotropic cells with an electric field often produced areas containing aggregated nanoclusters that could be seen by rotating one polarizer more and more away from the 90° orientation (uncrossed polarizers). As a result, only approximately every second cell filled with 5CB or 8CB containing 5 wt% of **Au1** or **Au2** produced homeotropic aligned domains that covered most or all of the field-addressed area (5 mm

$\times 5 \text{ mm}$) of the $5 \text{ }\mu\text{m}$ cells (Fig. 8.6a). Increasing the concentration of the gold nanoclusters, as for Felix-2900-03, only improved quality and homogeneity of the homeotropic alignment sometimes (Fig. 8.6b). Both findings were consistent with the better overall solubility (superior compatibility) of the Au nanoclusters in Felix-2900-03. The difference in solubility already affected the preparation of the mixtures, which was critical for ensuring well-dispersed nanoclusters in the N-LC host. In addition, the role of the anisotropic dispersion interactions, between the different N-LCs and the rubbed polyimide alignment layers [2], could affect the quality of the homeotropic alignment significantly. For this reason, the most detailed quantitative electro-optical experiments were performed using Felix-2900-03, in cells with a cell gap of $5 \text{ }\mu\text{m}$, doped with either 5 or 10 wt% of **Au1** or **Au2** using an automated liquid crystal test-bed (LC Vision, Inc.).

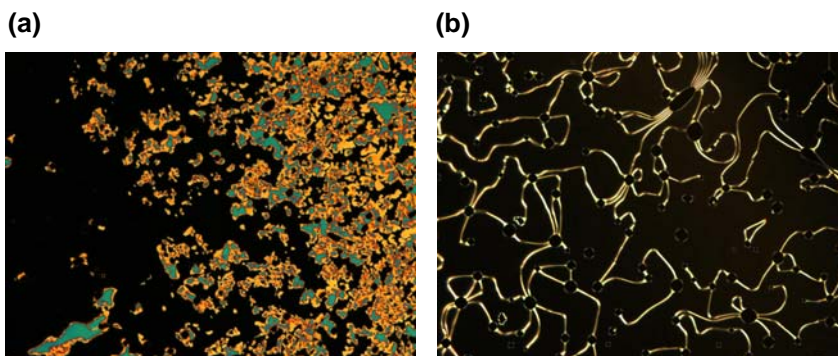


Fig. 8.6. a) POM image of 8CB doped with 5 wt% **Au1** (partial homeotropic alignment), b) POM image of 5CB doped with 10 wt% **Au1** (homeotropic alignment with linear particle aggregates (birefringent stripes)). Both images were obtained by slow cooling from the isotropic liquid phase at field-OFF.

8.3.2 Quantitative Electro-optics

For all cells of Felix-2900-03 containing either 5 or 10 wt% **Au1** or **Au2**, the threshold voltage (V_{th}), the dielectric permittivity along (ϵ_{\parallel}) and across (ϵ_{\perp}) the long molecular axis,

the dielectric anisotropy ($\Delta\varepsilon = \varepsilon_{\parallel} - \varepsilon_{\perp}$), (the elastic constants K_{11} , K_{22} , and K_{33} (splay, twist, bend), and the specific resistivity (R) were measured before and after treating the cell with the field- ON cooling approach (initially homeotropic vs. parallel alignment) using the “single cell” method described by Wu *et al.*[27], which is built into the software of the automated LC test-bed that was used. All measurements were performed, depending on temperature, by slow cooling from the isotropic liquid phase (at 1 °C min) starting at $T_{\text{Iso}}-T = 7$ °C taking the broadened phase transition (due to the presence of the nanoclusters) into account. For a comparison between the 5 wt% and the 10 wt% runs, it is important to note that the phase transition temperatures (low-temperature onset of the phase transition in the DSC traces) were only altered by approximately 1–2 °C when the nanocluster concentration was doubled from 5 to 10 wt%. Plots of the threshold voltage V_{th} versus $T_{\text{Iso}}-T$ are summarized, in Fig. 8.7a–d, for all measured cells.

As expected, V_{th} increased with decreasing temperature for pure Felix-2900-03 and for Felix-2900-03 doped with 5 wt% **Au1** or **Au2**. More significantly, V_{th} is much lower over the entire temperature range for both mixtures containing the nanoclusters, and **Au1** in Felix-2900-03 showed the lowest values for V_{th} (Fig. 8.7a). These data were consistent with the lower applied field necessary to obtain reorientation of the nematic director from a homeotropic to a planar alignment, which have been qualitatively observed before (~ 2 $\text{V}\mu\text{m}^{-1}$ for Felix-2900- 03 doped with 5 wt% **Au2** versus ~ 8 $\text{V}\mu\text{m}^{-1}$ for pure Felix-2900-03, see Fig. 8.3 compared to Fig. S8.1 in the Supporting Information).

A comparison of the plot of V_{th} with $T_{\text{Iso}}-T$ before and after treating the cell with the field-ON approach (Fig. 8.7b) indicates that the cells with the original homeotropic alignment had lower values of V_{th} than the cells cooled with field-ON showing planar

alignment. In fact, Felix-2900-03 doped with 5 wt% **Au2** and pure Felix-2900-03 had almost identical values of V_{th} at lower temperatures, which demonstrated that cells treated with the field-ON cooling regime have an electro-optical response similar to the pure N-LC host.

The plots in Fig. 8.7c and d show the concentration-dependence of V_{th} for both nanoclusters suspended in Felix-2900-03 with the initial homeotropic alignment. Taking the standard deviations of each data point into account, one can conclude that doubling the nanocluster concentration had no significant impact on V_{th} for **Au2**, but led to a minor decrease of V_{th} for **Au1**.

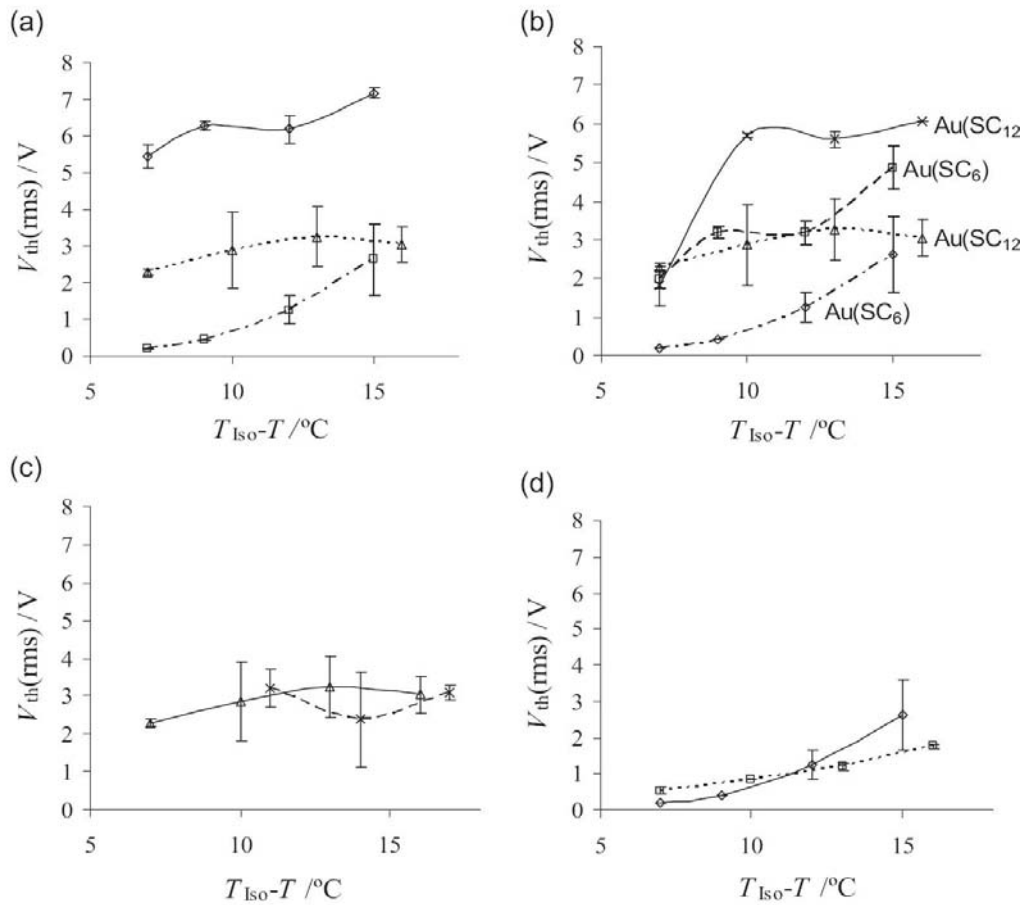


Fig. 8.7. Plots of threshold voltage V_{th} vs. $T_{Iso}-T$ of Felix-2900-03: (a) \diamond pure Felix-2900-03, \square doped with 5 wt% **Au1**, Δ doped with 5 wt% **Au2** starting with homeotropic alignment (1st experiment); (b) Δ , \diamond before (1st experiment) and \square , \times after cooling at field-ON (2nd experiment). (c) Δ doped with 5 wt% **Au2**, \times doped with 10 wt% **Au2**; (d) \diamond doped with 5 wt% **Au1**, \square doped with 10 wt% **Au1** starting with homeotropic alignment (1st experiment).

The trends in the dielectric permittivity along ($\epsilon_{||}$) and across the long molecular axis (ϵ_{\perp}), as well as the dielectric anisotropies $\Delta\epsilon$ depending on temperature for all mixtures with 5 wt% of both nanoclusters are collected in Fig. 8.8. The dielectric permittivities for pure Felix-2900-03 followed a trend common to most rod-like N-LCs and give an increasing $\Delta\epsilon$ with decreasing temperature. The samples of Felix-2900-03 doped with 5

wt% **Au1** (Fig. 8.8a) or **Au2** (Fig. 8.8b), however, show exactly the opposite trend. Both the dielectric permittivity parallel ε_{\parallel} and across the long molecular axis ε_{\perp} were larger than for pure Felix-2900-03. Moreover, $\Delta\varepsilon$ decreased with decreasing temperature (significantly for **Au1** and slightly for **Au2**, Fig. 8.8c). A comparison of the dielectric permittivity before and after treatment of the cell with the cooling at field-ON regime (Fig. 8.8d and e) again showed that all cells with the planar alignment induced by slow cooling at field-ON behaved in a similar way to the cells filled with pure Felix-2900-03 ($\Delta\varepsilon \approx +0.6$). Here, it is interesting to note that $\Delta\varepsilon$ of Felix-2900-03 doped with 5 wt% **Au2** was significantly smaller in the cooling with the field-OFF regime (in contrast to the larger $\Delta\varepsilon$ values for **Au1** at higher temperatures in the same regime, Fig. 8.8c). As was the case for V_{th} earlier, increasing the concentration of both Au nanoclusters in the NLC host did not result in major changes to either of the dielectric constants or $\Delta\varepsilon$ (Fig. 8.9).

The calculated, estimated, and derived elastic constants (K_{11} , K_{22} , and K_{33}) and the measured values for the specific resistivity (R in $\Omega\cdot\text{cm}$) of all cells, in both cooling regimes, are presented in the SI. Fundamentally, these follow the same trends as those that were discussed for V_{th} and $\Delta\varepsilon$. That is, the values for the cells treated with the cooling at field-ON regime are closer to those of pure Felix-2900-03. On the other hand, the cells treated with the cooling at field-OFF regime showed lower values of all three elastic constants and of the specific resistivity.

We also performed the same set of measurements for cells cooled in the field-OFF regime with an alternative setup in which we assumed that we were measuring the N-LC with $\Delta\varepsilon < 0$ ($\varepsilon_{\parallel} < \varepsilon_{\perp}$) in a homeotropic cell (see SI). Generally, the values of V_{th} , $\Delta\varepsilon$, K_{11} , K_{22} , and K_{33} from these measurements were identical to those values obtained from the

initial measurements, and differed only in the instrumentally reversed sign for $\Delta\varepsilon$ differed ($\Delta\varepsilon < 0$ as per setup).

Finally, measurements were also performed using cells filled with 8CB doped with the Au nanoclusters and show, as Felix-2900-03, reduced threshold voltages V_{th} and higher dielectric permittivity values (see Supplementary Information).

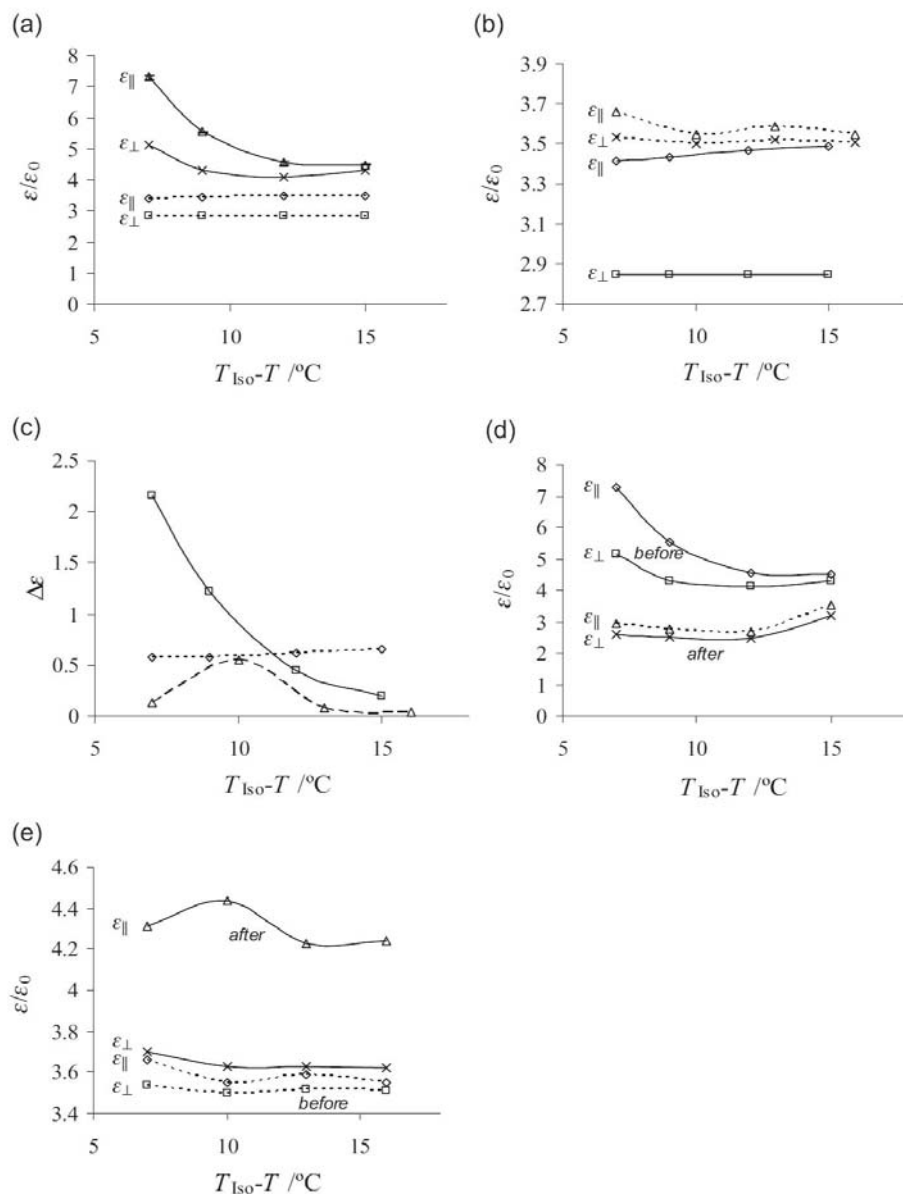


Fig. 8.8. Plots of the relative dielectric permittivity (dielectric constant) parallel ϵ_{\parallel} and across the long molecular axis ϵ_{\perp} (or $\Delta\epsilon$) vs. $T_{\text{Iso}}-T$ of Felix-2900-03: (a) \diamond and \square pure Felix-2900-03; Δ and \times doped with 5 wt% **Au1** starting with homeotropic alignment (1st experiment). (b) \diamond and \square pure Felix-2900-03; Δ and \times doped with 5 wt% **Au2** starting with homeotropic alignment (1st experiment). (c) $\Delta\epsilon$ vs. $T_{\text{Iso}}-T$ of: \diamond pure Felix-2900-03; \square Felix-2900-03 doped with 5 wt% **Au1**; and Δ Felix-2900-03 doped with 5 wt% **Au2** (1st experiment). (d) Felix-2900-03 doped with 5 wt% **Au1**: \diamond and \square before (1st experiment) and Δ and \times after cooling at field-ON (2nd experiment). (e) Felix-2900-03 doped with 5 wt% **Au2**: \diamond and \square before (1st experiment) and Δ and \times after cooling at field-ON (2nd experiment). The rather small standard deviations are only shown for one data set representative for all measured dielectric constants in (a), and were omitted for clarity in all other plots.

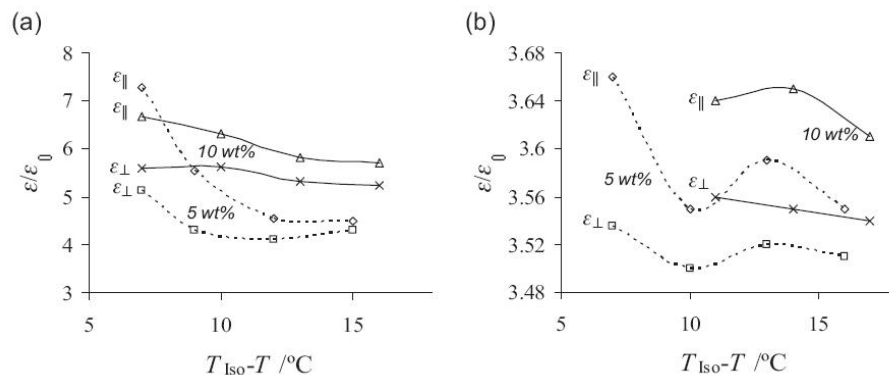


Fig. 8.9. Plots of $\epsilon_{||}$ and ϵ_{\perp} vs. $T_{Iso}-T$ of Felix-2900-03 doped with either 5 or 10 wt% of **Au1** or **Au2** using cells treated with the cooling at field-OFF regime (homeotropic alignment): a) **Au1**; b) **Au2**.

8.3.3 Model

To explain these phenomena, considering all qualitative optical observations and quantitative electro-optical data, we have formulated a model that, in principle, highlights the interplay and competition between the various perturbations (interactions) exerted on the N-LC molecules by alignment layers, the applied electric field, anchoring to the nanocluster surface [16–22], and a local contact between the N-LC and the charged (capacitive charging of Au nanoclusters in the applied electric field [28]) and conducting gold nanoclusters [29, 30] in the cell's field-ON or field- OFF states (Fig. 8.10).

In the first experiment, the electronically charged gold nanocluster cores residing at the alignment layer/N-LC interface acting as local capacitors [28–31] and dipoles [32] not only enhance the overall conductivity of the mixture, as discussed by other groups for similar systems [33], but as an assembly at the interface with the hydrocarbon chains on the cluster surface acting similar to a self-assembled monolayer (SAM) on a Au surface [34], they are also responsible for the induced homeotropic alignment of the N-LC molecules. Careful sample preparation (i.e., to produce well dispersed nanoparticles),

filling the cells with the N-LC mixture in the isotropic liquid phase, and slow cooling into the N-phase were critical for homeotropic alignment in the first set of experiments. Another approach that showed similar success in producing homeotropic alignment makes use of a very rapid cooling regime (filling the cell above $T_{\text{Iso-N}}$ and removing it rapidly from the heating stage). This regime initially produced planar alignment, which rapidly turned into homeotropic alignment for all N-LCs that were used. This indicates that the Au clusters, initially well-dispersed in the isotropic liquid phase, migrated to the interface and were excluded from the N-LC bulk.

Additional permanent magnetic properties reported for thiol-capped gold nanoclusters [35, 36] could, in principle, also facilitate the homeotropic alignment that was observed, because N-LCs with $\Delta\epsilon > 0$ would reorient with the director normal to the nanocluster surface [37]. However, preliminary results using hexane thiolate-capped Ag and CdTe nanoclusters (in the same size-regime) showed that systems in which the potentially magnetic Au core was replaced with Ag or CdTe cores still led to identical homeotropic alignment of N-LCs (Fig. 8.11). This highlights the role of the alkyl thiols coating the nanocluster surface, for the promotion of homeotropic alignment at the LC–alignment-layer interface.

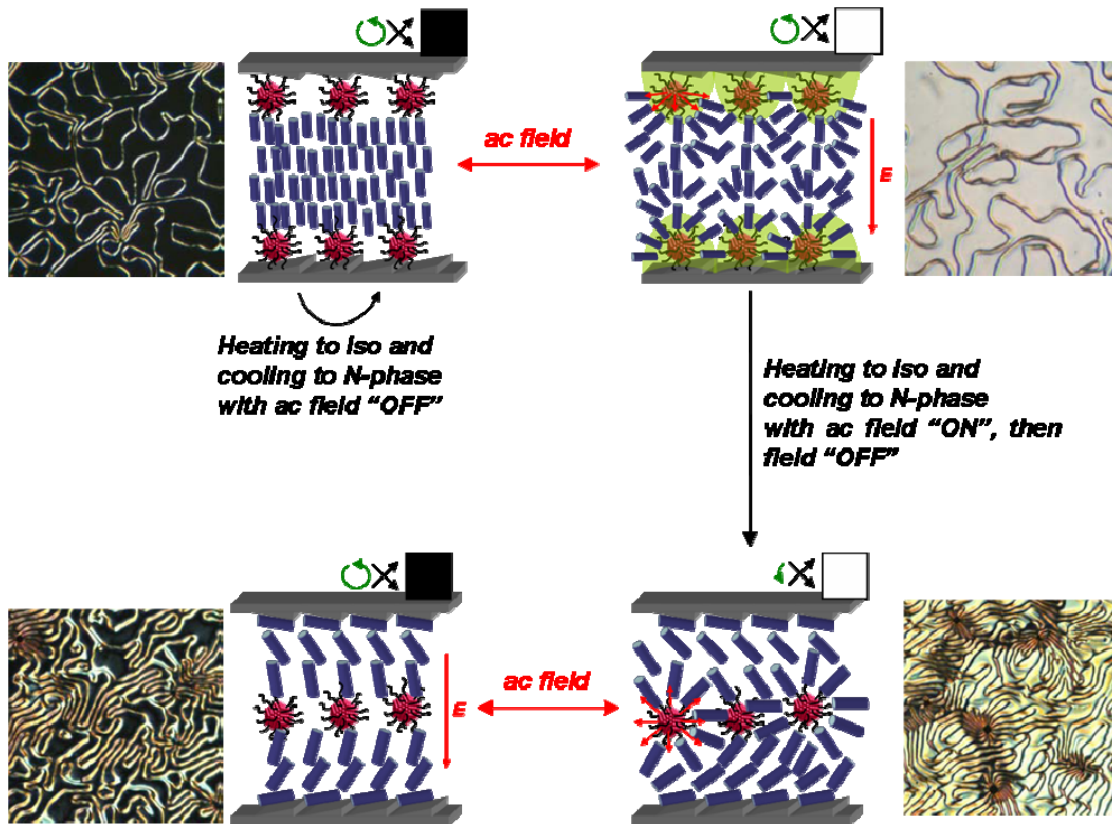


Fig. 8.10. Demonstration of the initial orientation and electric-field-driven reorientation of the N-LC molecules under cell preparation conditions described in the 1st experiment, that is, filling and cooling the cell at field-OFF (upper section), and after heating above the clearing point and subsequent cooling to the N-phase at field-ON (lower section). Representative thin-film textures (as observed between crossed polarizers) accompany each model. For cartoons above each model, see legend for Fig. 1.

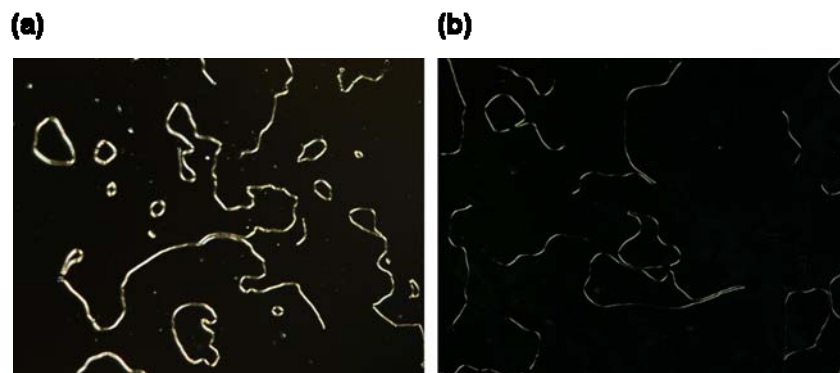


Fig. 8.11. Polarized optical photomicroscopy images of the homeotropic alignment and birefringent stripes of Felix-2900-03 doped with 5 wt% of: a) hexane thiolate-capped Ag nanoclusters (size: 4.2 ± 0.7 nm), b) hexane thiolate-capped CdTe quantum dots (size: 3.9 ± 0.3 nm).

The reorientation (switching) observed after applying an electric field in the first experiment, in which the birefringent domains cannot be brought into an extinction position by rotating the sample between crossed polarizers, must be caused by the capacitive-charged conducting Au nanoclusters. The lower threshold voltage and the lower specific resistivity are caused by the Au nanocluster cores. Both effects are more pronounced for the **Au1** clusters with shorter hydrocarbon chains. This is consistent with the more pronounced semiconducting nature of the hexane thiolate-capped gold clusters in comparison to the dodecane thiolate-capped **Au2** [38]. Consequently, the Fredericksz-type response of an N-LC with $\Delta\epsilon > 0$ observed on cooling the cell from the isotropic to the nematic phase at field-ON must have a different origin. Apart from the few molecules in near surface regions (alignment layers), at $E > E_{th}$ the N-phase formed with the bulk of the molecules oriented with the director parallel to the applied field (perpendicular to the surface). As a result of the interactions between the alignment layers and the applied field, and considering the observed reversed switching behavior, the gold nanoclusters must have been pushed away from the surfaces of the cell into the bulk of the sandwiched nematic film. Presumably, this effect was related to the levitation of nanowires in a twisted nematic cell mentioned earlier [14]. Removing the electric field will now result in a planar alignment in all domains surrounding the birefringent stripes. The domains of planar alignment will responded to the applied electric field with a Fredericksz transition of an N-LC with $\Delta\epsilon > 0$. This scenario is consistent with all data obtained from the electro-optical measurements.

All cells treated with the cooling at field-ON approach had values of V_{th} , $\Delta\epsilon$, K_{11} , K_{22} , K_{33} , and R that were closer to the values measured (calculated) for the pure N-LC. The

presence of the gold nanoclusters randomly dispersed in the N-LC bulk reduced the threshold voltage and the specific resistivity, which means these mixtures are potentially useful for electro-optical applications in TN and IPS modes requiring less power. However, this effect was much less pronounced than for the cells with induced homeotropic alignment in which the Au clusters formed an assembly at the interface.

A similar effect was recently reported for a phenylpyrimidine- based ferroelectric LC (FLC) doped with gold nanoclusters, where the presence of the nanoclusters generated higher tilt angles, memory effects, and lower threshold voltages. The authors hypothesized that these effects were the result of interactions between the electron wave oscillations in the gold cluster and the incident light traversing through the FLC molecules [39].

Although the disappearance of birefringent stripes above a certain threshold of the applied electric field in both experiments could not be fully explained at this stage, it seems likely that the conductivity of thiolate-capped gold nanoclusters and electronic charging of the Au cluster cores played a critical role. In this case, the elastic forces generated by the formation of topological dipoles and hyperbolic hedgehogs, leading to the formation of chainlike particle aggregates, were overridden by the forces exerted on the N-LC molecules by the charged nanoclusters in the applied electric field and the simultaneous reduction of energetically unfavorable defects in the N-LC film (i.e., by the formation of energetically more favorable defects at the interface).

8.4 Conclusion

In conclusion, we demonstrated an unprecedented dual alignment and switching mechanism in planar LC cells using N-LC molecules with $\Delta\epsilon > 0$ and small amounts of alkyl thiolate- capped gold nanoclusters. In both thermal- and field-history- dependent modes, the threshold voltages were lower and the dielectric constants were higher than the values obtained for the pure N-LCs. The results of these findings, coupled with the reported frequency-modulation electro-optical response for N-LCs doped with metal nanoclusters at low particle concentrations (0.1–0.3 wt%),[40] demonstrate the potential usefulness of functionalized gold nanoclusters for the development of new or improved LC display technologies [41].

Considering the unique effects and the competition between all the possible interactions of the N-LC with the applied electric field and all the surfaces (of nanoclusters and alignment layers), the system appeared to be strikingly simple. The qualitative electro-optical effects that were observed clearly differentiate this system from more common filled nematic LC cells that can be electrically driven from a highly scattering to a transparent state [42]. The minute amount of gold nanoclusters suspended in the N-LC effectively produced two different alignment modes, independent of the planar alignment layers of the cell. This is analogous to photochromic command surfaces based on azobenzene Langmuir–Blodgett films [43,44]. Based on our current model, this system could also be employed for electric far-field spectral tuning of plasmonic resonances [45] and eliminate the tedious fabrication of gold nanodot arrays on glass surfaces using nanoporous aluminum membranes as a stencil in electron beam evaporation. Finally, effective design of reliable LC based sensor devices with enhanced

sensitivity using N-LC cells (e.g., for globular proteins on homeotropic surfaces) has to take the polarized optical and electro-optical effects presented here into consideration.[46] Future work will now focus on establishing clear structure–property relationships between the nanoparticles (metals vs. semiconductor) and the structure of the N-LC with respect to the alignment quality and electro-optical characteristics.

References

- [1] K. Tarumi, M. Bremer, T. Geelhaar, *Annu. Rev. Mater. Sci.* **1997**, *27*, 423-441.
- [2] M. F. Toney, T. P. Russell, J. A. Logan, H. Kikuchi, J. M. Sands, S. K. Kumar, *Nature* **1995**, *374*, 709-711.
- [3] A. A. Sonin, *The Surface Physics of Liquid Crystals*, Gordon and Breach, Luxembourg **1995**.
- [4] B. J. Frisken, P. Palfy-Muhoray, *Phys. Rev. A* **1989**, *40*, 6099-6102.
- [5] H. Wang, T. X. Wu, X. Zhu, S.-T. Wu, *J. Appl. Phys.* **2004**, *95*, 5502-5508.
- [6] M. Schadt, *Annu. Rev. Mater. Sci.* **1997**, *27*, 305-379.
- [7] See for example: Y. Sun, H. Ma, Z. Zhang, X. Zhu, S.-T. Wu, *Appl. Phys. Lett.* **2006**, *89*, 041110.
- [8] Q. Hong, T. X. Wu, X. Zhu, R. Lu, S.-T. Wu, *Appl. Phys. Lett.* **2005**, *86*, 121107.
- [9] V. Freedericksz, V. Tsvetkov, *Phys. Z. Sowjetunion* **1934**, *6*, 490-504.
- [10] I. C. Sage, In *Handbook of Liquid Crystals*. (Eds: D. Demus, J. Goodby, G. W. Gray, H. W. Spiess, V. Vill), Vol. 1, Wiley-VCH, Weinheim **1998**, pp. 731-762.
- [11] P. Poulin, H. Stark, T. C. Lubensky, D. A. Weitz, *Science* **1997**, *275*, 1770-1773.

- [12] M. Zapotocky, L. Ramos, P. Poulin, T. C. Lubensky, D. A. Weitz, *Science* **1999**, 283, 209-212.
- [13] J.-C. Loudet, P. Barois, P. Poulin, *Nature* **2000**, 407, 611-613.
- [14] C. Lapointe, A. Hultgren, D. M. Silevitch, E. J. Felton, D. H. Reich, R. L. Leheny, *Science* **2004**, 303, 652-655.
- [15] I. Dierking, G. Scalia, P. Morales, *J. Appl. Phys.* **2005**, 97, 044309.
- [16] H. Stark, *Phys. Rep.* **2001**, 351, 387-474.
- [17] H. Stark, *Phys. Rev. E* **2002**, 66, 041705.
- [18] P. Poulin, V. Cabuil, D. A. Weitz, *Phys. Rev. Lett.* **1997**, 79, 4862-4865.
- [19] Y. D. Gu, N. L. Abbott, *Phys. Rev. Lett.* **2000**, 85, 4719-4722.
- [20] J.-C. Loudet, O. Mondain-Monval, P. Poulin, *Eur. Phys. J. E* **2002**, 7, 205-208.
- [21] P. Poulin, N. France's, O. Mondain-Monval, *Phys. Rev. E* **1999**, 59, 4384.
- [22] P. Kossyrev, M. Ravnik, S. Žumer, *Phys. Rev. Lett.* **2006**, 96, 048301.
- [23] a) For the selective segregation of the Pt-clusters at the periphery of the LC film (LC–air interface) see TEM images in: M. Mitov, C. Bougerette, F. de Guerville, *J. Phys.: Condens. Matter* **2004**, 16, S1981-S1988. b) M. Mitov, C. Portet, C. Bourgerette, E. Snoeck, M. Verelst, *Nat. Mater.* **2002**, 1, 229-231.
- [24] H. Qi, T. Hegmann, *J. Mater. Chem.* **2006**, 16, 4197-4205.
- [25] M. L. Dark, M. H. Moore, D. K. Shenoy, R. Shashidhar, *Liq. Cryst.* **2006**, 33, 67-73.
- [26] K. Abe, A. Usami, K. Ishida, Y. Fukushima, T. Shigenari, *J. Korean Phys. Soc.* **2005**, 46, 220-223.

- [27] S. T. Wu, D. Coates, E. Bartmann, *Liq. Cryst.* **1991**, *10*, 635-646.
- [28] T. Albrecht, S. F. L. Mertens, J. Ulstrup, *J. Am. Chem. Soc.* **2007**, *129*, 9162-9167.
- [29] Assemblies of Au nanoclusters display solid state conductivities of -10^{-4} – 10^{-5} S·cm⁻¹: a) S. W. Boettcher, N. C. Strandwitz, M. Schierhorn, N. Lock, M. C. Lonergan, G. D. Stucky, *Nat. Mater.* **2007**, *6*, 592-596. b) W. P. Wuelfing, S. J. Green, J. J. Pietron, D. E. Cliffel, R. W. Murray, *J. Am. Chem. Soc.* **2000**, *122*, 11465-11472. c) J. J. Pietron, J. F. Hicks, R. W. Murray, *J. Am. Chem. Soc.* **1999**, *121*, 5565-5570.
- [30] R. H. Terrill, T. A. Postlethwaite, C.-H. Chen, C.-D. Poon, A. Terzis, A. Chen, J. E. Hutchison, M. R. Clark, G. Wignall, *J. Am. Chem. Soc.* **1995**, *117*, 12537-12548.
- [31] A. N. Shipway, E. Katz, I. Willner, *ChemPhysChem* **2000**, *1*, 18-52.
- [32] K. E. Peceros, X. Xu, S. R. Bulcock, M. B. Cortie, *J. Phys. Chem. B* **2005**, *109*, 21516-21520.
- [33] S. K. Prasad, K. L. Sandhya, G. G. Nair, U. S. Hiremath, C. V. Yelamaggad, S. Sampath, *Liq. Cryst.* **2006**, *33*, 1121-1125.
- [34] Alkylthiols used in self-assembled monolayers (SAMs) are known to promote homeotropic anchoring of N-LCs: R. A. Drawhorn, N. L. Abbott, *J. Phys. Chem.* **1995**, *99*, 16511-16515.
- [35] Y. Yamamoto, H. Hori, *Rev. Adv. Mater. Sci.* **2006**, *12*, 23-32.
- [36] J. de la Venta, A. Pucci, E. Fernández Pinel, M. A. García, F. de Julián, P. Crespo, P. Mazzoldi, G. Ruggeri, *Adv. Mater.* **2007**, *19*, 875-877.
- [37] D. Dunmur, K. Toriyama, In *Handbook of Liquid Crystals*, (Eds: D. Demus, J.

- Goodby, G. W. Gray, H.-W. Spiess, V. Vill), Vol. 1, Wiley- VCH, Weinheim **1998**, pp. 253-280.
- [38] A. C. Templeton, W. P. Wuelfing, R. W. Murray, *Acc. Chem. Res.* **2000**, *33*, 27-36.
- [39] S. Kaur, S. P. Singh, A. M. Biradar, A. Choudhary, K. Sreenivas, *Appl. Phys. Lett.* **2007**, *91*, 023120.
- [40] S. Kobayashi, T. Miyama, N. Nishida, Y. Sakai, H. Shiraki, Y. Shiraishi, N. Tushima, *J. Disp. Technol.* **2006**, *2*, 121-129.
- [41] For a recent review highlighting the mutual benefits of nanoparticles and liquid crystals see: T. Hegmann, H. Qi, V. M. Marx, *J. Inorg. Organomet. Polym. Mater.* **2007**, *17*, 483-508.
- [42] N. J. Diorio Jr., M. R. Fisch, J. W. West, *Liq. Cryst.* **2002**, *29*, 589-596.
- [43] H. Knobloch, H. Orendi, M. Büchel, T. Seki, S. Ito, W. Knoll, *J. Appl. Phys.* **1994**, *76*, 8212-8214.
- [44] H. Knobloch, H. Orendi, M. Büchel, T. Seki, S. Ito, W. Knoll, *J. Appl. Phys.* **1995**, *77*, 481-487.
- [45] P. A. Kossyrev, A. Yin, S. G. Cloutier, D. A. Cardimona, H. Danhong, P. M. Alsing, J. M. Xu, *Nano Lett.* **2005**, *5*, 1978-1981.
- [46] O. Guzmán, N. L. Abbott, J. J. de Pablo, *J. Chem. Phys.* **2005**, *122*, 184711.
- [47] H. Choo, E. Cutler, Y.-S. Shon, *Langmuir* **2003**, *19*, 8555-8559.
- [48] M. Dasog, R. W. J. Scott, *Langmuir* **2007**, *23*, 3381-3387.

Appendix D

Supplementary Information for Chapter 8

S1. Response of Felix-2900-03 without gold nanoclusters in a planar LC test cell

The electric-field response (Freedericksz transition) of the N-LC used [Felix-2900-03 (Hoechst); Cr 52 (SmA 45) N 70 Iso] with positive dielectric anisotropy [$\Delta\epsilon = +0.62$] without addition of the gold nanoclusters in an ITO-test cell with polyimide alignment layers favoring planar alignment is shown in Fig. S1 below.

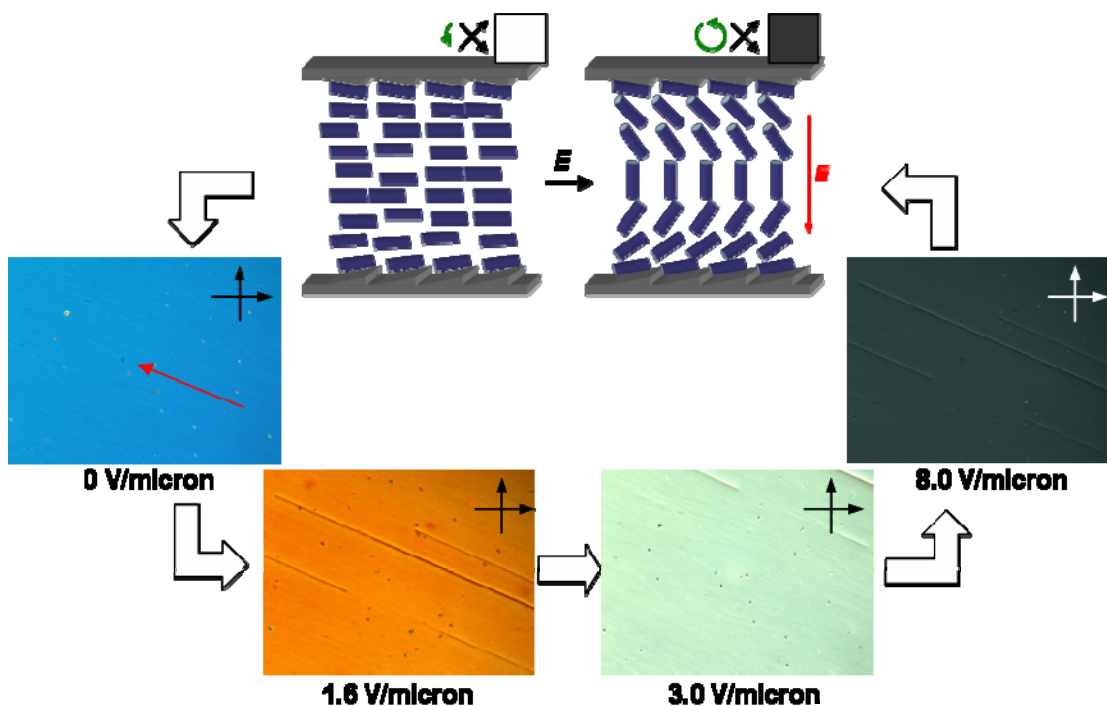


Fig. S8.1. Applying an electric field across the cell at ($E > E_{th}$) a director re-orientation is observed ($E = 1.6-3.0$ V/micron). A further increase of the applied field ($E \gg E_{th}$; $E = 8.0$ V/micron) the bulk of the N-LC molecules aligns along the applied electric field producing homeotropic alignment (black and white arrows indicate polarizer/analyser position, the red arrow indicates rubbing direction of the polyimide alignment layers).

S2. Importance of well-dispersed gold nanoclusters, as well as sample and cell preparation

Studies on different nanoparticles in nematic LCs such as 5CB, namely maghemite $\gamma\text{-Fe}_2\text{O}_3$, demonstrated that nanoscale particles form stable, homogeneous dispersion above the N-Iso phase transition temperature ($>T_{\text{NI}}$) [S1]. In addition, West and coworkers recently showed that particles of sufficient size are dragged by a flat, moving N-Iso interface [S2]. Based on these previous studies, we prepared cells by filling the cell gap with the mixture in the isotropic liquid phase to ensure a well-dispersed state when confined between the polyimide alignment layers in the test cell. While the isotropic state of the mixtures is a pre-requisite for stable, homogeneous mixtures, the viscous drag of particles at the N-Iso interface at slow cooling appears to be important to obtain homeotropic alignment in the first experiment.

It is also important to note that all gold nanoclusters were prepared by a modified Brust-Schiffrin method [S3], that of Shon and co-workers [S4], which does not use a biphasic system containing tetraoctylammonium bromide (TOAB) as a phase transfer reagent. A recent study on alkyl thiolate capped gold nanoclusters prepared by the two-phase method showed the reduced oxidative stability of the Au nanoclusters in the presence of halide ions introduced by the TOAB [S5].

Considering all of the above, the present results are not surprisingly different from the results obtained for a related system described by Prasad *et al.*[S6] The authors filled the obviously self-made test cells with the mixture containing the nanoclusters in the nematic phase, which results in local concentration differences and aggregation of nanoparticles. In fact, following their protocol, we were indeed able to reproduce their optical results

with cells showing planar alignment as commonly observed for pure N-LCs in planar cells. This clearly shows that the properties of dispersion of nanoclusters in N-LCs strongly depend on the mixtures as well as on the cell preparation. One has to ensure stable, homogeneous mixtures with concentration differences arising only from interactions of the N-LC molecules with the surface of the gold nanoclusters (such as linear particle aggregates) prior to discussing the properties of these dispersions.

S3. TEM/HR-TEM Images and size distribution of hexane thiolate-capped Ag and CdTe nanoclusters

The Ag nanoclusters were prepared by adapting the procedure used for the gold nanoclusters [S3,S4] using AgNO_3 as a starting material.[S8] The CdTe quantum dots were prepared following a procedure established by Weller *et al.* using a phase transfer (thiolate exchange) [S8].

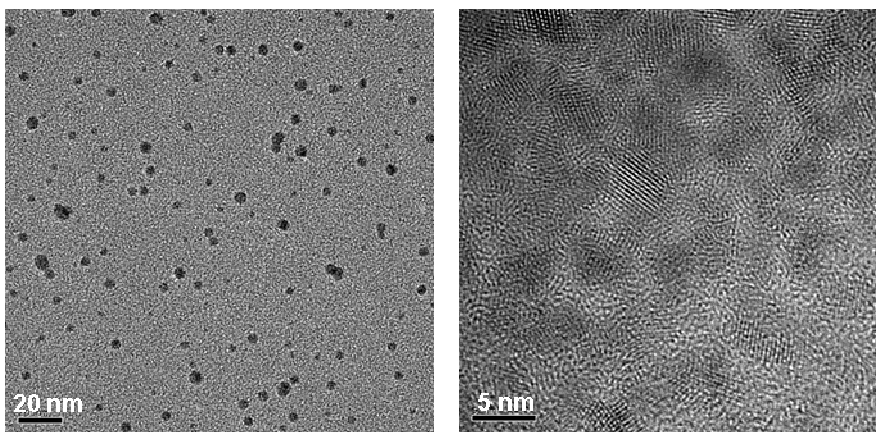


Fig. S8.2. (left) HR-TEM image of hexane thiolate-capped Ag clusters (4.2 ± 0.7 nm); (right) HR-TEM image of hexane thiolate-capped CdTe quantum dots (3.9 ± 0.3 nm).

S4. Table S8.1 Elastic constants K_{11} , K_{22} , and K_{33} (incl. standard deviations) of Felix-2900-03 doped with Au1 and Au2*

Sample	$T_{\text{Iso}}-T / ^\circ\text{C}$	K_{11}	St. Dev.	K_{22}	St.Dev.	K_{33}	St.Dev.
pure Felix	7	1.52E-11	0.16	9.11E-12	1.01	1.1E-10	0.91
	9	2.06E-11	0.14	12.4E-12	0.84	0.8E-10	0.27
	12	2.16E-11	0.28	13E-12	1.7	2.26E-10	1.37
	15	3.24E-11	0.29	19.6E-12	1.95	1.35E-10	0.7
Felix-5wt% Au1	7	6.09E-14	0.1	3.66E-14	0.06	1.34E-12	0.02
	9	17.49E-14	0.8	10.5E-14	0.5	3.85E-12	0.18
	12	93.97E-14	18	56.3E-14	10	0.44E-12	1.28
	15	145E-14	10	87E-14	16.4	5.54E-12	2.01
Felix-5wt% Au1 Cooling at field-ON	7	1.17E-12	0.21	7.05E-13	1.3	2.58E-11	0.47
	9	2.25E-12	0.18	13.5E-13	1.0	4.95E-11	0.40
	12	1.71E-12	0.33	10.25E-13	1.97	3.59E-11	0.55
	15	7.41E-12	1.6	44.5E-13	9.7	16.3E-11	3.6
Felix-10wt% Au1	7	2.79E-13	0.71	1.67E-13	0.42	6.1E-12	1.5
	9	4.31E-13	0.66	2.58E-13	0.4	9.5E-12	1.4
	13	6.15E-13	0.98	3.69E-13	0.6	2.7E-12	6.1
	16	1.28E-12	0.23	7.7E-13	1.3	4.5E-14	2.7

Sample	$T_{\text{Iso}}-T / ^\circ\text{C}$	K_{11}	St. Dev.	K_{22}	St.Dev.	K_{33}	St.Dev.
pure Felix	7	1.52E-11	0.16	9.11E-12	1.01	1.1E-10	0.91
	9	2.06E-11	0.14	12.4E-12	0.84	0.8E-10	0.27
	12	2.16E-11	0.28	13E-12	1.7	2.26E-10	1.37
	15	3.24E-11	0.29	19.6E-12	1.95	1.35E-10	0.7
Felix-5wt% Au1	7	6.09E-14	0.1	3.66E-14	0.06	1.34E-12	0.02
	9	17.49E-14	0.8	10.5E-14	0.5	3.85E-12	0.18
	12	93.97E-14	18	56.3E-14	10	0.44E-12	1.28
	15	145E-14	10	87E-14	16.4	5.54E-12	2.01
Felix-5wt% Au1 Cooling at field-ON	7	1.17E-12	0.21	7.05E-13	1.3	2.58E-11	0.47
	9	2.25E-12	0.18	13.5E-13	1.0	4.95E-11	0.40
	12	1.71E-12	0.33	10.25E-13	1.97	3.59E-11	0.55
	15	7.41E-12	1.6	44.5E-13	9.7	16.3E-11	3.6
Felix-10wt% Au1	7	2.79E-13	0.71	1.67E-13	0.42	6.1E-12	1.5
	9	4.31E-13	0.66	2.58E-13	0.4	9.5E-12	1.4
	13	6.15E-13	0.98	3.69E-13	0.6	2.7E-12	6.1
	16	1.28E-12	0.23	7.7E-13	1.3	4.5E-14	2.7

* $K_{11} = \left(\frac{V_{th}}{\pi}\right)^2 \Delta\epsilon\epsilon_0$, K_{22} is estimated as $0.6K_{11}$; K_{33} is obtained from a curve fitting algorithm of the $C-V$ curve.

S5. Table S8.2 Specific resistivity R (incl. standard deviations) of Felix-2900-03 doped with Au1 and Au2

Sample	$T_{\text{iso}}-T / ^\circ\text{C}$	Specific Resistivity / $\Omega\cdot\text{cm}$	St. Dev.	Sample	$T_{\text{iso}}-T / ^\circ\text{C}$	Specific Resistivity/ $\Omega\cdot\text{cm}$	St.Dev.
pure Felix	7	7.25E+10	0.16	Felix-5wt% Au2	7	8E+8	0.06
	9	20.5E+10	0.67		10	9.8E+8	0.01
	12	26.7E+10	1.5		13	12.8E+8	4.2
	15	32.6E+10	4.3		16	23.7E+8	0.2
Felix-5wt% Au1	7	10E+8	0.1	Felix-5wt% Au2 Cooling at field-ON	7	20E+8	0.1
	9	7.1E+8	0.05		10	25E+8	1
	12	6.5E+8	0.03		13	32E+8	4
	15	10E+8	0.07		16	49E+8	1.3
Felix-5wt% Au1 Cooling at field-ON	7	20E+8	0.15	Felix-10wt% Au2	11	49.6E+8	3
	9	22E+8	0.06		14	79E+8	1.2
	12	27E+8	0.86		17	137E+8	8.4
	15	26E+8	0.26				
Felix-10wt% Au1	7	9.1E+8	0.02				
	10	9.2 E+8	0.01				
	13	10.4 E+8	0.02				
	16	13.6 E+8	0.01				

S6. Table S8.3 Comparison of Felix-2900-03 doped with 10 wt% Au1 measured with two different initial setups

A) Conventional setup for N-LC with $\Delta\varepsilon > 0$ in planar cell (used for all measurements in the main text)

B) Setup assuming N-LC with $\Delta\varepsilon < 0$ in homeotropic cell

<i>Setup</i>	$T_{\text{iso}} - T / ^\circ\text{C}$	$V_{\text{th}}(\text{rms})$	ε_{\parallel}	ε_{\perp}	$\Delta\varepsilon$	K_{11} (E-14)	K_{22} (E-14)	K_{33} (E-12)	$R / \Omega \cdot \text{cm}$ (E+8)
A	10	0.833±0.004	6.31±0.19	5.623±0.066	0.691±0.09	43.07±6.615	25.84±3.969	9.476±1.455	9.242
A	13	1.193±0.104	5.87±0.01	5.323±0.14	0.494±0.13	61.54±9.857	36.92±5.914	2.756±0.612	10.42
B	10	1±0.04	5.28±0.0228	5.78±0.006	-0.497±0.01	44.60±2.85	26.76±0.79	0.446±0.013	8.416
B	13	1.48±0.04	5.21±0.031	5.65±0.005	-0.44±0.01	86.83±3.29	52.1±1.80	0.086±0.017	10.2

S7. References

- [S1] C. Da Cruz, O. Sandre, V. Cabuil, *J. Phys. Chem. B* **2005**, *109*, 14292-14299.
- [S2] J. L. West, K. Zhang, A. Glushchenko, D. Andrienko, M. Tasinkevych, Y. Reznikov, *Eur. Phys. J. E* **2006**, *20*, 237-242.
- [S3] H. Choo, E. Cutler, Y.-S. Shon, *Langmuir* **2003**, *19*, 8555-8559.
- [S4] M. Brust, M. Walker, D. Bethell, D. J. Schiffrin, R. Whyman, *J. Chem. Soc., Chem. Commun.* **1994**, 801-802.
- [S5] M. Dasog, R. W. J. Scott, *Langmuir* **2007**, *23*, 3381-3387.
- [S6] S. K. Prasad, K. L. Sandhya, G. G. Nair, U. S. Hiremath, C. V. Yelamaggad, S. ampath, *Liq. Cryst.* **2006**, *33*, 1121-1125.
- [S7] P. Ahonen, T. Laaksonen, A. Nykanen, J. Ruokolainen, K. Kontturi, *J. Phys. Chem. B* **2006**, *110*, 12954-12958.
- [S8] N. Gaponik, D. V. Talapin, A. L. Rogach, A. Eychmuller, H. Weller, *Nano Lett.* **2002**, *2*, 803-806.

Chapter 9: Effects of functionalized metal and semiconductor nanoparticles in nematic liquid crystal phases

This paper was reproduced with permission from Proc. SPIE. 2008, 6911, 691106. Copyright - 2008 Society of Photo-Optical Instrumentation Engineers. It is co-authored with B. Kinhead and T. Hegmann. The text is a verbatim copy of the published paper.

Equipped with the knowledge that ‘simple’ alkylthiol-capped Au NPs can effectively reverse the alignment of nematic LCs in cells with planar polyimide alignment layers, and that the same particles effectively induce two different alignment modes both at lower threshold voltages in comparison to the pure nematic LC, the next question was whether these phenomena are exclusively found for Au NPs in the size regime between 1 and 2 nm. Chapter 9 will continue to investigate electro-optic properties of nematic LCs now doped with Ag NPs, CdTe quantum dots (QDs) and larger Au NPs (~5-6 nm).

Abstract: To capitalize on the unique size and shape-dependent optical and electronic properties of nanoscale particles for liquid crystal (LC) applications, detailed structure and size-property relationship studies are critical. To enhance our understanding of the thermal, optical and electro-optic effects of nanoparticles in nematic LCs we produced numerous different nematic LC mixtures containing small quantities of dispersed metal nanoparticles (i.e., gold and silver nanoclusters) or semiconductor quantum dots (i.e., CdTe nanocrystals) and studied their optical (texture, alignment, defect formation, luminescence) and electro-optic properties. Depending on several experimental parameters such as nanoparticle functionalization and concentration, as well as thermal history in combination with an applied electric field, these nanoparticle/LC mixtures with the nanoparticles differing in surface functionality, size, and core material gave rise to unique alignment effects and electro-optic responses in the two investigated nematic LC (N-LC) hosts.

9. 1. Introduction

Recent years have seen a steady increase of the use of nanoparticles (metallic, semiconducting, ferromagnetic, or ferroelectric) in mixtures with liquid crystals (LCs) used in device and display applications (i.e., nematic, chiral nematic, or ferroelectric) [1]. An increasingly vast variety of new nanomaterials differing in size, shape, and properties as well as the need for LC displays to remain competitive with other display technologies created a surge of research activity to improve upon existing LC mixtures for flat panel display applications using nanoparticle/LC suspensions [2]. This research now spans over all switching or display modes from twisted nematic and in-plane switching to vertical

alignment mode and surface stabilized ferroelectric LC displays with dispersed nanoparticles inducing different alignment modes or altering electro-optic characteristics of the LC host material. However, detailed structure-property, size-property, and shape-property relationship studies of nanomaterials in LCs have not been the focus of recent investigations in this field. Most reports focus on some unique optical or electro-optic effects induced by one particular type of nanoparticle, and not on the evolution or on changes of particular effects with particle size, shape, core material, or structure of the nanoparticle capping agent.

Recent investigations of our group on functionalized gold nanoparticles in different types of LCs (nematic, smectic, columnar) have shown that the chemical nature of the monolayer protecting the gold nanoparticles from aggregation into ill-defined aggregates (or ripening) plays a major role in altering the bulk properties of LC materials (LC phases), chiefly driven by interactions commonly observed for pure organic additives (dopants) [3]. For example, gold nanoparticles decorated with a chiral dopant [(*S*)-naproxen] at concentrations as low as 0.5 wt% induce a bulk chiral nematic phase with a sign inversion (opposite helical sense) in comparison to the pure organic chiral dopant in the same nematic host [3b].

We have further shown that N-LCs upon doping with alkyl thiolate coated gold nanoparticles produced thin film textures characterized by birefringent stripe domains separated by areas showing homeotropic alignment of the N-LC molecules. [4] Considering the strong homeotropic anchoring of the N-LC molecules to the nanocluster surface *via* dispersion and van der Waals interactions, the observation of the birefringent stripes was explained by the formation of linear particle aggregates. These linear

aggregates resulted from the formation of topological defects (dipoles and hyperbolic hedgehogs) as discussed for many quasi-spherical particles in N-LCs [5]. Then, given the experimentally observed planar alignment of the pure N-LC on untreated glass slides, the gold nanoparticles residing at the glass/N-LC interfaces drive the homeotropic alignment in the domains separating the birefringent stripes.

These mixtures also produced identical thin films textures in ITO-coated LC test cells with rubbed polyimide alignment layers (Fig. 9.1) that should have produced planar alignment of the used N-LC featuring a positive dielectric anisotropy ($\Delta\epsilon > 0$) as observed for the pure LC in the same cells. We found that the homeotropic domains in these cells can be electrically reoriented and aligned either like N-LCs with a positive dielectric anisotropy in a planar cell or alternatively as N-LCs with a negative dielectric anisotropy in a homeotropic cell, and that both alignment modes reorient at lower Freedericksz transition threshold voltages (V_{th}) in comparison to the pure N-LC. This was achieved by changing the thermal as well as applied electric field history of the nanoparticle doped N-LC cells. Cells cooled from the isotropic liquid phase to the N-phase at field-OFF displayed homeotropic alignment (depending on the nanoparticle concentration with or without stripe defects), which could be electrically reoriented to a planar (or strongly tilted) orientation upon applying an electric field with threshold voltages approximately 4-times lower than the pure N-LC at the same reduced temperature ($T_{iso}-T$). The same cell cooled to the N-phase at field-ON showed homeotropic alignment in the field-ON state and bright, birefringent domains (planar or strongly tilted orientation) in the field-OFF state with threshold voltage just slightly lower than for the pure N-LC [6]. This unprecedented dual alignment mode and the lower V_{th} values were observed for hexane

thiolate (**Au1**; size: 1.9 ± 0.5 nm) and dodecane thiolate capped gold nanoclusters (**Au2**; size: 2.1 ± 0.7 nm) with the lowest V_{th} values in both alignment modes for the hexane thiolate capped **Au1** nanoparticles. To explain the two switching modes, we suggested a model in which the electronically charged gold nanoparticles, initially residing at the alignment layer/N-LC interface (cooling at field-OFF), acted as local capacitors [7, 8, 9] and dipoles [10] not only enhancing the overall conductivity, but as an assembly at the interface inducing homeotropic alignment similar to a mixed thiol self-assembled monolayer (SAM) on a flat Au surface.¹¹ The relative similarity of the electro-optic response (V_{th} , $\Delta\epsilon$, K_{11} , K_{22} , K_{33} , and R) after cooling the cell to the N-phase at field-ON suggested that this alignment mode is more similar to the pure N-LC in a planar cell, in which the gold nanoparticles are now dispersed in the bulk of the cell, away from the alignment layer interfaces, since the field- OFF state does not give rise to any homeotropic domains in the ITO-covered (field-addressed) area of the cell.

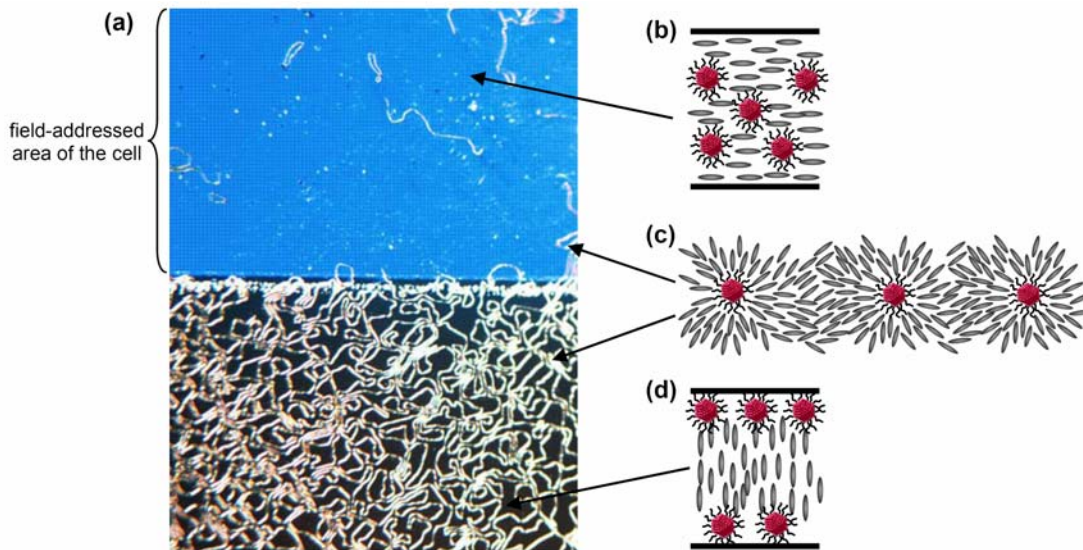
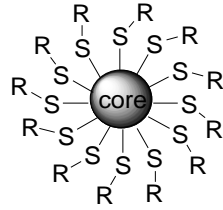
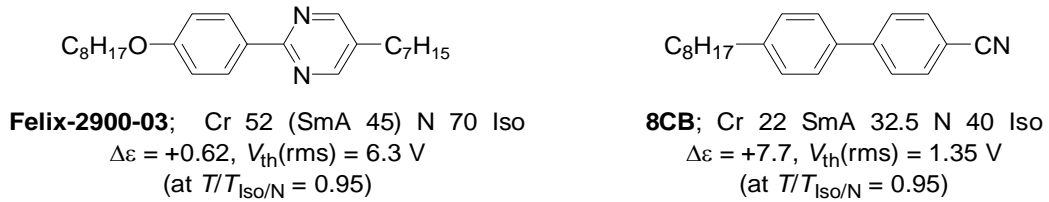


Fig. 9.1. (a) Polarized optical photomicrograph of the LC (Felix-2900-03) in the N-phase doped with 5wt% dodecane thiolate capped gold nanoparticles at 55 °C in a planar ITO-test cell on cooling from the isotropic liquid phase at field-ON – both the field addressed and non-field addressed area is shown to demonstrate the impact of the electric-field/thermal history (rubbed polyimide alignment layers, low pre-tilt, cell gap: 5 micron, source: Displaytech Inc.) showing the coexistence of birefringent stripes (linear particle aggregates) and homeotropic domains in the non-field-addressed area and a few stripe domains in an otherwise planar aligned field-addressed area, (b) origin of the planar alignment after cooling the cell at field-ON (c) origin of the birefringent stripes (formation linear particle aggregates), and (d) origin of homeotropic alignment due to particles at the N-LC/alignment layer interface (no field or cooling at field-OFF).

We also succeeded in obtaining the described homeotropic alignment mode (*via* cooling at field-OFF) using hexane thiolate capped silver nanoparticles as well as CdTe quantum dots (predominantly capped with alkyl thiols) [6], which excluded room temperature magnetism of the gold nanoparticles [12] as a cause for the homeotropic alignment. Based on these preliminary experiments, we here present the results of detailed electro-optic measurements using larger dodecane thiolate capped gold nanoparticles (**Au3**; size: 5.4 ± 0.9 nm), hexane thiolate capped silver nanoparticles (**Ag1**; size: 4.2 ± 0.7 nm), and mainly hexane thiolate (**QD1**, size: 3.5 ± 0.8 nm) as well as dodecane thiolate capped CdTe quantum dots (**QD2**, size: 4.1 ± 0.6 nm) [13] in the two

previously studied N-LCs (Felix-2900-03 and 8CB, Fig. 9.2). This will allow for a step-by-step comparison (including **Au1** and **Au2**) of the effects of size, nanoparticle core material, and capping agent (alkyl chain length) on the electro-optic characteristics and alignment modes of the nanoparticle doped N-LC cells.



NP	core	R	size [nm]
Au1	Au	C ₆ H ₁₃	1.9±0.5
Au2	Au	C ₁₂ H ₂₅	2.1±0.7
Au3	Au	C ₁₂ H ₂₅	5.4±0.9
Ag1	Ag	C ₆ H ₁₃	4.2±0.7
QD1	CdTe	C ₆ H ₁₂	3.5±0.8
QD2	CdTe	C ₁₂ H ₂₅	4.1±0.6

Fig. 9.2. Structure, phase transition temperatures, dielectric anisotropy $\Delta\varepsilon$, and threshold voltage $V_{th}(rms)$ (at $T/T_{Iso/N} = 0.95$) of the two N-LCs [6] (top), and schematic of the synthesized and investigated nanoparticles (bottom).

9.2 Experimental

9.2.1 Materials

The N-LCs used are commercially available pure LCs [Felix-2900-03 (Hoechst) and 8CB (Merck KGaA)]. The smaller alkyl thiolate capped gold nanoparticles **Au1** and **Au2** (~2 nm in diameter), included here for comparison, were prepared following a procedure described in an earlier paper and followed a modified Brust-Schiffrin approach [14] using THF and an aqueous solution of NaBH₄ without the use of a phase transfer agent such as tetraoctylammonium bromide (TOAB) [15]. The larger dodecane thiolate capped gold

nanoparticles **Au3** (5.4 ± 0.9 nm in diameter) were synthesized following a procedure reported by Zhong and coworkers [16]. The silver nanoparticles **Ag1** were prepared by adapting the procedure used for the gold nanoparticles [14, 17] using AgNO_3 as a starting material [18], and the CdTe quantum dots **QD1** and **QD2** were prepared following a procedure established by Weller *et al.* using a thiolate exchange in the final step [19]. Briefly for the CdTe quantum dots, thioglycolic acid capped CdTe quantum dots, initially synthesized by injecting freshly prepared NaHTe into an aqueous solution of $\text{Cd}(\text{ClO}_4)_2 \cdot 6\text{H}_2\text{O}$ and refluxing at 105°C , are transferred into organic-solvent soluble CdTe quantum dots capped mainly with alkyl thiolates [13] *via* phase transfer.

9.2.2 Sample preparation

All particles were stored as dry solids under a protective atmosphere of dry nitrogen in the dark, and can be repeatedly dispersed in and isolated from common organic solvents without change in size (no aggregation or ripening). All glass vials and Teflon-coated spatulas were rinsed with *aqua regia* prior to all mixture preparations. Mixtures were then prepared by combining solutions of both components in a common, pure, and dry solvent (e.g., ethyl acetate). The resulting solutions were stirred (agitated) for at least 10 minutes, and the solvent was evaporated by a steady stream of dry N_2 over open glass vials. Thereafter, all mixtures were dried in vacuum for 24 hours. Prior to filling the LC test cells by capillary forces with the LC in the isotropic liquid phase, all mixtures were heated just below the isotropic-nematic phase transition ($T_{\text{Iso/N}}$) and continuously mixed again.

9.2.3 Methods

High-resolution transmission electron microscopy (HR-TEM) images were obtained on a Jeol ultra-high resolution FEGT/ STEM operating at an accelerating voltage of 200 kV. A 10 μL drop of the cluster solution was drop-cast on a carboncoated copper grid (400-mesh) and dried for 1 h. Representative HR-TEM images are shown in Fig. 9.3. UV-vis spectra of all nanoparticles were obtained on a Varian Cary 5000 UV-vis-NIR spectrophotometer, and luminescence (emission) spectra of the CdTe quantum dots were collected using a Varian Cary Eclipse spectrophotometer. Polarized optical microscopy (POM) was performed using an Olympus BX51-P polarizing microscope in conjunction with a Linkam LS350 heating/cooling stage. Electro-optic tests were performed using an LCAS automated liquid crystal analyzer (LC Vision). The LC test cells used were planar 5.0 micron cells with antiparallel polyimide alignment layers and low pre-tilt (Displaytech Inc., purchased from Linkam Scientific Instruments) and planar 5.0 or 6.8 micron cells with parallel or antiparallel polyimide alignment layers and 1° to 3° pre-tilt (Instec, Inc.). The reproducibility of the alignment effects was checked on over 100 cells overall. All electro-optic measurements were obtained using three cells (Displaytech, purchased from Linkam Scientific Instruments) for each mixture and a series of ten measurements each (3×10 to obtain standard deviations for each data point).

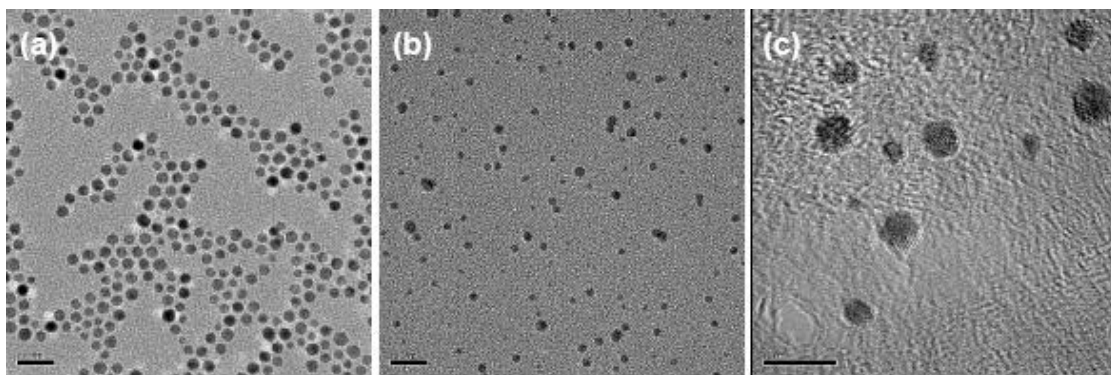


Fig. 9.3. High-resolution transmission electron microscope (HR-TEM) images of: (a) **Au3**, (b) **Ag1**, and (c) **QD2** [Scale bars in (a) and (b) = 20 nm, in (c) = 5 nm].

9.3 Results and Discussion

For all cells of Felix-2900-03 containing 5 or 10wt% **Au3**, **Ag1**, **QD1**, and **QD2** the threshold voltage (V_{th}), the dielectric permittivity along ($\epsilon_{||}$) and across the long molecular axis (ϵ_{\perp}), the dielectric anisotropy ($\Delta\epsilon = \epsilon_{||} - \epsilon_{\perp}$), the elastic constants K_{11} , K_{22} , and K_{33} (splay, twist, bend), as well as the specific resistivity R were measured (calculated/estimated [20]) before and after treating the cell with the field-ON cooling approach (initially homeotropic vs. parallel alignment, if obtainable) using the “single cell” method described by Wu *et al.*[21] built into the software of the automated LC test-bed. All measurements were performed depending on temperature by slow cooling from the isotropic liquid phase (at $1\text{ }^{\circ}\text{C min}^{-1}$) and start at $T_{iso}-T = 7\text{ }^{\circ}\text{C}$ (for Felix-2900-03) and at $T_{iso}-T = 3\text{ }^{\circ}\text{C}$ (for 8CB) taking into consideration the broadened phase transition due to the presence of the nanoparticles [22].

9.3.1 Felix-2900-03 doped with Au3

Plots of V_{th} vs. $T_{Iso}-T$ and $\epsilon_{||}$ (ϵ_{\perp}) vs. $T_{Iso}-T$ of cells treated with cooling at field-OFF for pure Felix-2900-03 and Felix- 2900-03 doped with **Au2** (5wt% and 10wt%) [6] or with **Au3** (5wt%) are shown in Figs. 9.4 and 9.5.

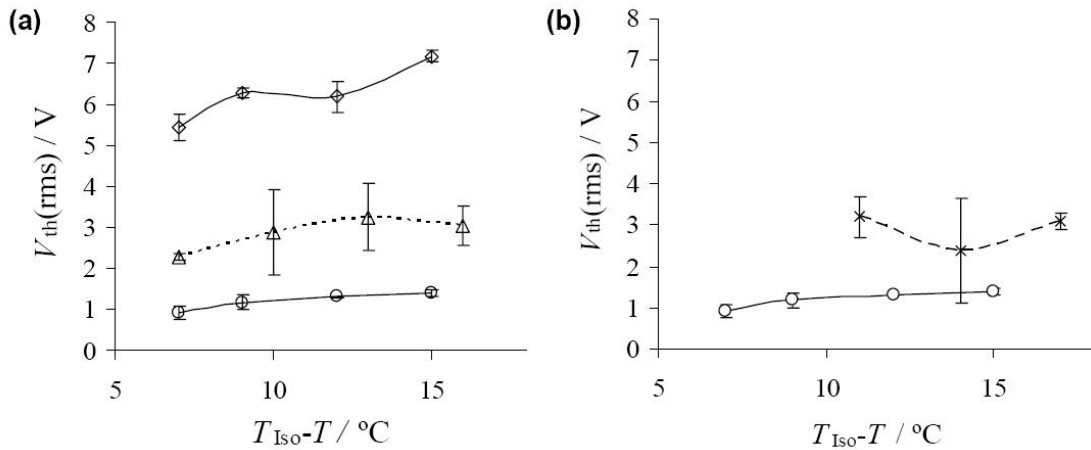


Fig. 9.4. $V_{th}(rms)$ vs. $T_{Iso}-T$: (a) \diamond pure Felix-2900-03, \triangle Felix-2900-03 doped with 5wt% **Au2**, \circ Felix-2900-03 doped with 10wt% **Au3**, (b) \times Felix-2900-03 doped with 10wt% **Au2**, \circ Felix-2900-03 doped with 10wt% **Au3**.

A comparison of V_{th} vs. $T_{Iso}-T$ of the mixtures doped with the two gold nanoparticles **Au2** and **Au3** (both capped with dodecane thiolate) with the pure N-LC reveals that the nanoparticle doped mixtures show reduced threshold voltages, with the larger **Au3** nanoparticles showing the lowest value for V_{th} in this series despite an overall lower total number of particles present in the mixtures (number of nanoparticles present: 10wt% **Au2**/10wt% **Au3** \approx 15/1).

Another interesting trend can be seen in Fig.9.5. Apparently, an increase in the gold nanoparticle size results in an increase of the dielectric anisotropy ($\Delta\epsilon = \epsilon_{||} - \epsilon_{\perp}$) in mixtures with Felix-2900-03, or more precisely, the relative dielectric permittivity

perpendicular to the long molecular axis (ϵ_{\perp}) decreases.

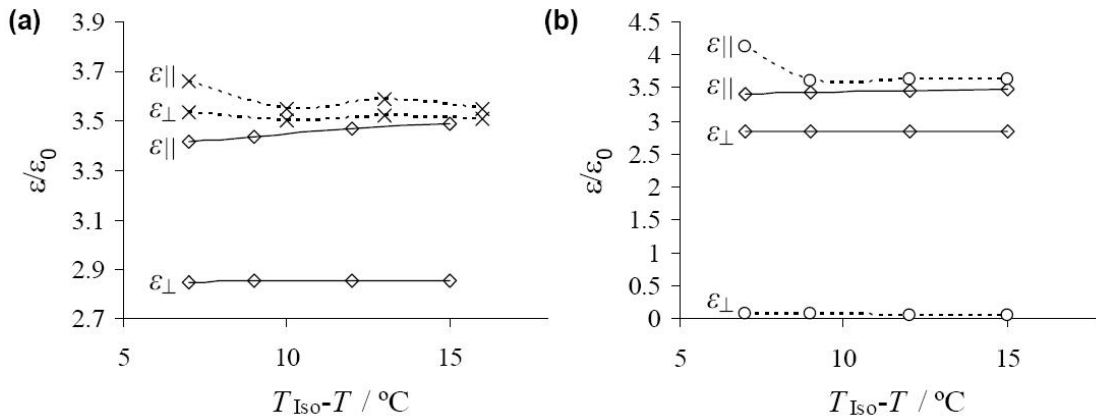


Fig. 9.5. ϵ_{\parallel} (ϵ_{\perp}) vs. $T_{\text{Iso}}-T$: (a) \diamond pure Felix-2900-03, \times Felix-2900-03 doped with 5wt% Au2, (b) \diamond pure Felix-2900-03, \circ Felix-2900-03 doped with 10wt% Au3.

9.3.2 Felix-2900-03 doped with Ag1

Plots of V_{th} vs. $T_{\text{Iso}}-T$ and ϵ_{\parallel} (ϵ_{\perp}) vs. $T_{\text{Iso}}-T$ of cells treated with cooling at field-OFF for pure Felix-2900-03, Felix-2900-03 doped with Au1 or doped with 5wt% or 10wt% Ag1 are shown in Figs. 9.6a and 9.7a, and a comparison of Felix-2900-03 doped with 5wt% Ag1 treated with both regimes (cooling at field-OFF or cooling at field-ON) are collected in Figs. 9.6b and 9.7b.

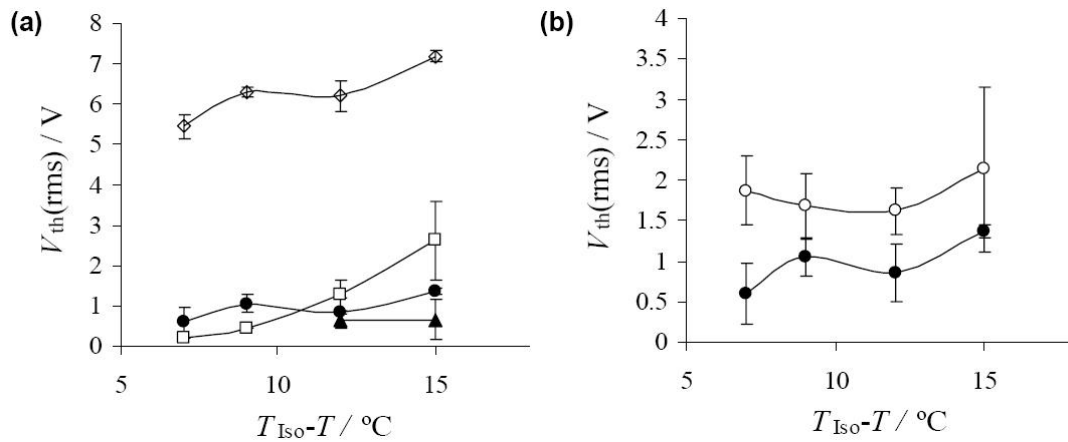


Fig. 9.6. (a) $V_{th}(rms)$ vs. $T_{Iso}-T$ of cells treated with cooling at field-OFF: \diamond pure Felix-2900-03, \square Felix-2900-03 doped with 5wt% Au1, \bullet Felix-2900-03 doped with 5wt% Ag1, \blacktriangle Felix-2900-03 doped with 10wt% Ag1, (b): \bullet Felix-2900-03 doped with 5wt% Ag1 treated with cooling at field-ON, \circ Felix-2900-03 doped with 5wt% Ag1 treated with cooling at field-ON.

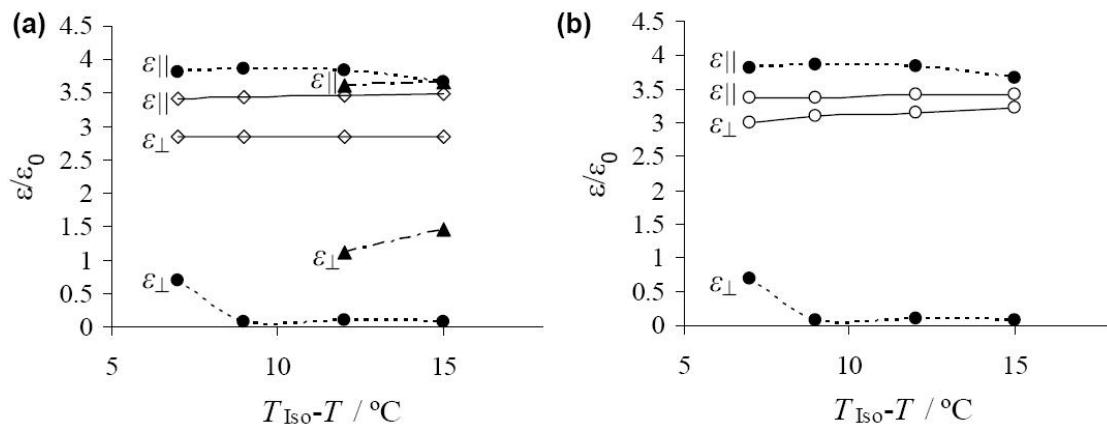


Fig. 9.7. $\epsilon_{||}$ (ϵ_{\perp}) vs. $T_{Iso}-T$: (a) \diamond pure Felix-2900-03, \bullet Felix-2900-03 doped with 5wt% Ag1, \blacktriangle Felix-2900-03 doped with 10wt% Ag1, (b) \bullet Felix-2900-03 doped with 5wt% Ag1 of cells treated with cooling at field-OFF, \circ Felix-2900-03 doped with 5wt% Ag1 of cells treated with cooling at field-ON.

Considering our current model with the gold nanoclusters residing at the alignment layer/N-LC interface in the cooling at field-OFF regime (homeotropic or vertical alignment), it is not surprising that similarly sized hexane thiolate capped silver nanoparticles reduce V_{th} in a similar way as gold nanoparticles monolayer-protected with the same thiolate (Fig. 9.6a). We again found that increasing the concentration of Ag1 in

Felix-2900-03 from 5wt% to 10wt% results in only a minor change of V_{th} , and that cooling the same cell at field-ON produces an electro-optic response closer to the pure N-LC, although the mixtures of Felix-2900-03 with the larger **Ag1** (in comparison to **Au1**), showing planar alignment in this cooling regime, still exhibit V_{th} values that are at least 50% lower than those measured for the pure N-LC. This would suggest that the capacitive charging effects known for metal nanoparticles such as silver and gold [7, 8, 9] play an important role in the reduction of the threshold voltage in these mixtures, and explains why this charging effect is most dominating when the metal nanoparticles assemble at the alignment layer/N-LC interface acting as an array.

The relative dielectric permittivity data (i.e., $\Delta\epsilon$) of these mixtures obtained from cells treated with cooling at field-OFF (vertical alignment) again confirm some of the already observed trends. The larger **Ag1** nanoparticles, as **Au3**, produce mixtures with an increasing $\Delta\epsilon$ (reduced ϵ_{\perp}) both at 5wt% and 10wt%, and the values obtained after cooling the cell at field-ON (planar alignment) are almost identical to the values obtained for the pure N-LC (Fig. 9.7b).

9.3.3 Felix-2900-03 doped with QD2

Plots of V_{th} vs. $T_{iso}-T$ and $\epsilon_{||}$ (ϵ_{\perp}) vs. $T_{iso}-T$ of cells treated with cooling at field-OFF for pure Felix-2900-03, Felix-2900-03 doped with 5wt% or 10wt% **QD2** in comparison to Felix-2900-03 doped with **Au2** or **Au3** (all dodecane thiolate capped) are shown in Figs. 9.8 and 9.9.

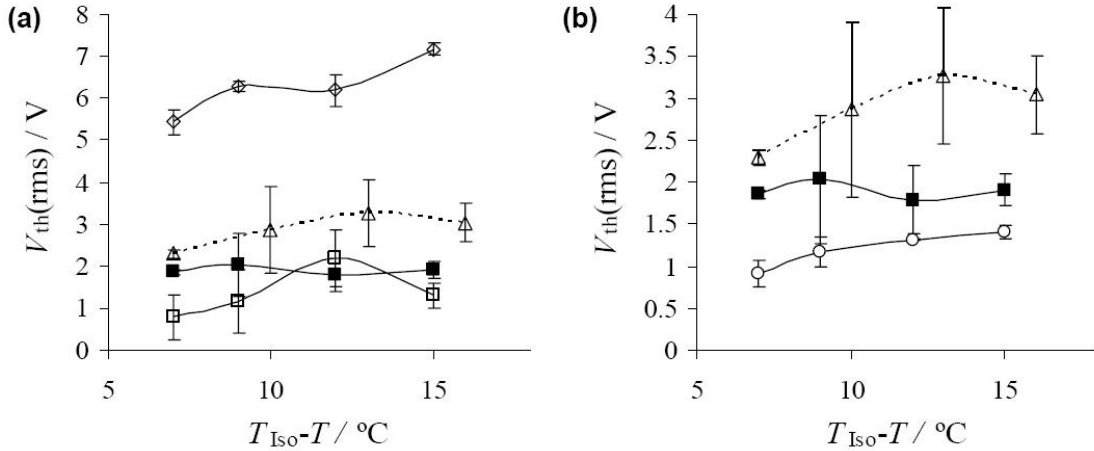


Fig. 9.8. $V_{th}(rms)$ vs. $T_{Iso}-T$ of cells treated with cooling at field-OFF: (a) \diamond pure Felix-2900-03, \triangle Felix-2900-03 doped with 5wt% **Au2**, \blacksquare Felix-2900-03 doped with 5wt% **QD2**, and \square Felix-2900-03 doped with 10wt% **QD2**, (b) \triangle Felix-2900-03 doped with 5wt% **Au2**, \blacksquare Felix-2900-03 doped with 5wt% **QD2**, and \circ doped with 5wt% **Au3**.

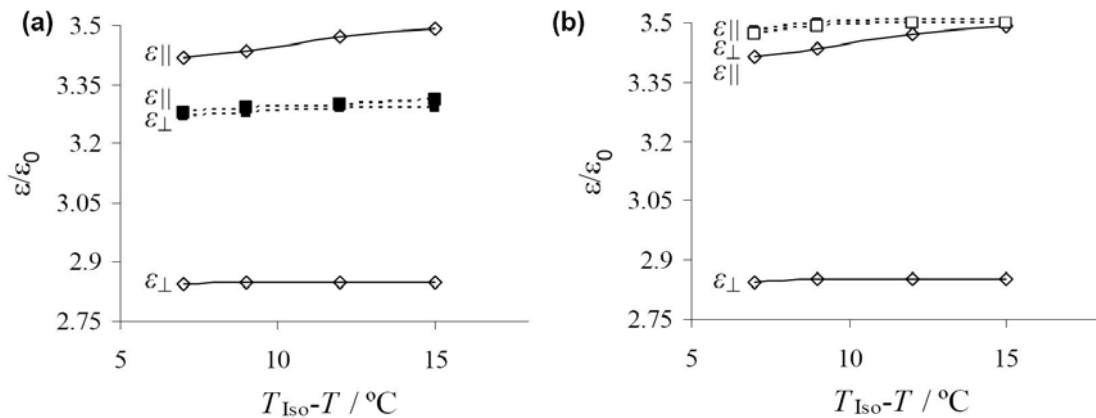


Fig. 9.9. $\epsilon_{||}$ (ϵ_{\perp}) vs. $T_{Iso}-T$: (a) \diamond pure Felix-2900-03, \blacksquare Felix-2900-03 doped with 5wt% **QD2**, (b) \diamond pure Felix-2900-03, \square Felix-2900-03 doped with 10wt% **QD2**.

It appears that the slightly larger dodecane thiolate capped CdTe quantum dots **QD2** outperform the smaller dodecane thiolate capped gold nanoparticles **Au2** by showing lower values for V_{th} over the entire temperature range at both 5wt% and 10wt% in Felix-2900-03 (Fig. 9.8a). However, at the same N-LC/nanoparticle ratio (5wt%) in the series **Au2**, **Au3** and **QD2** (all identically capped with dodecane thiolate [13]) dispersed in Felix-2900-03, the larger gold nanoparticles **Au3**, presumably due to the dominating capacitive charging effects described earlier, gave the lowest threshold voltages (Fig.

9.8b).

As for the relative dielectric permittivity $\epsilon_{||}$ and ϵ_{\perp} , and the dielectric anisotropy $\Delta\epsilon$, **QD2** seem to have the same effect on Felix-2900-03 as the smaller gold nanoclusters, i.e., the values of $\epsilon_{||}$ are in the range of pure Felix-2900-03 and ϵ_{\perp} increases resulting in overall lower $\Delta\epsilon$ values (Fig. 9.9).

While the electro-optic performance of the **QD2** doped Felix-2900-03 mixtures matches those observed for the gold and silver nanoparticle doped mixtures, the mixed monolayer (dodecane thiolate and thioglycolic acid capped [13]) nature of the quantum dots (prepared by the phase transfer process) does not allow for the dual alignment mode as described for **Au1- Au3** as well as **Ag1** (all homogeneously capped with alkyl thiolates), which we relate to the overall lower solubility (inferior compatibility) of the mixed monolayer **QD2** in Felix-2900-03 in addition to possible interactions between the polar thioglycolic acid -COOH groups (HSCH_2COOH ; particularly if ‘phase-separated’ on the quantum dot surface) and the polyimide alignment layers. In fact, textures featuring only homeotropic (vertical) alignment with very few (to none at 10wt%, see Fig. 9.10) birefringent stripes were observed, independent of the thermal and electric-field history of the cell (cooling at field-ON or field-OFF).

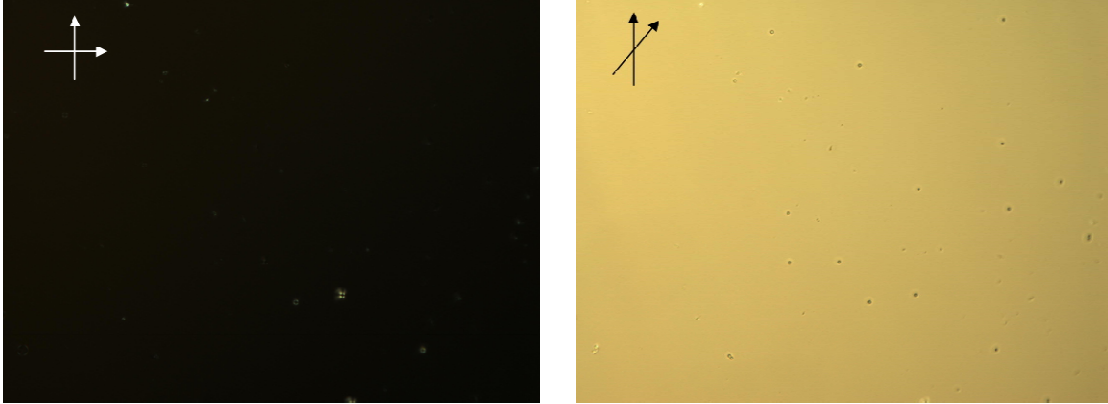


Fig. 9.10. Polarized optical photomicrographs of Felix-2900-03 doped with 10wt% **QD2** (arrows indicate polarizer/analyzer orientation) in cells with planar polyimide alignment layers (source: Displaytech Inc.; cell gap: 5 micron) treated with cooling to the N-phase at field-OFF at 67 °C. As described earlier [6], an increase of the nanoparticle concentration results in the disappearance of the birefringent stripe defects producing virtually homogeneous vertical (homeotropic) alignment of Felix-2900-03 in planar cells.

However, the alkyl thiolate capped CdTe quantum dots possess a quality not shared by the gold and silver nanoparticles; they are characterized by a size-dependent photoluminescence in solution as well as in the solid state. Figure 9.11 shows the absorption and photoluminescence spectrum of the **QD2** quantum dots in toluene (Note that the synthesis of these CdTe quantum dots allows for isolation and phase transfer of somewhat discrete sizes that differ in emission wavelength and intensity [19]).

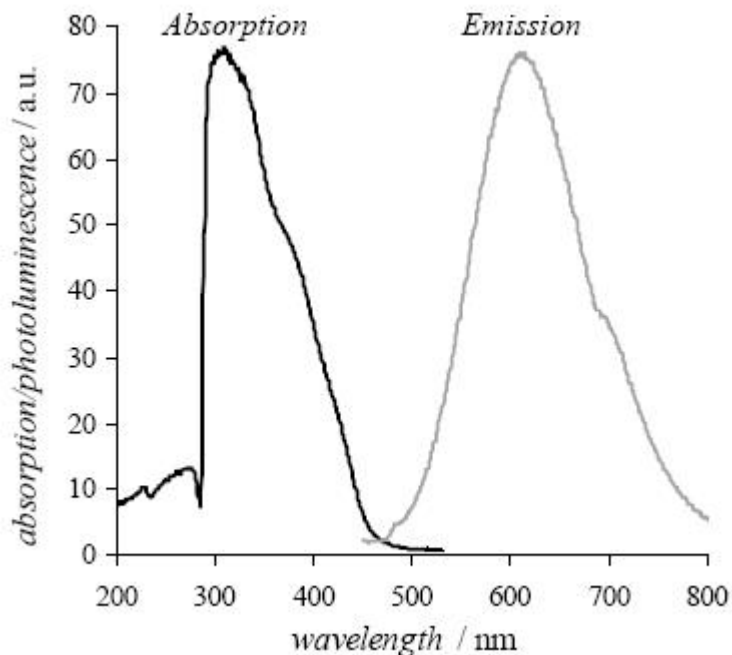


Fig. 9.11. Absorption and emission spectrum ($\lambda_{\text{exc.}} = 375 \text{ nm}$) of the dodecane thiolate capped quantum dots **QD2** in toluene.

9.3.4 8CB doped with QD1 and QD2

To further prove the importance of detailed structure-property relationships, we also measured the electro-optic response of two CdTe quantum dots differing in size and in surface functionality (hexane thiolate capped **QD1** and dodecane thiolate capped **QD2**) in the structurally different, polar N-LC 8CB23. As for the gold nanoclusters **Au1** reported earlier [6], doping 8CB with the two quantum dots **QD1** or **QD2** did not result in a significant change (slight decrease) of the threshold voltage despite an increase of $\Delta\epsilon$ for **Au1** as well as **QD2** (see Table 1). As with 5CB and other cyanobiphenyl based N-LCs tested, the incompatibility of the polar N-LCs with the hydrocarbon-capped nanoparticles (inferior compatibility in comparison to Felix-2900-03 flanked by two hydrocarbon chains) complicates a discussion of the electro-optic data obtained from these mixtures.

In addition, a reproduction of the dual alignment mode with the quantum dots proved as difficult as with the gold nanoparticles [6], with most cells showing no homogeneous homeotropic alignment (if at all) with cooling at field-OFF.

Table 9.1. Electro-optic data of 8CB and 8CB doped with **Au1**, **QD1**, and **QD2** at $T_{\text{Iso}} - T = 6$ °C.

	$V_{\text{th}}(\text{rms}) / \text{V}$	$\Delta\epsilon$
pure 8CB	1.46	8.4
8CB doped with 5wt% Au1	0.73	18.5
8CB doped with 5wt% QD1	1.07	6.12
8CB doped with 5wt% QD2	1.19	18.0

9.4 Conclusion

In conclusion, we have demonstrated a viable approach to alter the alignment of N-LCs with $\Delta\epsilon > 0$ in planar cells coated with polyimide alignment layers and improve their electro-optic characteristics, i.e., reduced threshold voltages, by doping nematic LCs with metal (gold, silver) nanoparticles as well as with semiconductor quantum dots. By changing critical nanoparticle parameters such as size, core material, and surface functionality, we were able to produce vertically (homeotropically) aligned cells that can be electrically reoriented at much lower threshold voltages in comparison to the pure N-LC. We have also shown, how size and core material of the nanoparticle impacted the threshold voltage, with the smaller **Au1** and **Ag1** as well as the largest **Au3** showing the

lowest values of V_{th} over the entire nematic phase range.

This is consistent with our previous assumption that the more semiconducting nature of metal nanoparticles with shorter hydrocarbon chain thiolates and capacitive charging effects of the metal nanocluster cores play an important role in the reduction of the threshold voltage considering the induced vertical alignment with the nanoparticles residing at the interfaces. The values obtained for the semiconductor quantum dots doped mixtures fit well into this model, since the quantum dot protected by a thiolate of equal alkyl chain length showed lower V_{th} values in comparison to the gold nanoparticle (**QD2** vs. **Au2**), and the quantum dot with shorter alkyl chain length showing lower V_{th} values in comparison to the quantum dot with longer chains in the same N-LC (**QD1** vs. **QD2**, see Table 9.1).

Finally, we have also shown that the nature of the nanoparticle monolayer protection, i.e., one-component vs. two component (mixed monolayer), influences our ability to produce cells of an N-LC with $\Delta\epsilon > 0$ featuring the thermal and electric field history-dependent dual alignment mode. Here, in particular the mixed monolayer protected CdTe quantum dots exclusively produce vertical alignment in planar cells in both regimes, cooling at field-OFF and cooling at field-ON, but have the added bonus of size-tunable photoluminescence for the use in self-illuminating LC displays.

Acknowledgements

This work was supported by Natural Sciences and Engineering Research Council (NSERC) of Canada, the Canada Foundation for Innovation (CFI), the Manitoba Research and Innovation Fund (MRIF), and the University of Manitoba (IPM

Demonstration Project Grant). The authors would also like to extend thanks to Prof. Chaturvedi and Dr. Tang for assistance with HR-TEM imaging. B.K. would like to thank NSERC for an USRA.

References

1. T. Hegmann, H. Qi, V. M. Marx, *J. Inorg. Organomet. Polym. Mater.* **2007** *17*, 483-508.
2. (a) D. Sikharulidze, *Appl. Phys. Lett.* **2005**, *86*, 033507; (b) Y. Williams, K. Chen, J. H. Park, I. C. Khoo, B. Lewis, T. E. Mallouk, *Proc.SPIE* **2005**, *5936*, 225-230; (c) T. Miyama, J. Thisayukta, H. Shiraki, Y. Sakai, Y. Shiraishi, N. Toshima, S.Kobayashi, *Jpn. J. Appl. Phys.* **2004**, *43*, 2580; (d) S. Kobayashi, T. Miyama, N. Nishida, Y. Sakai, H. Shiraki, Y. Shiraishi, N. Toshima, *J. Display Technol.* **2006**, *2*, 121-129 ; (e) T. Miyama, H. Shiraki, Y. Sakai, T. Masumi, S. Kundu, Y. Shiraishi, N. Toshima, S. Kobayashi, *Mol. Cryst. Liq. Cryst.* **2005**, *433*, 29-40; (f) S. Sono, T. Miyama, K. Takatoh, S. Kobayashi, *Proc. SPIE* **2006**, *6135*; (g) H. Yoshikawa, K. Maeda, Y. Shiraishi, J. Xu, H. Shiraki, N. Toshima, S. Kobayashi, *Jpn. J. Appl. Phys.* **2002** *41*, 1315-1317; (h) F. Haraguchi, K. Inoue, N. Toshima, S. Kobayashi, K. Takatoh, *Jpn. J. Appl. Phys.* **2007** *46*, 796-797; (i) Y. Reznikov, O. Buchnev, O. Tereshchenko, V. Reshetnyak, A. Glushchenko, J. West, *Appl. Phys. Lett.* **2003** *82*, 1917-1919; (j) E. Ouskova, O. Buchnev, V. Reshetnyak, Y. Reznikov, H. Kresse, *Liq. Cryst.* **2003** *30*, 1235-1239; (k) O. Buchnev, C.-I. Cheon, A. Glushchenko, Y. Reznikov, J. L. West, *J. Soc. Inf. Disp.* **2005** *13*, 749-754; (l) F. Li, J. West, A. Glushchenko, C.-I. Cheon, Y. Reznikov, *J. Soc. Inf. Disp.* **2006** *14*, 523-527; (m) F. Li, O. Buchnev, C.-I. Cheon, A.

- Glushchenko, V. Reshetnyak, Y. Reznikov, T. J. Sluckin, J. L. West, *Phys. Rev. Lett.* **2006** *97*, 147801; (n) O. Buchnev, A. Dyadyusha, M. Kaczmarek, V. Reshetnyak, Y. Reznikov, *J. Opt. Soc. Amer. B* **2007** *24*, 1512-1516; (o) V. Y. Reshetnyak, *Mol. Cryst. Liq. Cryst.* **2004** *421*, 219-224; (p) V. Y. Reshetnyak, S. M. Shelestiuk, T. J. Sluckin, *Mol. Cryst. Liq. Cryst.* **2006** *454*, 201-206; (q) M. Copic, A. Mertelj, O. Buchnev and Y. Reznikov, *Phys. Rev. E* **2007** *76*, 011702.
- 3 (a) H. Qi, A. Lepp, P. A. Heiney, T. Hegmann, *J. Mater. Chem.* **2007** *17*, 2139-2144; (b) H. Qi, J.O'Neil, T. Hegmann, *J. Mater. Chem.* **2008**, *18*, 374-380.
- 4 H. Qi, T. Hegmann, *J. Mater. Chem.* **2006** *16*, 4197-4205.
- 5 (a) H. Stark, *Phys. Rep.* **2001** *351*, 387-474 ; (b) H. Stark, *Phys. Rev. E* **2002** *66*, 041705; (c) P. Poulin, V. Cabuil, D. A. Weitz, *Phys. Rev. Lett.* **1997** *79*, 4862-4865; (d) Y. D. Gu, N. L. Abbott, *Phys. Rev. Lett.* **2000** *85*, 4719-4722; (e) J.-C. Loudet, O. Mondain-Monval, P. Poulin, *Eur. Phys. J. E* **2002** *7*, 205-208; (f) P. Poulin, N. France`s, O. Mondain-Monval, *Phys. Rev. E* **1999** *59*, 4384-4387; (g) P. Kossyrev, M. Ravnik, S. Žumer, *Phys. Rev. Lett.* **2006** *96*, 048301.
- 6 H. Qi, B. Kinkead, T. Hegmann, *Adv. Funct. Mater.* **2008**, *18*, 212-221.
- 7 T. Albrecht, S. F. L. Mertens, J. Ulstrup, *J. Am. Chem. Soc.* **2007** *129*, 9162-9167.
- 8 Assemblies of Au nanoparticles display solid state conductivities of $\sim 10^{-4}$ - 10^{-5} S·cm⁻¹: (a) S. W. Boettcher, N. C. Strandwitz, M. Schierhorn, N. Lock, M. C. Lonergan, G. D. Stucky, *Nat. Mater.* **2007** *6*, 592-596; (b) W. P. Wuelfing, S. J. Green, J. J. Pietron, D. E. Cliffler, R. W. Murray, *J. Am. Chem. Soc.* **2000** *122*, 11465-11472; (c) J. J. Pietron, J. F. Hicks, R. W. Murray, *J. Am. Chem. Soc.* **1999** *121*, 5565-5570 .
- 9 (a) R. H. Terrill, T. A. Postlethwaite, C.-H. Chen, C.-D. Poon, A. Terzis, A. Chen, J.

- E. Hutchison, M. R. Clark, G. Wignall, J. D. Londono, R. Superfine, M. Falvo, C. S. Johnson Jr., E. T. Samulski, R. W. Murray, *J. Am. Chem. Soc.* **1995** *117*, 12537-12548; (b) A. N. Shipway, E. Katz, I. Willner, *ChemPhysChem* **2000** *1*, 18-52.
- 10 K. E. Peceros, X. Xu, S. R. Bulcock, M. B. Cortie, *J. Phys. Chem. B* **2005** *109*, 21516-21520.
- 11 Alkylthiols used in self-assembled monolayers (SAMs) are known to promote homeotropic anchoring of N-LCs: R. A. Drawhorn, N. L. Abbott, *J. Phys. Chem.* **1995** *99*, 16511-16515.
- 12 J. de la Venta, A. Pucci, E. Fernández Pinel, M. A. García, F. de Julián, P. Crespo, P. Mazzoldi, G. Ruggeri, A. Hernando, *Adv. Mater.* **2007** *19*, 875-877.
- 13 The phase transfer of initially thioglycolic acid capped CdTe dots using hexane- or dodecanethiol in acetone produces mixed monolayer capped CdTe quantum dots, in which not all thioglycolic acid ligands are replaced by hexane- or dodecane thiolate ligands.
- 14 H. Choo, E. Cutler, Y.-S. Shon, *Langmuir* **2003** *19*, 8555-8559.
- 15 M. Dasog, R. W. J. Scott, *Langmuir* **2007** *23*, 3381-3387.
- 16 M. M. Maye, W. Zheng, F. L. Leibowitz, N. K. Ly, C.-J. Zhong, *Langmuir* **2000** *16*, 490-497.
- 17 M. Brust, M. Walker, D. Bethell, D. J. Schiffrin, R. Whyman, *Chem. Commun.*, **1994** 801-802.
- 18 P. Ahonen, T. Laaksonen, A. Nykänen, J. Ruokolainen, K. Kontturi, *J. Phys. Chem. B* **2006** *110*, 12954-12958.
- 19 N. Gaponik, D. V. Talapin, A. L. Rogach, A. Eychmuller, H. Weller, *Nano Lett.*

2002 2, 803-806.

- 20 $K_{11} = \left(\frac{V_{th}}{\pi} \right)^2 \Delta\epsilon\epsilon_0$; K_{22} is estimated as $0.6K_{11}$; K_{33} is obtained from a curve fitting algorithm of the $C-V$ curve.
- 21 S. T. Wu, D. Coates, E. Bartmann, *Liq. Cryst.* **1991** 10, 635-646.
- 22 To compare mixtures of the same N-LC with 5wt% and 10wt% nanoparticles, it is important to note that the phase transition temperatures (low-temperature onset of the phase transition in the DSC traces) are only affected by ca. 1- 2 °C by doubling the nanoparticle concentration from 5 to 10 wt%. Therefore, the reduced temperature scales are kept identical. However, for mixtures showing broader phase transitions, electro-optic data were collected starting at lower temperatures (ensuring the entire field-addressed area of the cell was in the N-phase).
- 23 8CB was here likely not the best choice because of its narrow nematic phase range.

Chapter 10: Miscibility and alignment effects of mixed monolayer cyanobiphenyl liquid crystal-capped gold nanoparticles in nematic cyanobiphenyl liquid crystal hosts

This paper was reproduced with permission from ChemPhysChem 2009, 10, 1211-1218. Copyright - 2009 WILEY-VCH Verlag GmbH & Co. KGaA, Weinheim. It is co-authored with B. Kinhead, V. M. Marx, H. R. Zhang and T. Hegmann. The text is a verbatim copy of the published paper.

To use LC/NP composites such as the ones discussed in the previous chapters in mixtures for flat panel LCD applications, one has to overcome a number of critical requirements. One of these requirements is the long-term stability of the NP dispersions in nematic hosts, for example, to electric field, temperature and LCD manufacturing conditions. It is widely believed that decorating the nanomaterials with liquid crystalline ligands would help improve solubility and miscibility of the NPs in the nematic solvent, and hence the stability of the final dispersion. In the following Chapter 10, an assessment of the validity of this assumption is made by introducing Au NPs capped with liquid crystalline, nematic thiols. The presented experiments will reveal that common miscibility rules known from organic dopants in nematics do not strictly apply for Au NPs in nematic phases.

Abstract: This study focuses on the miscibility of liquid crystal (LC) decorated gold nanoparticles (NPs) in nematic LCs. To explore if LC functional groups on the gold NP corona improve the compatibility (miscibility) with structurally related LC hosts, we examined mixtures of two LC hosts, **5CB** and **8CB** doped at 5 wt% with different types of gold NPs. Four alkanethiol-capped NPs were synthesized; two homogeneously coated with alkanethiols (**Au1** with C₆H₁₃SH and **Au2** with C₁₂H₂₅SH), and two that were additionally capped at a different ratio with a mesogenic cyanobiphenyl end-functionalized alkanethiol **HS10OCB** (C₆H₁₃SH + **HS10OCB** for **Au3** and C₁₂H₂₅SH + **HS10OCB** for **Au4**). Investigating these mixtures in the bulk for settling of the NPs, and in thin films using polarized optical microscopy (POM) between untreated glass slides as well as POM studies and electro-optic tests in planar ITO/polyimide test cells revealed that the alkanethiol capped NPs **Au1** and **Au2** are better compatible with the two polar cyanobiphenyl hosts in comparison to the NPs decorated with the cyanobiphenyl moieties. All NPs induce homeotropic alignment in **5CB** and **8CB** between untreated glass slides, with **Au1** and **Au2** showing characteristic birefringent stripes, and **Au3** and **A4** exhibiting clear signs of aggregation. In rubbed polyimide cells, however, **Au3** and **Au4** fail to induce homeotropic alignment and show clear signs of macroscopic aggregation.

10.1 Introduction

Liquid crystal (LC) nanoscience is a fairly young field of LC research, but has received increasing attention over the last few years [1]. Aside from the use of LC phases as templates and matrices for nanomaterial synthesis, the marriage between the mature field

of LCs, with its structural diversity on a molecular and supramolecular level as well as its demonstrated impact on technological areas such as information displays, and the exciting properties of materials at the nanoscale has produced very exciting new supermolecular LC materials [2, 3] and LC composites with very promising optical and electro-optic properties [4]. One of the major drawbacks in the area of dispersions (or composites) of nanoscale materials in LC phases has been the compatibility (i.e., solubility or miscibility) between zero, one and two-dimensional nanostructures (ranging from quasi-spherical nanoparticles over nanotubes and nanorods to nanoplatelets) and LC hosts [5-7]. While we believe that tuning *and not* improving of compatibility will be the key to application of LC/nanoparticle composites, the chemical decoration of nanoparticles (NPs) with liquid crystalline motifs seemed often viewed as the best approach to avoid the formation of NP aggregates at different length scales (nano-, micro- and macro-scale) and/or macroscopic (phase) separation with the formation of particle-rich and particle-poor domains [4, 8].

To shine more light on this assumption, we here present the results of detailed optical microscopy investigations and electro-optic measurements on dispersions of nematic LCs doped with two types of gold NPs; one type homogeneously capped with ‘simple’ alkanethiols ($C_6H_{13}SH$ for **Au1** and $C_{12}H_{25}SH$ for **Au2**) and another type capped with a mixed monolayer of alkanethiols ($C_6H_{13}SH$ for **Au3** and $C_{12}H_{25}SH$ for **Au4**) and simultaneously with the liquid crystalline 4’-(10-mercaptodecyloxy)-biphenyl -4-carbonitrile (**HS10OCB**) providing a structural match to the two chosen nematic cyanobiphenyl hosts, **5CB** and **8CB** (Fig.10.1).

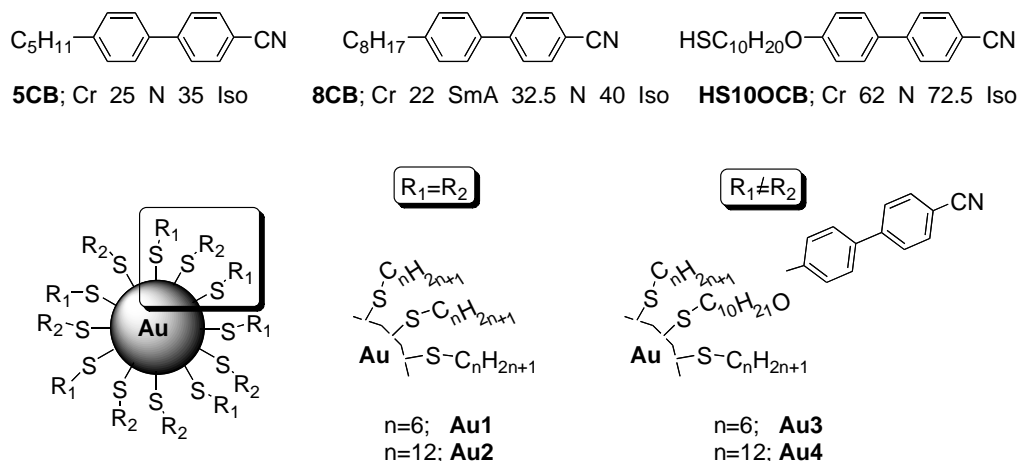


Fig. 10.1. Structures and LC phase transition temperatures of the LC hosts **5CB** and **8CB** and of the nematic **HS10OCB** (top). Schematics of the homogeneous and mixed monolayer gold NPs **Au1**–**Au4** (bottom). Thiolate ratios (for **Au3** and **Au4**), sizes and size distributions of all gold NPs are collected in Table 1.

A gold NP homogeneously capped with the nematic LC thiol **HS10OCB** was not investigated in the two hosts for the following reason. Previous tests performed by our group clearly showed that NPs end-capped exclusively with polar aromatic groups had a far inferior solubility in nematic LC hosts (and in the organic solvents used for sample preparation) in comparison to mixed monolayer-capped metal NPs featuring ‘simple’ alkyl thiolates as the other type of capping thiolate [9, 10].

10.2 Experimental

10.2.1 General

The nematic LCs used were commercially available pure **5CB** and **8CB** (Merck KGaA). Transmission electron microscopy images were obtained on a Jeol ultra-high resolution FEG-T/STEM operating at an accelerating voltage of 200 kV. A 10 μ L drop of the cluster solution was drop-cast on a carbon-coated copper grid (400-mesh) and dried

for 1 hour. All particles were stored as dry solids under a protective atmosphere of dry N₂ in the dark, and can be repeatedly dispersed in and isolated from selected organic solvents without change in size (no aggregation or ripening). All glass vials and Teflon[®]-coated spatulas were rinsed with *aqua regia* prior to all mixture preparations. All mixtures were prepared by combining solutions of the LC and the NP in a common, pure, and dry solvent (e.g., ethyl acetate). The resulting solutions were stirred (agitated) for at least 10 minutes, and thereafter, the solvent was evaporated under a steady stream of dry N₂ over open glass vials, and all mixtures were then dried in vacuum for 24 hours. Prior investigating the mixtures between untreated microscopy glass slides and prior to filling the LC test cells by capillary forces with the LC in the isotropic liquid phase, all mixtures were heated just below the isotropic-nematic phase transition ($T_{\text{Iso/N}}$) and continuously mixed again.

Polarized optical microscopy (POM) was performed using an Olympus BX51-P polarizing microscope in conjunction with a Linkam LS350 or an Instec HCS302 heating/cooling stage. Electro-optic measurements were performed using an LCAS I automated liquid crystal analyzer (LC Vision, LLC) in conjunction with the Instec heating/cooling stage. The LC test cells used were planar 5.0 micron cells with antiparallel polyimide alignment layers and 1° to 3° pre-tilt (Instec, Inc.). The reproducibility of the alignment effects and EO measurements was checked on several cells for each mixture.

10.2.2 Synthesis

The nematic **HS10OCB** was synthesized in three steps as described by Kim *et al.*[11] starting from 4'-hydroxybiphenyl-4-carbonitril and 1,10-dibromodecane. **HS10OCB** forms an enantio-tropic nematic phase between 62 and 72.5 °C (on heating). The alkyl thiolate-capped NPs **Au1** and **Au2** were prepared as described in our earlier papers.[12, 13] The synthesis of the two mixed monolayer gold NPs **Au3** and **Au4** followed a similar approach with both thiols in the desired ratio added in close succession.[14] The size and size distribution of the purified gold NPs was determined by transmission electron microscopy (TEM) and TEM image analysis (Fig. 10.2), and the ratio between the two thiolates for **Au3** and **Au4** was calculated from the integration of characteristic peaks in the ¹H NMR spectra (similar values were obtained with and without I₂ decomposition,[15] see Table 1 and Fig. 10.3). By controlling the rate of addition and concentration of the reactants we have made sure that: (1) all NPs are in the same size regime (and similar in size to LC hosts), and (2) one of the mixed monolayer NPs has a different ratio between the two capping thiolates, so we could evaluate this effect as well.

10.2.3 Compatibility Studies

To study the compatibility, miscibility and alignment effects, all mixtures of the four NPs in both nematic LC hosts were initially inspected in the bulk and thereafter as thin films between untreated microscopy glass slides as well as ITO-cells with polyimide alignment layer inducing antiparallel planar alignment (source: Instec). Bulk inspection, i.e., observing the sample in the V-vial[®] used for sample preparation as described in the experimental section, was always used as the first means to determine if a particular NP

was soluble (miscible or, more accurately, well-dispersed) in a nematic LC host. Observations such as settling of the NPs in the nematic phase or already in the isotropic liquid during sample preparation were always taken as an indication of incompatibility. In contrast, the formation of clear or slightly opaque (for the nematic phase) and dark burgundy or purple colored dispersions (because of the surface plasmon resonance of the gold NPs [16]), which did not show any signs of settling in the isotropic liquid as well as in the nematic phase over extended periods of time, were taken as a sign of compatibility between NP and nematic LC host.

Equally important is the fact that we were particularly interested in the higher concentration regime of NPs in the nematic LC phase, i.e., around 5 wt%. Lower concentrations of the NPs (usually around 1 wt% or lower) commonly produced well-dispersed NP dispersions in the two nematic LCs and showed no significant textural or alignment effects in POM investigations [12]. The most drastic effects were always observed for mixtures containing ~ 5 wt% of NPs (or more), and therefore our discussion will focus on mixtures with this NP concentration. Mixtures containing between 1 and 5 wt% of NPs usually showed bimodal miscibility and alignment effects with some domains behaving as the 1 wt% and others like the 5 wt% mixtures.

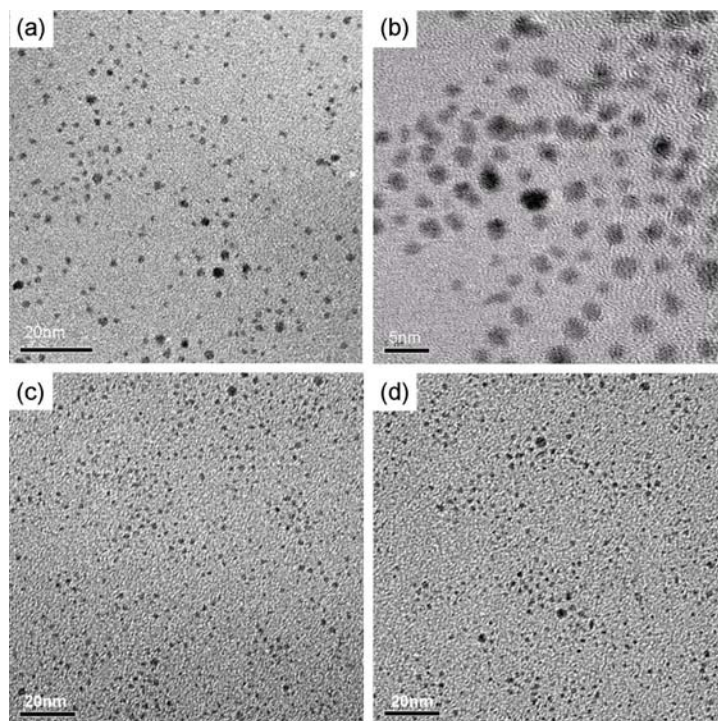


Fig. 10.2. TEM images of the gold NPs: (a) **Au1**, (b) **Au2**, (c) **Au3**, and (d) **Au4**.

Table 10.1. Size, size distribution, and NP composition of **Au1–Au4**.^[a]

Au NP	Size \pm SD ^[b] (nm)	Ratio of thioliates ($-\text{SC}_n\text{H}_{2n+1} : -\text{S10OCB}$)
Au1	1.59 ± 0.44	— ^[c]
Au2	1.93 ± 0.47	— ^[c]
Au3	1.85 ± 0.32	1 : 1 (n = 6) ^[d]
Au4	1.98 ± 0.41	9 : 1 (n = 12) ^[d]

[a] TEM image analysis of all NPs in each image was performed with the following software: Scion Image Beta 4 (Scion Corp.) or Image J. [b] SD = standard deviation. [c] Homogeneously capped with either hexanethiol (**Au1**) or dodecanethiol (**Au2**). [d] The ratio of thioliates was determined using ¹H NMR and found identical with and without R. W. Murray's I₂ decomposition method [15] using characteristic peaks of each thiol[17].

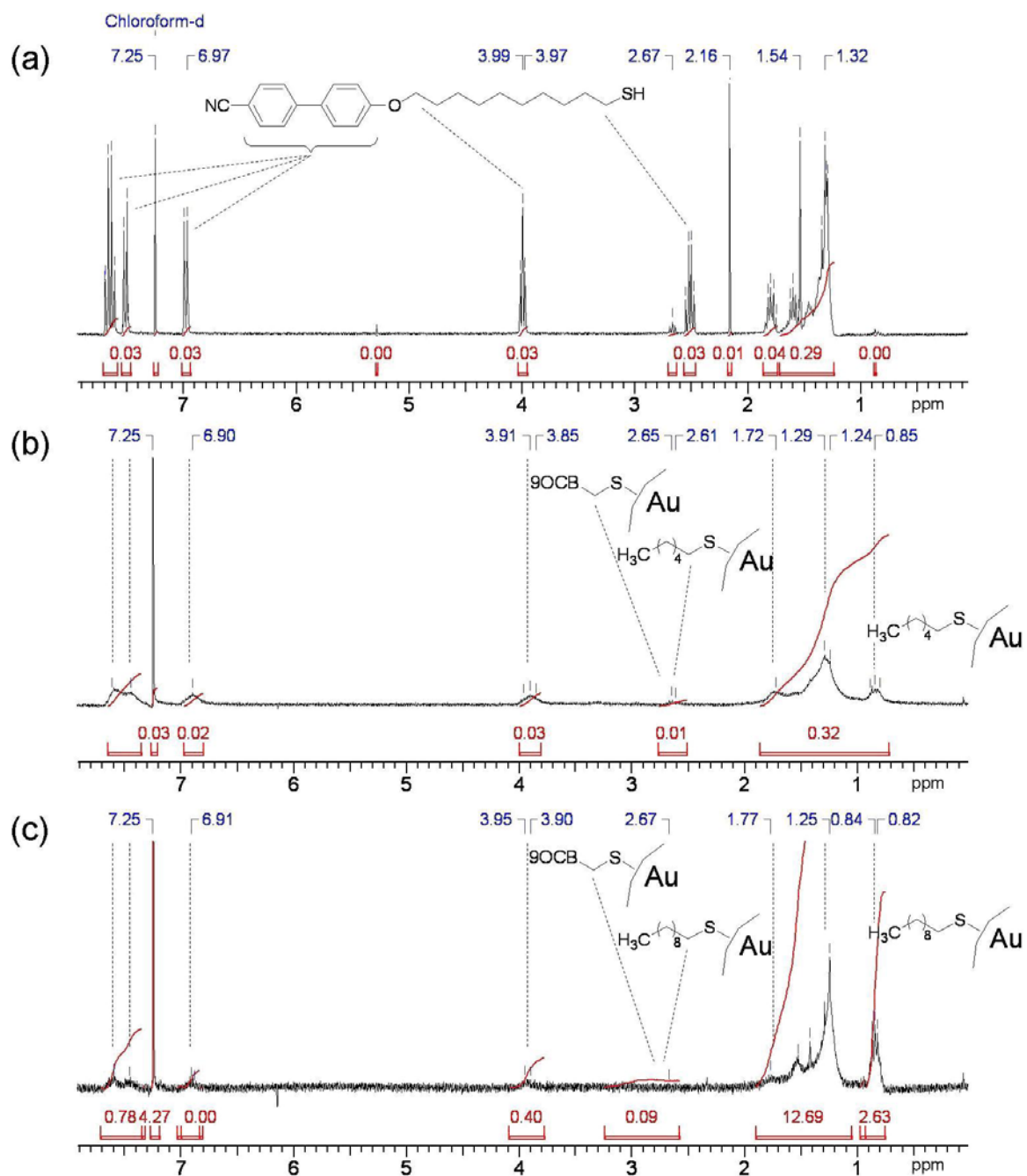


Fig. 10.3. ¹H NMR spectra of **HS10OCB** (a) and of the corresponding mixed monolayer-protected gold NPs **Au3** (b) and **Au4** (c).

10.3 Results and Discussion

10.3.1 Optical inspection and effects between untreated glass slides

The importance of the initial inspection of as-prepared mixtures in V-vials[®] cannot be overemphasized, as it provided the first critical clues that there might be a key difference between alkyl-coated and cyanobiphenyl-capped gold NPs in the two **CB** hosts.

The two alkanethiol-capped NPs **Au1** and **Au2** were discernibly well dispersed both in the isotropic liquid as well as in the nematic phase of **5CB** and **8CB** as indicated by the formation of clear (isotropic liquid phase) and opaque (in the N phase), dark burgundy or purple colored dispersions. The two cyanobiphenyl end-capped gold NPs **Au3** and **Au4**, however, proved to be much more difficult to disperse in both hosts as judged by the settling of these NPs at lower temperature and particularly with time such as on standing overnight (see Fig.10.4 for a comparison between **Au1** and **Au3** – the red arrow clearly shows the settling only of **Au3** in the N-phase of **5CB** overnight). Nevertheless, freshly prepared dispersions of **Au3** and **Au4** in **5CB** or **8CB**, to the naked eye, were indistinguishable to mixtures containing **Au1** or **Au2**.

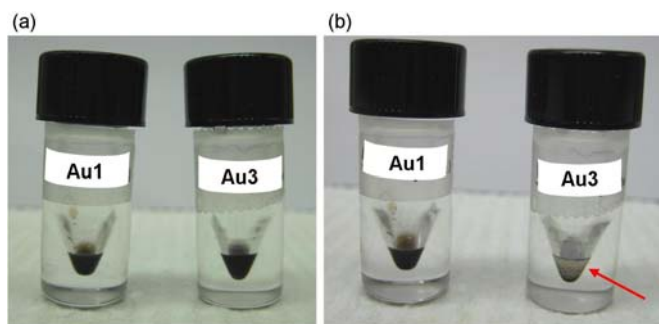


Fig. 10.4. V-vials[®] containing **5CB** doped with **Au1** or **Au3**: (a) right after sample preparation as described in the experimental section and (b) after standing at room temperature overnight (in the nematic phase of **5CB**).

Some significant differences between the two sets of NPs, hydrocarbon versus cyanobiphenyl end-capped, however, were quite noticeable when we observed these mixtures of **Au1–Au4** in **5CB** and **8CB** between untreated microscopy glass slides. All films were prepared by sandwiching a drop of the as-prepared mixtures between a 1 × 4" microscope glass slide and a 1" cover slip. These samples were heated to the isotropic phase and subsequently cooled to the nematic phase at 1 °C · min⁻¹ to the middle of the nematic range.

Representative POM images of these tests are collected in Figs.10.5 and 10.6 for **5CB** and **8CB**, respectively. For comparison, images are grouped in such way that the homogeneously capped and the mixed monolayer capped NP with identical hydrocarbon chain length are grouped together (right above one another, e.g. **Au1** and **Au3** in Figs.10.5a and 10.5b for **5CB** and in Figs. 10.6a and 10.6b for **8CB**). Images on the left are taken with crossed polarizers and images on the right with uncrossed, but not parallel polarizers.

As previously reported by our group [12, 13, 18], the alkyl thiolate capped NPs **Au1** and **Au2** dispersed in **5CB** or **8CB** produce textures featuring birefringent stripes of equal width (between 3 and 4 μm, depending on the individual mixture) surrounded by larger domains of homeotropic orientation of the nematic director (Figs. 10.5a, c and 6a, c).

In prior work, we have also discussed the role of the NPs in inducing (1) the unusual homeotropic alignment (given that the pure nematic LCs used would naturally prefer a planar orientation on untreated glass), and (2) the origin of the birefringent stripes at or near the glass/nematic LC interface [12, 13] (linear NP aggregates producing stripes, or local defects caused by the NPs migrating to domain boundaries with strong director

distortions leading to stripe formation [7, 19]). We have established that these birefringent domains are particle-rich, not only because of strong local director field distortions, but also because these stripe domains appear visibly colored at the wavelength of the surface plasmon resonance of the NPs in the absence of polarized light.

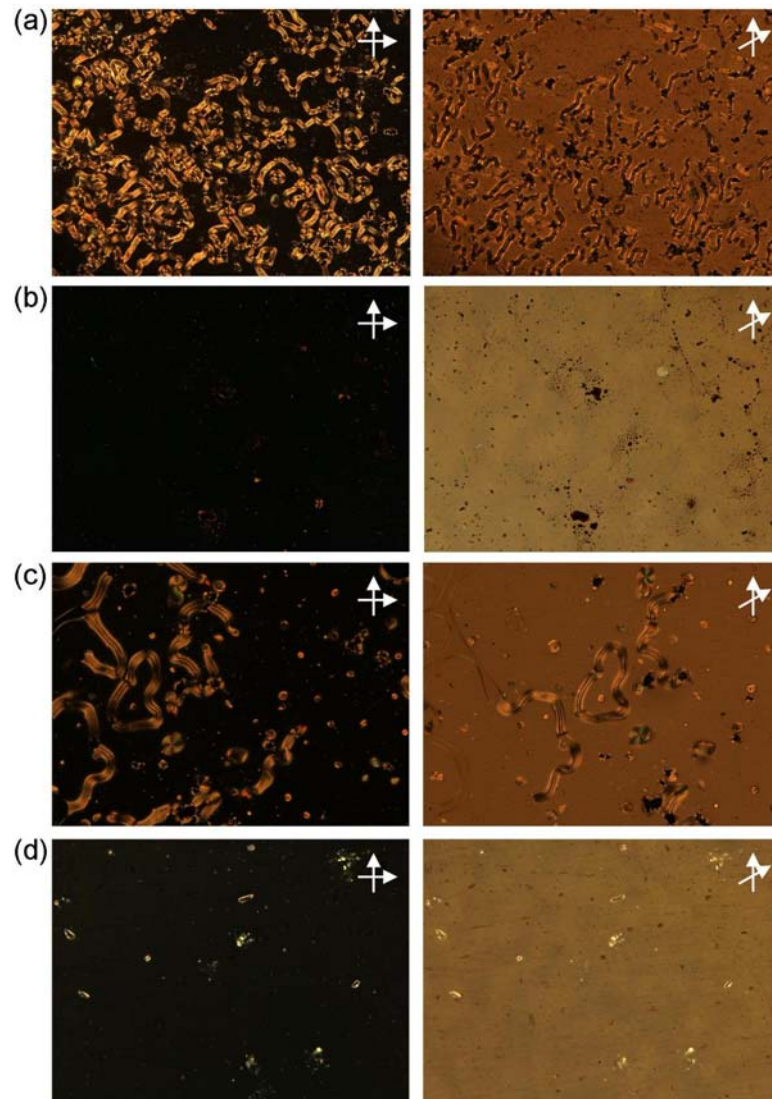


Fig. 10.5. Polarized optical photomicrographs (crossed polarizers left column, slightly uncrossed polarizers right column) of 5 wt% NPs in **5CB** (at $T = T_{\text{Iso/N}} - 5 \text{ }^\circ\text{C}$): (a) **Au1**, (b) **Au3**, (c) **Au2**, and (d) **Au4**.

The images in the right columns of Figs. 10.5a and 10.5c resp. 6a and 6c with slightly uncrossed polarizers confirm that most NPs are well dispersed in both nematic hosts, since there is only slight evidence of some aggregated particles, which appear similar to crystalline or amorphous ‘impurities’. It becomes evident, that aggregation is almost entirely prevented for the NPs with longer hydrocarbon chains **Au2** (compare Fig. 10.5a with 5c in **5CB** and Figs. 10.6a with 6c in **8CB**). We attribute this behavior to the greater flexibility of the longer C12 chains of **Au2** in comparison to the relative stiff and dense packed shorter C6 alkyl chains of **Au1** [20].

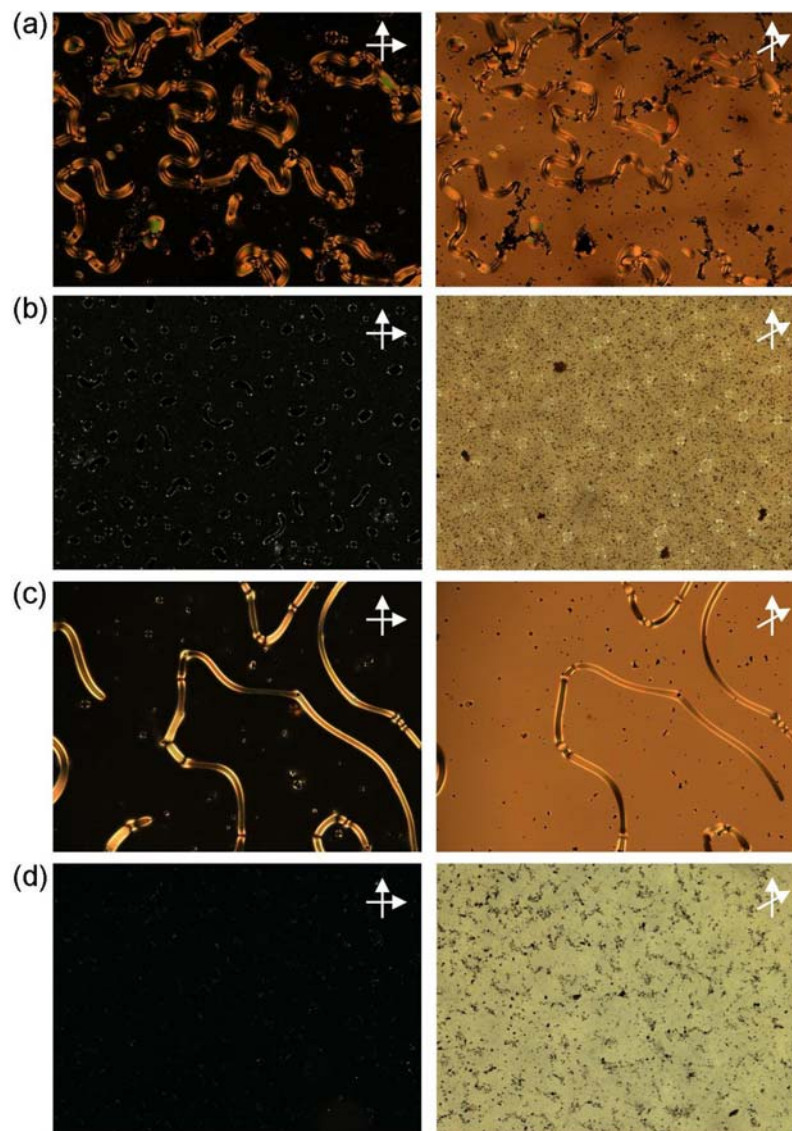


Fig. 10.6. Polarized optical photomicrographs (crossed polarizers left column, slightly uncrossed polarizers right column) of 5 wt% NPs in **8CB** (at $T = T_{\text{Iso/N}} - 5 \text{ }^\circ\text{C}$): (a) **Au1**, (b) **Au3**, (c) **Au2**, and (d) **Au4**.

Surprisingly, mixtures of the mixed monolayer 10OCB end-capped gold NPs **Au3** and **Au4** displayed somewhat different textures. At a first glance, observing these preparations between crossed polarizers led us to conclude that these particles also induce homeotropic alignment in **5CB** and **8CB** between untreated glass slides without separation into particle-rich and particle-poor domains, i.e., the formation of the

birefringent stripes (Figs. 10.5b, 10.5d, 10.6b and 10.6d – left column). Yet, a closer look at these thin film preparations with slightly uncrossed polarizers (same Figs., right column) clearly revealed that these 10OCB end-capped NPs severely aggregate in the two structurally related nematic hosts. Better compatibility, if any, was here observed with the **5CB** host, and again that the NP with the longer hydrocarbon chain in the mixed monolayer, **Au4**, seemed more compatible than the one with the shorter C6 alkyl chains, **Au3** as discussed for **Au2** vs. **Au1** earlier.

10.3.2 Effects in planar ITO cells with polyimide alignment layers

In prior experiments, we have seen that the textural phenomena induced by alkyl thiolate-capped NPs (Au, Ag and CdTe) using untreated glass slides are reproducible also in ITO-coated electro-optic test cells with rubbed polyimide alignment layers (parallel or antiparallel) favoring planar alignment of the nematic molecules (i.e., the director along the long molecular axis) [12]. We unraveled that changes in preparation conditions as well as concentration of the NPs were critical to obtain homeotropic alignment, as observed between normal glass slides, and that the area density of the birefringent stripes can be minimized either by increasing the NP concentration or by raising the magnitude of an applied electric field [12].

We were now interested if the mixtures of the 10OCB end-capped gold NPs in **5CB** and **8CB** would also produce identical or at least similarly altered alignment effects in planar test cells as between untreated glass slides. The polarized light optical photomicrographs of **Au3**, **Au4**, and for comparative reasons **Au1** are collected in Figs. 7

and 8. More images for mixtures of **Au1** and **Au2** in nematic LCs can be found in an earlier paper [12].

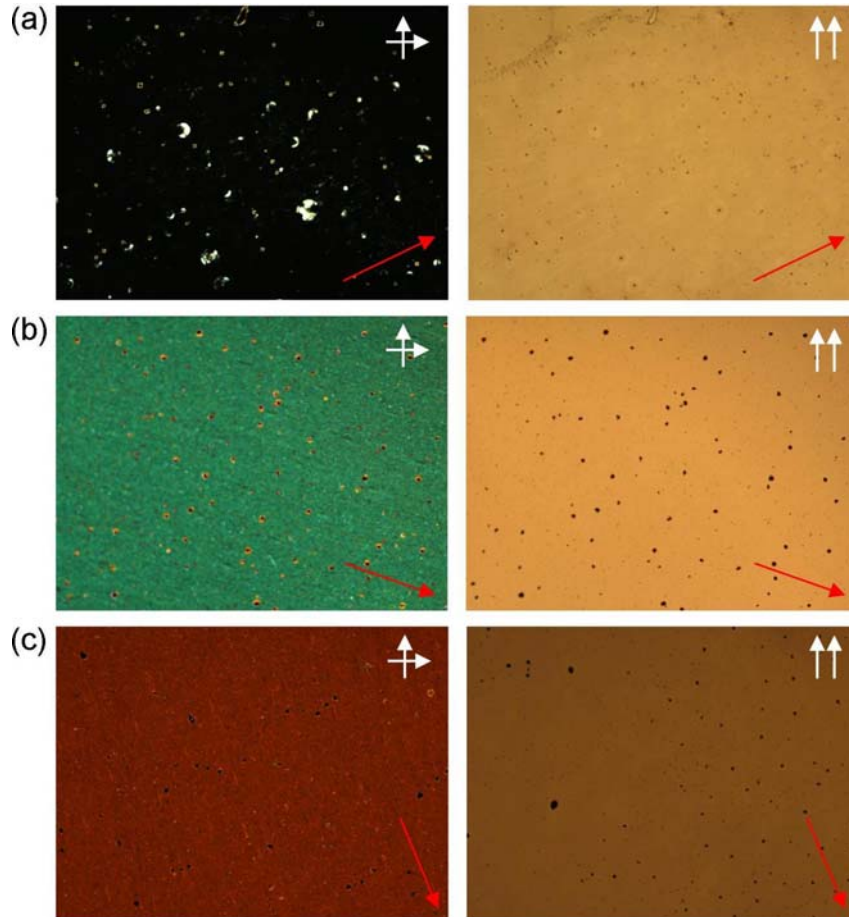


Fig. 10.7. Optical photomicrographs (N phase with crossed polarizers left column, N phase with parallel polarizer orientation right column) of 5 wt% NPs in **5CB** (at $T = T_{\text{Iso/N}} - 5 \text{ }^\circ\text{C}$): (a) **Au1**, (b) **Au3**, (c) **Au4**.

As expected, the hexane thiolate-capped **Au1** and **Au2** in most cells tested completely reverse the planar alignment set out by the cells polyimide alignment layers [21] and produce mostly homogeneous homeotropic alignment with little indication of NP aggregation (see Figs. 10.7a and 10.8a for **Au1**, images for **Au2** were identical and are not shown here) [12]. **Au3** and **Au4** in mixtures with **5CB** and **8CB**, however, show

the exact opposite alignment effect to the untreated glass slides discussed earlier. These NPs in both LC hosts show planar alignment with changing birefringence upon sample rotation, which in all cases allows one to detect the rubbing direction applied to the polyimide (Figs. 10.7b and 10.7c resp. 8b and 8c – left column).

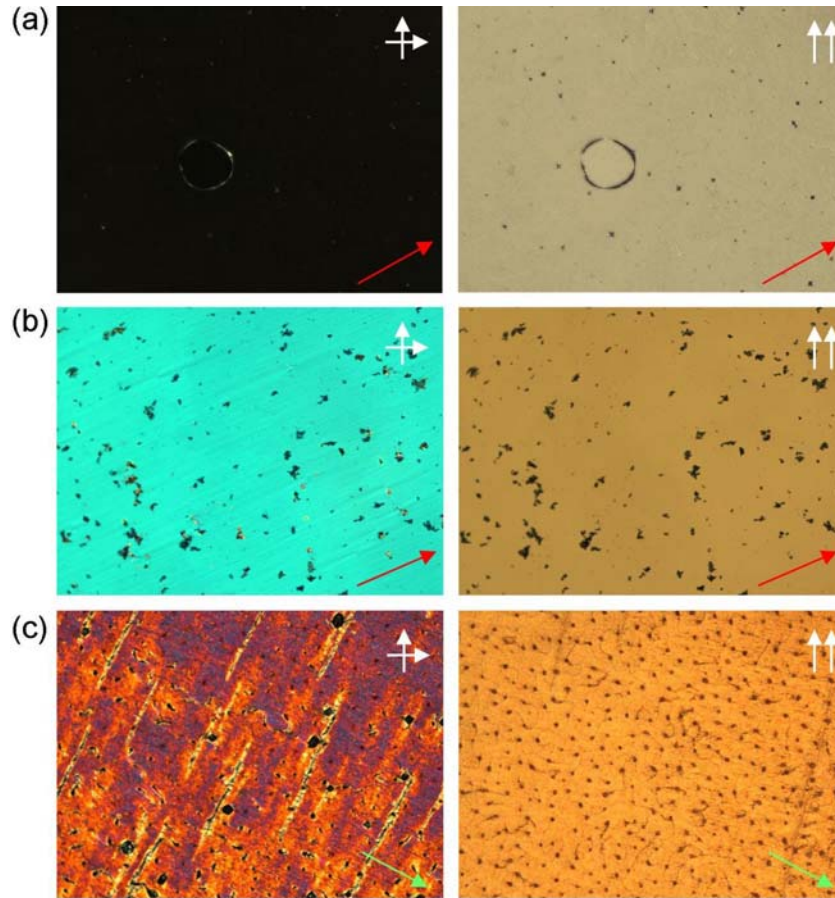


Fig. 10.8. Optical photomicrographs (N phase with crossed polarizers left column, N phase with parallel polarizer orientation right column) of 5 wt% NPs in **8CB** (at $T = T_{\text{Iso/N}} - 5 \text{ }^\circ\text{C}$): (a) **Au1** (air bubble in the centre of the image), (b) **Au3**, (c) **Au4**.

This behavior significantly differs from the alignment effects observed for the alkyl thiolate monolayer-capped **Au1** and **Au2**. While this may seem an advantage for application in LCDs using planar alignment such as in-plane switching or twisted nematic

(with reference to the electro-optic effects observed for NP-doped nematics), the clearly discernible NP aggregates (both with crossed and even more so with parallel polarizers, see right columns in Figs. 10.7 and 10.8) would likely prevent use of these LC motif end-capped NPs.

To again make a statement about the quality of the planar alignment and the degree of visible NP aggregation, **Au3** with shorter hexanethiols in the mixed monolayer shows an alignment quality similar to **Au4**, but appears now, in the rubbed polyimide (planar) LC test cells, to form slightly smaller NP aggregates.

Between the cyanobiphenyl-decorated Au NPs, **Au3** has a significantly higher number of **HS10OCB** ligands on the NP surface, which indicates that both building principles, i.e., more mobile CB units due to the shorter, additional C6 alkyl chains (not C12 as in **Au4**) and a lower overall amount of structurally related CB moieties as in **Au4**, work against one another.

This result, however, provides the opportunity to fine-tune the compatibility between CB hosts and CB end-capped NPs by varying the lengths of the hydrocarbon chains as well as the ratio between the two capping ligands.

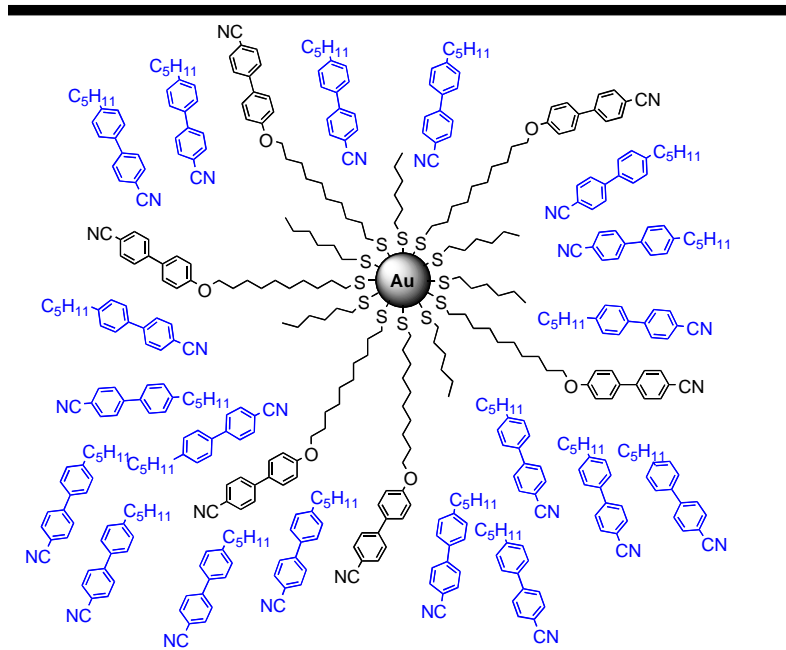
To explain the planar alignment of **Au3** and **Au4** in planar cells, despite the homeotropic alignment induced using normal untreated microscopy glass, we propose a simple model that would explain the alignment effects and demonstrate, in principle, the competitiveness of all surfaces and interfaces present in these systems (the NP surface forcing homeotropic anchoring of the surrounding nematic LC molecules, glass in one case, and polyimide alignment layers in the other case). Cartoons of this model are shown in Fig. 10.9.

Since all NPs induce homeotropic alignment between normal glass slides, we trust that this alignment, as previously discussed, has its origin in the segregation of the well-dispersed NPs (not the NP aggregates) to the interface between the bulk nematic and glass. This segregation is energetically less costly, as the isolated NPs and particularly the NP aggregates induce defects that are easily detectable by POM (Fig. 10.9a). Keep in mind that untreated microscopy glass slides and ITO/polyimide cells used in this study both strongly favor planar alignment of the nematic LCs used, **5CB** and **8CB**; a well documented behavior [22] that we verified prior to our investigations in probe experiments.

Hence, we propose that dispersion interactions [23] between the rubbed polyimide alignment layers and the LC molecules responsible for homogeneous planar alignment in planar cells could align the CB moieties attached to the NPs **Au3** and **Au4** (at least the well-dispersed portion). This, in turn, would alter the orientation of the surrounding cyanobiphenyl host molecules and produce planar alignment in the EO test cells (see Fig. 10.9b).

Recent examples of LC decorated NPs forming nematic liquid crystalline phases would lend some support for the possibility of alignment, orientation and pre-organization of LC moieties attached to NP surfaces due to attractive interactions [2]. Other explanations would be based on the idea that the alignment layers inducing planar alignment in the LC host could: (1) cause a migration of the NPs and NP aggregates towards the bulk, or (2) change the elastic energy landscape to an extent that forces the NPs to more severely aggregate.

(a)



(b)

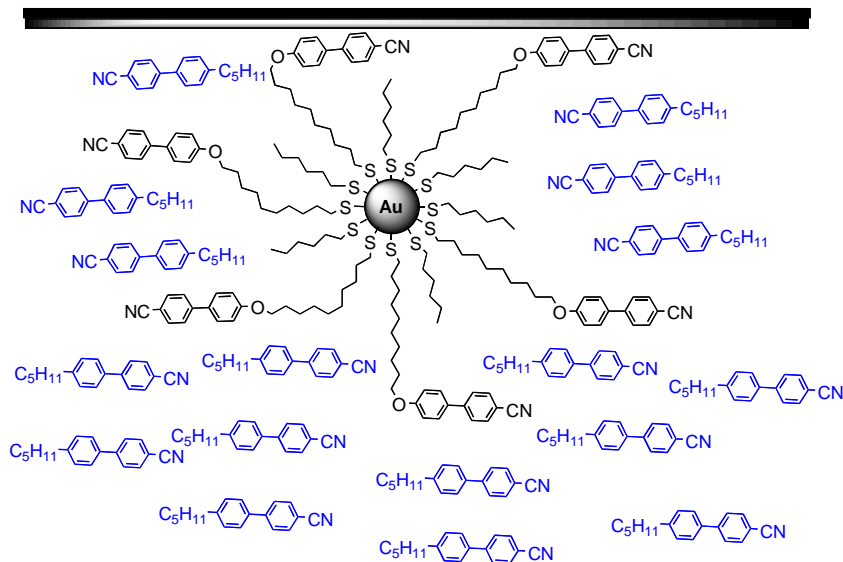


Fig. 10.9. Simplified model for the organization of the LC-capped Au NPs (black) and surrounding **5CB** host molecules (blue) at the interface between: (a) glass and bulk nematic phase, and (b) rubbed polyimide alignment layers (low pre-tilt) and the bulk nematic phase. Note, the two simplified cartoons only show 2-dimensional representations of 3-dimensional, quasi-spherical (cuboctahedral) gold NPs and surrounding LC host molecules.

To see how the difference in alignment and the degree of aggregation of the two different sets of nanoparticles (LC coated **Au3** and **Au4** vs. non-LC coated **Au1**) affect the electro-optic properties of the mixtures, we measured threshold voltage (V_{th}), dielectric permittivity along and across the long molecular axis ($\epsilon_{||}$ and ϵ_{\perp}) giving the dielectric anisotropy ($\Delta\epsilon = \epsilon_{||} - \epsilon_{\perp}$), electrical resistance (R) and the splay elastic constant (K_{11}) and compared the values to the values obtained for pure **5CB** and **8CB** [20,24]. All data obtained from these cells are summarized in Table 2. Given that we do not know if and to what extent the soluble portion of the NPs (residing at the LC/alignment layer interface) affects the pre-tilt of the nematic molecules [25], the three examined NPs appear to have only a minor effect on the electro-optic properties of **5CB** and **8CB**. Significant is here maybe only that **Au4** in both **5CB** and **8CB** produces mixtures with the lowest threshold voltage, **Au3** appears to show no effect at all (identical values to pure **5CB** and **8CB**), and **Au1** gave slightly higher V_{th} values in **5CB** and slightly lower values in **8CB**. As expected from theory, mixtures showing lower V_{th} values showed higher values for $\Delta\epsilon$.

The final point of the discussion will deal with the possibility of alkylthiol group migration (mobility) on the Au NP surface. Rotello *et al.* described quite beautifully that the mobility of thiols on the gold surface could be used to realize binding events (i.e., host-guest interactions *via* π - π stacking) [26]. Their investigations into mixed monolayer-capped Au NPs also revealed that the length of the ‘simple’ alkylthiol initially separating the alkylthiols functionalized with the aromatic moieties is critical in facilitating host-guest interactions in general and π - π stacking to an external guest in particular (e.g. C8 thiol vs. C11 spacer). For the mixed monolayer-capped Au NPs

described here, thiol mobility could, in an extreme case, produce Janus-type Au NPs [27] for **Au3**, which feature shorter ‘simple’ alkylthiols and 10OCB-functionalized thiols with longer hydrocarbon spacers (C6 thiol vs. C10 spacer). In theory, this could promote self-aggregation of the **Au3** NPs in both LC hosts. However, such self-aggregation would be much more noticeable and favored in simple organic solvents (like ethyl acetate used for sample and mixture preparation) and would be detectable by TEM as well as by a shift in the surface plasmon resonance (SPR) band, both of which were not observed for **Au3** or **Au4**. In addition, **Au4**, by design, has two structural factors that would prevent agglomeration (migration due to π - π stacking interactions) of the LC thiols on the Au NP surface: (1) longer ‘simple’ alkylthiols and (2) only one out of ten thiols is functionalized with the cyanobiphenyl unit (C12 thiol vs. C10 spacer). With reference to Rotello’s work [26], the current system should strictly not be regarded as a host-guest system because of the structural identity between the nematic CB hosts and the CB end-capped Au NPs **Au3** and **Au4**. An eventual driving force for alkylthiol mobility on the Au NP surface is here compensated by the high local concentration of structurally identical host molecules. Since both Au NPs (**Au3** and **Au4**) show virtually identical behavior in both cyanobiphenyl hosts, we conclude that the alkylthiol mobility is not the cause of NP aggregation in both nematic hosts. In a related study on (*S*)-naproxen-functionalized, mixed monolayer-capped Au NPs, we also found little to no evidence that π - π stacking of aromatic moieties promotes thiol migration/mobility in the presence of conformationally flexible C12 alkylthiol spacers between the Au NP surface and the aromatic (*S*)-naproxen cores.[10] Hence, we believe that phase separation effects of a spherical nematic monolayer around the Au NPs from a nematic continuum are the main driving force for

the partial aggregation of the two CB-functionalized Au NPs observed in the two CB hosts.

Table 10.2. Electro-optic data for pure **5CB**, pure **8CB** and 5 wt% mixtures of **Au1**, **Au3** and **Au4** in **5CB** as well as **8CB**.^[a-c]

Pure LC or gold NP doped LC		$T_{Iso/N} - T$ (°C)	$V_{th(rms)} \pm SD$ (V)	$\Delta\epsilon \pm SD$	$R \pm SD$ ($10^9 \Omega$)	$K_{11} \pm SD$ (10^{-12} N)	
5CB	pure, non-doped	3	0.82 ± 0.01	10.91 ± 0.12	0.89 ± 0.01	6.53 ± 0.08	
		6	0.85 ± 0.01	11.89 ± 0.05	0.99 ± 0.01	7.76 ± 0.07	
	+ 5 wt% Au1 ^[d]	3	1.31 ± 0.13	10.50 ± 0.96	17.60 ± 0.19	16.20 ± 1.89	
		6	1.16 ± 0.03	13.42 ± 0.44	18.20 ± 0.64	16.30 ± 1.32	
	+ 5 wt% Au3	3	0.90 ± 0.03	16.37 ± 0.09	10.20 ± 0.60	12.00 ± 0.84	
		6	0.84 ± 0.04	16.45 ± 0.16	7.86 ± 0.37	10.40 ± 0.95	
	+ 5 wt% Au4	3	0.63 ± 0.20	20.46 ± 0.22	6.78 ± 0.27	8.02 ± 0.49	
		6	0.47 ± 0.09	20.08 ± 0.34	6.63 ± 0.16	4.04 ± 1.54	
	8CB	pure, non-doped ^[12]	3	1.28 ± 0.01	7.75 ± 0.07	1.51 ± 0.01	11.30 ± 0.12
			6	1.46 ± 0.01	8.41 ± 0.05	1.85 ± 0.02	16.10 ± 0.30
+ 5 wt% Au1 ^{[d][12]}		3	0.85 ± 0.01	20.20 ± 0.43	26.80 ± 6.86	13.10 ± 0.30	
		6	0.73 ± 0.01	18.50 ± 1.05	101.05 ± 7.83	8.94 ± 0.17	
+ 5 wt% Au3		3	1.12 ± 0.03	12.02 ± 0.03	6.54 ± 0.09	13.50 ± 0.75	
		6	1.34 ± 0.02	10.37 ± 0.05	3.38 ± 0.05	17.20 ± 0.48	
+ 5 wt% Au4		3	0.69 ± 0.08	13.76 ± 1.17	8.11 ± 0.59	3.33 ± 0.09	
		6	0.88 ± 0.01	8.46 ± 0.15	4.08 ± 0.20	5.85 ± 0.10	

[a] Measured values with standard deviations (SD) include: $V_{th(rms)}$ = threshold voltage (root mean square), $\Delta\epsilon$ = dielectric anisotropy ($\Delta\epsilon = \epsilon_{||} - \epsilon_{\perp}$), where $\epsilon_{||}$ = dielectric permittivity along the long molecular axis and ϵ_{\perp} = dielectric permittivity across the long molecular axis, R = electrical resistance, and K_{11} = elastic constant (splay).^[23] Two reduced temperature (3 °C and 6 °C below the isotropic/nematic phase transition $T_{Iso/N}$) were chosen for the electro-optic measurements for both **5CB** and **8CB** because of the narrow nematic phase range of **8CB** (see Fig. 1). [b] Variations in pre-tilt angle due to NPs residing at the LC-alignment layer interface cannot be excluded (the manufacturer specifications indicate pre-tilt values ranging from 1° to 3°). [c] The nematic phase of both **5CB** and **8CB** on cooling from the isotropic liquid

10.4 Conclusion

The continued search for LC mixtures with improved characteristics for display and other electro-optic applications has encouraged many groups to explore nanoscale materials as potential dopants. This area of research is still in its infancy, and many interesting effects reported in the literature are not yet entirely understood.

One particular drawback that this research needs to address and overcome prior to integration in electro-optic applications is the compatibility and miscibility of the nanoscale materials in the LC materials of interest. Most nanoscale materials are of too high density, too large size, and not appropriately shaped to allow for excellent solubility in a given LC host. In addition, many nanomaterials aggregate quite strongly in solution or suspension (e.g. carbon nanotubes, magnetic NPs, and others).

One of the most pursued classes of nanomaterials in this field is metal NPs. Gold NPs are likely the best understood, and are therefore the most frequently studied.

To explore if the compatibility of alkyl thiolate-capped gold NPs with nematic host can be tuned or improved, we first synthesized and then investigated mixed monolayer capped gold NPs with liquid crystalline cyanobiphenyl moieties as end groups in two cyanobiphenyl nematic LC hosts (**5CB** and **8CB**). Finally, we compared the results of optical inspections in the bulk as well as of thin films using POM with mixtures containing similar amounts of ‘simple’ alkanethiol-capped gold NPs. Quite surprisingly, we found that the structurally related CB end-capped gold NPs were less compatible (less miscible/dispersible) in comparison to NPs homogeneously covered ‘only’ with alkanethiols of different chain lengths. At least for the systems presented here, maybe for all polar nematics, or eventually also for many other LC/nanomaterial combinations, it

appears that common concepts of solubility and miscibility between two components in LC mixtures do not strictly apply.

Decorating NPs with functional molecules such as polar aromatics poses the risk of increasing self-attraction through van der Waals forces, π - π stacking and/or dipole-dipole interactions in addition to the attractive forces already active between NPs (predominantly between metallic, magnetic and ferroelectric NPs). Electro-optic tests, unfortunately, did not hint at any significant difference between partly LC and non-LC decorated NPs. Future work will now focus on developing an understanding how general the presented findings are for other LC/NP combinations, and if tuning rather than improving the compatibility will result in NP/LC formulations that can improve the characteristics of LC mixtures used in current and future liquid crystal display modes.

Acknowledgements

This work was financially supported by the Natural Sciences and Engineering Research Council (NSERC) of Canada, by the Canada Foundation for Innovation (CFI), the Manitoba Research and Innovation Fund (MRIF), and the University of Manitoba (via an IPM Demonstration Project Grant). The authors would also like to extend thanks to Prof. M. Chaturvedi for access to TEM. V.M.M. and B.K. would like to thank NSERC for USRA awards.

References:

- [1] T. Hegmann, H. Qi, V. M. Marx, *J. Inorg. Organomet. Polym. Mater.* **2007**, *17*, 483-508.
- [2] L. Cseh, G. H. Mehl, *J. Mater. Chem.* **2007**, *17*, 311-315; L. Cseh, G. H. Mehl, *J. Am. Chem. Soc.* **2006**, *128*, 13376-13377.
- [3] B. Donnio, P. García-Vázquez, J.-L. Gallani, D. Guillon, E. Terazzi, *Adv. Mater.* **2007**, *19*, 3534-3539.
- [4] H. Qi, T. Hegmann, *J. Mater. Chem.* **2008**, *18*, 3288-3294
- [5] M. Čopič, A. Mertelj, O. Buchnev, Y. Reznikov, *Phys. Rev. E* **2007**, *76*, 011702.
- [6] K. A. Park, S. M. Lee, S. H. Lee, Y. H. Lee, *J. Phys. Chem. C* **2007**, *111*, 1620-1624.
- [7] M. Mitov, C. Bougerette, F. de Guerville, *J. Phys.: Condens. Matter* **2004**, *16*, 1981-1988.
- [8] J. W. Goodby, I. M. Saez, S. J. Cowling, V. Görtz, M. Draper, A. W. Hall, S. Sia, G. Cosquer, S.-E. Lee, E. P. Raynes, *Angew. Chem., Int. Ed.* **2008**, *47*, 2754-2787;
- [9] V. M. Marx, H. Girgis, P. A. Heiney, T. Hegmann, *J. Mater. Chem.* **2008**, *18*, 2983-2994.
- [10] H. Qi, T. Hegmann, *J. Am. Chem. Soc.* **2008**, *130*, 14201-14206.
- [11] In, Y.-W. Jun, Y. J. Kim, S. Y. Kim, *Chem. Commun.* **2005**, 800-801.
- [12] H. Qi, B. Kinkead, T. Hegmann, *Adv. Funct. Mater.* **2008**, *18*, 212-221.
- [13] (a) H. Qi, J. O'Neil, T. Hegmann, *J. Mater. Chem.* **2008**, *18*, 374-380. (b) H. Qi, T. Hegmann, *J. Mater. Chem.* **2006**, *16*, 4197-4205.

- [14] H. Choo, E. Cutler, Y.-S. Shon, *Langmuir* **2003**, *19*, 8555-8559.
- [15] A. C. Templeton, M. J. Hostetler, C. T. Kraft, R. W. Murray, *J. Am. Chem. Soc.* **1998**, *120*, 1906-1911.
- [16] M.-C. Daniel, D. Astruc, *Chem. Rev.* **2004**, *104*, 293-346.
- [17] The ratios between three sets of peaks in the ^1H NMR spectra were used to calculate the ratio between the two thiols in **Au3** and **Au4** (always one signal, which is specific to one of the two thiols only). Specifically, we used the integration of the aromatic peaks from 7.45 - 7.70 ppm, the integration of the aromatic peaks at around 6.90 ppm, and the integration of the PhOCH_2 peaks of the LC thiol all vs. the integration of the methyl group of the aliphatic thiol centered at 0.83 ppm. Analyzing always both spectra (using the broadened peaks from the Au NPs as well as the sharp peaks of the disulfides after I_2 decomposition) led to the same ratio between the two thiols (1:1 for **Au3** and 9:1 for **Au4**). Elemental analysis for **Au3** confirmed this result as well as the size determined by TEM
- [18] H. Qi, B. Kinkead, T. Hegmann, *Proc. SPIE* **2008**, *6911*, 691106.
- [19] (a) M. Mitov, C. Bougerette, F. de Guerville, *J. Phys.: Condens. Matter* **2004**, *16*, 1981-1988. (b) M. Mitov, C. Portet, C. Bougerette, E. Snoeck, M. Verelst, *Nat. Mater.* **2002**, *1*, 229-231.
- [20] A. C. Templeton, W. P. Wuelfing, R. W. Murray, *Acc. Chem. Res.* **2000**, *33*, 27-36.
- [21] Cells filled with **Au1** as well as **Au2** doped **5CB** and **8CB** (all at 5 wt%), occasionally, fail to show homeotropic alignment or show a coexistence of

domains with homeotropic alignment and domains with planar alignment (ca. 2 out of 10 cells). So far, we have not been able to identify the cause for this lack of consistency. It does not appear to depend on the cell gap, which varied from 2.8 to 5 micron depending on the supplier or batch ordered (commonly, the cell gap differs even within one batch of cells purchased from the same supplier). Cells filled with **5CB** and **8CB** doped with **Au3** or **Au4** do always show planar alignment and no deviations were noticed in all tested cells and different cell gaps. Fortunately, however, the ‘odd’ planar cells of **5CB** and **8CB** doped with **Au1** or **Au2** were used to measure the electro-optic effects (data collected in Table 2) to allow for alignment-independent measurements and comparison of the electro-optic properties of all cells doped with the gold nanoparticles **Au1–Au4**.

- [22] For a recent example of random planar anchoring of 5CB on/between untreated glass, see: J.-W. Park, J. Cho, E. L. Thomas, *Soft Matter* **2008**, *4*, 739-743.
- [23] M. F. Toney, T. P. Russell, J. A. Logan, H. Kikuchi, J. M. Sands, S. K. Kumar, *Nature* **1995**, *374*, 709-711.
- [24] The electro-optic data were measured with the single cell method described by Wu *et al.* built into the software of the automated liquid crystal tester (operating manual, LCAS I). For more details see: S. T. Wu, D. Coates, E. Bartmann, *Liq. Cryst.* **1991**, *10*, 635-646. The relationship between the splay elastic constant K_{11} and the threshold voltage V_{th} is given by: $K_{11} = \left(\frac{V_{th}}{\pi}\right)^2 \Delta\epsilon\epsilon_0$. The twist elastic constants K_{22} (values not shown) is estimated to be $0.6 \times K_{11}$ and the bend elastic

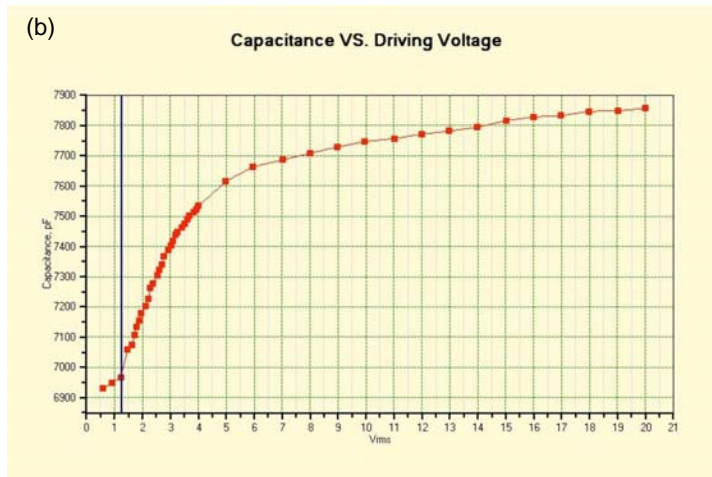
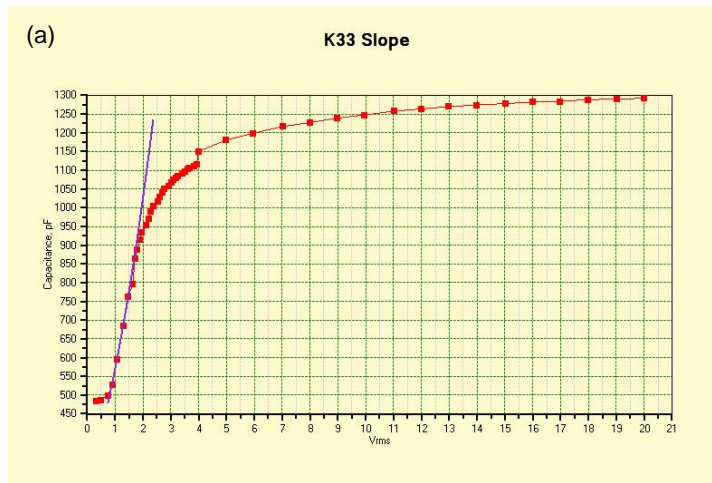
constants K_{33} (values not shown) is obtained from a curve fitting algorithm of the $C-V$ curve (see supporting information for some examples of $C-V$ curves obtained from the electro-optic tests).

- [25] For the alignment layer effect (i.e., pre-tilt) in VA mode cells see, for example: M. Jiao, Z. Ge, Q. Song, S.-T. Wu, *Appl. Phys. Lett.* **2008**, *92*, 061102. Remember that the NPs presented here induce vertical alignment between untreated glass slides and two of them also in planar test cells.
- [26] U. Drechsler, B. Erdogan, V. Rotello, *Chem. Eur. J.* **2004**, *10*, 5570-5579.
- [27] See, for example : C. Vilain, F. Goettmann, A. Moores, P. Le Floch, C. Sanchez, *J. Mater. Chem.* **2007**, *17*, 3509-3514.

Appendix E

Supplementary Information for Chapter 10

Selected C-V plots from EO measurements



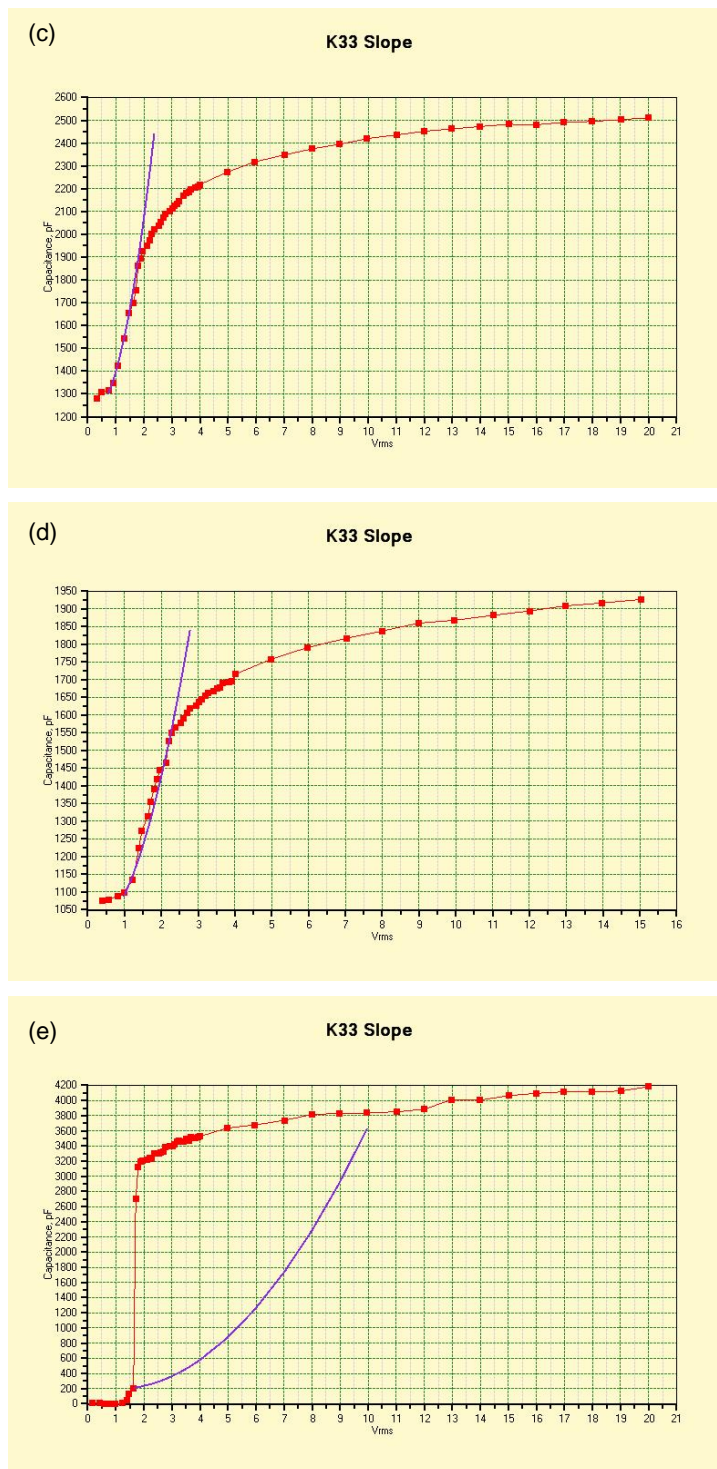


Fig. S10.1. Selected C - V plots (red) and slope of K_{33} (for some plots) at $T_{\text{Iso/N}} - T = 6 \text{ }^\circ\text{C}$ of: (a) pure **5CB**, (b) **5CB** doped with 5 wt% **Au1**, (c) **5CB** doped with 5 wt% **Au3**, (d) **8CB** doped with **Au3**, and (e) **8CB** doped with 5wt% **Au4**.

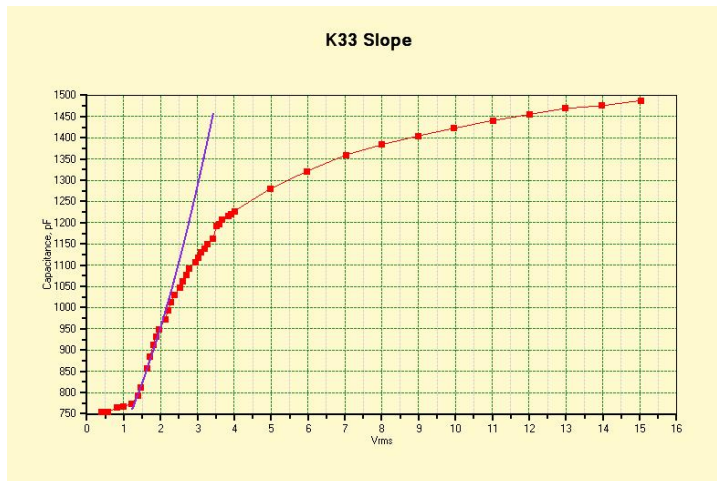
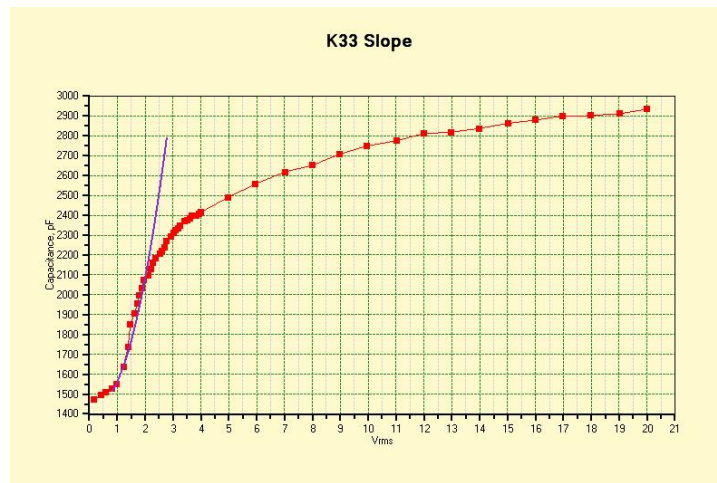
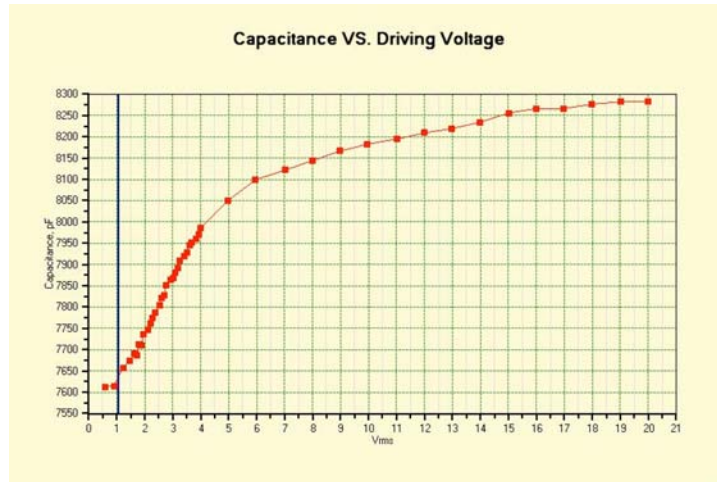


Fig. S10.2. Selected C - V plots (red) and slope of K_{33} (for some plots) at $T_{\text{Iso/N}} - T = 3 \text{ }^\circ\text{C}$ of: (a) **5CB** doped with 5 wt% **Au1**, (b) **5CB** doped with 5 wt% **Au3**, (c) **8CB** doped with **Au3**.

Graphical summary of EO data

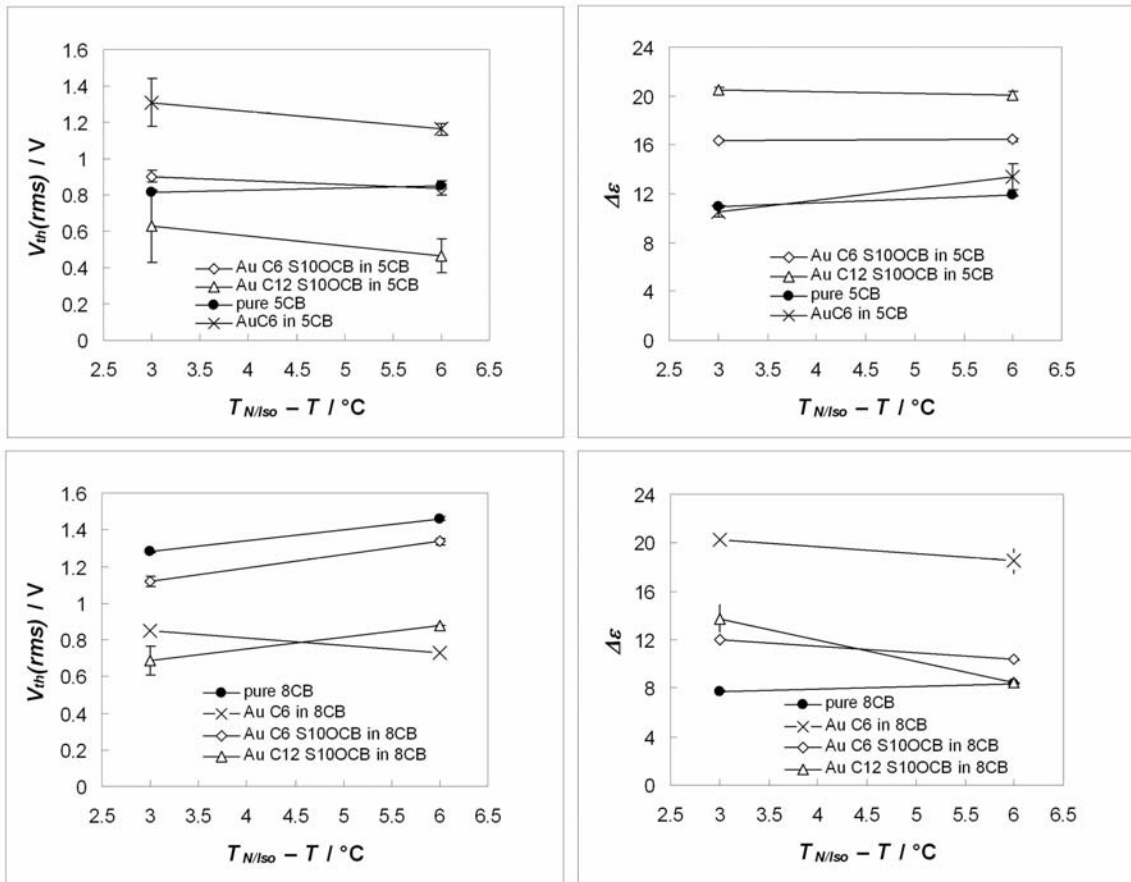


Fig. S10.3. Threshold voltage and dielectric anisotropy vs. reduced temperature for **Au1–Au4** in both **5CB** and **8CB**. Lines between data points are used to show trends (rise or fall of V_{th} or $\Delta\epsilon$) with decreasing temperature (normally no line would be drawn between only two data points).

Elemental analysis on two selected Au NPs (**Au1** and **Au2**)

Table S10.1. Elemental analysis for **Au1** and **Au2**^a

Au NPs	%C found	%H found	%N found	%O found	%S found	%C calc.	%H calc.	%N calc.	%O calc.	%S calc.
Au1 ^b	9.32	1.68	-	-	4.14	9.95	1.99	-	-	3.79
Au2 ^c	17.30	2.13	0.69	0.80	3.18	17.16	2.32	0.94	1.03	2.85

^a Terazzi *et al.* prepared an excellent list of common polyhedron associated to metallic nanoparticles and listed specific properties such as volume (*V*) and surface (*S*). Their calculations with respect to elemental analysis also showed that assuming both a spherical or a polyhedron model give essentially identical theoretical values for %C, %H, etc. [1] Using these calculations, we assumed a spherical shape of our Au NPs, and used the size determined by analyzing TEM images for the calculation of the expected composition. ^b The average formula for **Au1** based on the size measured by TEM (1.59 nm) is Au₁₂₃(SC₆H₁₃)₃₇. ^c The average formula for **Au2** based on the size measured by TEM (1.85 nm) and taking a 1:1 ratio of both thiols as determined by ¹H NMR (prior and after I₂ decomposition [2]) is Au₁₉₇(SC₆H₁₃)₂₅(SC₁₀H₂₀O-C₆H₄-C₆H₄-CN)₂₅.

References

- [1] B. Donnio, P. García-Vázquez, J.-L. Gallani, D. Guillon, E. Terazzi, *Adv. Mater.* **2007**, *19*, 3534-3539.
- [2] For the use of the I₂-decomposition method and subsequent analysis of the disulfides by ¹H NMR see: A. C. Templeton, M. J. Hostetler, C. T. Kraft, R. W. Murray, *J. Am. Chem. Soc.* **1998**, *120*, 1906-1911.

Chapter 11: Conclusions, Future Work and Outlook

11.1 Conclusions

The goal of the work summarized in this thesis was to gain deeper insights into structure-property relationships of thermotropic liquid crystal - gold NP composites. Over the past few years, LC nanocomposites have emerged as one of the most promising topics in liquid crystal R&D with fascinating opportunities for both basic research and device applications (in the high tech and medical device sectors).

Several original and important contributions to this area have been discussed in this thesis. These contributions include: (1) Tuning the functionality of the Au NP surface, for example, from hydrophobic to hydrophilic can result in mesophase stabilization as well as inducing a different phase morphology in the case of bolaamphiphilic tri-block LC molecules. (2) Novel alignment and defect formation phenomena have been observed for non-chiral nematic LCs doped with non-chiral as well as chiral Au NPs. These include the formation of somewhat periodic, birefringent stripe patterns that are separated by domains with NP-induced homeotropic alignment of nematic LC molecules. (3) It was shown that chirality can be transferred from a chirally-decorated Au NP to nematic LC hosts providing the first example of NP-induced chirality in a condensed phase. (4) A powerful methodology has been developed to study the origin of chirality in chiral ligand-capped Au NPs. (5) An unprecedented, thermal history-dependent dual alignment and electro-optic switching mode was observed for Au NP-doped nematics in polyimide-coated ITO test cells commonly promoting planar alignment. (6) This dual alignment and electro-optic mode was also extended to nematic LCs doped with

alkylthiol-capped Ag NPs, CdTe quantum dots as well as much larger Au NPs (5 - 6 nm in diameter). (7) Finally, the thesis addresses the conundrum of compatibility enhancement between LC and NP by investigating nematic LCs doped with NPs that are decorated with a structurally related nematic LC. These studies showed that widely accepted solubility/miscibility rules for organic additives in LC phases do not apply to NP dopants.

To summarize these contributions, we have learned that how to tune structure-property relationships between LCs and NPs, that NPs are capable of at least one-dimensional self-assembly in nematic LC hosts, that chirality can be transferred from a chiral NP to a bulk LC phase, and that NP doping can be used to control LC alignment and improve electro-optic properties of nematic LCs.

We have gathered some fundamental insights into structure-property relationships, which could be used as a guide for a more rational design of NP dopants for LC applications. In addition, some of the presented results are in contrast to what was previously described in the literature, for example to reports indicating that NPs below a certain size regime (<10's of nanometers) are 'invisible' to the LC host phase (macroscopically no difference to the un-doped phase) [1]. The macroscopic induction of a chiral nematic phase using chiral-decorated NPs shows, for example, those NPs as small as 1-5 nm are not invisible to the LC host.

Self-assembly, i.e., LC and LC defect-driven self-organization of NPs in LC hosts is one of the most basic principles for almost all phenomena described in this thesis. Experiments that would provide a direct proof of all types of self-assembly in these systems are still ongoing in our lab, and a precise knowledge of the locations of the NPs

is believed to be the key for a further development of Au NP-doped nematic LCs. An image of the one-dimensional, chain-like array of the Au NPs in a nematic host would provide undisputed evidence of a type of LC-guided NP self-assembly driven by defect formation (and controllable by temperature) that is quite different from all other assembly techniques described in the introduction of the thesis such as chemical linking via dithiols or using DNA.

Providing TEM-based evidence that the remaining part of the NPs can segregate to the interfaces and re-disperse in the bulk driven by electric fields would show that these processes are “dynamic” and not “static”, which could provide the basis for new types of sensors. In principle, one could use the fact that the suspended NPs (or other nanoscale entities) have a temperature - as well as electric field - dependent solubility or tendency to be finely dispersed.

Chirality is another intriguing part of this thesis. While there are many ways to create periodic, birefringent stripe patterns in nematic LCs (using patterned surfaces [2] or photolithographic techniques using azo-dyes [3]), the striking similarity of the nanoparticle-doped nematic textures with planar chiral nematic textures with large helical pitch prompted a lot of curiosity. While the formation of topological defects near the glass/LC interface (that could also be interpreted as surface inversion walls) inducing the chain-like aggregates of NPs appears as the best model so far, the reflection of light of these stripe domains with un-crossed (parallel) polarizers (see Fig. 5.5) also indicates a local twist in the director configuration (i.e., that local chirality with a rather tight helical pitch is present). This lead into the discussion of the racemic mixtures obtained in the synthesis of non-chiral Au NPs (non-chiral thiol ligand-protected Au NPs) in the

extended discussion of the CD signal in the support information of chapter 5 which found further experimental proof in a breakthrough study by the Kornberg group [4].

A burning question would be, to what extent could the racemic nature of non-chiral ligand-capped Au NPs contribute to the birefringent stripe textural phenomenon? Is there a remote possibility of enantioselective segregation of the Au NPs in the nematic LC phase? The chiral ligand-capped Au NPs are much easier to understand. With the broad use of organic chiral dopants in nematic LC for display application using the TN or STN mode [5, 6], as well as in surface-stabilized ferroelectric LC displays using the chiral smectic-C phase [7, 8], chiral metal nanoparticles could open a new opportunity of inducing and tuning the chirality of LC host phases by NPs.

This also leads to the development of a powerful methodology to study the chirality of Au NPs using the same chiral ligand-capped Au NPs used as chiral dopants. The methodology described in this thesis could be applied to all other (past and future) chiral-ligand-capped nanoparticles to evaluate or exclude contributions from the three mechanisms proposed by Whetten *et al.* in their first experimental study of chiral Au NPs [9]. This established protocol, particularly post-NP synthesis racemization reactions, could potentially be a benefit for this entire area of research including future studies on carbon nanotubes [10, 11] and other nanoparticles not only containing Au or Ag. In general, it is anticipated that chirality in nanomaterials (or chirality at the nanoscale) will become a fascinating area of nanomaterials research.

Other groups also reported the control of alignment of LCs by doping with silsesquioxane NPs [12, 13] following our initial demonstration that homeotropic alignment of nematic LC molecules can be obtained independent of the cell's alignment

layers by doping nematic LCs with ‘simple’ alkylthiol-capped AuNPs. A comparison of these studies covering a range of NPs from siloxane-based NPs over metal NPs to CdTe quantum dots seems to indicate that this alignment induction is a universal phenomenon, if the NPs are properly modified to achieve the right solubility in a given nematic LC host. Compared with the traditional methods of surface modification to induce LC alignment, using NPs could be a new concept with great simplicity. The dual alignment phenomenon discussed in Chapter 8 could also have a profound impact on current flat panel LC display as well as LC sensor related applications, as it allowed for a merger of two, currently separated systems (IPS and VA mode), which require two different types of LC materials (one with positive and another one with negative dielectric anisotropy), to one single system. In addition, lower threshold voltages and altered/improved dielectric and elastic properties of nematic LCs and LC mixtures obtained by NP doping will continue to attract interest for NP-doped LC mixtures for display applications. To use LC/Au NP composite for real applications, a number of requirements are needed; Chapter 10 is regarded as the starting point for this type of research. Miscibility as well as long-term stability is not the only, but one of the most important aspects that need to be addressed. Based on these results, more careful NP designs are needed, rather than simply matching the structure between the protecting groups of the Au NPs and the LC host.

11.2 Future Work and Outlook

As highlighted in the Conclusion section, there are numerous questions and opportunities which will continue to drive this area of LC nanoscience forward. These questions and opportunities include, but are not be limited to the follow aspects: (1) The

search for a direct proof and visualization of the NP locations in nematic hosts either by using polymerizable nematic mixtures that can be isolated as thin films and sectioned for TEM or by using fluorescence confocal polarizing microscopy introducing small amounts of an anisometric luminescent dye [14, 15]. (2) The development of other chiral-ligand-capped nanomaterials that can be used to transfer chirality from NPs to other LC phases such as the SmA or SmC phase (electroclinic and ferroelectric switching). (3) A more extensive and systematic study of the electro-optic properties of LC/NP composites in conjunction with industry partners will offer true benefits to the flat panel LCD industry. (4) A rational design of nanomaterials with different shapes (e.g. rods), core materials (e.g. Si), and other surface functionalities will provide new opportunities not only for display-related NC nanocomposites.

At this point in time and considering world-wide research progress in the area of LC nanocomposites, there seems to be enough evidence that liquid crystal-nanoparticle composite research and development will become one of the most exciting areas within the LC community. The outcomes of these research initiatives will create benefit for both research themes Liquid Crystals and Nanoparticles. New NP arrays that can be manipulated by electric fields or temperature using LCs will stimulate nanomaterials integration into devices, and new types of nanomaterials will likely lead to more energy-efficient applications of LCs in flat panel as well as flexible displays or lead to the creation of novel types of sensors – even for medical applications such as optical sensing of proteins and other biomolecules [16 - 18].

References:

- [1] Y. Reznikov, O. Buchnev, O. Tereshchenko, V. Reshetnyak, A. Glushchenko, J. West, *Appl. Phys. Lett.* **2003**, *82*, 1917-1919.
- [2] B.-W. Lee, N. A. Clark, *Science* **2001**, *291*, 2576-2580.
- [3] T. Galstian, Y. Chenard, Y. Zhao, *Opt Lett.* **1999**, *24*, 1865-1867.
- [4] P. D. Jadzinsky, G. Calero, C. J. Ackerson, D. A. Bushnell, R. D. Kornberg, *Science* **2007**, *318*, 430-433.
- [5] M. Schadt, W. Helfrich, *Appl. Phys. Lett.* **1971**, *18*, 127-128.
- [6] S. T. Wu, C. S. Wu, *Appl. Phys. Lett.* **1996**, *68*, 1455-1457.
- [7] N. A. Clark, S. T. Lagerwall, *Appl. Phys. Lett.* **1980**, *36*, 899-901.
- [8] R. P. Lemieux, *Chem. Soc. Rev.* **2007**, *36*, 2033-2045.
- [9] T. G. Schaaff, R. L. Whetten, *J. Phys. Chem. B* **2000**, *104*, 2630-2641.
- [10] M. De, P. S. Ghosh, V. M. Rotello, *Adv. Mater.* **2008**, *20*, 4225-4241.
- [11] V. Kitaev, *J. Mater. Chem.* **2008**, *18*, 4745-4749.
- [12] C.-W. Kuo, S.-C. Jeng, H.-L. Wang, C.-C. Liao, *Appl. Phys. Lett.* **2007**, *91*, 141103.
- [13] W.-Y. Teng, S.-C. Jeng, C.-W. Kuo, Y.-R. Lin, C.-C. Liao, W.-K. Chin, *Opt. Lett.* **2008**, *33*, 1663-1665.
- [14] I.I. Smalyukh, S.V. Shiyonovskii, O.D. Lavrentovich, *Chem. Phys. Lett.* **2001**, *336*, 88-96.
- [15] I.I. Smalyukh, O.D. Lavrentovich, in *Topology in Condensed Matter*, 205-250, M. Monastyrsky, Ed. (Springer, Berlin, **2006**).
- [16] C-H. Jang, L. L. Cheng, C. W. Olsen, N. L. Abbott, *Nano Lett.* **2006**, *6*,

1053-1058.

- [17] N. A. Lockwood, J. C. Mohr, L. Ji, C. J. Murphy, S. P. Palecek, J. J. de Pablo, N. L. Abbott, *Adv. Funct. Mater.* **2006**, *16*, 618-624.
- [18] V. K. Gupta, T. B. Dubrovsky, N. L. Abbott, *Science* **1998**, *279*, 2077-2080.